IDENTIFICATION OF THE MECHANISM OF OXIDE SCALE FRACTURE, AND ITS CORRELATION WITH STRAIN USING ACOUSTIC EMISSION

MICHAEL MARTIN NAGL

A thesis submitted in partial fulfilment of the
requirements of the Council of National Academic Awards
for the degree of Doctor of Philosophy

September 1992

The University of Glamorgan in collaboration with the
National Physical Laboratory (NPL)

Declaration

This thesis has not been nor is currently submitted for the award of any other degree or similar qualification.

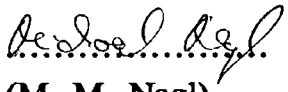

(M. M. Nagl)

Copyright

Acknowledgements

I would like to acknowledge with gratitude the guidance and encouragement offered by my Director of Studies, Dr. W. T. Evans and my other supervisors D. J. Hall and Dr. S. R. J. Saunders, throughout the period of this work. Thanks also to my adviser Prof. Dr. R. König for guiding me in this direction.

I would also like to thank the European Community for the financial support which was provided under the BRITE/EURAM-Program. The British Council provided a travel grant to Germany.

Further thanks are due to T. Tsongas for evaluating some of the commercially available coatings, Y. S. Chin for performing some of the signal analysis and D. Gohil for carrying out the X-ray strain measurements.

The help and support of members of staff at the University of Glamorgan and the National Physical Laboratory is also gratefully acknowledged.

Abstract

Thermally formed oxides scales can protect metals from aggressive environments at high temperatures. However the barrier function is destroyed when the oxide fails. Therefore a new 4-point bend test technique has been developed to measure the failure strains and to study the failure mechanisms of brittle layers in tension and compression. Tests were made with iron oxide and nickel oxide at room temperature and 550 or 900 °C, respectively, using strain rates of $\sim 10^{-4}$ and $\sim 10^{-5}$ s^{-1}. Brittle lacquer was used as a model layer. Acoustic emission (AE) was employed to monitor and interpret failure mechanisms together with post test metallography.

Equi-distant cracks were formed during failure in tension. Further cracking was affected by elastic and plastic stress relaxation processes, and interface delamination only started after these processes were exhausted. The crack spacing increased with oxide thickness and the results indicated that plastic relaxation processes were dominant at growth temperature conditions. The shear strength of the interface was lower at growth temperature.

Shear failure within the layer was found in NiO and brittle lacquer when tested in compression. Failure in iron oxide under compression always started at the interface. The failure mechanism and initiation in compression was determined by the relative shear strength of interface, the shear strength of the layer and the buckling stability of the layer. However, spallation always required crack growth at the interface.

Measured failure strains in tension and compression agreed well with the predictions of a model incorporating the fracture mechanics condition for tensile cracking or interface crack growth respectively and factors like residual strains, oxide creep and lateral oxide growth which accounted for the behaviour of a thin growing scale on a thick substrate. The critical fracture mechanics parameter in tension was the composite void size.

A K_{IC}-value of ~ 1.1 MN $m^{-3/2}$ was obtained for iron oxide for room temperature and 550 °C. Values of 0.41 and ~ 1.61 MN $m^{-3/2}$ were found for NiO at room temperature and at 900 °C, respectively. The residual growth stresses in iron oxide were determined as approximately zero and the cooling strain from 550 °C was ~ 0.05 - 0.06%. The residual stresses in NiO were ~ 175 MPa at room temperature. The strain energy release rate for interfacial failure in iron oxide was 27 J m^{-2} and the fracture surface energies were 3.4 and 0.8 J m^{-2} for iron and nickel oxide, respectively.

AE was a useful tool for explaining the failure mechanisms and a numerical analysis showed a slight difference in the AE signal released during tensile and compressive failure.

Table of Contents

List of Figures

a 10 μm thick iron oxide grown on mild steel and tested in tension at room temperature. 200

List of Tables

Nomenclature

A	Cross-section area; subscripts m and ox for metal and oxide, respectively
ΔA	Area of incremental crack growth
c	Composite void size
d	Specimen thickness
E	Young's modulus; subscripts m and ox for metal and oxide, respectively
E_{AE}	Energy of the acoustic emission signals
f	Crosshead speed
F	Fracture mechanics factor depending on shape, size and position of the void
F_n	Normal force in oxide or metal
F_s	Shear force in a unit depth cross-section of the oxide
g	Stress wave amplitude associated with the crack growth
G_{IC}	Critical energy release rate
h	Thickness; subscripts m and ox for metal and oxide, respectively
h_c	Critical oxide thickness
K	Applied stress intensity factor
K_{IC}	Critical stress intensity factor or fracture toughness
k, k_1..	Constants
l	Length of the oxide/substrate system
L	Crack spacing
M_m	Membrane correction factor
N	Number of acoustic emission counts
p	Pressure amplitude
p_o	Reference pressure amplitude
Q_o	Shape parameter
r	Amplitude of the wavy interface
R	Radius of the delamination
R_c	Critical radius of delamination for spallation
s	Distance between the two outer rollers of the 4-point bend jig
t	Time
T	Temperature
ΔT	Temperature difference
T_m	Melting temperature
u	Distance between the outer and inner roller of the 4-point bend jig
V	Amplitude
V_o	Reference amplitude
w	Sliding length at the interface
W^*	Stored energy per unit volume layer

z	Distance from the source of the AE wave
α	Thermal expansion coefficient; subscripts ***m*** and ***ox*** for metal and oxide, respectively
λ	Absorption coefficient
γ	Fracture surface energy values; subscripts ***m***, ***ox*** and ***interface*** for metal, oxide and interface, respectively
$\dot{\gamma}$	Shear strain rate
ϵ	Applied strain
ϵ_c	Critical failure strain
ϵ_{cool}	Cooling strain
ϵ_{gr}	Oxide growth strain
ϵ_{lat}	Strain compensated by lateral oxide growth
ϵ_{pl}	Strain compensated by plasticity
ϵ_{th}	Thermal strains
ϵ_n^{max}	Maximum strain normal to the interface
ϵ_I^{init}	Critical strain for initiation of Route I failure
ϵ_{II}^{init}	Critical strain for initiation of Route II failure
ϵ_I^{spall}	Critical spallation strain for Route I failure, i.e. critical strain for crack propagation at the interface
ϵ_{II}^{spall}	Critical spallation strain for Route II failure
$\dot{\epsilon}$	Applied strain rate
$\dot{\epsilon_c}$	Critical strain rate
ζ	Crack length
ν	Poisson's ratio; subscripts ***m*** and ***ox*** for metal and oxide, respectively
ρ	Radius of Curvature
σ	Stress; subscripts ***m*** and ***ox*** for metal and oxide, respectively
σ_c	Critical failure stress
σ_{cool}	Cooling stress
σ_g	Average tensile stress in the oxide
σ_{gr}	Oxide growth stress
σ_r	Residual stress
σ_y	Yield stress
τ	Shear stress
τ_{max}	Maximum shear stress at the interface
τ_y	Shear yield stress
φ	Geometrical divergence

CHAPTER 1: Introduction and Terminology

1. INTRODUCTION AND TERMINOLOGY

1.1 Introduction

Components operating at high temperatures in aggressive environments have to withstand mechanical and chemical degradation arising from the operating conditions. The mechanical conditions require high static and dynamic strength at operating temperature. Chemical stability requires a high resistance against the attack of oxygen, sulphur, carbon, hydrogen, etc. The effects of a single form of attack are well researched and in most cases sufficient data and accurate models are available for the engineer to select the most suitable material.

In practice it is seldom the case that a single form of attack is dominant and in most high temperature environments situations exist in which different types of mechanical and chemical attack occur simultaneously [1]. Models have been developed to describe attacks in high temperature environments but they are not generally applicable for these interactions and only few data are available. In addition, as the complexity of the interactions increases, so too does the difficulty in simulating them in laboratories, and the results will be that much more specialised.

In the following, only the effects of oxidation and mechanical stress are considered. Three idealised failure scenarios are possible:

(i) The mechanical loading is the critical parameter and the effects of oxidation are negligible in the short and long term. This scenario is governed by the model of pure mechanical loading at operating temperature.

(ii) The oxidation rate determines the rate of material consumption and hence the rate of degradation and the influence of the mechanical loading is minute. This case can be approximated by the sole use of the kinetic oxidation laws.

(iii) Mechanical loading and oxidation interact. The laws for scenario (i) and (ii) are not applicable and new models have to be established for the different conditions.

In practice the borders between the scenarios are not clear and the presence of oxygen has a small effect on scenario (i) even though the mechanical loading is the determining process [1].

Oxide scales are formed at the surface of metal components as a result of a reaction between metal and oxygen at elevated temperatures. Unlike other chemical reaction products, oxide scales can be beneficial in high temperature applications because they can act as hard resistant surface layers which increase the wear resistance of the materials. Oxides are also chemically stable and act as diffusion barriers, which reduce the rate of further attack. However, in most practical applications these protective layers are stressed, either by externally applied loads, by oxide growth

stresses or by thermal stresses induced by the mismatch of the thermal expansion coefficients of oxide layer and substrate. Oxide scales are therefore prone to mechanical failure, because they are ceramic materials, and thus do not have the ductility of the underlying metal [2]. The diffusion barrier function is destroyed when oxide failure occurs which allows the oxygen to regain direct access to the metal. This has the most severe consequences when delamination and spallation of large areas of oxide exposes clean metal surfaces leading to a sharp increase in the oxidation rate and breakaway kinetics.

It is almost impossible to achieve both good mechanical stability of the oxide and a low oxidation rate or a low rate of material consumption, because high mechanical stability requires good deformation properties, i.e. high creep rates. However, the creep rate is determined by the slower moving elements in the oxide whereas the oxidation rate is determined by the faster moving elements. Therefore the task is to arrive at the best trade-off between good deformation properties and low rate of material consumption in order to achieve a maximum component lifetime. This requires a detailed knowledge of both the oxidation characteristics of the substrate and the mechanical failure behaviour of the oxide in tension and compression.

This study has been focused on the deformation and failure behaviour of oxides at room temperature and growth temperature (see also section 2.1). To date, many hypotheses and mechanisms for the oxide failure in compression have been proposed [e.g. 3-7] and these are outlined in section 2.1.2.4. The underlying theory for oxide failure in tension is simpler and better understood [e.g. 3,8-10] (see also section 2.1.2.3). However, for both cases only very limited experimental data are available. These are for oxide failure in compression mainly on Cr_2O_3 [e.g. 5,6,11,12] and were obtained only by detecting the onset of cracking and spalling during cooling and not by mechanical loading in compression. In this context thermo-cycling and cooling or heating can be regarded as another form of mechanical loading, where stress and strain rate depend on the relative magnitude of the expansion coefficients and the rate of cooling/heating. Other areas of major concern have been the effects of low deformation rates $< 10^{-6}$ s^{-1} and low cyclic fatigue deformation on the growth, creep and creep failure behaviour of oxide scales [13-18].

However, hardly any work has been done with deformation rates $> 10^{-6}$ s^{-1} and only little experimental data are available for scale deformation at oxide growth temperature [2,13,18,19]. The present study was therefore devised to establish failure strains and the failure behaviour for oxides in tension and compression at room temperature and at growth temperature using strain rates of $\sim 10^{-4}$ s^{-1} and $\sim 10^{-5}$ s^{-1}.

Acoustic Emission (AE) has been known for many years as a remote monitoring technique which can be used to record acoustic waves generated by the sudden release of strain energy during plastic deformation or cracking. Its capabilities in detecting and

locating remote cracks has been demonstrated mainly in pressure vessel testing and fracture mechanics testing. Detection of fracture processes at high temperatures can be achieved by placing the transducer away from the source of emission, e.g. outside the furnace. Its higher sensitivity in recording oxide failure compared to other techniques is now generally acknowledged [20]. Therefore, AE has been used in the present study to monitor oxide failure and to characterise the different stages of the entire failure process together with optical and electron microscopy. Preliminary work has also shown that two distinctive signal shapes existed in tests with the oxide in tension and compression (Figure 1.1) [21] and it was believed that this would allow a determination of the failure mode, i.e. tension or compression. Importantly, it has also been shown previously that different sources give rise to different AE signals [22] and that the same sources show reproducible AE signals [23].

This study was the first where oxides grown under identical conditions have been tested under externally applied load in tension and compression using strain rates $> 10^{-5}$ s^{-1}. Therefore a new 4-point bend test technique has been developed using specimens that had an oxide raft of 10x10 mm on only one side which could be placed between the inner rollers of the bend jig (Figure 1.2). Compressive and tensile forces were applied by placing the oxide on the top or bottom side within the jig. The sample was coupled to an AE system in order to monitor failure. AE was also used more comprehensively than thus far in oxide testing. The variation of AE parameters, such as energy counts etc. with strain was investigated as well as the signal shape. The aims of the project were:

(i) to measure oxide failure strains in tension and compression
(ii) to obtain other oxide parameters such as fracture toughness, interfacial strength etc.
(iii) to improve the understanding of the oxide failure mechanisms
(iv) to establish a more general model for oxide failure
(v) to maximise the use of AE in characterizing oxide failure mechanisms and failure modes, i.e. tensile or compressive.

However, several obstacles had to be overcome before the experiments began. Firstly, a method had to be found to produce an oxide area of 10x10 mm on only one side of the bend test specimens for tests at room and at oxide growth temperature condition (see also section 3.2.4). In this context only two of the investigated techniques solved the problem satisfactorily:

(i) mechanical abrading of the oxide from all sides except for an oxide raft on one side for the tests at room temperature and
(ii) selective oxidation using commercially available coatings which reduced oxidation considerably but did not eliminate it for the tests at room and at growth temperature. In this context tests were made at room temperature on samples

oxidised with or without protective coating and oxide structure, failure strains, crack patterns and AE were compared to verify whether the coating interfered with oxidation or changed the oxide failure characteristics. The selected coating was not universally applicable for the different materials being tested and hence the selection procedure had to be repeated for each newly tested material.

Secondly, an environmental furnace with a ceramic 4-point bend test assembly was acquired for the tests at oxide growth temperature (Figure 1.3). In this case the signals were transmitted outside the furnace by using an acoustic waveguide or an elongated specimen as its own waveguide. Resulting signal distortion had to be kept to a minimum so that signal shapes could be analysed and compared with signals obtained in the tests at room temperature where the AE transducer could be coupled directly to the specimen. An elongated specimen was selected as waveguide, because it offered the best solution compared to other waveguides (see also section 3.2.3).

Finally, it was necessary to minimise the background noise level during all stages of the development (see also section 3.6.1). Similarly the influence of the experimental arrangement on the signal shape was investigated since the two distinctive signal shapes shown in Figure 1.1 could have been due to the experimental configuration (see also section 3.2.2).

After having solved these problems, the first tests were performed with iron oxide. The test programme was started with the tests at room temperature because of the simple experimental arrangement. In this case it was possible to relate AE directly to the progress in oxide fracture by stopping the tests at different strain levels and to correlate the increase in damage with the increase in AE. Thus expertise in interpreting AE from oxide failure was gathered. Subsequent tests were made at oxide growth temperature in tension and compression. However, AE caused by the coating or the unwanted oxide underneath the coating, interfered with the normal observations in compression at higher strains (see also section 4.1.2) and failure could not be detected using AE. At this stage it was decided to test additional coatings in the hope of finding a more effective material. Unfortunately, none of the new coatings performed better and more promising, but also more expensive coatings such as amorphous silica layers, were not available for the present study. Thus the tests at growth temperature with the oxide in compression were limited to the observation that failure strains were higher than at room temperature, but it was not possible to say when exactly the oxide would fail.

Nickel was used as a second material because of its uniform oxide which is easy to model. As mentioned above a new coating had to be selected for nickel which reduced or stopped oxidation and, at the same time, did not interfere with the oxidation process. Although the selected coating stopped oxidation almost completely, it became a sticky liquid at 900 °C. Therefore the rollers of the bend jig had to be covered with

additional disposable ceramic parts in the tests at growth temperature to avoid contamination of the rollers. Fortunately, the ceramic parts did not cause additional noise and hence the experimental arrangement could be used without further modifications for the tests at growth temperature. As in the tests with iron oxide no complications arose, except for the tests at oxide growth temperature with the oxide in compression. The oxide could not be strained to failure, and observations were stopped at a maximum strain of 2.8% where the oxide had not fractured at 900 °C. These complications arose due to the limited movement within the furnace.

Brittle lacquer was used as a model layer for oxide failure and tests were made simultaneously to the work on oxides. This material was chosen because of its brittle nature and it was believed that it would be a good simulation of the failure modes expected in the oxide systems. Samples were easy to prepare because brittle lacquer rafts could be produced by masking the sample prior to spraying. The same experimental configuration was used for the tests in tension and compression (see also section 4.3).

The results from the three materials are compared in section 4.4. Generally, crack patterns were established by optical and electron microscopy and AE provided additional information to assist in explaining the failure mechanisms.

Furthermore, the AE signal of a few representative tests from all materials were analysed using the signal shape, auto-correlation and fast fourier transformation (FFT) in order to see whether the AE technique was able to determine the mode of failure, i.e. tension or compression without the support of microscopy (see also section 4.5). As shown here, there was evidence of a slight difference in the AE signals from tensile or compressive failure. However, the results were not significant enough to determine the mode of failure on the basis of a few AE signals.

The new 4-point bend test technique was capable of producing important new experimental data on the mechanical behaviour of brittle layers which was required to validate a more comprehensive model for oxide failure (see also section 4.4). In this context AE provided crucial information to improve the understanding of the failure mechanism, which was complimented by the microscopic studies.

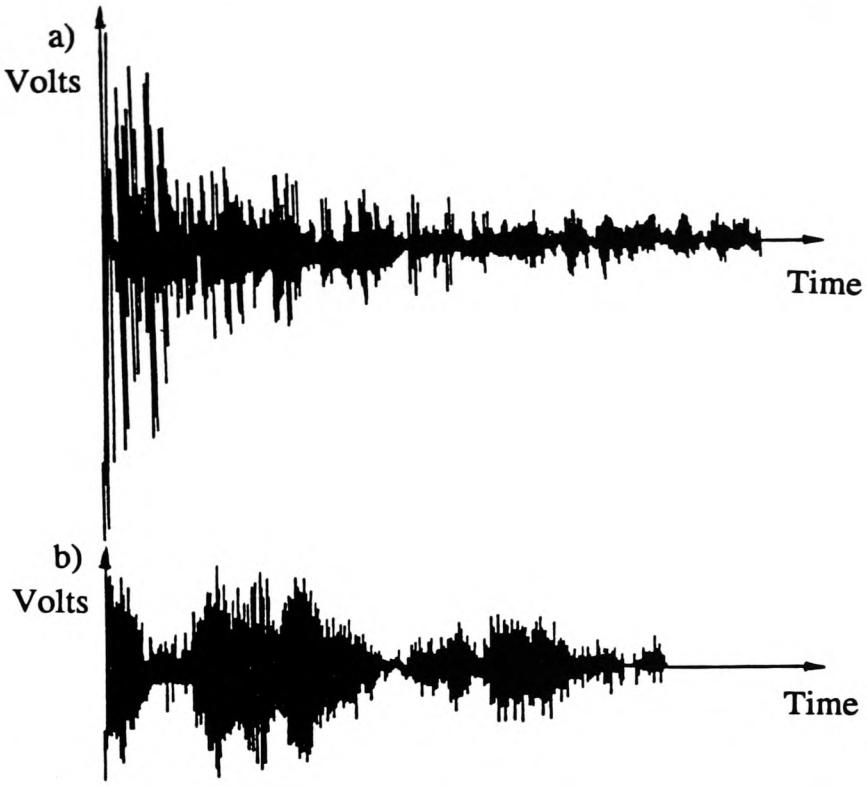

Figure 1.1: AE signals showing the characteristic shape of (a) a tensile or (b) compressive failure event [21].

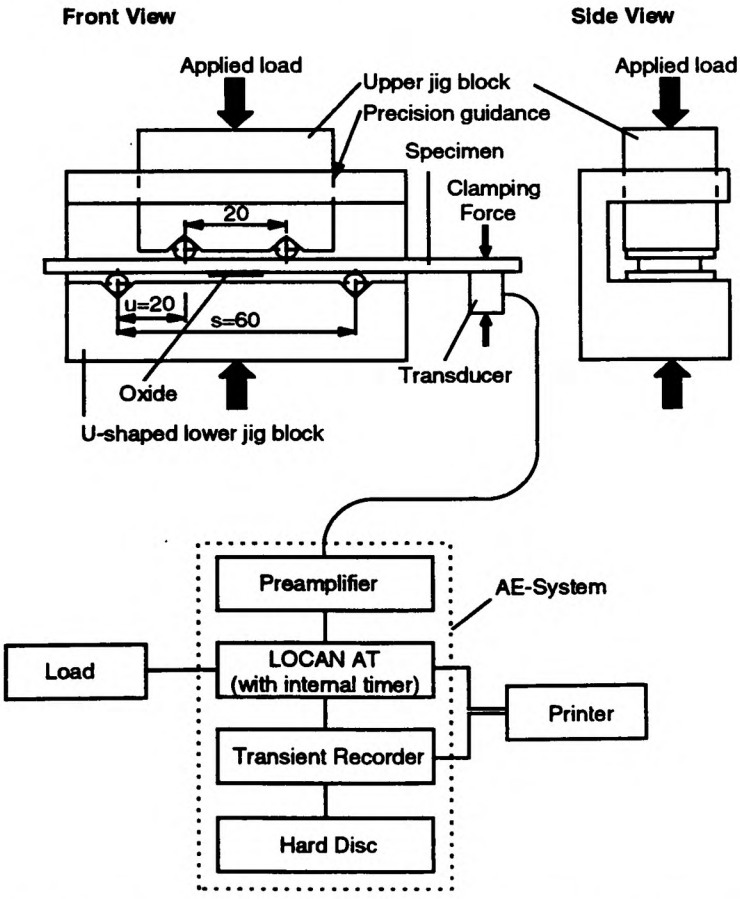

Figure 1.2: Schematic diagram of the experimental arrangement for the room temperature tests.

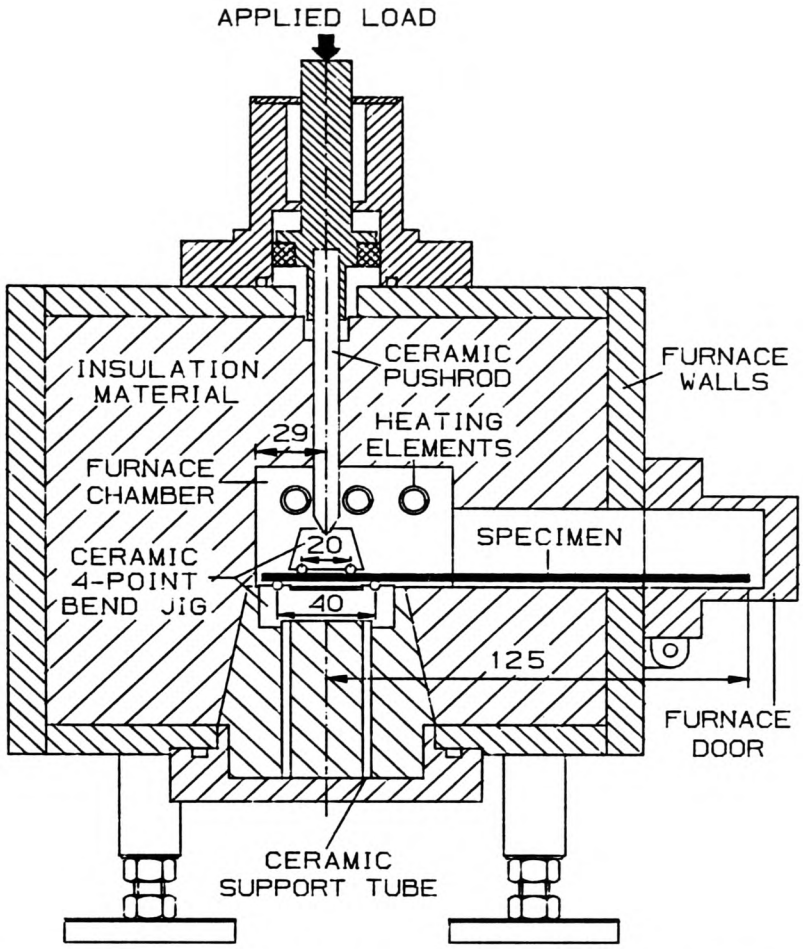

Figure 1.3: Schematic diagram of the high temperature bend test furnace showing the specimen location.

1.2 Terminology

Microcrack/Macrocrack: Both terms are frequently used in the literature, although most of the quoted work does not give a clear distinction. In this work, the term microcrack was used for cracks which were shorter than three times the average grain size of the oxide and macrocrack was used for longer cracks.

Plasticity of oxides scales: was understood as any type of deformation (including time dependent creep) allowing strains larger than those that could be expected from linear elastic behaviour to be accommodated by the oxide.

Wrinkle/wrinkled area: was a small grown dome or delamination with relative high curvature and no cracks (Figure 1.4a).

Buckle/buckled area: was a larger area of delamination with cracks at the points of highest curvature. In this case the oxide particles seemed to physically support each

other (Figure 1.4b).

Calibration specimens: were samples which had undergone exactly the same preparation and oxidation procedure as all specimens of the same type, except that no metal surface was directly exposed to oxygen, i.e. no oxide layer was present during the bend test. These specimens were tested in so called **'calibration tests'** using the same experimental configuration as in the test with an actual layer to establish the necessary threshold and to check the experimental arrangement at regular intervals.

Hit/Event: are commonly used in AE terminology and stand for a single signal or waveform (Figure 1.1).

Tensile signal/shape: characterised AE signals with an exponentially decaying amplitude (Figure 1.1a)

Compressive signal/shape: characterised AE signals whose amplitude periodically increased and decreased, showing a kind of echo (Figure 1.1b).

High/low activity: was a measure of the rate with which AE signals were released.

High/low intensity: was a measure of the amplitude or energy of the AE signals.

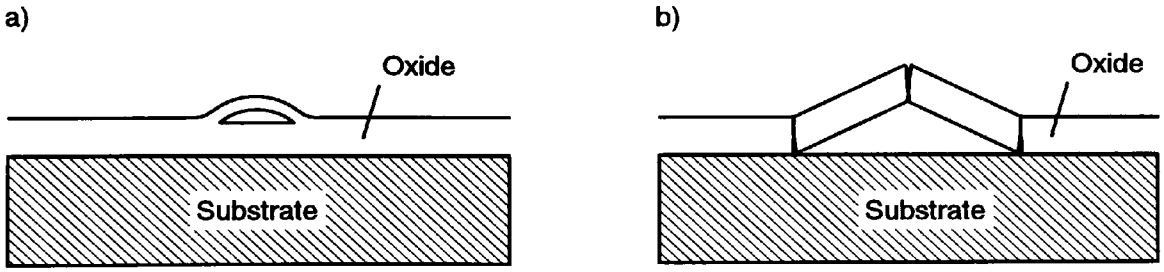

Figure 1.4: Schematic diagram showing a cross-section of (a) a wrinkle and (b) a buckle.

CHAPTER 2: Literature Review

2. LITERATURE REVIEW

There is a large body of published information available on oxides and oxidation of metallic materials. Most of this focuses on the oxidation behaviour of different alloys under specific conditions. In this review only publications on the mechanical stability of oxide layers were considered with particular emphasis on proposed failure mechanisms and models for prediction of failure. The stresses which cause failure were reviewed together with simple mechanical models which could be used to calculate these stresses. Stress induced oxide growth and plasticity which bypass failure were also discussed. Finally, the merits of different techniques for measuring oxide failure were evaluated before the chosen technique was discussed, together with results from previous applications. A small chapter on coatings was included because the samples were covered with a protective coating and also because many models which were developed for coating failure are also applicable for oxides, and *vice versa*.

2.1 Mechanical Stability of Oxide Scales

The formation of oxide scales is determined by the thermodynamic and kinetic laws of oxidation. Classic thermodynamics can be used to determine the temperature and the gas pressure at which oxide can be formed [20].

The kinetic laws determine the rate of oxidation. The growth of a layer can take place either by oxygen diffusion to the substrate (anion-transport), by metal diffusion to the surface (cation-transport) or by both at the same time. The diffusion can proceed through the grain and along grain boundaries. This results in power or logarithmic laws of oxidation or combinations of them depending on the structure of the scales and change of the diffusion parameters with increasing thickness. However, oxidation kinetics are changed considerably when the oxide fails. This phenomenon is termed breakaway oxidation because cracks destroy the barrier function of the oxide and create short-circuit paths which allow the oxygen direct access to the substrate, i.e. the oxidation rate returns to its initial high rate. It is, therefore, very important to maintain oxide integrity or at least be able to predict its failure.

2.1.1 Stresses in Oxides

Surface oxides grown on metal substrates fail at a critical stress. It is possible to determine the stress by considering the mechanical deformation of the composite. However, the oxide layer is commonly polycrystalline with varying grain structure, mechanical properties, inhomogeneous pore and flaw distribution and an indefinite interface between the metal and oxide. Furthermore, thin layers have a strong local

variation in thickness and finally, external loading stresses are superimposed onto the complex internal growth stresses acting in the oxides [18]. It is clear that such a system is complex. Nevertheless, it is necessary to describe the mechanical deformation of an idealised layer on a metal substrate on the basis of simple assumptions in order to understand the failure mechanisms proposed in the literature and to create a starting point for more detailed models.

In the following section such a treatment of the mechanical stresses is presented for an idealised oxide/substrate system on flat specimens. The consideration for oxide/substrate systems on circular specimens (i.e. tubes and wires) can be found elsewhere [18]. In addition, the sources of stresses in oxides and their measurement techniques are explained.

2.1.1.1 Sources of Stresses in Oxides

Growth stresses arise mainly from the volume change during formation of the oxide. It is suggested that if the ratio of volume of oxide to that of metal which it replaces, i.e. the Pilling-Bedworth ratio, exceeded unity, the oxide grows under compressive stress, or *vice versa*, but this only applies to oxide formed at the metal/oxide interface [20]. Growth stresses are mainly compressive because most materials exhibit a volume expansion during oxidation [4,24]. However there is still some discussion on how growth stresses develop from the volume change and how some of the stress is relieved during growth.

The other most common sources of stresses in oxides are thermal stresses due to cooling/heating or thermo-cycling as a result of differences in thermal expansion coefficients of metal and oxide [10]. Thermal stresses are also induced under thermal shock condition or when a heat flow is removed [10].

Similarly the substrate geometry can cause stresses, in particular at corners [25-26]. Finally mechanical stresses can arise in the oxide from axial loading or bending [10].

2.1.1.2 Mechanical Models for Stresses in Oxides

In the following analysis plasticity and creep effects are disregarded and elastic isotropy is assumed.

Growth stresses σ_{gr} are a result of volume change during growth, when the expansion of the scale ϵ_{gr} is suppressed without plastic deformation of the scale and substrate [18]. The condition of geometrical continuity and constraint for the composite system imposes mechanical stresses of opposite sign in both metal and oxide. The forces in metal and oxide must therefore be in equilibrium:

$$F_n = \sigma_m A_m = - \sigma_{OX} A_{OX} \qquad (2.1)$$

where the subscripts m and ox stand for metal and oxide respectively and σ and A are the stress and the cross-section area, respectively. Under the condition of elastic oxide and substrate deformation it follows that:

$$\epsilon_{gr} = \frac{\sigma_{OX}}{E_{OX}} (1-\nu_{OX}) - \frac{\sigma_m}{E_m} (1-\nu_m) \qquad (2.2)$$

where E is the Young's modulus and ν is the Poisson's ratio which is ~0.3 for most metals and oxides during elastic deformation [3]. The condition of constant volume results in a material independent value of 0.5 for plastic deformation [18].

Combining equation (2.1) and (2.2) the stress in the oxide is:

$$\sigma_{OX} = \frac{\epsilon_{gr} E_{OX}}{\frac{E_{OX}}{E_m} \frac{A_{OX}}{A_m} (1-\nu_m) + (1-\nu_{OX})} \qquad (2.3)$$

and in the substrate:

$$- \sigma_m = \frac{\epsilon_{gr} E_m}{\frac{E_m}{E_{OX}} \frac{A_m}{A_{OX}} (1-\nu_{OX}) + (1-\nu_m)} \qquad (2.4)$$

For very thin oxides or $A_{OX}/A_m \rightarrow 0$ the equation (2.3) can be rewritten as:

$$\sigma_{OX} = \frac{E_{OX}}{1-\nu_{OX}} \epsilon_{gr} \qquad (2.5)$$

Cooling or thermal strains arise in each layer independently according to:

$\epsilon_{th\ ox} = \alpha_{OX} \Delta T$

$\epsilon_{th\ m} = \alpha_m \Delta T$

where α is the thermal expansion coefficient and ΔT is the temperature difference. Both are assumed constant throughout the substrate and oxide. If different phases could expand and contract independently such thermal cycling or cooling would induce no stresses into the system [4]. However, geometrical continuity imposes mechanical strains in both layers. Strain compatibility demands that the total strain in both layers is equal at the interface, or that [4]:

$$(\alpha_m - \alpha_{OX}) \Delta T = \frac{\sigma_{OX}}{E_{OX}} (1-\nu_{OX}) - \frac{\sigma_m}{E_m} (1-\nu_m) \qquad (2.6)$$

The terms on the right side represent the mechanical strains which arise from the different expansion/contraction of oxide and substrate. A comparison of equation (2.2)

and (2.6) shows that they differ only in the term on the left side, i.e. the equations (2.3) - (2.5) can also be used to calculate thermal stress when ϵ_{gr} is replaced by $(\alpha_m - \alpha_{OX})\ \Delta T$.

The previous models were based on semi-infinite layers. However, actual oxide/substrate systems are of a finite length l. The normal tensile and compressive forces within the layers may then be supported by opposing shear stresses at the interface. If stress relief due to fracture, creep, bending, etc. is ignored, the shear force F_s in a unit depth cross-section of the oxide is [4]:

$$F_s = h_{OX}\ \sigma_{OX} \tag{2.7}$$

where h is the thickness. It can be balanced with the shear stress τ at the interface which is:

$$F_s = \int_0^{\frac{l}{2}} \tau(x)\ dx = \frac{\tau_{max}}{4}\ l \tag{2.8}$$

assuming an elastic situation with the shear stress increasing linearly from zero at the middle of the interface to a maximum at the end [4]. The value for the maximum interfacial stress τ_{max} follows using equations (2.3), (2.7) and (2.8):

$$\tau_{max} = \frac{4\ h_{OX}\ E_{OX}\ \epsilon}{l\left(\frac{E_{OX}}{E_m}\ \frac{A_{OX}}{A_m}\ (1-\nu_m) + (1-\nu_{OX})\right)} \tag{2.9}$$

where ϵ is either the oxide growth strain, the thermal strain or the applied strain. The interfacial shear stress increases linearly with the oxide thickness for small values of A_{OX}/A_m according to equation (2.9). Therefore, the thicker the oxide the more likely is oxide spallation via interfacial shear failure. It can also be seen that the oxide length l is a critical parameter which may vary from the dimensions of the alloy specimen itself, to the very small spacing between through-scale cracks or surface line defects (see also section 2.1.2.3) [4].

Tien and Davidson [4] derived the radius of curvature, the bending stresses and the bending moment which arises if a heat flow from the hotter gas/oxide interface to the colder oxide/substrate interface is present. Such a moment is basically the mechanical action which can cause the oxide buckling phenomenon (see also section 2.1.2.4). Since the oxide is constrained by the substrate a normal stress at the interface will be required to counteract the bending moment.

It is also interesting to note that when multi-layered oxides exist, then neither heat flow, phase transformations or non-homogeneities are needed for oxide buckling, because the differences in thermal expansion of the single oxide phases themselves will provide the bending moment within the multi-layer oxide scale. For example, a double

layered oxide should develop a radius of curvature ρ according to [4]:

$$\frac{1}{\rho} = \frac{6\,(\alpha_2-\alpha_1)\,\Delta T\,(1+m)^2}{n\left[3\,(1+m)^2 + (1+mn)\left(m^2 + \frac{1}{mn}\right)\right]} \qquad (2.10)$$

where $m=h_1/h_2$, $n=E_1/E_2$, and the subscripts 1 and 2 refer to the different phases.

As seen in equation (2.10) stress calculation for multi-layered oxides requires a knowledge of the material parameters for each single layer. On that basis mean values can be calculated treating the structure as a composite [27].

2.1.1.3 Measurement Techniques for Stresses in Oxides

There is currently no method available to measure the stresses in oxides during mechanical deformation [18]. X-ray strain analysis (X-ray diffraction) has been widely used to determine the residual and growth stresses present within the oxide scales. Other methods are based on the extension of a sample during oxidation or the deflection of a thin metallic strip oxidised on only one surface (deflection method) [28].

2.1.2 Options for Stress Relief in Oxide Scales

The substrate/oxide system can accommodate strain by elastic deformation. If the elastic limit is exceeded stress relaxation can take place by (i) stress induced growth processes, (ii) plastic deformation of oxide and/or metal and by (iii) mechanical failure of the composite. Failure can start within the oxide, the substrate or at the interface by delamination [27].

2.1.2.1 Stress Induced Growth Processess

Whisker formation is the most common stress induced growth process and is caused by compressive stresses arising from growth or phase transformation [27]. Similarly, stress induced lateral oxide growth can increase the critical failure strains during tensile loading with sufficient low deformation rates [10,13]. This was observed by Schütze [13] on 18Cr and 24Cr steel during deformation with rates $\leq 10^{-6}$ s^{-1} at 800 °C. The contribution of lateral oxide growth towards failure strains is difficult to assess. However a first valuable attempt was made by Schütze [29].

Importantly, both whisker formation and lateral oxide growth relax stresses and maintain the integrity of the oxide during deformation.

2.1.2.2 Plasticity of Oxide Scales

Plastic deformation of polycrystalline solids by dislocation glide requires five independent slip systems. However most of the oxides contain less than five independent primary slip systems. Below a transition temperature the stresses necessary to activate secondary slip systems are higher than those for the initiation of cracks. Therefore, below this transition temperature only elastic deformation of the oxide occurs before fracture, leading to extremely low fracture strains; unless a sufficiently high hydrostatic confining pressure is applied to prevent crack initiation and allow stresses high enough to activate secondary slip systems [9].

Frost and Ashby [30] analysed a wide range of experimental data on the creep of ceramic materials and developed so called deformation mechanism maps which summarise the information on the deformation behaviour of a material. These define ranges of dominance for the various deformation mechanisms as a function of applied stress and temperature and yield the resulting strain rate values. In the maps cracking is excluded by applying a sufficiently high hydrostatic pressure.

Schütze [9] developed deformation mechanism maps for oxides using the following fields (Figure 2.1):

(i) Plasticity, i. e. low temperature plasticity due to the motion of dislocation only.

(ii) Power law creep, i. e. glide plus climb of dislocations. For diffusion, lattice diffusion or dislocation core diffusion may dominate.

(iii) Diffusional flow; mechanical stress can induce a diffusive flux of matter through (Nabarro-Herring creep) and around (Coble creep) the oxide grains.

The equations that describe these mechanisms were taken from ref. 30. Schütze [9] also incorporated in these maps the critical stress σ_c at which an oxide would fracture depending on the composite void size (see also section 2.1.2.3), if no hydrostatic pressure is applied which would activate five independent slip systems. Therefore plastic deformation of the oxide is only possible at stresses less than σ_c. He obtained good agreement between experimental data and those from the respective maps for Al-, Cr-, and Ni-oxide. He also argued that the low failure strain values, even at strain rates where creep can contribute to deformation, should not be surprising, because it must be borne in mind that creep causes growth of the physical defects by vacancy transport and vacancy condensation. This increases the value of composite void size c and $\dot{\epsilon}_c$ (the strain rate below which creep can occur) is decreased. If $\dot{\epsilon}_c$ falls below the applied strain rate $\dot{\epsilon}$ sudden cracking occurs [9]. The void size can increase rapidly during creep due to an interaction or interlinkage of several coplanar physical defects lying close together [9]. Figure 2.1 can be used to determine the critical strain rate $\dot{\epsilon}_c$ below which creep can contribute towards the overall oxide deformation prior to failure.

The high strains of 2% found in oxide grown on mild steel (13CrMo44) at 873 K when deformed with a rate of $\sim 10^{-8}$ s^{-1} could be explained by plasticity [31]. At the same time Berchthold *et al.* [31] regarded lateral oxide growth as very unlikely in this case because oxide growth occurred predominantly by iron diffusion.

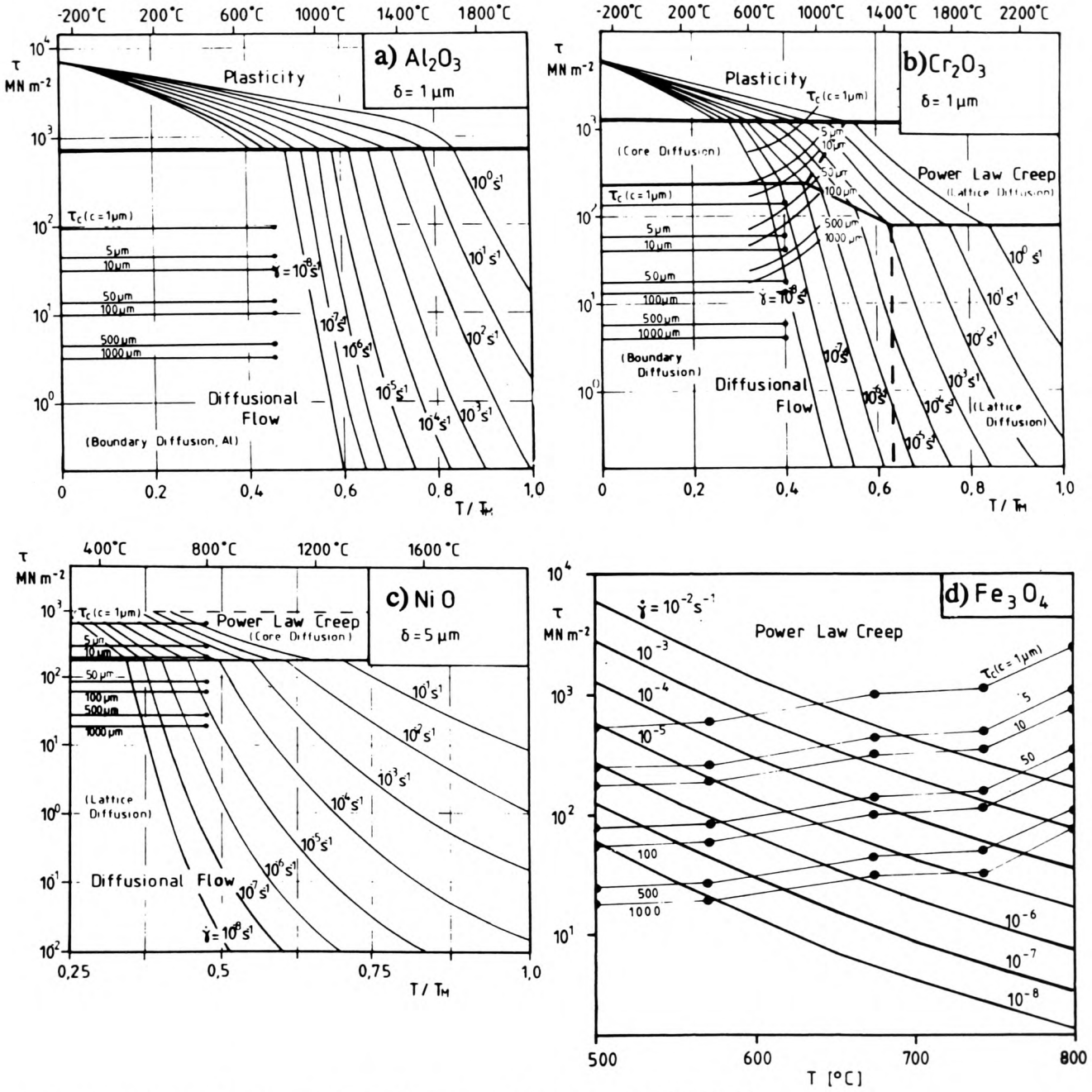

a) Al_2O_3, grain size δ = 1 μm; b) Cr_2O_3, 1 μm; c) NiO, 5 μm and d) Fe_3O_4.
where the shear stress τ is $\sigma/\sqrt{3}$ and the shear strain rate $\dot{\gamma}$ is $\dot{\varepsilon}\sqrt{3}$ assuming uniaxial tension.

Figure 2.1: Deformation mechanism maps for oxides with the grain sizes, δ. Lines for critical shear stresses τ_c, at which cracking occurs are also shown for different composite defect sizes, c [9].

One of the important differences between a bulk oxide and an oxide scale seems to be the effect of scale crack healing which gives rise to a type of 'pseudo-plasticity' of the scale under certain conditions [9]. Pseudo-plasticity can result from the combination of scale cracking and healing. At low strain rates the rate at which the scale crack faces move apart is lower than the oxide growth rate within the scale crack. Thus, the oxidation processes close the crack more or less instantly [9]. Examples of the healing of through-scale cracks can be found in refs. 13-15. Repeated cracking and healing can result in subsurface depletion of protective scale forming alloying elements [14] and a method for evaluating this process has been suggested [29].

Another form of pseudo-plasticity is quasi 'grain boundary sliding' by microcracking, oxide grain movement, and healing [9]. The critical strain rates assessed for pseudo-plasticity lie above or in the upper range of strain rates encountered in long term creep tests or under service conditions [9]. Therefore, it is not surprising that quite often macroscopically intact scales are observed even though the scale may have cracked several times [9].

Recent approaches suggest that microcracking can account for missing slip systems in brittle layers, e. g. MgO [18]. Microcracking increases the creep rate but reduces the Young's modulus of the layer [18,32,33] giving the layer additional plasticity [32]. This increases the critical failure strain but only as long as the crack tip stress fields of the uniformly distributed microcracks do not influence each other [27].

Finally, Barnes *et al.* [34] have shown that substrate creep can relieve some of the cooling stresses depending on the cooling rate, the creep properties of the substrate and the ratio of the metal thickness to oxide thickness.

All the mechanisms given in this section add to the overall deformation that the oxide can undergo before macroscopic failure. It can be determined from Figure 2.1 and from microscopic observations whether these mechanisms were active under the test conditions. However, at present it is impossible to quantify the strain increment they add to the measured failure strains, which would be vital for accurate predictions of failure (see also section 4.4). Therefore, it would be very important to have a set of data which show the contribution of lateral oxide growth and plasticity as a function of temperature and strain rate for the most important oxides.

2.1.2.3 Failure of Oxide Scales under Tensile Stress

Evans [12] proposed a failure mechanism for oxides under tensile stress. Accordingly first through-scale cracks develop at regions of high stress concentration, i.e. the oxide breaks up into a finite number of segments (Figure 2.2). Elastic stress relaxation in the vicinity of these cracks can reduce the local stress concentration within the oxide segment. Plastic stress relaxation within the oxide is possible if sliding can

occur at the oxide/metal interface [12]. The shear translation may induce fracture damage at the interface which could result in delamination and subsequent spallation [12]. Another mechanism producing plastic stress relaxation is substrate yielding at the base of through-scale cracks [3], however this should not lead to interface delamination.

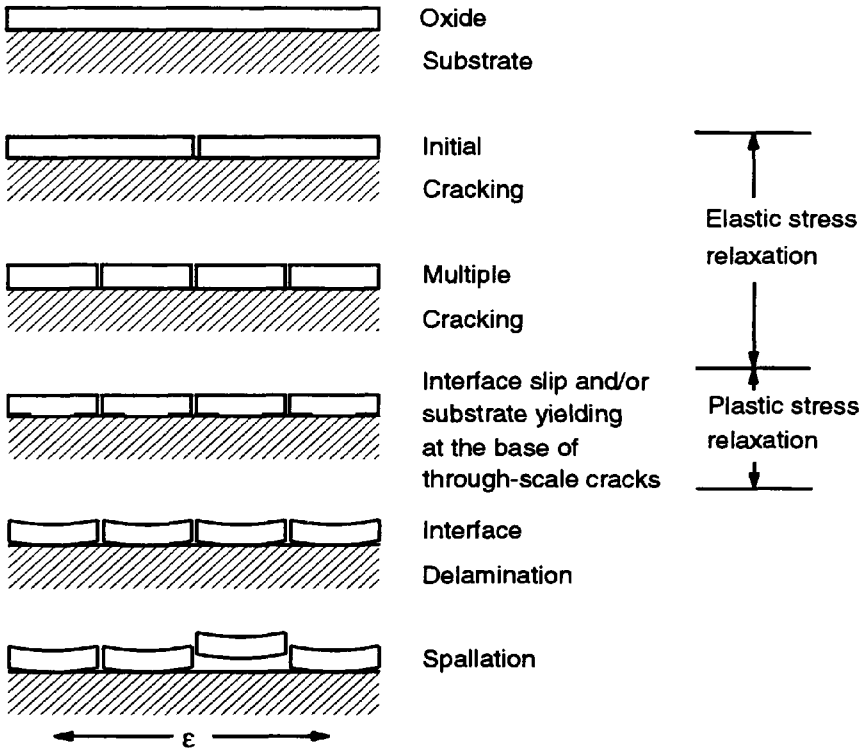

Figure 2.2: Schematic diagram of cracking and spallation caused by tensile oxide stress [12].

Linear elastic fracture mechanics has been applied to determine the critical failure strains under tensile stress. This is justified at temperatures where creep is not expected ($T < 0.5T_m$). Through-thickness cracks are likely to develop by propagation of pre-existing defects either within or at the surface of the oxide layer [2,8]. The critical applied tensile strain ϵ_c needed to produce unstable crack growth is:

$$\epsilon_c = \frac{K_{IC}}{EF\sqrt{(\pi c)}} \qquad (2.11)$$

where K_{IC} is the critical stress intensity factor, c is the size of the physical defect (length of a surface defect or half-length of an embedded defect) [9], E is the Young's modulus and F is a numerical factor depending on shape, size and position of the void.

A second approach based on the critical energy release rate G_{IC} was made by Armitt *et al.* [10] and Robertson and Manning [3]. According to that, fracture occurs when the energy release rate exceeds a critical value G_{IC} which is related to the fracture surface energy γ by $G_{IC}=2\gamma$. This gives the following equation:

$$\epsilon_c = \sqrt{\frac{2\gamma}{F^2 \pi E c}} \qquad (2.12)$$

Both approaches are related via:

$$G_{IC} = \frac{K_{IC}^2}{E} \qquad (2.13)$$

for the plane stress condition.

In general, two limiting cases govern the relationship between defect size and the thickness of oxide scale [1]:

(i) the defect size is independent of scale thickness, thus the critical failure strains are independent of the thickness;

(ii) the defect size is directly proportional to scale thickness.

Robertson and Manning [3] introduced a relationship between the defect size c and the scale thickness h which is based on the second condition from above and has the following form:

$$c = k\,h \qquad (2.14)$$

where k is a constant.

Evans and Cannon [35] calculated the lateral extension of a crack initiated at tensile stress concentration sites, e.g. holes, pores, voids and concave undulations at edges. Stable crack propagation occurs when:

$$h_c = \frac{2}{\pi}\left(\frac{K_{IC}}{\sigma_{OX}}\right)^2 \approx 0.6\left(\frac{K_{IC}}{\sigma_{OX}}\right)^2 \qquad (2.15)$$

where K_{IC} is the critical stress intensity factor of the oxide, σ_{ox} is the stress and h_c is the critical oxide thickness. This is effectively equation (2.11) when $c=h/2$ and with a F value of 1.

A final approach to model the scale fracture was made by Grosskreutz and McNeil [36]. They assumed that the substrate deformed by crystallographic slip and that fracture of the oxide may occur at the slip step when the oxide is not strong enough to support the tension necessary to develop the peeling or delamination stresses. It was shown that fracture at the slip step is more likely in thinner films and a thickness of 0.05 μm was given as a dividing line between the fracture at slip steps and tensile fracture by equi-distant through scale cracking for an anodised Al_2O_3 layer. In addition a tensile failure strains of 0.1 - 0.3% were measured for 0.1 - 3.0 μm thick films [36]. Schütze [13-14] investigated the tensile failure behaviour of oxides on alloy 800, 18Cr and 24Cr steel using strain rates between 10^{-6} - 10^{-8} s^{-1} at 800 °C. The Cr_2O_3 layer on 800 did not show lateral oxide growth and the failure strains were ~0.1% when deformed with rates $>3x10^{-7}$ s^{-1}. Lower strains rates allowed some plasticity which

increased the failure strain to ~0.5%. However strains of up to 2.5% were found with the scales on the 18Cr and 24Cr steels (containing 0.8 and 1.4 wt% Al and 1.48 and 1 wt% Si), respectively) which showed lateral oxide growth and consisted mainly of Al_2O_3.

Following the development of through-scale cracks, further stress relief in response to higher strains can proceed by [10]:

(i) multiple cracking with pure elastic stress relaxation
(ii) multiple cracking with interfacial slip and/or plastic deformation of the substrate at the base of through-scale cracks
(iii) delamination at suitable interfaces.

These different cases are discussed below.

Multiple Cracking with Pure Elastic Stress Relaxation

A first approach to determine the increase in crack density has been made by Grosskreutz and McNeil [36]. They assume that the substrate deforms continuously, and regularly spaced cracks appear in the coating. The spacing L at any strain ϵ is given by:

$$\ln\frac{\epsilon}{\epsilon_o} = k\left(\frac{1}{L}\right)\left(\frac{1}{L_o}\right) \qquad (2.16)$$

where L_o, ϵ_o are any convenient set of data points. The constant k is expected to show a linear or parabolic dependence on the film thickness and must be determined by experiment.

A planar specimen which is undergoing thermal stressing has no shear stresses as long as there is no bending component. Important complications arise at the edges of specimens of finite dimensions (see also section 2.1.1.2, page 31), but for the present such edge effects are ignored. There will also be in reality a transition zone at the oxide-metal interface where rapid changes in the sign of the stress will occur over short distances [37]. The stress state changes significantly once through-thickness cracks are formed since stresses now develop along the oxide-metal interface [8].

A first attempt to model the shear stress distribution along the oxide-metal interface was made by Tien and Davidson [4] which assumed a linear variation of shear stress with the maximum value at the interface next to the tensile cracks (see also section 2.1.1.2, page 31). This gives a limiting crack spacing of:

$$L = \frac{4h}{\tau_{max}}\sigma_{OX} \qquad (2.17)$$

For stresses higher than τ_{max} or σ_{OX} fracture will occur at the oxide/substrate interface or within the oxide, respectively.

Evans [8] reviewed this model together with another by Nicholls *et al.* and compared both predictions for a 10 μm thick Cr_2O_3 layer on a 400 μm thick stainless

steel sample. The maximum shear stress predicted by Nicholls *et al.* was an order of magnitude smaller than that predicted by Tien and Davidson for a crack spacing of 100 μm (Figure 2.3) [8]. In addition, the stress normal to the crack surface drops to zero as soon as a through-thickness tensile crack has developed, thus the tensile stress will vary with position. Again Evans [8] has recently reviewed the models proposed by Grosskreutz and McNeil and Nicholls *et al.* As for the shear stress he found a significant difference between the two predictions (Figure 2.3) [8].

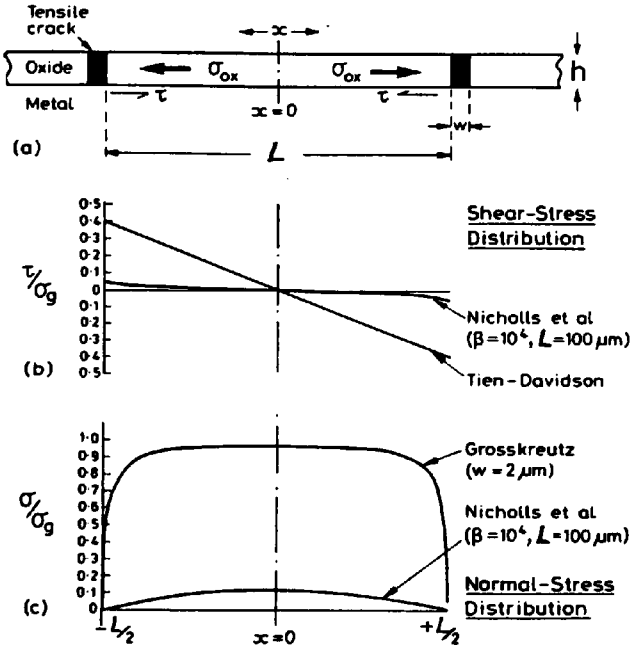

τ is the shear stress in the oxide segment, σ_g is the average tensile stress in the oxide, σ is the local tensile stress in the oxide segment and β is a constant containing the Young's moduli and oxide and metal dimensions.

Figure 2.3: Comparison of (b) the predicted shear stress distribution and (c) the tensile stress distribution for the configuration shown in (a) which shows the cracks in an oxide after loading in tension [8].

Interfacial Slip and/or Plastic Deformation of the Substrate at the Base of Through-Scale cracks

In thin films, **interfacial slip** provides an option for stress relief over a longer range than the purely elastic relaxation considered above. Armitt *et al.* [10] modelled this situation assuming the shear stress to be constant along the interface. This gave a limiting crack spacing L of:

$$L = \frac{2\,h\,\sigma_{ox}}{\tau_y} \qquad (2.18)$$

where τ_y is the shear yield stress of the substrate. Thus, cracking occurs over a range

of stresses until the spacing between cracks is of the order of the oxide thickness. Assuming that τ_y and σ_{OX} are of the same order of magnitude the limiting crack spacing is $2h$, which is half the spacing compared to the case of pure elastic relaxation (equation (2.17)). In fact, the factor 2 in equation (2.18) is only an integration constant ≥ 2 which depends on the assumed shear stress distribution in the oxide.

Another valuable attempt to analyse the stress distribution and the interfacial creep processes after cracking has been made by Riedel [38]. He derived a continuum-mechanical equation for thin second-phase layers on deforming metals under plane stress condition, taking into account elastic and creep deformation, as well as stress independent straining such as thermal expansion. Linear and non-linear viscous sliding was also allowed at the interface. He used experimental data of Berchthold *et al.* [31] and creep data of Manning [26] to verify the equation. The crack spacing L was found to decrease with the applied strain rate as $L=k(h/\dot{\epsilon})^{1/2}$ for small strain rates. In this case k is a constant which has to be determined by experiment. Below a certain minimum strain rate no oxide scale cracking was predicted nor found. It was also concluded that sliding of the scale is controlled by stress-directed diffusion leading to a linear viscous law rather than by dislocation creep in a thin interface layer, which would lead to non-linear viscous behaviour. However, Barbehön [18] found later that the model cannot be used to predict the crack spacing in nickel oxide when deformed at 800 °C.

Plastic deformation of the substrate at the base of through-scale cracks provides another option for stress relief after initial failure if one considers the fact that stresses can only be applied to the scale through the metal substrate [3]. Hence, if the substrate itself is strained beyond yielding, no further stress can be applied to the scale. Thus, the strain in the substrate can increase, but the stress in the oxide segments cannot and the metal then accommodates the increase in strain by localised yielding at the base of through-scale cracks [3]. Hence only the crack surfaces move apart. This produces a regime of extended oxide adherence in which the oxide is discontinuous and non-protective, but remains attached to the metal. In practice, the metal yield strain gives only an indication of the boundary of this regime as yielding is not a sudden transition [3]. It is gradual at high strains rates because of work hardening and at high temperatures because substrate creep may reduce work hardening and facilitate interfacial slip [3].

Delamination at Suitable Interfaces

A final option for stress relief following through-scale cracking is crack deflection along a suitable interface, thereby initiating delamination of some or all of the scale [10]. Cracks can develop either at the metal/oxide interface or parallel to it within the oxide layer. However, the deflection of the crack will occur along the surface of

lowest energy release rate G_{IC} [3].

Evans [8] reviewed the possible mechanisms for the crack deflection. Equation (2.9) suggests that the high shear stresses which develop at the oxide-metal interface in the vicinity of the crack tips can initiate a shear crack. Tien and Davidson [4] also state that once cracks in the oxide are initiated, l decreases and loss of adherence becomes more likely, i.e. nucleation is the more difficult stage. In contrast, Evans [8,12] suggested a process of interfacial shear where the interface is expected to develop voids which produce sufficient weakening and which may lead to subsequent delamination. This mechanism is only likely if the shear creep strength of the interface is low. According to Evans, such a situation did arise in the presence of a thin silica interlayer or in cases where the segregation of trace elements has produced a significant weakening of the interface.

Other researchers have investigated the deflection of tensile cracks at interfaces. There is general agreement that the interfacial fracture energy must be less than the cohesive fracture energy [10,39].

An initial attempt to characterise the failure of oxide in the form of **oxide failure maps** has been made by Armitt *et al.* [10]. The results of their work have been used in the subsequent work by Robertson and Manning [3]. They found that the thinnest scales fail in a ductile manner since the stress required to propagate a flaw increases as the flaw size decreases. As the scale thickness is an upper limit to the flaw size, reducing h increases σ_c until it eventually exceeds the yield stress of the oxide σ_y. This defines the comminution limit of the material using equations (2.12) and (2.14)

$$h = \frac{2\gamma E}{F^2 \pi k \sigma_y^2} \qquad (2.19)$$

In contrast to component testing, where failure occurs once the largest flaw has failed, the presence of a substrate allows an increasing strain to be applied to a scale even after initial cracking. This allows the progressive exploitation of flaws in the scale. Also, as cracks are generated over a wide range of strain levels in the scale, the condition for failure is expected to be described by a spectrum of strain values [3] (Figure 2.4).

Schütze [40] established corrosion creep interaction diagrams (CCID), which cover the whole range of strain rates and strain values required for creep, pseudoplasticity etc. up to fast failure. So far, there have been too little data available to draw a complete CCID for a given material. The purpose of the maps was to find a way of illustrating the interaction of corrosion and mechanical factors in order to divide the whole process of materials degradation into different stages. Some of these stages can be tolerated in practical conditions, others not.

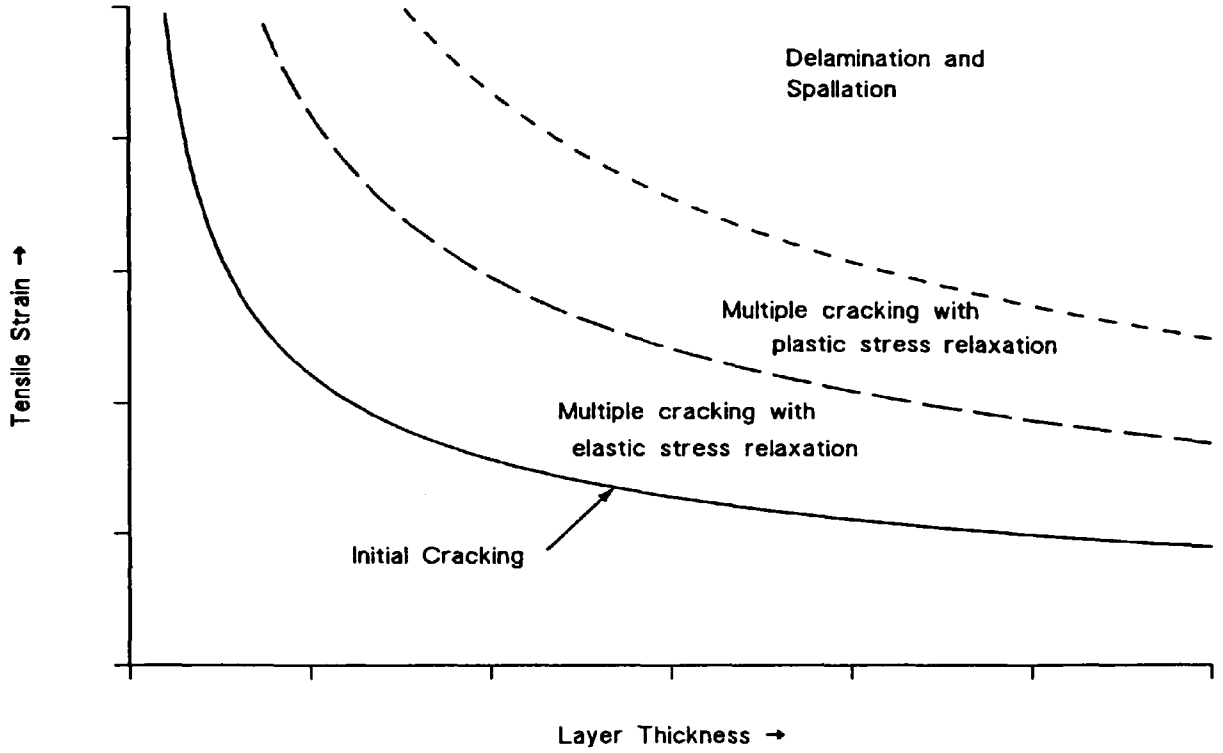

Figure 2.4: Schematic failure mode map for oxides tested in tension showing the different stages of the failure process.

Discussion:

It can be seen from the previous analysis that the different proposed models for oxide failure are related to each other even though the starting point or the initial assumptions were quite different. In general, simple linear elastic fracture mechanics was used to predict failure except for very thin scales which might yield or fail at slip steps. The models for subsequent multiple cracking with elastic and plastic stress relaxation show considerable difference in the analysis, and processes such as substrate yielding at the base of through-scale cracks cannot be quantified at all. Several mechanisms were also proposed for the process of interface delamination. However, there are important issues which are yet to be resolved.

Even though the problem of oxide failure in tension has been discussed in many publications, experimental data is very limited and when obtained mainly bulk oxides were used. Some data however are available on thermally formed scales using very low strain rates $\leq 10^{-6}$ s^{-1} where lateral oxide growth or creep was possible [13,31]. Even then there was no discussion of the oxide thickness or the void size which are very important parameters as will be shown in this study. Furthermore there is no experimental evidence available to allow discrimination between the elastic and plastic stress relaxation mechanisms.

2.1.2.4 Failure of Oxide Scales under Compressive Stress

Figure 2.5 shows the observed failure mechanisms, together with the designation and the critical condition for initiation. Cases B and E are similar except that for Case E the oxide delaminates along a line of least cohesive strength within the oxide. In case C a shear crack develops under 45° as a result of shear failure. This failure mechanism was observed in NiO [18]. In case D the oxide delaminates as a result of grain boundary sliding in the substrate adjacent to the interface. This can also lead to tensile failure as suggested by Grosskreutz and McNeil [36] (see also section 2.1.2.3, page 37). Cases A and B are discussed in the following. Case A, termed Route I or wedging, was originally proposed by Evans [12]. It is characteristic of a strong interface and a weak oxide. Oblique shear cracks are initiated within the oxide. The sliding of the oxide along these cracks during further straining drives the oxide away from the substrate and finally it spalls off [12]. Case B, termed Route II or buckling, was originally proposed by Wells *et al.* [41]. It is the result of a weak interface and a relatively strong oxide. An initial delamination originates along areas of loose interfacial strength, i.e. along pores, voids and impurities. This initial delamination or buckle creates a driving force causing the delamination to extend in both directions along the interface. Tensile cracks develop when the buckle reaches a critical curvature and the oxide spalls off [12]. In both Routes, the cracks parallel to the interface propagate along the area of least adhesive/cohesive strength, either within the oxide scale or along the substrate/scale interface [3].

A first approach to understand the spallation process was made 1948 in by U. R. Evans. He proposed that oxide metal debonding would occur when the strain energy within the oxide layer was equal to, or exceeded, the interfacial fracture energy. The idea has been developed by a number of researchers [3-6,8,10-12].

The stored energy W^* per unit volume of the layer is:

$$W^* = \frac{1}{2}\sigma_1\epsilon_1 + \frac{1}{2}\sigma_2\epsilon_2 = \frac{\sigma_{ox}^2}{E_{ox}}(1-\nu) \qquad (2.20)$$

where σ_i and ϵ_i are the principal stresses and strains, respectively. E_{ox} is the Young's modulus, σ_{ox} is the stress in the oxide and ν is the Poisson ratio of the oxide. The energy release rate G_{IC} is:

$$G_{IC}^{cohesive} = 2\gamma_{ox} \qquad (2.21)$$

where γ_{ox} is the fracture surface energy value of the oxide and the '2' accounts for the fact that two new surfaces were created. Equation (2.21) is applicable for Route I and Route II failure if delamination takes place within the oxide. In the more likely case of delamination at the oxide/metal interface the energy release rate G_{IC} becomes [5]:

Designation	Critical initiation condition	Schematic diagram of the failure mechanism	Ref
Case A: Route I (shear failure by wedging)	critical shear strength		[5]
Case B: Route II (buckling)	critical buckling stability		[41]
Case C: (shear failure)	critical shear strength	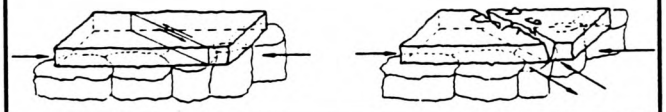	[18]
Case D:	substrate yielding		[36]
Case E:	critical buckling stability	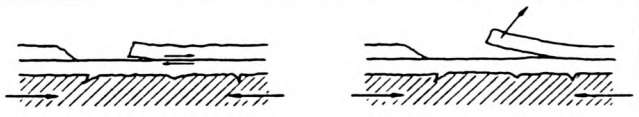	

Figure 2.5: Schematic diagram for different oxide failure mechanisms which were observed in oxides under compressive stress [18].

$$G_{IC}^{interface} = (\gamma_{OX} + \gamma_{m} - \gamma_{interface}) \qquad (2.22)$$

where the subscripts, *ox* and *m* stand for oxide and metal, respectively and $\gamma_{interface}$ is the stored energy due to the constraints at the original metal/oxide interface. Since $G_{IC}^{interface}$ contains contributions from both the fresh oxide and the metal surface, it is not necessary to include a factor of 2 [5]. For Route I failure Evans and Lobb [5,6] derived the strain ϵ_I^{init} to produce a single shear crack of the length ζ as:

$$\epsilon_I^{init} = \sqrt{\frac{G_{IC}^{cohesive}}{k_1 \zeta E_{OX}(1-\nu)}} \qquad (2.23)$$

where $k_1 (<<1)$ is a factor related to the fraction of stored energy within the layer that is used for the fracture process. Spallation can only proceed when the initial shear crack is deflected at the interface and the oxide is driven away from the substrate by the wedging effect of the shear crack surfaces. Thus, a second criteria was required to account for the loss of adherence or the initiation of spallation, ϵ_I^{spall} [5,6]:

$$\epsilon_I^{spall} = \sqrt{\frac{G_{IC}^{interface}}{k_2 E_{OX} h(1-\nu)}} \qquad (2.24)$$

where h is the oxide thickness and $k_2(\sim 1)$ is the stored energy in the volume $\zeta^2 h$ used in the fracturing process.

Similarly, Route II behaviour has to be described by two equations, where the first equation governs the initiation of buckling and the second the initiation of spallation. The failure is initiated by buckling of the oxide over the regions of initial decohesion.

To date, two approaches have been made. In the first, the critical compressive stress to initiate buckling was approximated by that to produce buckling of a clamped, circular plate of radius R (which equates in this context to the radius of the initial decohesion). Thus, the critical buckling strain ϵ_{II}^{init}, is given as [42,43]:

$$\epsilon_{II}^{init} = \frac{1.22}{(1-\nu^2)}\left(\frac{h}{R}\right)^2 \qquad (2.25)$$

where $2R$ is the diameter of the initial decohesion. However, in order to initiate spallation without unstable propagation of the buckled zone, it remains necessary for tensile cracks to develop at regions of high curvature within the buckle so that a fragment of the oxide layer can be released [43].

An alternative approach has been proposed by Wells *et al.* [41] who defined the spall criterion as that to initiate unstable propagation of the buckle. This is expected to give an upper limit to the spallation strain ϵ_{II}^{spall} of [5,41,43]:

$$\epsilon_{II}^{spall} = \sqrt{\frac{1.052h^4}{R^4} + \frac{1.041G_{IC}}{E_{OX}h}} \qquad (2.26)$$

where the value of G_{IC} depends on the energy release rate at the plane of delamination. The first expression in equation (2.26) governs the initiation and the second spallation. A comparison of the second term with equation (2.24) shows that they differ only by a numerical factor, indicating that spallation is governed in both cases by the propagation of a tensile crack at the interface [43]. Equations (2.25) and (2.26) also indicate that it becomes more difficult to buckle as the oxide thickness increases (Figure 2.6). In addition, the presence of an initial delamination does not disturb the stress field until the oxide layer has buckled, i.e. a driving force for buckling must exist [43]. Such driving forces can be heat flow and thermal expansion of multi-layered scales [4] (see also section 2.1.1.2, page 31). Likewise, compositional changes in a single layer can induce differential stresses and bending moments.

Evans and Lobb verified their models in tests with 20Cr austenitic steel oxidised at 1123 and 1173 K and controlled cooling (rate 86 K h^{-1}). The mass gain during pre-oxidation up to 1500 h and during cooling was recorded using a microbalance. The tests showed cracking and spalling above a critical threshold mass gain or thickness. An initial increase in mass at the beginning of cooling was interpreted as a loss of protection of the surface film due to cracking [6]. The release of spalled particles

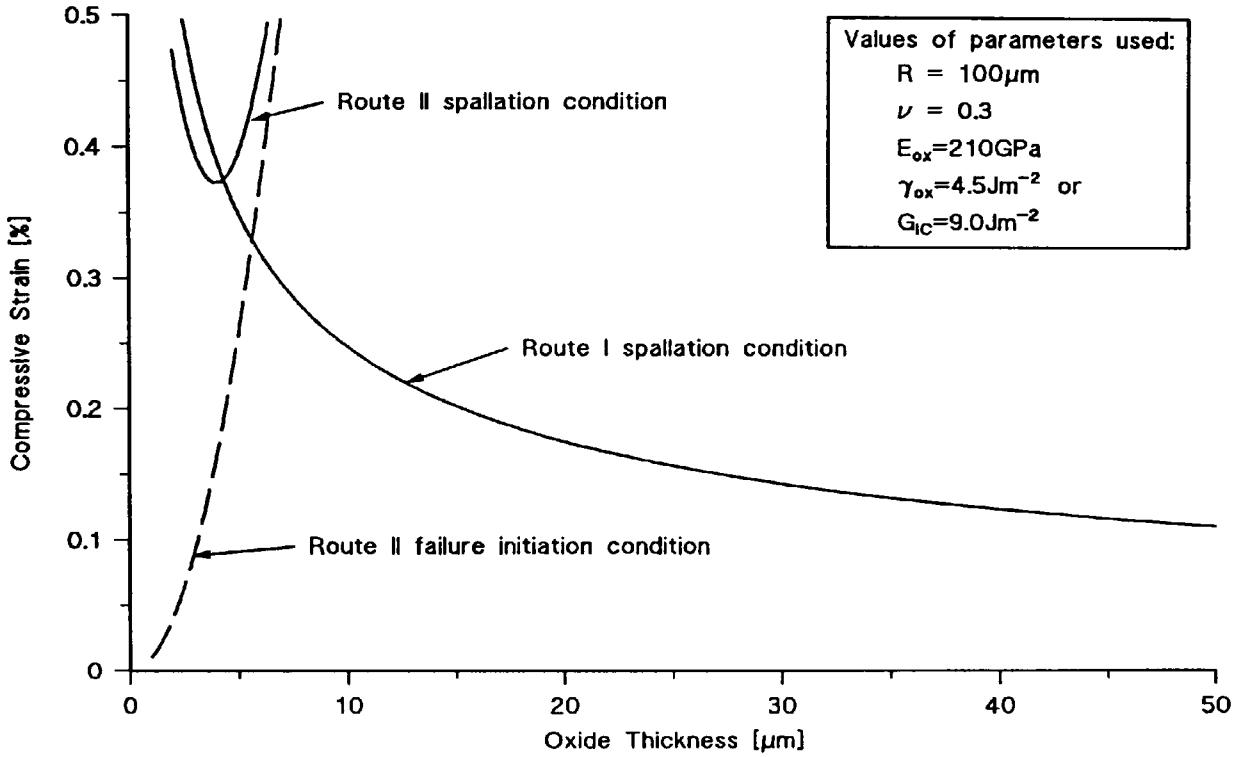

Figure 2.6: Comparison of the compressive failure strain as a function of thickness predicted from models after ref. 6.

occurred subsequent to this stage and so identified the process of spallation as Route I. This was supported by metallographic observations showing inclined fracture surfaces in the remaining oxide on the 20Cr austenitic steel containing 0.56 wt% Si [44]. The strain, i.e. temperature drop at which spallation of 0.5% of the oxide occurred decreased for all test conditions with increasing oxide thickness according to the predictions of equation (2.24) [12]. Evidence for Route II buckling was found in the spalling of oxide grown on an aluminide coating during high frequency cycling testing in a burner rig [41] and in 20Cr austenitic steel with low Si-content [44].

The feasibility of Route I and II failure was also demonstrated by a finite element analysis undertaken on the same steel and test conditions by Evans *et al.* [43]. It was assumed that the oxide behaved elastically and the creep response was determined by the properties of the substrate. In fact, the model which included creep relaxation agreed better with the experimental data and a value of 1 - 2 J m^{-2} was found for the fracture energy of the oxide-metal interface, which is 1 - 2 orders of magnitude higher than that expected for purely elastic deformation [43]. This suggested that the substrate creep properties determine the rate of the interfacial crack growth.

Robertson and Manning [3] used the geometrical approach of linear elastic

fracture mechanics with $K=\sigma\sqrt{h}$ for a long crack below a strip of thickness h [3,45]. Together with equation (2.13) the critical failure strain ϵ_c becomes:

$$\epsilon_c > \sqrt{\frac{G_{IC}}{hE}} \qquad (2.27)$$

which corresponds to the model proposed by Armitt *et al.* [10] and is very similar to the failure criterion under tensile stress. In addition, a comparison with equation (2.24) shows that both agree up to a numerical factor, indicating that linear elastic fracture mechanics could be used to model interface delamination in oxides. However, the situation is more complex because the tensile crack at the interface represents a crack showing partly elastic behaviour in the oxide and partly plastic behaviour in the substrate. At present, the situation at the crack tip and its plastic deformation cannot be determined mathematically, only finite element modelling can be used to determine stresses and strains at the crack tip.

Schütze [7] criticised this model (equation (2.27)) because it does not take account of the size of possible defects at the interface or within the oxide. He used, therefore, a model which was originally proposed by Evans *et al.* [37] to calculate the interfacial strain that arises from the compressive loading of a wavy interface. Assuming that the substrate deforms plastically, i.e. $\nu_m=0.5$, the maximum strain normal to the interface is [7]:

$$\epsilon_n^{max} = \frac{\epsilon\, m}{\left(1+\frac{r}{h}\right) E_{ox}} \qquad (2.28)$$

where ϵ is the applied compressive strain, r characterises the amplitude of the wavy interface, h is the mean scale thickness and m is a constant given by $m=2E_{ox}/(1+\nu_{ox})$. Assuming the worst case, that the physical defect size $2c$ lies at the position of maximum interfacial strain a combination of equation (2.11) and (2.28) gives the critical applied compressive strain:

$$\epsilon_c = \frac{K_{IC}}{F\sqrt{\pi c}} \frac{\left(1+\frac{r}{h}\right)}{m} \qquad (2.29)$$

Tien and Davidson [4] proposed a simple buckling model for thin oxides by the way of critical buckling. From beam theory a single beam which is pinned only at the ends can suddenly buckle at a point of instability when the axial compressive stress exceeds a critical value. However, this model appeared too crude an approximation for the situation of an oxide layer on a metal substrate.

It was found by Evans *et al.* [11,12] that continued cooling increased strain levels within the oxide layer, which led to further spallation. Such an increase was interpreted by different areas of the specimen surface reaching their critical energy value for

spallation [12]. It was believed to be a result of the combined intrinsic variation in both fracture energy G_{IC} and oxide thickness [11]. After fractional oxide losses of 30 - 40% the spallation rate decreased due to stress relaxation in the residual oxide. This approach was quite different from the proposal of Schütze [7]. It implied that G_{IC} could vary within the oxide. However, Schütze proposed that G_{IC} is constant and that the variation in the critical strain energy to cause spallation was solely due to the void size. This is very similar to what was found in tension, but it would require a detailed assessment of the voidage at the interface which is difficult to achieve.

Discussion:

To date there has been little experimental data to support one or the other failure mechanism. Quite often the results were only obtained in thermo-cycling or cooling experiments rather than under applied load. In addition the results from monitoring techniques such as thermogravimetry, AE, etc. were not supported by metallographic evidence showing the cracks, or *vice versa*. It also appears that there are many publications which were mainly concerned with substantiating the earlier work and the previously proposed mechanisms. It was believed that more could have been achieved if a more general approach were taken. Regardless of the different lines of thought all proposed failure mechanisms have an initiation condition and a spallation condition. The spallation condition is in all cases the same. Its requirement is crack propagation along the interface or within the oxide parallel to the interface. Reference to Figure 2.5 (Page 46) and the preceding analysis shows that initiation can only occur when the stress exceeds the shear strength of the oxide (Cases A and C), the buckling stability of the oxide layer (Cases B and E) or when the substrate yields (Case D).

2.1.3 Critical Parameters for Prediction of Oxide Scale Failure

The preceding analysis demonstrated the critical parameters governing tensile and compressive oxide failure. These are the overall state of stress, the effects of lateral oxide growth, plasticity and creep of oxide and substrate, the Young's modulus, the fracture surface energy of oxide and interface and the composite void size.

The amount of lateral oxide growth or plasticity cannot be determined at present, but it is possible to define the minimum temperature and the maximum strain rate below which they might contribute to failure (see section 2.1.2.1, page 34 and section 2.1.2.2, page 35).

Table 2.1 gives a summary of oxide parameters. It also demonstrates the scatter of the values found in the literature. Young's modulus values and surface energy values have recently been provided by Robertson and Manning [3]. In addition, a value of 0.04 nm for γ/E was given for a range of polycrystalline ceramic materials and γ

varied between 4 and 40 J m^{-2} [10]. The relationship between γ and E was also found by Robertson and Manning [3] for polycrystals, but with a constant value of 0.02 nm.

In all models spalling will occur along the surface of lowest energy release rate G_{IC}, which can be either within the scale or along the scale/metal interface. This leads to the question of whether or not the interface is intrinsically weak [3]. Robertson and Manning [3] have pointed out that the scale/metal interface is intrinsically strong on an atomic scale and models for estimating the increase of the interface surface energy with increasing interface roughness have been proposed [3,46]. On the other hand, the scale/metal interface is also a site for segregation of elements which are relatively insoluble in the scale or for oxides which have the highest thermodynamic solubility at low oxygen partial pressures, e.g. SiO_2 with respect to a Cr_2O_3 scale. Similarly, sulphur segregation was assumed to have a negative influence on the interface strength [35]. It is difficult to separate each of these aspects at the present state of experimental knowledge [3,29].

Evans and Lobb [6] obtained an interfacial energy value of 5.8 J m^{-2} for a Cr_2O_3-layer on 20Cr austenitic steel. Evans and Lobb [11] also gave an average value of about 40 J m^{-2} for 50% spallation for the same oxide and a value of 1 - 2 J m^{-2} which was obtained by a finite element analysis [43]. A value of 11.5 J m^{-2} for G_{IC} was found for a fractional loss of 50% for the outer layer scales (Fe_2O_3) on Type 316 steel [10] and it was assumed that it is the same for ferritic and austenitic steels. Robertson and Manning [3] also obtained good results assuming an idealised interface with a surface energy value equal to that of the oxide, i.e. $G_{IC}^{adhesive} = G_{IC}^{cohesive}$ and methods for measuring $G_{IC}^{interface}$ have been suggested [29].

So far, little attention has been directed towards the effects of voids within the oxide or at the oxide/metal interface on the failure process, although it is an important factor in all the quoted models for through-scale cracking and spalling. Recently a method for evaluating the composite void size in an oxide containing multiple randomly scattered voids and pores was proposed by Hancock and Nicholls [2]. The analysis follows guidelines used for the assessment of defects in welds and requires that each defect is idealised and compared with its neighbours to assess whether the interaction conditions apply (Figure 2.7). Interacting defects are considered as a single defect and the assessment procedure continues, until a single composite equivalent defect results for the scale. The composite defects are normally expected to be of a certain size, which is a proportion of the oxide thickness, but infinitely long since interaction will occur in all directions. Therefore a shape parameter Q_o (which accounts for the ratio of void thickness to void length) and a membrane correction factor M_m (which accounts for the ratio of void size to overall size) have to be determined from the respective graphical representation of the functions of Q_o and M_m. This allows $\hat{c}$ to be determined via:

$$\pi \hat{c} = \frac{c\, M_m^2}{Q_o^2} \qquad (2.30)$$

where $\hat{c}$ is an equivalent crack length, which represents the half length of an idealised through thickness crack as shown in Figure 2.8a which would have the same effect as the measured defect. Hence, a plot of the failure stress σ_c as a function of $1/(\pi\hat{c})^{1/2}$ should have K_{IC} as slope and an intercept value which represents the residual stress. In this way Hancock and Nicholls [2] provided values of K_{IC} for FeO/Fe_3O_4 on iron and Cr_2O_3 on Nimonic 75 (~Ni-20%Cr). For both cases, K_{IC} was insensitive to temperatures below 873 K, with a value of about 1.7 MN $m^{-3/2}$, but increased at higher temperatures.

However, the determination of M_m required a very long extrapolation by a factor of 3 or more in the graphical representation. It was believed that this procedure involves too large an extrapolation for use with thin oxide layers since the procedure was developed for much larger structures >10 mm thick. These reservations were confirmed by McLauchlin [47]. Therefore a slightly different approach was used in this study. The interaction was considered critical only in the direction normal to the applied strains. Thus, the composite void size c could be obtained directly without extrapolation (Figure 2.8b). However, the K_{IC}-values are expected to be approximately up to 4 times smaller than those obtained with the extrapolation. Such is the effect of this large extrapolation.

The effects of pores on the fracture strength were investigated by Birchall *et al.* [48] for cement and by Rice [49] for bulk ceramics. It seemed apparent that the defect size is a crucial factor for the determination of the strength of oxides. It was also suggested that a major role of active element additions is to reduce the macro defects present within the oxide scales with consequent benefit on scale adherence and spalling resistance [3,20]. Hancock and Nicholls [2] also found that thicker oxide layers failed at lower levels of applied stress than thin films. This was thought to be due to a higher probability of finding of larger composite defects in the thicker oxides.

Material	Temp. [°C]	Young's Modulus [GPa]	Growth Stresses [MPa]	α_{Oxide} [$10^{-6}K^{-1}$]	Surface energy [J m^{-2}]	Reference	Notes:
Oxide on Armco Iron	500 600 700 800 850	192 178 164 151 144				[19]	0.2% C steel
Fe_2O_3	20	220		13	6.0	[3]	γ_{th}=2-2.3
Fe_3O_4	20	210		12	4.5		γ_{th}=1.5-2.2
FeO	20	130		15	3.0		γ_{th}=0.94
Fe_2O_3	20	122 205-266				[10] (from various refs.)	Scale Bulk oxide
Fe_3O_4	20	140-260					Scale
Fe_3O_4 + 20%Fe_2O_3	20	61-84					
FeO	570-800	190-120					Mainly FeO
FeO	20	128					Bulk oxide
FeO	600-900	75					Mainly FeO
Fe_3O_4 + Fe_2O_3	500		+/-100			[50]	
NiO	20	220	-400	1.03 (α_{ox}/α_m)		[24]	
NiO	20	190		17.1	3.6	[3]	γ_{th}=1.15-2.77
NiO	900		335 300 240 185 85			[51]	5.4μm 12.1μm 18.1μm 25.2μm 32.3μm
NiO	900		+/-50	17.6 0.82 (α_{ox}/α_m)		[52]	σ_{cool}= 0-500 MPa

Table 2.1: Summary of oxide parameters from various references. γ_{th} is the theoretical surface energy which was calculated using Coulombic potentials and allowing for some relaxation of atomic positions at the surface [3]; σ_{cool} is the cooling stress.

Schematic defects	Criterion for interaction	Effective dimensions after interaction
Coplanar surface defects		
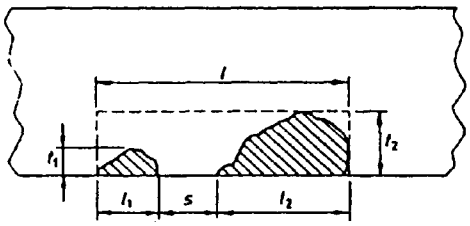	$s \leqslant \frac{l_1 + l_2}{2}$	$t = t_2$ $l = l_1 + l_2 + s$
Coplanar embedded defects		
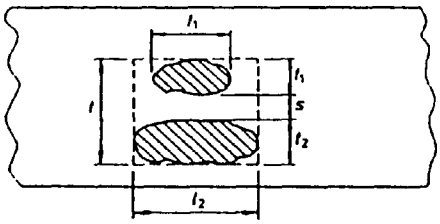	$s \leqslant \frac{t_1 + t_2}{2}$	$t = t_1 + t_2 + s$ $l = l_2$
Coplanar embedded defects		
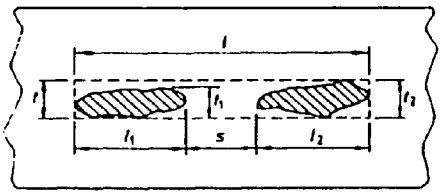	$s \leqslant \frac{l_1 + l_2}{2}$	$t = t_2$ $l = l_1 + l_2 + s$
Coplanar surface and embedded defects		
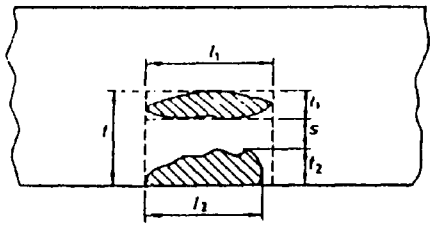	$s \leqslant \frac{t_1}{2} + t_2$	$t = t_1 + t_2 + s$ $l = l_1$
Coplanar embedded defects		
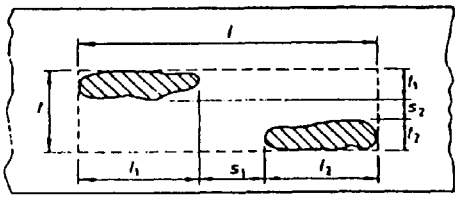	$s_1 \leqslant \frac{l_1 + l_2}{2}$ and $s_2 \leqslant \frac{t_1 + t_2}{2}$	$t = t_1 + t_2 + s_2$ $l = l_1 + l_2 + s_1$
Coplanar surface and embedded defects		
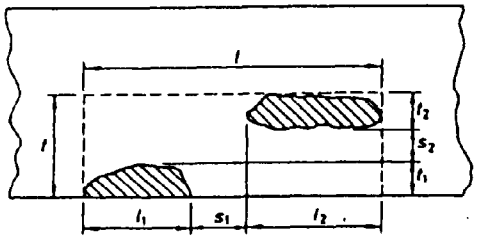	$s_1 \leqslant \frac{l_1 + l_2}{2}$ and $s_2 \leqslant t_1 + \frac{t_2}{2}$	$t = t_1 + t_2 + s_2$ $l = l_1 + l_2 + s_1$

Figure 2.7: Planar defect interaction rules [2].

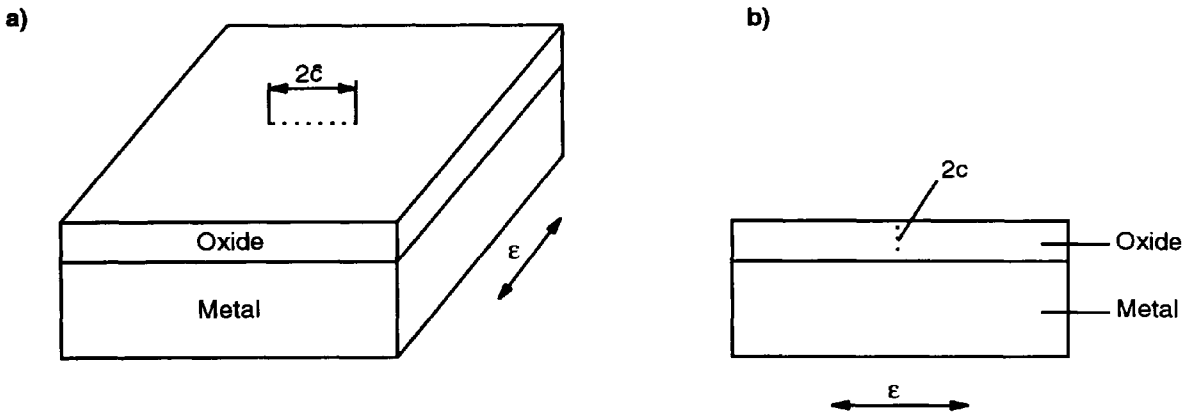

Figure 2.8: Schematic diagram of (a) the ideal through thickness crack in the surface oxide and (b) the crack size which was used in the present study without applying the extrapolation.

2.1.4 Measurement Methods for Oxide Scale Failure

To date, four different methods have been used to detect scale cracking. These were optical methods, thermogravimetry, vibration technique and acoustic emission.

Optical methods, using a long focal length microscope and a stage having heating and loading facilities, can be used to detect scale cracking [29,31]. However the spatial resolution is only limited (~ 0.5 μm). Thermogravimetry is normally used to monitor mass gains during oxidation in order to measure rates of oxidation. It can also reveal through-scale cracking which manifests itself in an sharp increase in mass or oxidation rate and scale spallation which produces a sudden mass loss [6]. However, it is restricted to metal/oxide systems where mass changes caused by scale cracking can be readily detected [20]. Importantly it requires a freely suspended specimen which is not the case in the present study where load or strain were applied externally. The vibration technique monitors the change in the natural frequency of a freely suspended specimen. The natural frequency of the specimen depends on the oxide and substrate dimensions, i.e. stiffness. Therefore monitoring the natural frequency changes can yield information about the oxide thickness [53]. It can also be used to detect the onset of scale cracking, because crack formation results in a reduction of stiffness of the composite system and hence a discontinuity in the resonant frequency is observed. Continued cracking would result in a continual decrease in the recorded frequency [20]. Should scale repair occur then a change in frequency is observed with the frequency recorded after repair approaching that observed before cracking. However, this technique is limited to simple

rod-shaped specimen geometries and requires care in preparing and setting up the specimens [20]. Furthermore, the specimen should be freely suspended during the measurement of the natural frequency. Therefore, loading must be interrupted if the oxide is tested under external load. This might result in crack healing during periods when the specimen is unloaded. AE was selected to monitor oxide failure mainly because it allows continuous loading, can be monitored automatically, is not limited to particular specimen geometries and has similar sensitivities to scale cracking (Figure 2.9) [20,54]. It has recently replaced the vibration technique as a route to measure *in situ* early scale failure [14,54,55-57]. Although, the additional advantage of the vibration technique is that the Young's modulus can also be determined *in situ* [20].

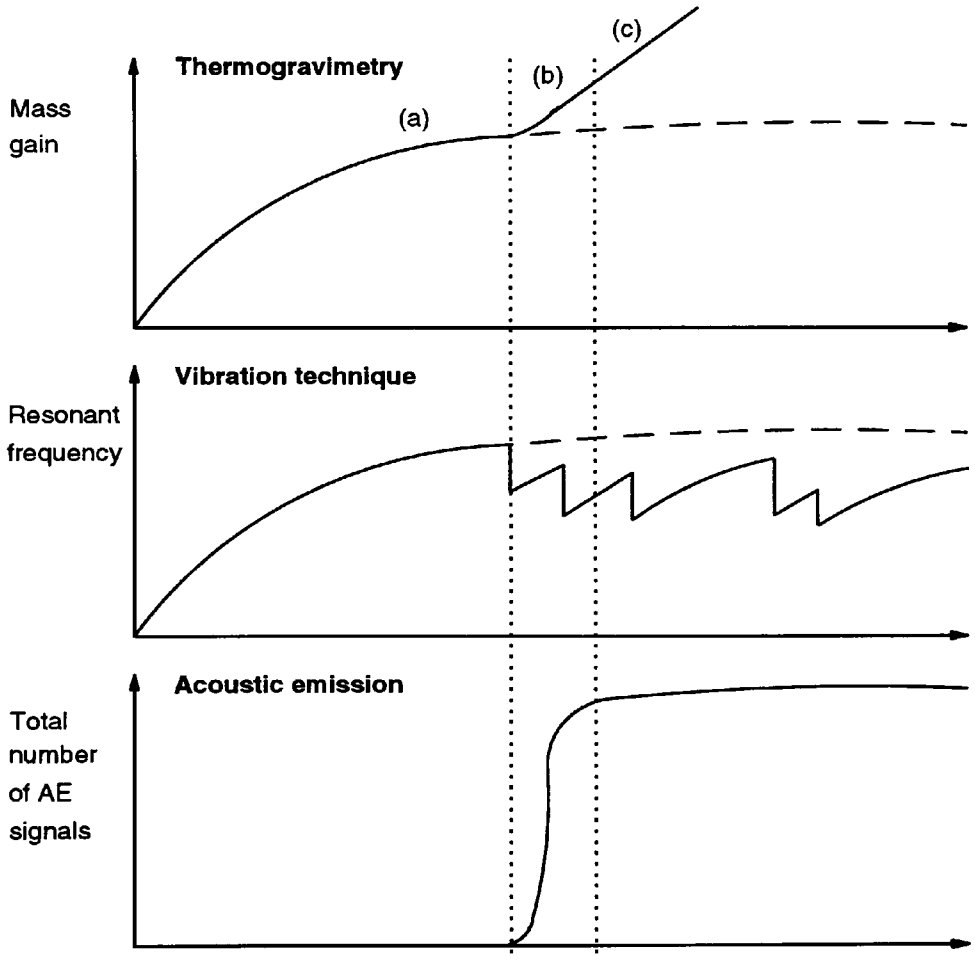

Figure 2.9: Schematic diagram showing the response to breakaway oxidation. a=normal oxidation, b=initial cracking, c=continued cracking and crack repair [20].

2.2 Acoustic Emission (AE)

Acoustic emission (AE) was used in the present study only as a monitoring technique to record mechanical failure of the oxide scales and a detailed study into the generation and theoretical aspects was outside the scope of the current study. Therefore the following survey gives only the more important practical aspects of AE relevant to this study and is by no means an exhaustive review on AE theory.

AE is a term describing a class of phenomena whereby transient elastic waves are generated by the rapid release of energy from localised sources within a material [58]. Eisenblätter [59] classified AE as nothing more than an earthquake on a small (microscopic) scale.

The first documented observation of AE in 1953 by J. Kaiser was the modern day starting point for its active use [58], although mention of the sound emitted from metals undergoing deformation appears in the literature at least as early as 1928 [60]. In fact, Kaiser characterised a basic irreversibility phenomenon which bears his name. In the Kaiser effect, when a material is stressed to a given level and the stress removed, there is an absence of detectable emission at a fixed sensitivity level during reloading until previously applied stress levels have been exceeded [58].

The technique developed rapidly in the last two decades due to the arrival of inexpensive electronic components, which made fast comprehensive capture of the signals feasible. This has brought AE to the forefront of new non-destructive testing methods (NDT).

In materials testing, AE is used as a highly sensitive technique for monitoring active microscopic events in a material. Since these events give rise to elastic waves which propagate in the material, it is not necessary to focus in on the exact location of the source event in order to detect it [58].

AE, of course, also has disadvantages, e.g. the emission has an energy which is, in some cases, close to the detection limit of piezoelectric transducers. The main difficulty, however, is associated with the background noise which is frequently present during in-service tests of structures [61] and classification of the captured signals in those from erroneous and real AE sources is difficult. Recent advances in electronics (e.g. digital filtering, location techniques) have eased the problem considerably, although, it is still difficult to exclude erroneous signals. Figure 2.10 gives an impression of the overlapping of AE signals with other noise.

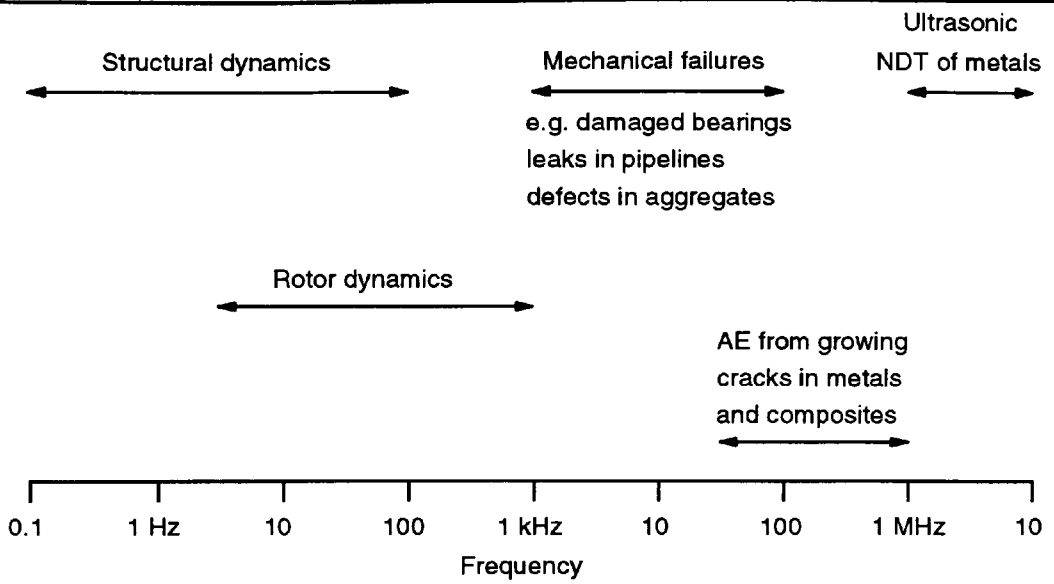

Figure 2.10: Spectrum of vibration and sound used for inspection and testing [61].

2.2.1 Acoustic Emission Sources

AE sources can be classified in 4 different groups, (i) dislocation movement, (ii) phase transformation, (iii) friction and (iv) crack formation and extension. The signals emitted can be broadly divided into two types, (i) continuous emissions (resembling white noise) and (ii) burst type emissions, but no clear distinction between the two different types can be made since there is no physical transition point [62].

Eisenblätter [59] compared various types of AE-sources, viz. earthquake, crack growth and dislocation movement. The results are given in Table 2.2 indicating that the parameters were smallest for the dislocation source. As a rule the signals emitted especially in connection with crack propagation or burst emission during deformation are very brief [63].

Waschkies *et al.* [63,64] and Eisenblätter [59] have investigated the directionality of the sound wave from AE sources. They found that AE does not radiate isotropically in all directions. Figure 2.11a shows the directionality of the sound distribution of longitudinal (L) and transverse (T) waves for mode I (tensile mode fracture), with the crack opening in the Y direction. Figure 2.11b illustrates the relations in connection with mode II (shear mode fracture) [63].

A linear relationship between the mechanical energy of deformation and the acoustic energy of the total field, longitudinal and transverse fields was found by Muravin *et al.* [65]. The AE energy distribution of the total field and of its individual components around a crack tip was similar to the configuration of the plastic deformation zone, confirming that individual wave components describe the processes as effectively as the total signal.

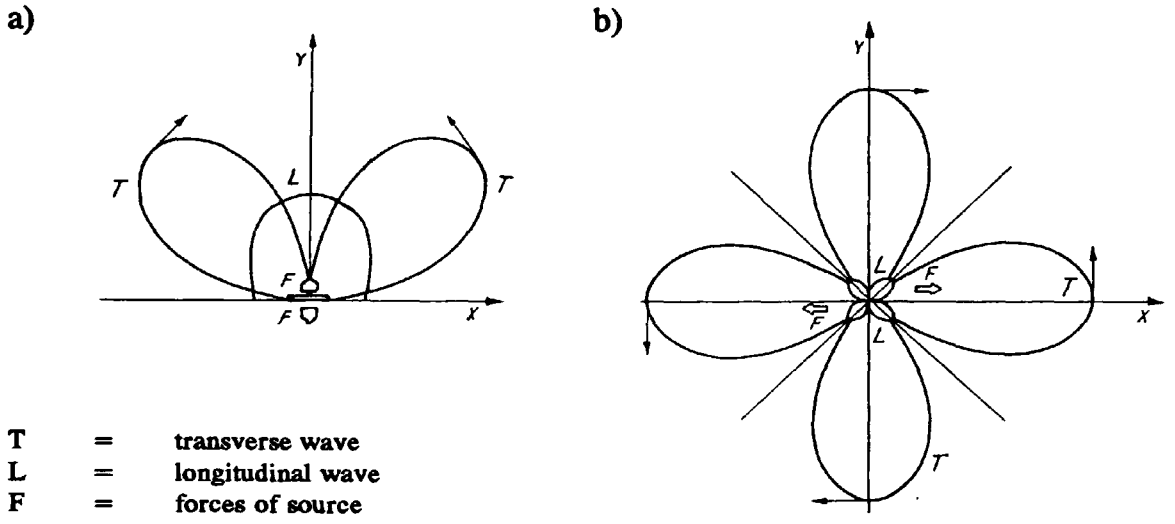

Figure 2.11: Directionality of the sound distribution for the different fracture modes, (a) tensile mode fracture (mode I) and (b) shear mode fracture (mode II and III) [63].

Source	F_o [m^2]	b [m]	ξ [m s^{-1}]	$\Delta\sigma$ [kp mm^{-2}]
Earthquake	10^4-10^{10}	10^{-2}-10	10^3	~10^2
Crack Growth	10^{-10}-10^{-2}	-	10^2-10^3	<10
Dislocation	10^{-12}-10^{-6}	$5x10^{-10}$	1-10^3	<1

Table 2.2: Comparison of AE source parameters: F_o=slip area, b=dislocation vector (Burgers vector), ξ=slip velocity and $\Delta\sigma$=stress drop [59].

2.2.2 Waves and Wave Propagation in Solids

The physical principles of AE rely mainly on the propagation, reflection, interference and attenuation of elastic waves in solids. In real structures the propagation will be affected by surfaces (which create reflection and surface waves), grain boundaries, microcracks, inclusions, etc. (which create reflection and diffraction), anisotropy (which causes deformation of the spherical wave packets on account of the difference in wave velocity in different directions), inhomogeneities (which distort the waveforms) and non-linear elastic behaviour (which is responsible for damping and dispersion) [62]. All these influences result in a strong modulation of the original wave during propagation. Here only the most important facts are considered but more details can be found in ref. 66.

Generally, all waveforms including all longitudinal and transverse modes can be emitted from an AE source in a body (Figure 2.12a-b). If a surface or boundary is

introduced, i.e. in a half-space, the longitudinal and transverse waves which propagate in the bulk of the material combine in the region close to the surface and produce a surface wave or Rayleigh wave (Figure 2.12c). The wave particle motion is neither purely longitudinal nor transverse and these waves can only exist in plates in which the thickness is larger than the wavelength [67]. Typical velocities are for Rayleigh waves ~ 3000 m s^{-1} and for longitudinal waves ~ 5000 m s^{-1} in steel [27].

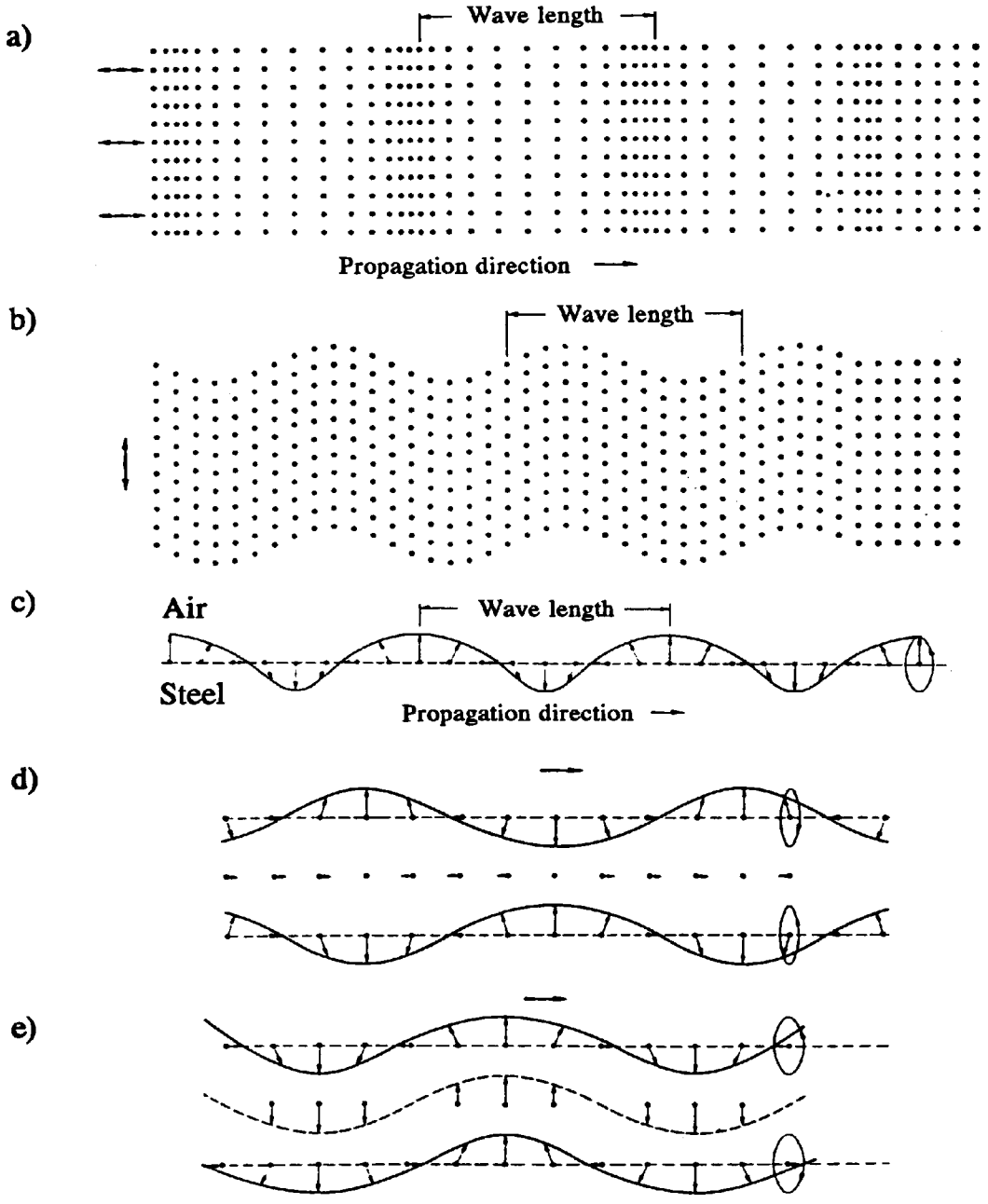

Figure 2.12: Schematic diagram showing (a) a longitudinal wave, (b) a transverse wave, (c) a Rayleigh wave, (d) a symmetrical lamb wave and (e) a asymmetrical lamb wave [66].

In a medium bounded by two surfaces, i. e. a plate (2 infinite dimensions), the waveforms couple at the surfaces to produce the Lamb waves [66,67]. Lamb waves always have a component oscillating normal to the surface. There are two modes, the dilatational or symmetrical wave and the flexural or asymmetrical wave (Figure 2.12d-e). In the first the neutral ligament performs only a longitudinal oscillation; in the second only a transverse oscillation. The other wave particles oscillate elliptically in both types. As the wavelength becomes shorter, relative to the plate thickness, higher order symmetric and asymmetric modes are possible, each with more than one neutral ligament and a characteristic group velocity dependent on the plate thickness. This causes dispersion in a plate of fixed thickness (see also later in this section) [67]. The propagation of the Lamb waves takes place by zigzag reflections between the two surfaces. The velocity can be determined from geometrical relations and Figure 2.13 shows the group velocities as a function of the product of plate thickness and frequency. Waschkies [64] found that only waves reflected under approximately 45° propagate in a plate. Surface or Rayleigh waves are also excited in very thin plates. However, if the thickness is smaller than the wavelength, they degenerate into the initial portions of the curves a_0 and s_0 in Figure 2.13 with different propagation velocities [66].

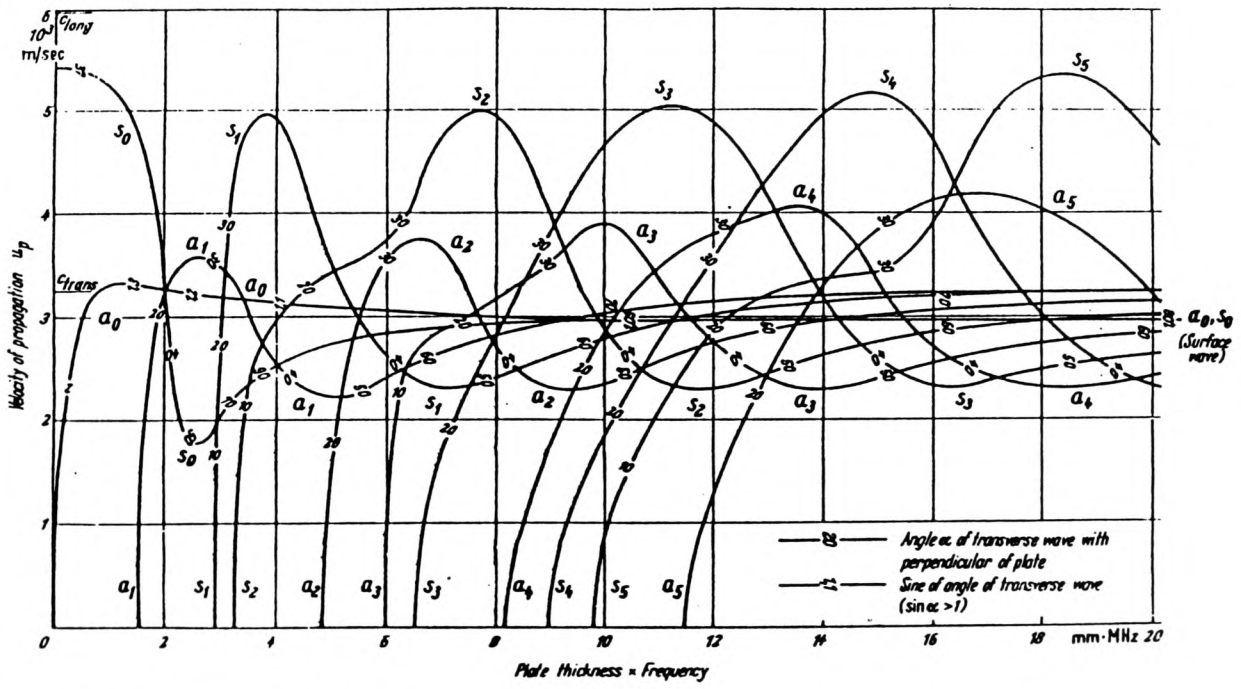

Figure 2.13: Lamb wave diagram [66].

Two effects influence wave propagation in all structures, viz. the attenuation and the dispersion. Attenuation is a measure of the energy loss of an elastic wave as evidenced by the decrease in the amplitude. Dispersion is the dependence of the phase velocity of harmonic waves upon their frequency.

Attenuation consists of geometrical divergence due to the propagation of the waves and absorption by direct transfer of wave energy into heat and by indirect transfer via wave scattering along particles, impurities, pores and grain boundaries and subsequent heat transfer [66]. Surface roughness introduces additional absorption in Rayleigh and Lamb waves [66]. Geometrical divergence depends on the structure [66]. For Lamb waves the geometrical divergence is $1/\sqrt{z}$ [66]. Absorption has the form of an exponential function [66]:

$$p = p_o \, e^{-\lambda z} \qquad (2.31)$$

where p_o and p are the pressures at the beginning and at the end, z is the distance and λ is the total absorption coefficient. Absorption is also frequency dependent resulting not only in a decrease in amplitude with distance, but also in a shift of the mean frequency towards the lower end of the spectrum [60]. Using equation (2.31) attenuation can be written as:

$$p = p_o \, \varphi \, e^{-\lambda z} \qquad (2.32)$$

where φ is the geometrical divergence. For example, the measured attenuation for shear waves in A-212-B carbon steel was about 4.3 dB m^{-1} for a frequency of 1.5 MHz and shear wave attenuation was higher than that for longitudinal waves [68].

Dispersion causes a spectrum of frequencies applied as an impulse to a point on or within a plate to arrive at another point on the plate, strung out in time with a time-varying amplitude and frequency content [69].

Elastic waves undergo various changes at boundaries. The proportion of energy transmitted and reflected can be calculated if the acoustic properties of the boundary media are known. If the second media is a gas such as air, the transmission into it can often be neglected because it is too small [70].

Wave propagation in thin plates has been investigated by various researchers [64,68,69,71]. Fowler and Papadakis [69] and Graham and Alers [71] dealt with dispersive wave propagation in plates, and comparison with theory was carried out by a frequency analysis at intervals (gates) of the captured signals. The principal propagation modes were the symmetric and antisymmetric Lamb modes [71] with the symmetric mode arriving first [67,71].

The energy contribution of the different waveforms has been investigated by Waschkies [64] for thick plates depending on the source position (Figure 2.14). Fitch [68] studied the change in signal shape when the transducer was placed on different sides of the specimen. He found that the signal shape was altered to some extent but the basic signal shape remained. Rindorf [67] found that a distinctive surface wave is present on the same side as the source but absent on the opposite side of a 50 mm thick aluminium plate.

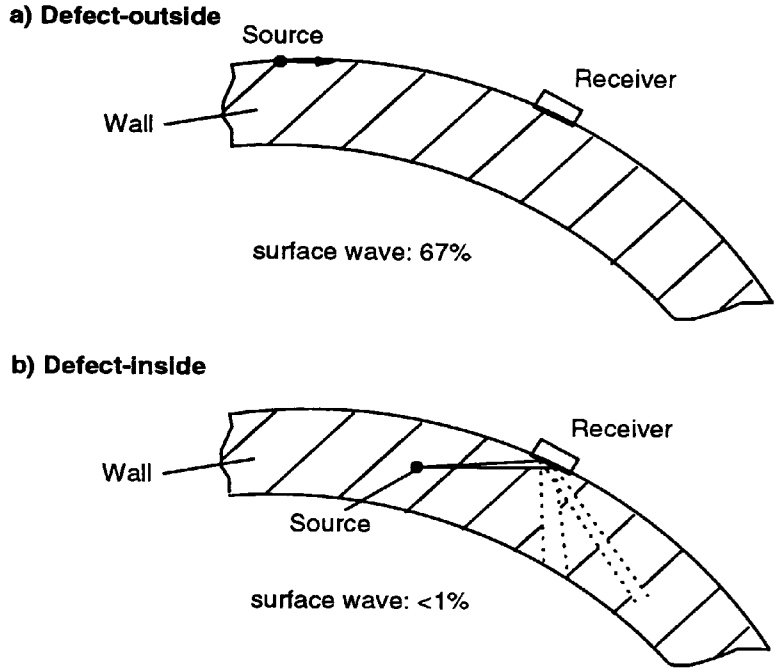

Figure 2.14: Sound propagation as a function of source position [63].

2.2.3 Some Aspects of AE Instrumentation

The necessary equipment for AE measurement has remained the same in principle since its early days (Figure 2.15) [60]. In order to arrive at the source signal S one has to calculate or measure the transfer functions of the propagation medium P, transducer I, signal conditioning C and analyser R, according to the following equation:

$$O = S * P * I * C * R$$

where O is the recorded signal and the * represents signal convolution [72].

Determination of the propagation medium transfer function involves the same problems as in section 2.2.2 (page 59) viz. the attenuation of the wave due to absorption and dispersion. Normally, signal conditioning C and the analyser R should not induce any unknown signal distortion. Preamplification is necessary to limit noise problems in AE field work and to overcome the problem of signal loss and interference in long cables. The main purpose of the amplifier is to allow a variable gain to adjust the signal amplitude to the input range of the storage and analysing facility in order to harness the whole input range. Storage facilities are all kinds of transient recorders, hard discs, etc., which either store the whole signal in A/D converted form or only the extracted AE-parameters in real time (low storage capacity necessary), or both.

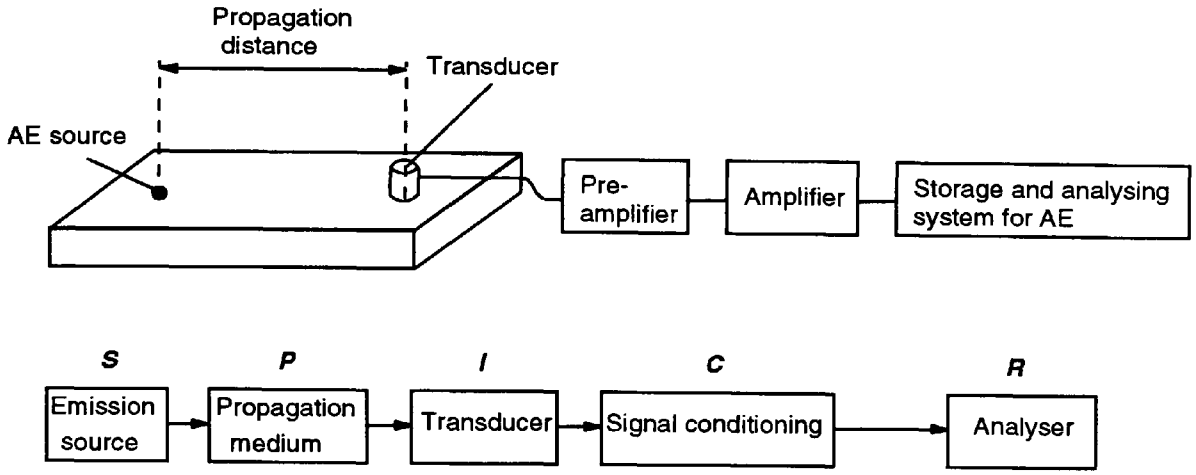

Figure 2.15: Schematic diagram showing a typical experimental arrangement for AE monitoring.

The transducer and the couplant that is used to affect maximum energy transfer across the interface is the last unknown variable of the arrangement. The thickness of the couplant (solid or liquid) should be only a small fraction of a wavelength since non-uniform and thick films may produce signal distortion and interference [60]. In general, the higher the viscosity of a couplant the higher the sensitivity for shear waves [73] and the better the coupling for higher frequencies [71].

Transducers are an important feature in AE testing. They are available in a great variety with trade-offs between sensitivity and flat frequency response. Broad band transducers are generally less sensitive than frequency type transducers. The most common transducers are piezoelectric contact transducers, which take advantage of the piezoelectric effect. Other so called non-contact transducer types are capacitive and electro-magnetic acoustic transducers, which can be used to measure the absolute surface displacement [58].

Graham and Alers [71] have compared the output signal of a capacitive displacement transducer and a piezoelectric transducer and concluded that the piezoelectric one was principally velocity sensitive. However, piezoelectric transducers have a higher sensitivity of up to 10^{-14} m [58,74].

Other types of transducers are single and differential piezoelectric transducers. Single transducers contain only one piezoelectric crystal, whose output is then amplified. Differential transducers contain two opposite polarised piezoelectric crystals and the difference of the two signal outputs is then amplified. This reduces electromagnetic interference and improves the performance [73].

The most widespread method of transducer calibration is the excitation of a transducer with a standard broadband transducer and noting the resulting frequency

response [58]. A great deal of effort has gone into using mechanical sources such as fracture of pencil leads, graphite and glass rods as standard AE sources to compare transducer outputs [71,75]. A simple source is an AE transducer which is used as a transmitter, but this source is subject to variability in the couplant used making it difficult to reproduce [70,75]. Similarly, reciprocity calibration via interchanging of three transducers was proposed [76]. Recently Scruby and Drain [70] developed an absolute calibration method for transducers and/or AE systems, including propagation medium and medium sensor interface, using a laser pulse as source. It was also shown that the thermo-elastic laser pulse source closely approximated the elastic wavefield of a cracking source [70,74]. However, it is uncertain whether transformation of source energy in AE energy is the same. Other drawbacks are the costs, safety aspects and the varying reflectivity of the specimen surface.

Discussion:

The preceding sections highlight the most troublesome aspects associated with AE. These are (i) the elimination of background noise and the identification of AE from different sources, (ii) the attenuation and modulation of the signal during propagation and (iii) the calibration of transducer and the whole system. Recent advances in location and filtering techniques have eased the first problem considerably. The problem of absolute AE calibration is still unresolved even though it might offer a whole new range of possibilities in AE testing. The most promising technique appears to be the laser calibration technique proposed by Scruby *et al.* Signal distortion during propagation makes the task of relating AE to a particular source and fracture event very difficult. Therefore, mainly parameters which characterise the whole signal which includes different arrivals and multiple reflections are used in AE signal analysis assuming that differences in the source signals are reflected in the recorded signals even after propagation (see below).

2.2.4 AE Signal Analysis

Figure 2.16 illustrates the different AE parameters of rise time, amplitude, signal duration, counts, hits and decay time. Modern AE facilities offer a vast range of analysing methods, including spectral analysis prior to or after software filtering. In addition, all methods of wave analysis viz. auto-correlation, cross-correlation, averaging, convolution etc. can be applied.

Generally two approaches for AE-signal analysis are possible. The first one is based on the assumption that only the first cycle of an AE burst, which is assumed to be the first and direct arrival, represents the source of AE. All subsequent cycles of the AE signal are assumed to be due to multiple reflections, different propagation paths,

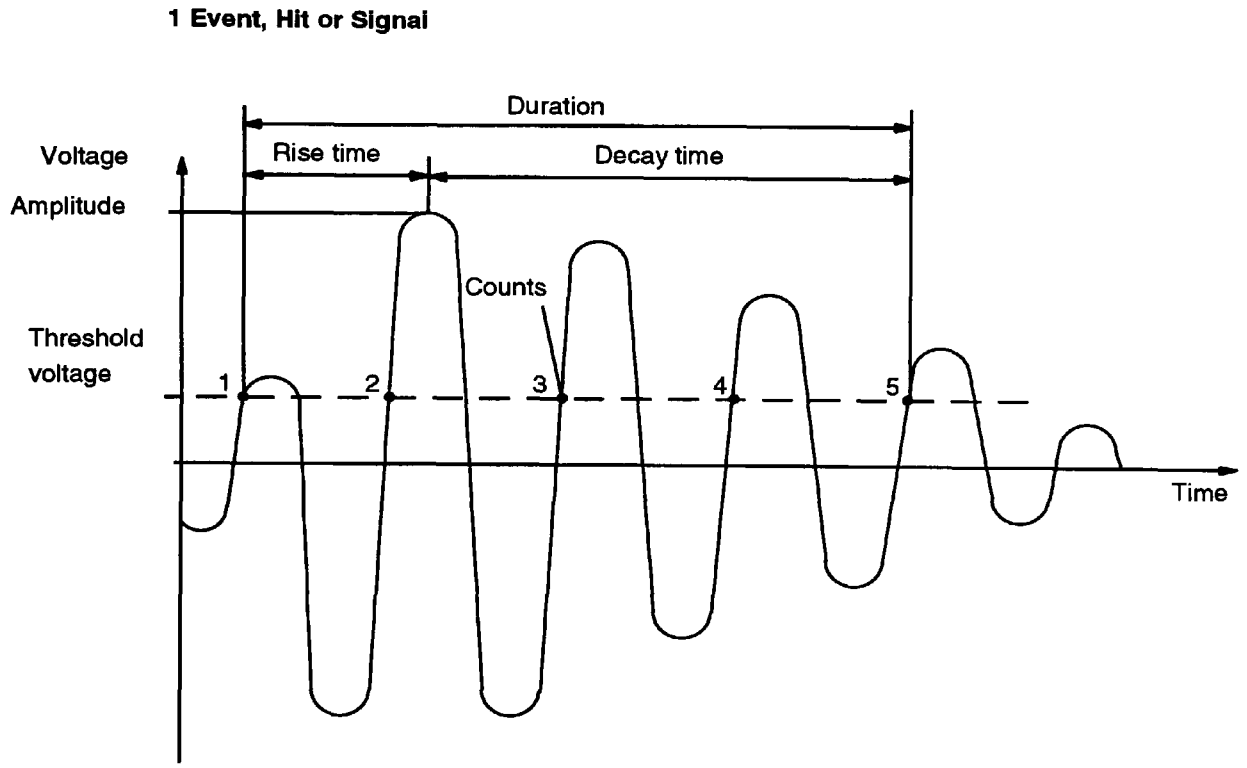

Figure 2.16: Schematic diagram illustrating the different AE parameters.

reverberation and ringing of the transducer, etc [73]. The second approach looks at the whole AE signal, assuming that the signal distortion is the same for all signals. If there are two different source processes which produce two different AE source signals it should still be possible to distinguish the two different signals after propagation. In the first case all parameters characterising one AE-cycle, viz. polarity, duration, frequency, amplitude, etc., can be used, in the latter all AE-parameters characterising the whole signal, viz. counts, energy, maximum amplitude, rise time, duration etc.

The maximum AE signal amplitude V_i is proportional to the intensity of the source mechanism and is generally measured using a logarithmic analyser so that the amplitude in dB is:

$$V\ (dB) = 20 \log \left(\frac{V_i}{V_o} \right) \qquad (2.33)$$

where V_o is the reference amplitude [77]. If the number of signals in the amplitude distribution curve is also plotted on a logarithmic scale it often approximates to a linear relationship, the slope of which is designated as the b-value. It is described using an power law of the form:

$$n(V_i) = \left(\frac{V_i}{V_o}\right)^{-b} \qquad (2.34)$$

where $n(V_i)$ is the number of AE signals whose amplitude exceeded a given value of V_i. The b-value has a simple meaning when a deformation process occurs by a small number of large steps, there is a large proportion of high amplitude emissions and the value of b is small. When the deformation proceeds in a large number of small steps, small emissions dominate and b is large [78]. Another advantage of the b-value is that it is not dependent on attenuation because all the emissions are attenuated by the same factor. Pollock [78] concluded that smaller b-values correspond to more brittle behaviour and a shift towards smaller b-values was also observed as failure approached in a tensile test.

It has been shown that AE signals from different sources have different frequency contents [22] and frequency analysis was used to characterise AE [22,71,79,80]. For any kind of frequency analysis the natural frequency of the specimen and the transducer must be excluded (by the use of broadband transducers). The recorded frequency is a superposition of the source spectrum and transfer characteristics of specimen and transducer [27]. It was not found to be substantially affected by the size of the structure or mode conversion due to multiple reflections [71]. Frequency analysis is also a fundamental tool for transducer selection [27].

Plastic flow in A533-B steel was characterised by a broad frequency peak around 1 MHz and crack growth showed frequency components predominately below 200 kHz [79]. Raj *et al.* [80] found a characteristic frequency of 0.14 MHz during necking of 316 type stainless steel as a result of microvoid coalescence and/or crack growth. During uniform elongation the frequency increased from ~0.47 MHz (yielding) to ~0.66 MHz at the ultimate tensile strength.

A change in the count rate (number of threshold crossings) was used as a qualitative tool to indicate a change in the failure mechanisms [81]. Figure 2.16 (Page 66) shows that the count number depends on amplification and threshold, hence comparisons can only be made if the same test parameters were used [77].

Lottermoser *et al.* [82] questioned the information content of the count number due to its dependence on various parameters and concluded that parameters such as energy, number of hits, amplitude and energy distribution are more powerful. Various attempts were made to relate counts or count rates to fracture mechanics parameters (see also section 2.2.5).

Energy analysis seems particularly powerful since AE is caused by the sudden release of stored internal energy. Moreover, energy analysis takes both signal amplitude and length into account in contrast to all other analyses, but it requires sophisticated electronic circuits [73]. The energy E_{AE} of a AE signal is:

$$E_{AE} = \int_0^{\bar{t}} (V_i)^2 \, dt \qquad (2.35)$$

where V_i is the amplitude and t is the signal duration. In practice, the signal is squared and its envelope integrated over the signal duration and the area is then related to a reference energy value using a dB-scale. Lottermoser *et al.* [82] was able to distinguish between plastic deformation, microcracking and macroscopic crack propagation on the basis of the energy release of 10^{-15},10^{-12},10^{-10} J, respectively for compact tension (CT) specimens. AE from shearlike martensite transformation had rather the shape of what was suggested to be a compressive signal by Hall *et al.* [21] and not the decaying shape, which has been reported in various reports for tensile tests [83].

Sklarczyk [84] has examined the fracture characteristics of bulk Al_2O_3 ceramic specimens by using both approaches of signal analysis (see above). The polarity of the first cycle in connection with location techniques made it possible to correlate AE with microcrack and macrocrack initiation.

2.2.5 AE Application

Relationship between AE and Fracture Mechanics Parameters

It was postulated that the total AE count number N was directly proportional to the plastic zone linear dimension. By using the zone size for a wide centre-cracked plate in uni-axial tension a relationship of the form:

$$N = \sigma^m \qquad (2.36)$$

was obtained, where σ is the applied stress [61]. Investigators have shown that exponent m varies between 2 and 8 [61].

Gerberich and Hartbower [85] have established a semi-empirical relationship between the energy of the stress wave and the available elastic energy from incremental crack extension;

$$\Delta A \approx \frac{(\sum g)^2 E}{K^2} \qquad (2.37)$$

where ΔA is the area of the incremental crack growth, Σg is the sum of the stress-wave amplitudes associated with that increment of growth, E is the elastic modulus and K is the applied stress-intensity factor. This relationship was valid for about 100 data points obtained from crack growth in high-strength aluminium, titanium and steel alloys using a threshold which eliminated AE caused by plastic deformation.

Khan *et al.* [86] related AE data to crack growth and obtained:

$$\sum E_{AE} = k \, (\Delta A)^{1.5} \qquad (2.38)$$

with ΣE_{AE} being the accumulated AE energy, k is a constant depending on material toughness and electronic instrumentation and ΔA is the crack area.

The models given above are quite different, which shows that there is still some uncertainty as how to relate cracking and AE.

Relationship Between AE and Coating Parameters

Wen *et al.* [87] used AE during bend testing of plasma sprayed Ni-Al coating to show that first cracks formed at primary defects and then propagated along intergranular boundaries in a direction perpendicular to the internal stresses. Finally the cracks penetrated the whole thickness and the coating spalled at the interface. Almond *et al.* [88] found lower b-values with poorly adherent coatings suggesting that interfacial failure caused high amplitude signals.

Cohrt and Thümmler [32] proposed that AE recorded in bend tests of thermal barrier coatings was related to tensile cracking at low strains and interface delamination and spalling at higher strains. The two regions overlapped for stiff coatings without microcracks or separated along the strain axes for weak coatings with microcracks.

Cox [89] found a nearly one-to-one correlation with the number of cracks and high amplitude AE signals (> 100 dB) in 4-point bend tests. Two other types of damage were identified, microcracking was characterised by low amplitude signals and medium long cracks gave signal amplitudes between 76-88 dB [89].

Relationship Between AE and Oxide Parameters

Khanna *et al.* [54,90] have studied the oxidation of 2.25Cr-1Mo steel using AE and compared it with thermogravimetric results. AE was able to detect the onset of breakaway oxidation earlier than it was possible with thermogravimetry [54] and showed that microcracking preceded breakaway or spallation [91,92]. AE during pre-breakaway had a wider spectrum indicating that many processes such as dislocation climb, grain boundary sliding etc. were involved. Post-breakaway crack nucleation showed a frequency peak at 660 kHz and spalling/internal cracking during cooling a frequency peak at 490 kHz with internal cracking being the most energetic of all processes [93]. AE from oxidation and subsequent cooling of 9Cr-1Mo was more energetic at 950 °C (b-values 1.4) than at 900 °C (b-value 2.0) due to higher cooling strains [94].

Christl *et al.* [55-57] investigated the damage of oxide scales formed on a low alloy steel (containing 2.25 wt% Cr and 1 wt% Mo) at 600 °C in Ar-50% H_2O, O_2 and air, which occurred during cooling to 300 °C every 8 h using AE technique. The amplitude and intensity of AE events was determined by the failure mode of the scale, whereas the total number of AE events was mainly determined by the cyclic corrosion rate and the healing rate of delaminations. The b-value seemed to be constant for

amplitude distributions of the same corrosion run but changed with the failure mode and was approximately 2 for buckling and delamination of haematite-rich scales and approximately 1 for through-scale cracking of magnetite scales. Different count rates were observed for microcracking and macrocracking in NiO [81]. To date, the AE signal shape and the dependence of AE on oxide thickness have not been investigated.

2.3 Coatings

This section on coatings was included in the review, firstly, because a coating was employed to selectively grow an oxide at the surface of the bend specimens on only one side between the inner rollers of the 4-point bend jig. Secondly, laws derived to predict the mechanical failure of coatings could be used to describe the failure of oxide scales.

2.3.1 Failure of Thin Films and Layers

Evans *et al.* [95] reviewed the cracking and decohesion of thin films. The failure of thin films subject to tension on ductile substrates is similar to the failure of brittle oxide layers [96]. As with oxides conditions for cracking, multiple cracking, interface sliding and film decohesion were given. Assuming interface sliding, the minimum spacing between the cracks L was of the order of $w<L<2w$, where w was the sliding length (see also section 2.1.2.3, page 37). Crack spacings larger than the minimum value can, however, exist which are determined by statistical consideration.

The validity of the equations was shown with Cr-films on aluminium and stainless steel. The critical cracking stress for the Cr/Al system decreased as the film thickness increased. At stresses above σ_c additional cracks formed until saturation occurred. The crack spacing was larger for thicker films. The crack surface separation was relatively uniform through the thickness, indicating that inelastic effects occurred at the substrate surface in the cracks. Aluminium with a lower yield strength enhanced film cracking tendencies but inhibited decohesion by blunting the film cracks at the interface. The high yield strength of stainless steel and an oxide layer formed at the interface during deposition reduced the fracture toughness of the interface and thus promoted film decohesion [96].

The delamination and spalling of films in compression was, as with oxides, governed by the initial buckling condition (see also section 2.1.2.4, page 45) [97]. Once buckling had occurred a stress concentration at the tip of the interface crack existed and the crack propagated in both directions if the critical energy release rate was exceeded. The process of subsequent spallation is not well understood. Two models exist. In the first model the interface crack is deflected to the surface causing the film to spall. This occurs at a characteristic crack radius R_c of [95]:

$$\frac{R_c}{h} = 1.6\sqrt{\frac{E}{\sigma}} = 1.6\sqrt{\frac{1}{\epsilon}} \qquad (2.39)$$

where E is the Young's modulus of the layer, h is the thickness of the layer and σ is the stress in the layer. In the second model it has been suggested that crack deflection to the surface is most likely to occur when the bending strain at the circumference of the buckle attains its maximum. This hypothesis provides a spalling criterion of the form [97]:

$$\frac{R_c}{h} = 1.9\sqrt{\frac{E}{\sigma}} = 1.9\sqrt{\frac{1}{\epsilon}} \qquad (2.40)$$

It should be noted that in all equations the thickness is a critical parameter. Thin films favour buckling and spalling, thick films favour crack growth.

Ramsey *et al.* [98] used 4-point bending to study the fracture and interfacial behaviour of steel samples with 5 μm thick hard TiN coatings. The bending produced crack arrays running across the sample width and the crack spacing decreased with increasing strain. The cross-section showed that no debonding occurred and the cracks did not continue into the substrate. The crack surfaces were almost parallel, which was assumed to be a result of plastic stress relaxation. Thus a force balance according to equation (2.18) was established.

2.3.2 Coatings Used to Prevent Oxidation

In general, coatings have to be chemically and mechanically stable and act as a diffusion barrier [33]. However for the purpose of this work chemical and mechanical stability were not important because it did not matter whether the coating was attacked by the environment or failed during the deformation as long as the deformation of the coating did not cause AE above the set threshold. On the other hand the coating should not interfere with the oxidation process. This section is, therefore, restricted to the few reports where coatings have been used to reduce oxidation and/or where the AE emitted by the coating during deformation and failure was assessed.

Clark [99] investigated oxidation prevention of commercially available overlay coatings and their possible use in AE testing at 500 - 700 °C (Table 2.3). Only Berkatekt 29 and Berkstop N.T reduced oxidation to a very low level and at the same time did not cause AE above the used threshold.

Ramachandra-Rao and Madhu [100] evaluated the oxidation resistance of inorganic coatings, e.g. TiO_2, ZnO, Al_2O_3 and Cr_2O_3, and their mixtures on mild steel. Metallic

coatings such as chromium and aluminium were also investigated at 600 - 800 °C in air. Among the single oxide coatings TiO_2 coating gave the best oxidation reduction efficiency of 76.81% at 800 °C in air. In the case of coatings of mixtures of oxides, TiO_2 + Borate mixture coating gave the best performance with a reduction of 89.99% at 600 °C in air. The metallic coatings chromium and aluminium had a reduction efficiency of 20 - 65%.

Snowpake	TiO_2 suspension in organic carrier fluid
White emulsion paint	TiO_2 suspension
DAG 2102	Commercial preparations for protection and lubrication of Ti and Ni alloys during hot working in the temperature range 800 - 900 °C.
Deltaglaze 47	
Berkatekt 29	Commercial coating for oxidation resistance up to 850 °C
Berkstop N.T	Commercial coating for stopping off during nitriding.

Table 2.3: Summary of the coatings investigated [99].

2.4 Conclusions

The preceding survey showed that there have been several attempts to model oxide failure. There was general agreement for using fracture mechanics to model failure. However, a fracture mechanics approach requires a knowledge of the actual void size. This is a parameter which has been ignored until recently. Another common problem with all models was that they do not account for the total state of stress in the oxide prior to testing nor did they make any allowance for creep or lateral oxide growth. In addition, the full potential of the models could not be explored because no reliable data were available for the critical parameters in the models, viz. Young's modulus, surface energy, fracture toughness, nor were measured failure strains available which could be used to verify the predictions. Certainly, the difficulties involved in measuring these parameters at growth temperature have contributed to the lack of data as well as the cost and the complexity of such equipment. This also leads to the question of whether data from bulk oxides can be used to predict the failure of thermally formed scales.

AE appears to have considerable potential in detecting and analysing fracture processes. The study was designed to explore this potential. The distortion of the signal and the fact that no absolute calibration technique was available made it necessary to rely in principle on a simple comparison of AE from different tests and materials.

CHAPTER 3: Experimental

3. EXPERIMENTAL

This work was devised to study the failure of brittle layers under applied load. A 3-point bend test technique was used by Hall *et al.* [21] for preliminary work at room temperature in tension and compression. They used flat specimens with the scale on only one side. In this way tensile and compressive forces could simply be applied by placing the layer on the bottom or top side within the bend jig without modification of jig or specimen. The work produced good results, however the experimental arrangement had drawbacks (Figure 3.1), viz.:

(i) The oxide stress and strain varied with position along the length of the beam in the three point bend jig which meant that a study of the AE signal distribution with strain was impossible since signals from different stages of the failure process overlapped.

(ii) The upper roller was at the position of highest stress, i.e. in the fracture zone during loading in compression which might have influenced the failure mechanism.

(iii) Roller/oxide contact might have caused erroneous signals in compression.

(iv) No measurements could be made at oxide growth temperature.

(v) The waveform analysis was subjective, since classification was only based on the signal shape as perceived by the experimenter.

Therefore a revised experimental configuration was developed which could be used at room and growth temperatures (see also section 3.3). It was based on a 4-point bend test arrangement (Figure 1.2, page 26). The main idea was to use a flat specimen having an oxide area of 10x10 mm on only one side which could be placed between the inner rollers of a 4-point bend jig, where stress and strain were constant (see also section 3.2.1, for choice of specimen). An environmental high temperature furnace having a ceramic 4-point bend assembly was acquired for the tests at growth temperature (Figure 1.3, page 27) and constant strain rates were applied by placing the bend jig or the furnace in an Instron test machine. The AE was recorded using an AE system with a transient recorder board and a broadband piezoelectric transducer (see also section 3.6). Failure mechanisms were established in conjunction with results from electron and optical microscopy investigations (see also section 3.7). This revised experimental arrangement had the following advantages:

(i) A study of the signal distribution as a function of strain was possible since stress and strain within the oxide raft were constant at a given radius.

(ii) Failure was not influenced by roller contact.

(iii) Tests could be performed at room and oxide growth temperatures.

(iv) Wave analysis software could be used to analyse and classify the signal shapes since the AE data were available in digital form.
(vi) A frequency analysis of the AE signals could be carried out.
(vi) Environmental tests and sulphur decoration tests could be made.
(vii) The specimens acted as waveguides and thus had no discontinuities which could distort the AE signals.

However, the modified configuration caused some experimental difficulties which had to be overcome before tests with an actual scale could be made (see also section 3.2.2 to 3.2.4) and a detailed description of the experimental arrangement including the AE system can be found in section 3.3 to 3.6.

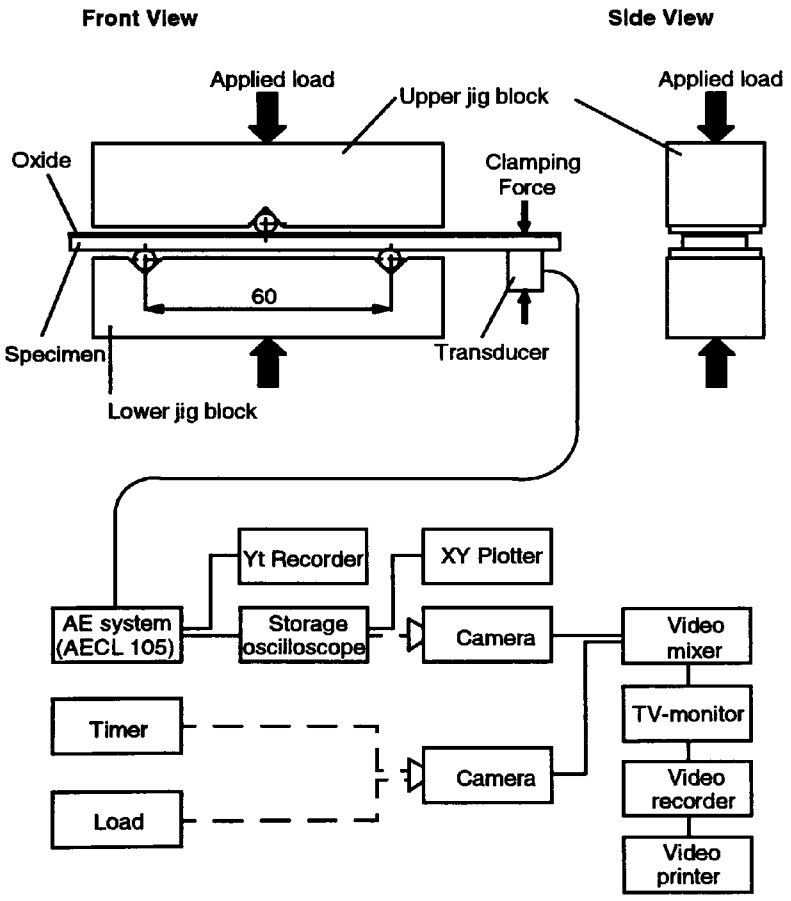

Figure 3.1: Experimental arrangement of the preliminary work [21].

3.1 Materials

Tests were made with iron and nickel oxide scales grown on mild steel and 99% pure nickel (chemical composition given in Table 3.1). Tests were made at room and growth temperature (550 °C for iron oxide and 900 °C for NiO) using strains rates of

$\sim 10^{-4}$ and $\sim 10^{-5}$ s^{-1}. Tenslac brittle lacquer layers (Measurements Group, USA) were used as model layers to simulate the AE obtained from oxide cracking (see also section 3.4, for specimen preparation)

Mild steel composition in element %

Al	Si	S	Mn	Mo	Cr	Ni	Fe
0.17	<0.07	<0.25	0.50	<0.6	<0.12	<0.19	Bal

99% pure Nickel composition in ppm (total purity includes Cobalt)

Cu	Fe	Mg	Mn	Si	Ti	C	S
<2500	<4000	<2000	<3500	<1500	<1000	<1500	<100

Table 3.1: Chemical composition of the materials being tested.

3.2 Development of the Bend Test Technique

In order to make the revised experimental arrangement applicable preliminary investigations were necessary to establish:

- whether the AE signals were influenced by experimental parameters such as transducer location, couplant, etc;
- a method of transmitting the signal outside the furnace in the tests at oxide growth temperature; and
- a method for producing an area of oxide on only one side of the sample.

These studies are discussed below together with an assessment of the advantages and disadvantages of the specimen geometry used.

3.2.1 Choice of the Specimen Geometry

Two basic sample geometries have been used to study the failure of oxide scales, i.e. round [14,15,18] and flat specimens [31]. Flat specimens having an area of oxide (10x10 mm) on only one side of the specimen were used in the present study. The advantages and disadvantages of these flat specimens compared to round specimens were:

Advantages:

(i) Tensile and compressive stresses in the oxide could be applied without changing the dimensions of the specimens or the test rig.

(ii) Uncertainties involved in the stress calculation for round specimen using a scale displacement vector to account for inward or outward movement of the previously

formed oxide as a result of the volume change during the thickening of the layer could be avoided [25,26].

(iii) The oxide growth stresses and thermal stresses created only a two dimensional stress field with the same stress components in x- and y-direction. The z-component was zero [4]. Oxides on curved substrates would have been subjected to a three dimensional stress field due to oxide displacement during growth and/or substrate contraction during cooling. This would have favoured buckling or delamination depending on the relative movement of the scale and the curvature of the sample (convex or concave).

(iv) Models based on buckling theory could be used to describe scale buckling under compressive stress. In this context the oxide was approximated as a thin plate on a thick substrate [41]. Oxides on circular specimens could have been described as a composite consisting of an outer oxide tube which was grown on a cylindrical substrate. A mathematical treatment for this case would not have been available and models describing the buckling stability of single tubes could not have been used for such a composite [18].

(v) Round specimens as well as flat specimens with an oxide raft on only one side as used in the present study did not have sharp oxide corners, which would have drastically increased the magnitude of the growth stresses and would have been zones of preferential delamination and spalling of the oxide [25,26].

Disadvantages:

(i) The present study with an oxide area of 10x10 mm introduced edge effects, where the oxide or the oxide failure was influenced by the presence of the coating or the gradual increase in thickness at the boundary. The length of this boundary was approximately 500 - 1000 μm. These effects were present in the x- and y-direction. Circular specimens would have shown these effects only along the length of the specimen; along the circumference the oxide would have been continuous.

(ii) The linear variation of the bending stresses with distance from the neutral axis created a stress increment $d\sigma$ which favoured delamination in tension and buckling in compression (Figure 3.2). Calculations showed that the variation in stress was of the order of +/- 1% and +/- 3% for 10 or 50 μm thick oxides, respectively.

(iii) The increase in curvature during deformation of a flat specimen introduced a moment which promoted delamination of the oxide when it was subjected to tension (Figure 3.3) and reduced the likelihood of buckling and spallation when the oxide was subjected to compression (Figure 3.4). Similarly, spalling would have been more likely on round specimens under tensile stress due to elongation of the substrate and less likely under compressive stresses due to substrate

expansion. In both cases, the stresses arose from the resistance of the oxide to a change of its shape or curvature.

In summary, the stress field in flat specimens was certainly simpler, however the oxide geometry created additional edge effects. Both flat and round specimens would have produced additional forces which might have encouraged delamination and spalling during deformation depending on the relative stress direction. The main reason for selecting flat bend test specimens was that tensile or compressive forces could be applied using the same test rig without changing the specimen dimensions, which was very important for the AE work since every modification could have influenced the propagation of the AE signals and made a comparison of AE from tensile and compressive failure events impossible.

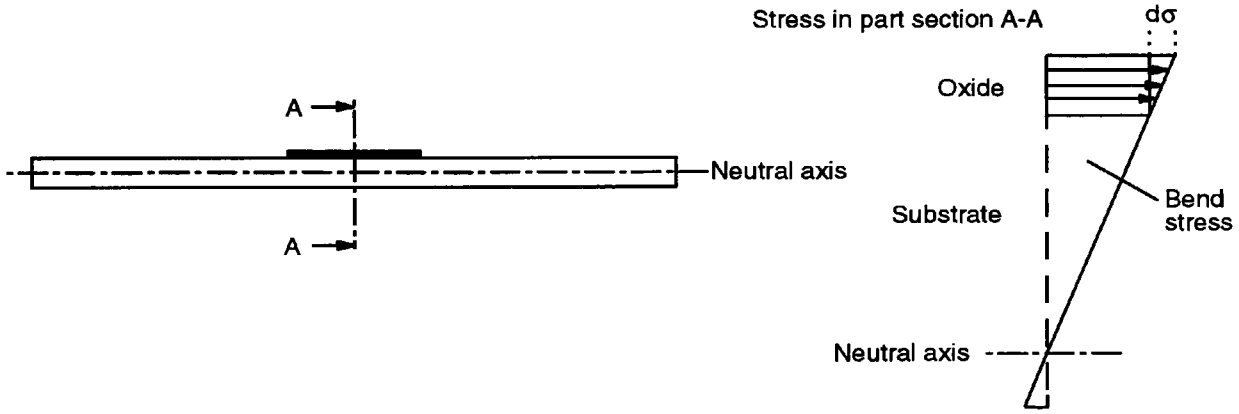

Figure 3.2: Schematic diagram of the bend stresses in the oxide layer. ***dσ*** introduces a moment reducing the probability of scale buckling under compressive stress and making delamination more likely under tensile stress.

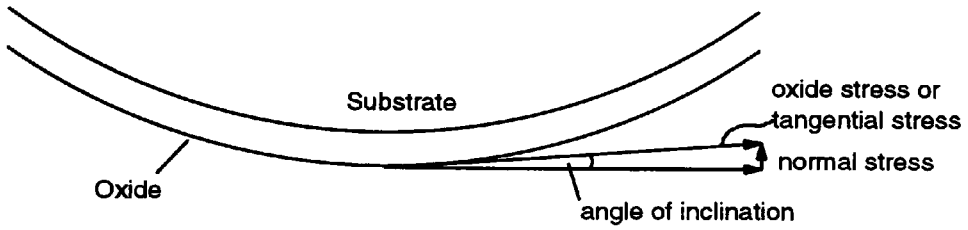

Figure 3.3: Schematic diagram of the normal stress arising from the curvature which supports the delamination of the oxide scale.

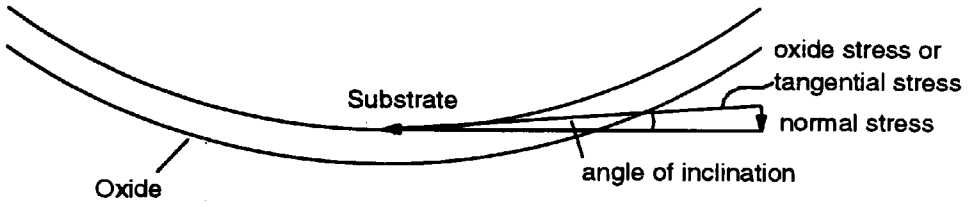

Figure 3.4: Schematic diagram of the normal stress arising from the curvature which reduces the probability of oxide buckling and delamination.

3.2.2 Effects of Experimental Parameters on the AE Signal

The influence of experimental parameters, such as transducer mounting technique, couplant, source location, etc. on the AE signal was investigated to select the best experimental configuration for maximum signal reception and to determine their effect on the two characteristic signal shapes (cf. Figure 1.1, page 26).

The **natural frequency** of the specimen was calculated and measured (Appendix A), since its knowledge was essential for frequency analysis and specimen resonance might have influenced the AE signal, i.e. it might have caused the different signal shapes. The results for both longitudinal waves and transverse waves are given in Table 3.2 and show that both were outside the frequency range of 100 kHz - 1 MHz used in this study.

Different couplants were assessed by pressing two transducers together with a specimen clamp having a force of 10 N. One transducer was connected to the pulse output of the Locan AT system and thus used as source and the other was used as receiver in the usual way (Figure 3.5). The best results, i.e. the highest amplitudes were obtained with Apiezon grease (Apiezon Products Ltd, UK), followed by silicon compound MS_4 (Midlands Silicones Ltd, UK) and water (Table 3.3). The worst response and the highest scatter of the data was recorded without a couplant. The frequency content and the shape of the signals remained very similar with all couplants, only the signal itself became smaller due to increased damping. The results indicated the lower the viscosity of the couplant was, the lower were the AE response and the transmission of shear waves [68]. Thus the best solution would have been to glue the transducer to the specimen, but this would have caused problems in the tests carried out at oxide growth temperature due to mismatch in thermal expansion coefficients of metal and glue.

Different transducer mounting arrangements involving insulating tape or specimen clamps with 2.5 or 5 N force were assessed by measuring the change in AE signal amplitude and shape (Figure 3.6a). In this and the following tests breaking a 0.5 mm HB pencil lead at 45° was used as a standard source [75]. The specimen

(dimensions 100x10x1.8 mm) was always placed in the 4-point bend jig. The specimen clamp with the higher force gave a slightly better response and both clamps gave considerably higher signal amplitudes than insulating tape. Frequency content and shape of the signals were similar for the three arrangements tested.

The effect of the **transducer location** on the AE signal was studied by mounting the transducer at different positions (Figure 3.6). There was no apparent change in the amplitude, shape, and rise time when the transducer was mounted at opposite sides. The transducer mounted at the side gave a smaller amplitude and the shape was changed slightly.

The influence of the **source location** was assessed by breaking the pencil lead at different positions (Figure 3.7). There was no change in shape or frequency content, only the signal amplitude varied slightly with the distance from the source.

Tensile or compressive oxide failure was simulated by placing both transducers, transmitter and receiver, on the bottom or top side of the specimen, respectively (Figure 3.8). In this context additional spacers were used to create sufficient space to accommodate the transmitter transducer between the rollers of the 4-point bend jig. The results were very similar for both simulations, in particular the shape and the frequency content of the signals were not affected at all.

The **signal attenuation** was measured by using a specimen of 200 mm length and placing the receiving transducer at varying distances from the transmitter transducer. The signal amplitude decreased slightly with distance giving a signal attenuation of 5 - 6.5 dB m^{-1}. The shape and the frequency of the signals were not affected. Finally the same measurement was performed with the long specimen not in the bend jig. A slightly higher amplitude ($\sim$0.9 dB) was measured indicating that some of the AE energy was being dissipated via the roller contact zones, but this did not affect the signal shape or frequency content.

Summary:

The natural frequencies of the specimen were well below the frequency range of 100 kHz - 1 MHz used to detect AE and thus did not affect the AE signal. Of the mounting techniques and couplants studied, Apiezon grease used together with a specimen clamp of 5 N force, gave the best response. Both transducer and source location had no apparent effect on the AE signal, however it seemed reasonable to always mount the transducer on the same side of the specimen as the signal source. The attenuation of the specimen was 5 - 6.5 dB m^{-1} and some energy was dissipated via the specimen roller contact. In addition, an amplitude variation of 2 - 3 dB was found when repeating the tests, presumably due to variation in the source energy and coupling film thickness. More importantly, none of the parameters investigated distorted the signal to the extent required to transform the characteristic signal shape of a tensile failure

event to that of a compressive failure event, or *vice versa* (cf. Figure 1.1, page 26). The frequency content of the signals was even less affected than amplitude or shape. Therefore the two characteristic signal shapes could not have been due to signal distortion caused by the experimental configuration.

Specimen length [mm]	Transverse waves [Hz]		Longitudinal waves [kHz]
	calculated	measured	
100	421	450	25.8
200	375	-	17.4

Table 3.2: Measured and calculated natural frequencies for mild steel specimens of 100 and 200 mm length.

Couplant	Amplitude [dB]
Apiezon grease	55.7
Silicon compound	54.0
Water	53.2
without couplant	46.6

Table 3.3: Comparison of the measured amplitudes with the different tested couplants.

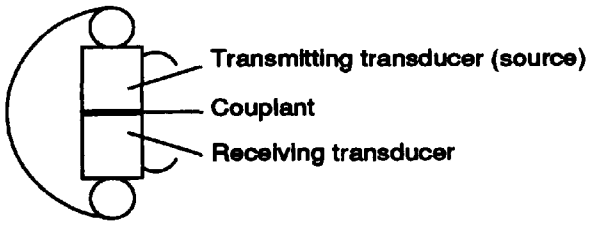

Figure 3.5: Schematic diagram showing the transducer arrangement for testing different couplants.

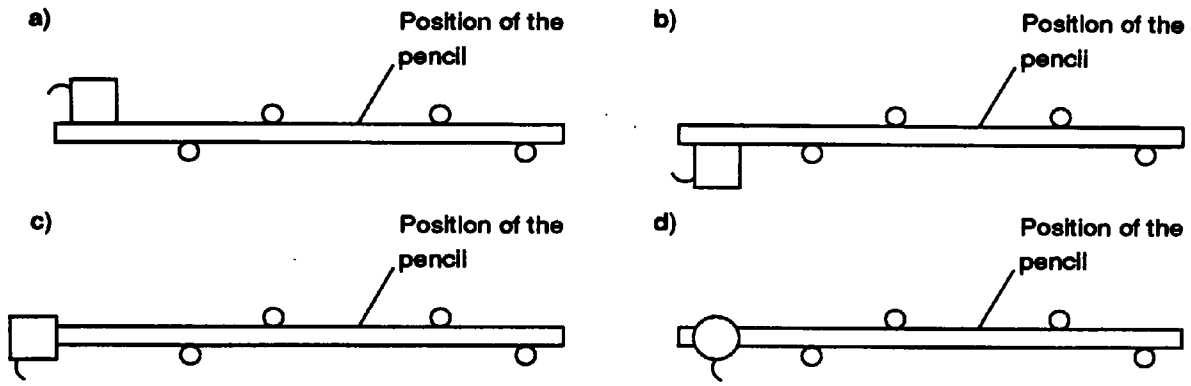

Figure 3.6: Schematic diagram showing the different transducer locations.

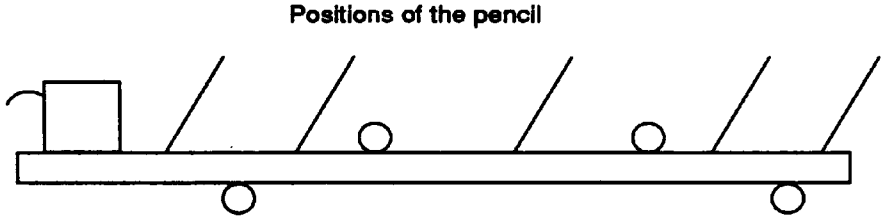

Figure 3.7: Schematic diagram showing the different positions of the pencil lead break, i.e. AE source positions.

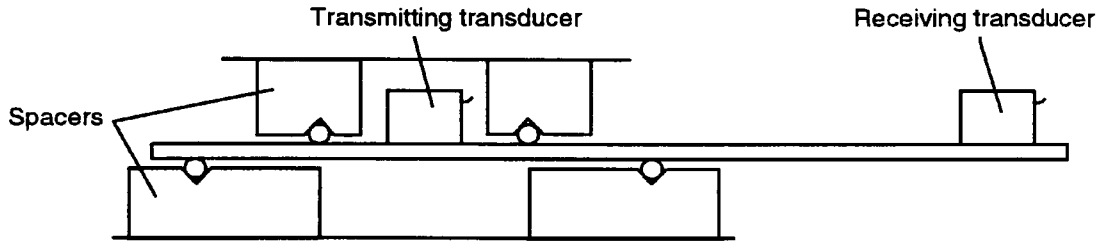

Figure 3.8: Schematic diagram showing the arrangement for compressive failure simulation.

3.2.3 Influence of a Waveguide on the AE Signal

For the tests at growth temperature it was necessary to find a waveguide that would transmit the signals to the outside of the furnace without too much signal distortion, since large distortion would have made signal shape analysis and comparison with the AE from tests at room temperature impossible. Three different arrangements were used to assess various waveguides (Figure 3.9) and as before breaking a 0.5 mm HB pencil lead under 45° was used as a standard AE source [75].

(i) Both, transducer and specimen were mounted on the waveguide with insulating

tape and grease as couplant. Different alumina, glass and silica rods and tubes with a maximum diameter of 4 mm and a maximum length of 250 mm were used (Figure 3.9a).

(ii) A platinum waveguide (diameter 0.45 mm, length 250 mm) was welded to the specimen on one side and to a piece of metal on the other side on which the transducer was mounted with insulating tape and grease (Figure 3.9b).

(iii) The specimen itself was the waveguide by using a metal beam of 300 mm length and the transducer was mounted on one end with tape and Apiezon grease (Figure 3.9c).

Summary:

The best results, i.e. the highest amplitude and the least signal distortion, were obtained when using the specimen as its own waveguide. With a separate waveguide good results were achieved with silica and alumina with hardly any difference in performance between these two materials. Platinum caused substantial attenuation and distorted the waveform. It appeared the more brittle the material the less the distortion and attenuation of the signal. The diameter of the waveguide had only a slight influence on the amplitude, the greater the diameter the smaller was the amplitude. In general, the number of additional interfaces created by using the waveguide had a much greater influence on the AE signal than the material itself, because every interface attenuated, reflected and distorted the AE signal [66]. This explained the good results obtained by using the specimen itself as a waveguide which also solved the problem of how to mount the waveguide to the specimen at oxide growth condition.

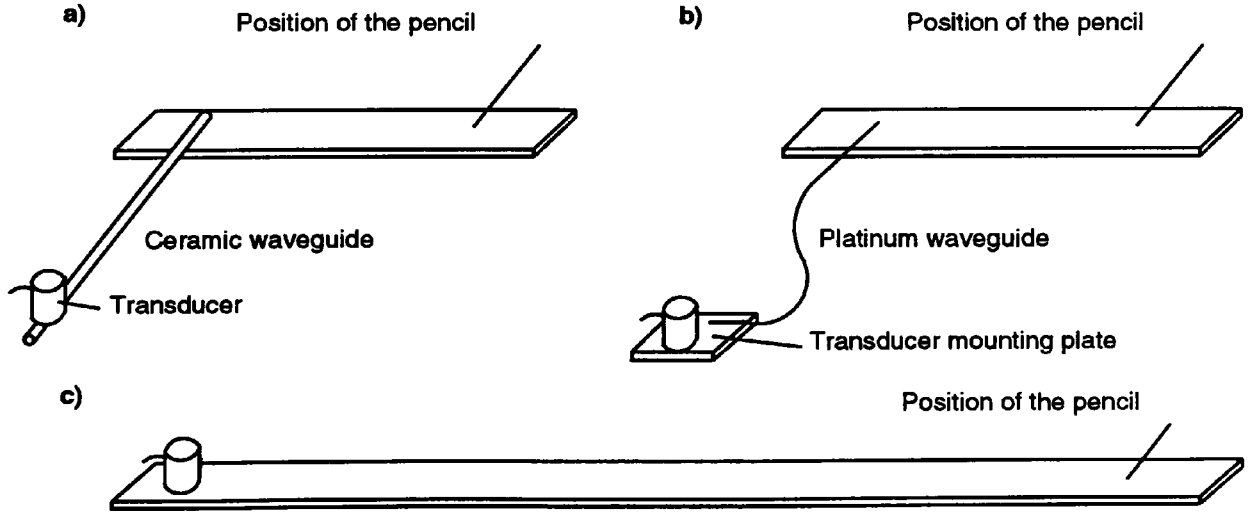

Figure 3.9: Schematic diagram showing the different arrangements used for testing different waveguides.

3.2.4 Investigation of Different Methods for Producing a Finite Oxide Area

A basic requirement for the new test scheme was to find a method for producing an oxide segment of 10x10 mm on only one side of the specimen which could be placed between the two inner rollers of the 4-point bend jig. There were basically two different ways in which this could be achieved. Either removal of the oxide from the rest of the specimen after pretest oxidation to leave an oxide raft in the area required, or protection of the surface by a stop-off coating or an inert atmosphere which prevented growth of oxide on the rest of the specimen. Five possible methods were investigated for their applicability in the tests at oxide growth temperature, their ability to reduce the oxidation rate and the amount of erroneous AE resulting from the use of the method, of which the last criterion was the most important. Mild steel specimens were used in all tests and the samples were oxidised in air at 550 °C for 1.5 and 60 h which would normally have given a ~10 or 40 μm thick oxide layer, respectively. The specimens were then bent to 1.12% strain and the AE was recorded during bending. The performance of the three most promising coatings was then also assessed on nickel samples at 900 °C. In the following a description of the different methods is given together with the experimental results:

(i) The **abrading** of the oxide from all sides except for an oxide raft of 10x10 mm on one side of the specimen with grinding paper up to grit size 600. Metallography after abrasion showed some damage at the edge of the oxide area in the first 200 - 500 μm, which was caused by cracks spreading into the area when the neighbouring oxide was removed. No other damage was found and no AE study was conducted since this technique did not introduce additional sources of AE. However, the technique could only be applied for the tests at room temperature.

(ii) Use of **different gas atmospheres** so that an oxide raft could be grown by exposing only a part of the specimen to air, while all the other parts were protected from oxidation by an inert atmosphere. An initial test was made to see whether the oxygen partial pressure in an argon inert gas atmosphere of a tube furnace was in principle low enough to stop oxidation. The furnace was flushed thoroughly prior to the oxidation, however post test examination showed a 0.5 - 1.5 μm thick oxide layer after only 1.5 h oxidation and furnace cooling of the sample, which is approximately 10 - 15% of the normal oxide thickness found after oxidation in air under the same conditions. This technique was therefore not pursued further since the use of different atmospheres would make the bend test arrangement very complex and hence it would be unlikely to achieve a sufficiently low oxygen partial pressure to keep oxidation at acceptable levels.

(iii) A **sputter coated palladium film** was used since it was a ductile layer unlikely to produce AE during deformation. The film was applied to act as a diffusion

barrier for most of the specimen except for a raft of 10x10 mm on which no film was applied and where the oxide could form. In preliminary tests the samples were completely covered with a 3 - 4 μm thick palladium (Pd) film[1], oxidised and bent. Cross-sections showed a layered structure indicating that Pd-film did not stop the diffusion of iron and oxygen through the film. Only the inward diffusion of oxygen through the layer was reduced as shown by a thin oxide layer below the original palladium layer. The fracturing of the oxide during bending produced considerable AE with high amplitudes, and hence the technique was not successful.

(iv) The use of an **electroplated nickel film** was based on the same principle as for the Pd-film. Similarly a 5 - 6 μm thick nickel film was applied onto the whole specimen by electroplating[2]. Cross-sections showed on top of the Ni-layer a magnetite scale with the inner half enriched in nickel and a thinner haematite layer at the outside after 60 h oxidation, indicating that the Ni-layer did not stop the outward diffusion of iron. In contrast, it did stop the inward diffusion of the oxygen and no oxide had formed underneath the Ni-layer. As with the Pd-film the failure of the oxide during loading gave rise to substantial AE, which made the technique not applicable.

(v) A series of **commercially available high temperature stop-off coatings and paints** were tested with the same principle in mind as for the sputter coated film (Table 3.4) [101]. All of them were available in paint or slurry form and applied by dipping and spraying according to the manufacturers instructions. The coatings could be divided into three groups according to their ability to reduce oxidation and avoid AE:

Those which did not prevent oxidation and failure of oxide and coating during loading produced substantial AE. These coatings were Heat Resistant Al-Si 319, Permoglaze HPC-PZ10, Ruskilla Aluminium 2845 and Temalac SA-100. Those which reduced the rate of oxide growth considerably but had a high AE activity due to the failure of the brittle coating during loading. These coatings were Berkstop C4 and Berkatekt 39. Those which reduced the oxidation rate dramatically and at the same time they were very soft and gave only rise to a few AE signals during deformation even though they showed cracks and spallation (Figure 3.10). These coatings were Berkatekt 12, Berkatekt 311 and DPG 3582. Berkatekt 12 caused slightly less AE and was therefore selected for the tests with mild steel.

None of the coatings stopped the oxidation altogether, the last three showed a 0.2 - 3 μm thick layer of oxide underneath the coating after 60 h of oxidation, i.e. the

---

[1]) Edwards sputter coater: Type S150A — Atmosphere: Argon
HT voltage control: Level 11 — Current:10-14 mA

[2]) Solvent: $NiSO_4$ solution — Current: 0.05 A cm^{-2}
Solvent temperature: 70° C — Time: 25 min

oxidation rate was reduced by 90 - 95% (Figure 3.11). Cross-sections of the samples after testing confirmed that the unwanted oxide layer was thickest around the edges of the sample where the coating was thinnest after application. This unwanted layer gave rise to AE signals when deformed above a critical strain. The critical strain decreased with increasing oxidation time, in line with the thickness increase of the unwanted layer. Similarly the intensity and the AE activity from both the coating and unwanted oxide increased with increasing oxidation time for the tests with mild steel and Berkatekt 12 coating, making it necessary to establish different thresholds depending on the oxidation time (see also section 3.6.1 and 4.1.2).

Only the last three coatings were assessed on nickel for oxidation at 900 °C. Berkatekt 12 and 311 formed a strong sintered layer which reduced the oxidation rate but their failure during bending produced a high AE activity, and hence these coatings were not applicable at those conditions. DPG 3582 formed a sticky liquid at 900 °C which stopped oxidation almost completely (Figure 3.12). X-ray microprobe analysis of some the grey shades next to the nickel substrate in Figure 3.12 showed that they are oxide particles. The DPG 3582 coating did not give rise to AE when bent at 900 °C. However, the layer solidified during cooling and appeared as an enamel at room temperature which was brittle and cracked during deformation and caused AE, making it only applicable for the tests at growth temperature.

Summary:

Berkatekt 12 was the best coating in terms of reduction of oxidation rate and number of AE signals for the tests with mild steel oxidised at 550 °C. Berkatekt 311 and DPG 3582 reduced the oxidation under those conditions to the same level. However, the deformation of the coating produced slightly more AE. The abrading method was used as an alternative to Berkatekt 12 for the tests at room temperature, but there was always an unknown amount of work induced into the oxide in addition to the damage observed at the edges of the oxide area.

All the coatings gave rise to AE when applied on nickel, oxidised at 900 °C and tested at room temperature, even though DPG 3582 stopped oxidation almost altogether. Therefore only abrading of the oxide was possible for the tests at room temperature with nickel. However, DPG 3582 became a sticky liquid at 900 °C which deformed readily without causing AE and was therefore used for the tests with nickel at this temperature. In this case the rollers of the ceramic bend jig were covered with ceramic parts to avoid the coating and hence the specimen sticking to the rollers.

Description	Composition	Manufacturer
Permoglaze HPC PZ-10	Suspension of zinc chromate and other anticorrosive pigments	Akzo Coatings Ltd, UK
Heat Resistant Al-Si 319	Silicon resin based aluminium coating	Thomas Howse Ltd, UK
Berkstop C4	Blend of clays, boric oxide and an organic filler in xylene	Acheson Colloids Ltd, UK
Berkatekt 311	Glass, mica, inorganic and mineral filler in chlorinated and hydrocarbon solvent	"
Berkatekt 12	Dispersion of clays in a solution of an organic resin in toluene	"
DPG 3582	Dispersion of glass in isopropanol with vinyl and natural resin binders	"
Berkatekt 39	Dispersion of clays, boric oxide, refractory solids and organic resin in trichloroethane	"
Ruskilla Aluminium 2845	Metallic paint	Croda Paints Ltd, UK
Temalac SA-100	Silicon aluminium paint	MacPherson Paints, UK

Table 3.4: Summary of the coatings and paints investigated as stop-off media.

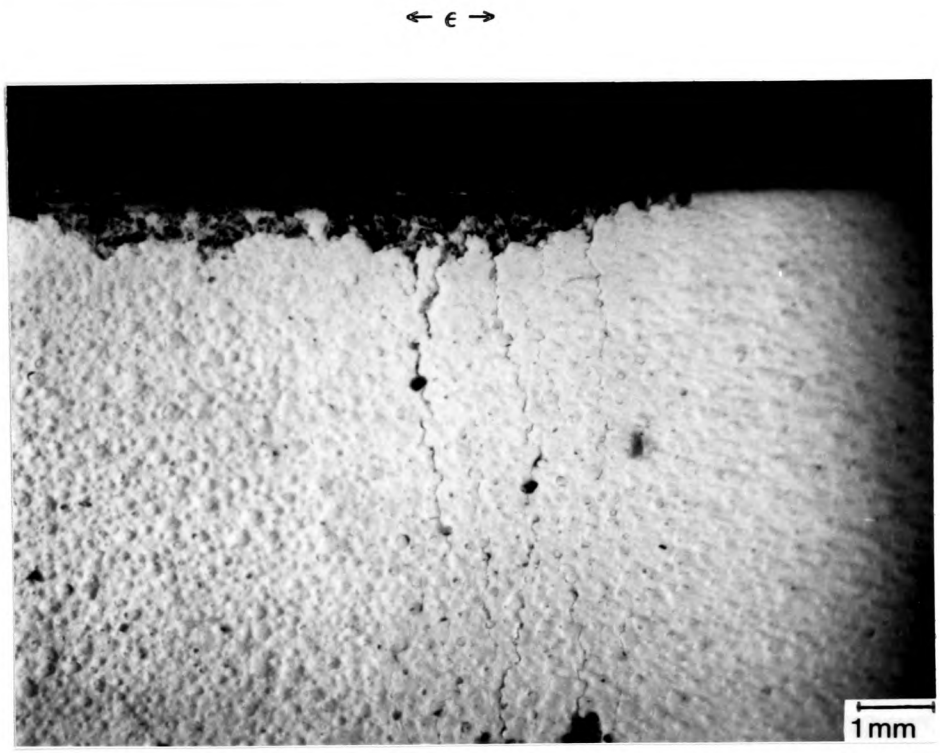

Figure 3.10: Optical surface micrograph showing cracks and spallation in the soft Berkatekt 12 coating after 60 h oxidation at 550 °C and bending.

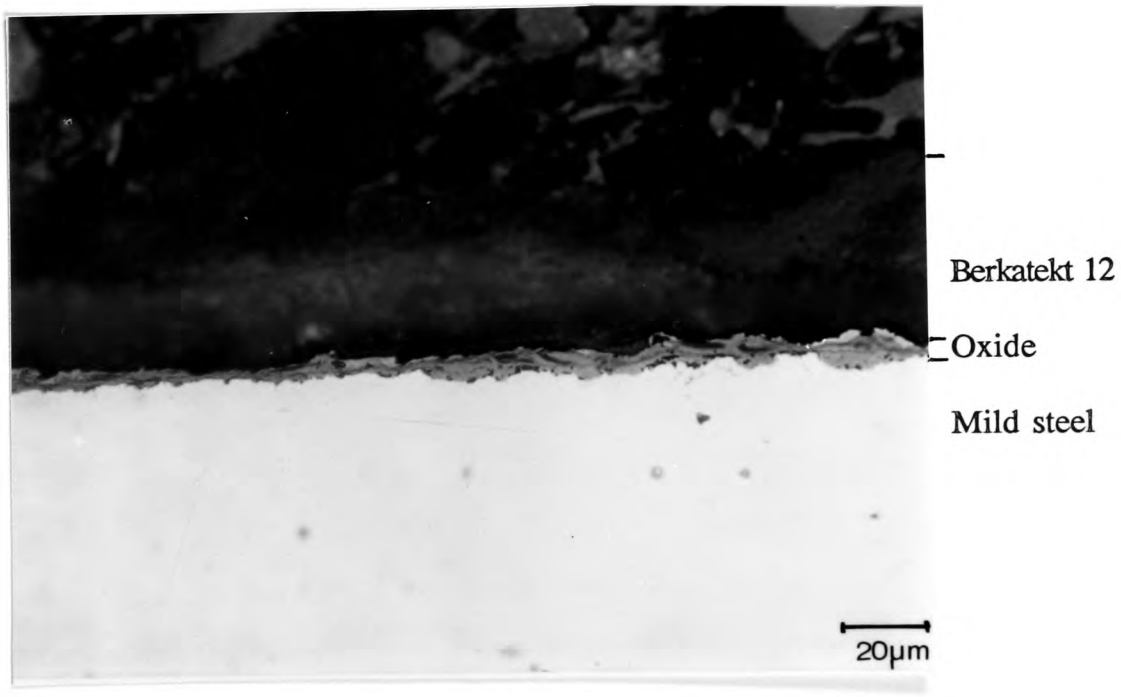

Figure 3.11: Cross-section showing the thin unwanted oxide layer underneath the Berkatekt 12 coating after 60 h oxidation at 550 °C.

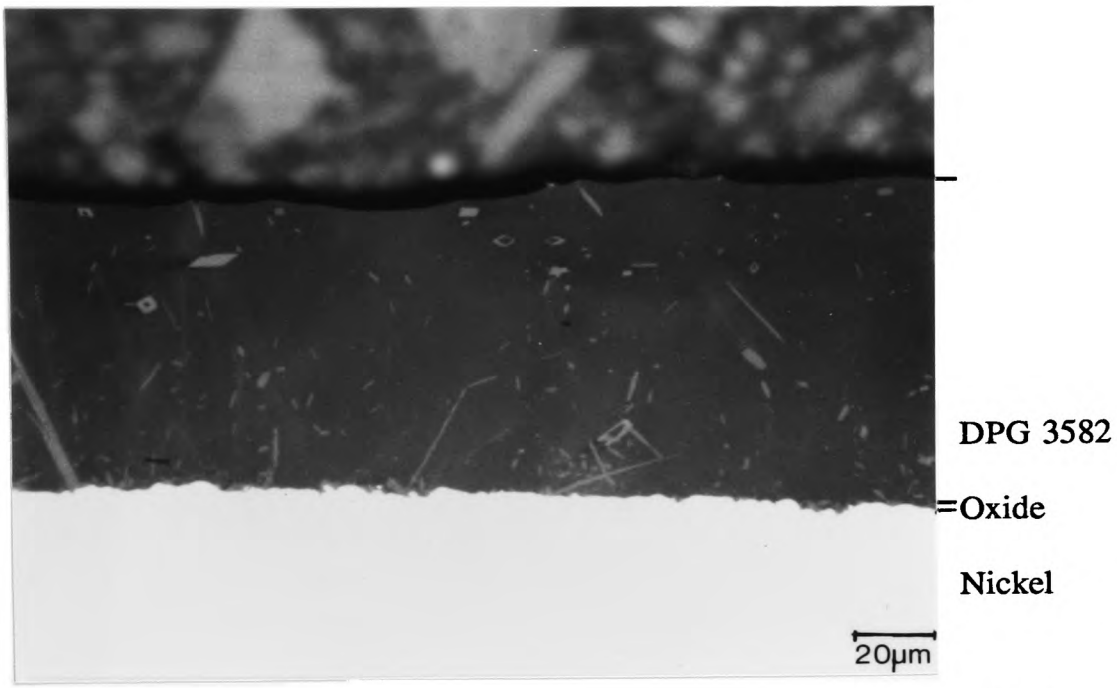

Figure 3.12: Cross-section showing the DPG 3582 coating after 60 h oxidation at 900 °C.

3.3 Experimental Arrangements

3.3.1 Experimental Arrangement for the Room Temperature Tests

The 4-point bend jig (roller distance 20/60 mm) was placed between the compression plates of the Instron table model TML test machine. The upper jig block was precision guided and could slide within the U-shaped lower jig block to guarantee accurate uniform loading (Figure 1.2, page 26). The dead weight of the upper jig block caused an erroneous load and was, therefore, fixed to the upper compression plate using double sided tape. The specimens were positioned in the jig with the layer on the top or bottom side in the middle of the two inner rollers so that compressive or tensile stresses were applied to the layer. The differential broadband AE transducer type WD (Physical Acoustics Ltd, USA) was always mounted on the same side as the brittle layer on the protruding end of the specimen to attain maximum signal reception [64,67] and least signal distortion [68]. Apiezon grease was used as couplant and a specimen clamp with $\sim$5 N force held the transducer in place. Care was taken to avoid tilting and out-of-centre mounting of the transducer and the specimen was tapped slightly with a pencil before testing to check whether good coupling existed. The transducer was connected to the Locan AT AE system with a transient recorder board type TRA (also Physical Acoustics Ltd, USA) via a 1220A series preamplifier with a built-in band pass filter.

3.3.2 Experimental Arrangement for the Oxide Growth Temperature Tests

The environmental bend test furnace model HTTF1 (Severn Furnaces Ltd, UK) with a ceramic 4-point bend assembly (roller distance 20/40 mm) was placed on the support table of the tensile test machine. The adjustable furnace feet were used to level the furnace which guaranteed, together with the roller guided upper push rod, uniform central loading of the specimens (Figure 1.3, page 27). The upper push rod was connected to the load cell with a purpose built connector and constant strain rates were applied by driving down the crosshead of the test machine. The furnace was supplied with a Eurotherm Type 818 furnace controller/programmer (temperature accuracy +/- 1% at the thermocouple). The water cooled furnace walls, support tube assembly and upper push rod assembly avoided overheating of the seals. Similar to the tests at room temperature, the exposed area of the specimens was placed on the top or bottom side between the two inner rollers. The furnace door was opened after oxidation and the protruding specimen end cooled to room temperature with compressed air before the AE transducer was mounted. This was sufficient to keep the transducer temperature below 100 °C (below the critical operating temperature of 200 °C) during the tests. The AE system and amplifications were the same as for the tests at room temperature.

3.4 Specimen Preparation

A summary of the test programme is given in Table 3.5 and accordingly, specimens of the given dimensions (Figure 3.13) were machined from as received cold rolled and tempered sheet, then ground to a 600 grit finish using SiC paper and cleaned with absolute alcohol.

The high compressive strength and good adhesion of NiO caused the nickel/NiO composite beam to yield locally and deform non-uniformly in tests with the oxide in compression. Evidence for most ceramic materials showed that the compressive strength is at least 2 - 3 times higher than the tensile strength [102]. A 50 μm thick oxide on a 1.8 mm thick specimen represented $\sim$3% of the sectional area of the beam, however its load bearing capability might have been at least 9% of the total load when considering that the compressive yield strength of the oxide was about three times higher than that of the nickel substrate. Such a large influence resulted in localised yielding of the beam at both ends of the oxide raft. Similar effects would have been expected for iron oxide grown on mild steel. However, the iron oxide interface delaminated and spalled more readily (see also section 4.1.2) before the high compressive strength of the oxide could show its effect on the overall deformation of the beam. Therefore, the specimen thickness was increased for nickel samples in order to off-set the relatively large influence of the NiO on the deformation of the nickel/NiO

composite beam. Nickel specimens 3.7 and 3.2 mm thick deformed again uniformly in the tests at room and at growth temperature, respectively.

Further preparation of the specimens was done by abrading the oxide for the tests at room temperature, by selective oxidation using a stop-off paint for some of the tests at room temperature and all the tests at growth temperature, and by masking for the tests with brittle lacquer (see below for further detail). Generally batches of 10 - 15 specimens were prepared at the same time of which up to two specimens were used as calibration specimens to set the threshold and to check the experimental arrangement at regular intervals.

(i) Room temperature tests with the oxide abraded

Mild steel specimens were used in the as received condition. However, residual stresses in the nickel after machining and oxidation times < 15 h caused considerable AE when tested at room temperature. These specimens were therefore annealed at 900 °C in pure argon for 64 h, ground to 600 grit finish and cleaned with alcohol prior to oxidation. Oxides of different thicknesses were grown in a muffle furnace at 550 °C (823 K) or 900 °C (1173 K) in air, on mild steel or nickel, respectively. After slow furnace cooling, the oxide was abraded from all sides (using SiC paper up to grit size 600) except for an oxide raft of 10x10 mm on one side of the specimen (Figure 3.13). The specimens were cleaned and degreased with alcohol prior to testing to avoid AE by debris being squeezed at the roller contact (see also section 3.6.1).

(ii) Room temperature tests with Berkatekt coating

18 layers of Berkatekt 12 coating were applied to the entire mild steel specimens by dipping with drying periods in between. After the last layer had been applied the specimens were left for 15 h at room temperature and then baked for 10 min at 600 °C to evaporate the residual solvent trapped in the coating, in order to avoid interference with oxidation[1]. The coating was then carefully abraded from an area of 10x10 mm (with 600 grit SiC paper) with the grinding marks parallel to the specimen length, followed by careful cleaning and degreasing with alcohol (Figure 3.13). The samples were oxidised for up to 64 h in a muffle furnace at 550 °C in air to grow an island of oxide on the exposed area. After slow furnace cooling, the coating was abraded from a small area situated on the same side as the oxide on one end of the specimen on which the AE transducer was mounted.

---

[1]) Preliminary tests showed that residual solvent trapped in the coating reacted with metal or oxide at the beginning of the oxidation and made the oxide less adherent, i.e. the failure behaviour was changed.

(iii) Oxide growth temperature tests with protective coatings

Berkatekt 12 coating was applied to the mild steel specimens, baked and abraded from an area of 10x10 mm and from the long end of the specimen on which the transducer was mounted, in the same manner as in section (ii). Seven layers of DPG-coating were applied to the nickel specimens in the same way as Berkatekt 12 on the mild steel specimens, except for the baking at 600 °C. The abraded long end oxidised only slightly since the temperature varied in the furnace (see also section 3.5) and did not exceed 200 - 300 °C. Hence the transducer was mounted on a smooth clean surface even after oxidation in the bend test furnace.

(iv) Tests with brittle lacquer

The mild steel and Al-alloy specimens (see also section 4.3) were masked with tape to leave an area of 10x8 mm on one side of the specimens on which Tenslac brittle lacquer layers of different thicknesses were built up by spraying according to the manufacturers instructions. The masking tape was carefully removed after drying for at least 24 h at 21 °C and the previously masked areas were cleaned and degreased with alcohol.

Material	Test mode	Thickness [μm]	Threshold [dB]	Strain rate [s^{-1}]	Temp. [°C]	Protective coating	Comment
Iron oxide	T/C	5-30	37	$\sim 10^{-4}$	20	none	oxide abraded
"	"	5-15 16-30 31-60	40 45 48	"	"	Berkatekt 12	
"	"	5-30 31-60	45 48	"	550	"	
"	"	5-30 31-60	45 48	$\sim 10^{-4}$	"	"	different grinding mark direction
"	"	5-30 31-60	45 48	$\sim 10^{-5}$	"	"	
NiO	T/C	3-45	37	$\sim 10^{-4}$	20	none	oxide abraded
"	"	3-45	45	"	900	DPG 3582	
Brittle lacquer	"	75-180	42	"	20	none	

Table 3.5: Summary of the test program (T = Tension, C = Compression).

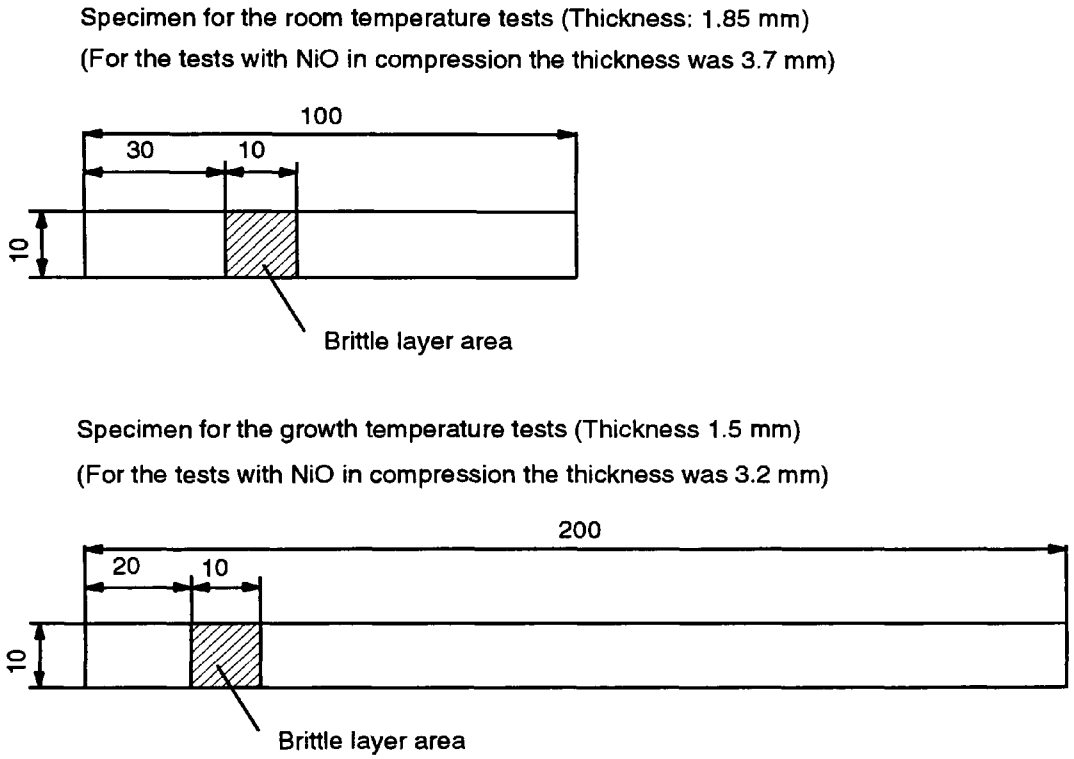

Figure 3.13: Specimen dimensions and brittle layer position.

3.5 Test Parameters and Data Recording

3.5.1 Temperature and Oxidation Time

It was observed earlier that the temperature varied slightly with position in the muffle furnace. Therefore a calibrated Pt-Rh-thermocouple (+/-2 °C) was placed in the furnace so that the furnace could be controlled to give the required oxidation temperature at this position. When the furnace had stabilised at the set temperature the specimens were placed in the furnace adjacent to this thermocouple. The stated oxidation time was the elapsed time until the furnace was switched off for slow furnace cooling.

The situation was more complicated in the bend test furnace since the heating elements were positioned only above the bend jig which resulted, together with additional heat fluxes due to the water cooled seals and walls, in a temperature variation throughout the furnace. Measurements of the temperature profile at 550 and 900 °C showed that the temperature was 5 - 7 or 12 - 15 °C, respectively, lower in the bend jig where oxidation took place than that measured by the control thermocouple. Hence the set temperatures were increased to 557 and 915 °C to compensate for the difference. The temperature at the long ends of the specimen did not exceed 200 - 300 °C causing heat conduction in the specimen and since AE testing does not allow direct contact of

oxide and thermocouple due to possible noise the actual surface temperature was probably less than the stated oxidation temperature. Therefore, the measured oxide thickness, rather than the oxidation time was used as plot parameter. In the tests at oxide growth temperature, the specimens were always placed at the same position within the bend jig at room temperature, so that the stated oxidation times included the heating up period using a rate of 8 °C min^{-1}, but did not include the furnace cooling with the same rate.

3.5.2 Load Measurement

The load was measured using an Instron compression/tension load cell (Type 2511-312) and its output was either recorded on an Instron chart recorder or fed into the AE system as a parametric input (range 0 - 10 V). The load readings could not be used to calculate the oxide failure stress since it would require an exact knowledge of the materials parameters of substrate, interface and oxide at room and at growth temperature.

3.5.3 Strain and Strain Rate

Mechanical stresses were applied to the oxide by loading the samples in the 4-point bend jig. In such a case, the strain compatibility at the interface demands that the strain in the oxide is equal to that in the substrate, i.e. applied strain and oxide strain were the same (see also section 2.1.1.2, page 31).

Strain and strain rate were linearly proportional to crosshead movement and crosshead speed since the measured crosshead speed was constant within 0.5% of the set value, the whole bending assembly including connectors was free of play to insure a constant loading and the specimens were preloaded with 5 - 10 N to guarantee uniform roller/specimen contact prior to testing. Hence, strain and strain rate could be calculated using the following equation for a 4-point bend jig:

$$\epsilon = \frac{3ftd}{u(3s-4u)} \qquad (3.1)$$

$$\dot{\epsilon} = \frac{3fd}{u(3s-4u)} \qquad (3.2)$$

where f is the crosshead speed in mm sec^{-1}, d is the specimen thickness in mm, u is the distance in mm between outer and inner roller, s is the distance in mm between the two outer rollers and t is either the test time for total strain calculations or the time in seconds when significant AE was detected for critical failure strain calculations. The AE-system and the crosshead were started simultaneously so that the internal timer of the Locan AT could be used for the time measurement. Additional factors which were

incorporated in t to compensate for the effect of the pre-loading and an error estimation are given in Appendix B.

3.6 Acoustic Emission Adjustment, Recording and Analysis

The Locan AT equipment was a computerised AE system that performed in real time AE signal measurements (such as amplitude, counts, energy counts, rise time, duration etc.) and stored, displayed and analysed the resulting numerical data. The system could also record up to four parametric inputs, such as load, simultaneously. The additional TRA transient recorder and analyser board converted the electrical AE signal into digital form and stored the digital waveform data in the memory[1], from which the data were then transferred to the hard disc or floppy discs. Both systems allowed direct output of the data via a matrix printer or as ASCII-code, which could be read into other software packages. Hence, both AE parameters as well as the whole AE signals were available for post test analysis.

3.6.1 Influence of System Noise on the AE Threshold and its Determination

It was necessary for the AE study to reduce the background noise level to a minimum. Only then could the AE threshold, i.e. the trigger amplitude for signals to be recorded, be set low enough to give a high AE sensitivity. In this context, electronic and mechanical background noise from the laboratory environment, the tensile test machine and the AE equipment was assessed using an oscilloscope. Most of the white noise was in the low frequency region (<25 kHz) and therefore not critical since the AE equipment was operated with a band pass filter between 100 kHz and 1 MHz (see also section 3.6.2). In addition, bare metal specimens were bent to 1.12% strain to determine the roller/specimen contact contribution to the AE. Only careful cleaning of the specimen surfaces with detergent and alcohol allowed use of a low threshold for the tests at room temperature since residual grinding debris if squeezed under the roller contact pressure would give rise to high amplitude AE signals. Further reduction of the threshold to 37 dB was achieved by covering the rollers with a layer of insulating tape.

A similar series of tests was conducted for the high temperature work with the bend test furnace. The rubbing of loose parts within the ceramic four point assembly during loading gave rise to considerable AE. These loose parts, i.e. rollers and lower support block were glued together with Autostick high temperature cement (Carlton Brown & Partners Ltd, UK). This reduced the noise level considerably, however the noisier furnace environment and the ceramic 4-point bend jig required a minimum

---

[1]) Extra RAM-memory allowing high data acquisition rate of up to 4000 signals per second.

threshold at least 7 dB higher than that used for the tests with the room temperature bend jig.

Eisenblätter [59] had shown that dislocation sources had a considerably smaller slip area, slip velocity and stress drop than the crack growth source leading to the conclusion that various other AE parameters, such as energy release, amplitude, etc. differ to the same extent (see also section 2.2.1, page 58). This was used in the present study to eliminate AE from dislocation movement in the substrate, i.e. the threshold amplitude was set so that it was not exceeded by the AE from dislocation sources. Therefore, a two step approach was used in all tests, after the initial assessment of the system noise level. Firstly the threshold was established at room and at growth temperature with 'calibration specimens' which had no brittle layer present but had undergone the same preparation procedure as other specimens of the same type of test, i.e. either bare metal specimens with the whole oxide removed or specimens which were completely coated with a stop-off coating. Adjustments of the threshold were made until AE signals emanating from the substrate during deformation or from the deformation of the stop-off coating caused less than 10 randomly distributed low amplitude AE signals in a single test. Secondly, tests with a brittle layer, oxide or brittle lacquer, were made using the same configuration and threshold. Hence the recorded signals were due to deformation and cracking of the brittle layer. Generally the thresholds obtained from the calibration tests were equal or only slightly higher than the thresholds found when loading a bare metal specimen (see earlier in this section). A summary of the thresholds used for the different types of test is given in Table 3.5 (page 92).

3.6.2 AE Adjustment and Technical Data

A preamplifier with a built-in band pass filter of 100 kHz - 1 MHz was used to harness the flat frequency response of the transducer within that band. Muravin *et al.* [65] have shown that wave components within a frequency band describe the process as well as the total signal. The frequency band included all relevant frequencies according to earlier results (see also section 2.2.5, page 68) and the frequencies of the initial portions of the curves a_0 and s_0 in Figure 2.13 (page 61) which propagated in the specimen (see also section 2.2.2, page 59) [64,66]. The transducer contact area (equal to the specimen width of 10 mm) was smaller than the wavelength of the highest recorded frequency of 1 MHz, which was a prerequisite for signal reception [74].

Preliminary tests were used to set the preamplification to 40 dB and the gain amplification to 20 dB and 25 dB for the tests with oxide and brittle lacquer, respectively. The threshold was set between 37 and 48 dB depending on the type of test which gave medium sensitivity according to Pollock [73]. A threshold of 0 dB was

defined as 1 μV at the transducer. From this dB specification the system computed the actual threshold voltage that it used as comparator to perform signal detection and to generate AE counts (Table 3.6). When the gain was changed the threshold voltage changed also and AE counts, duration and rise time of the signal remained constant, being influenced only by the threshold setting (Figure 3.14) [77]. This was different for the energy circuitry, since it measured the area under the rectified signal envelope (amplitude x time) from the beginning to the end of the signal definition, hence measured energy count values were directly proportional to gain amplification and less influenced by the threshold setting (Figure 3.15) [77,103]. The measured energy counts were related to real energy which is given by ((amplitude)^2 x time), but a real conversion could not be made without making assumptions about the signal shape [103]. A quantitative comparison of AE counts, signal number, rise time and duration could only be made when the threshold was the same. AE energy count values from different tests could be compared by considering the gain, i.e. a 5 dB higher gain meant that the respective values had to be divided by a factor of 1.78. This was done when comparing the results from tests with brittle lacquer and oxide.

The Locan AT signal definition parameters of peak definition time (PDT), hit definition time (HDT) and hit lock-out time (HLT) were set to 200, 400 and 400 μsec according to the recommendations by Pollock [73].

The sampling rate of the TRA board was set to 2 MHz, i.e. twice as high as the highest recorded frequency (Shannon theorem) [84] and the input range was 0 - 10 V, which gave a digitation error in amplitude of 10/256 $\sim$0.04 V or 0.4 % for the 8 bit digitiser. The pretrigger was 5% so that the beginning of the signal could also be analysed.

Preamplification [dB]	Gain amplification [dB]	Threshold [dB]	Comparator voltage [mV]
40	20	37	71
40	20	40	100
40	20	45	178
40	20	48	251
40	25	42	224

Table 3.6: Comparison of the actual comparator voltage for signal recognition used in the different settings shown in Table 3.5 (page 92).

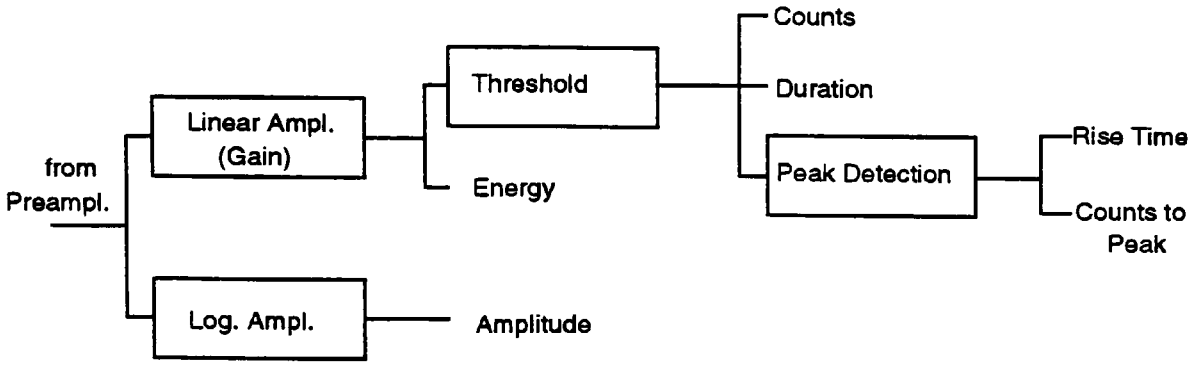

Figure 3.14: Schematic diagram showing the AE measurement circuitry.

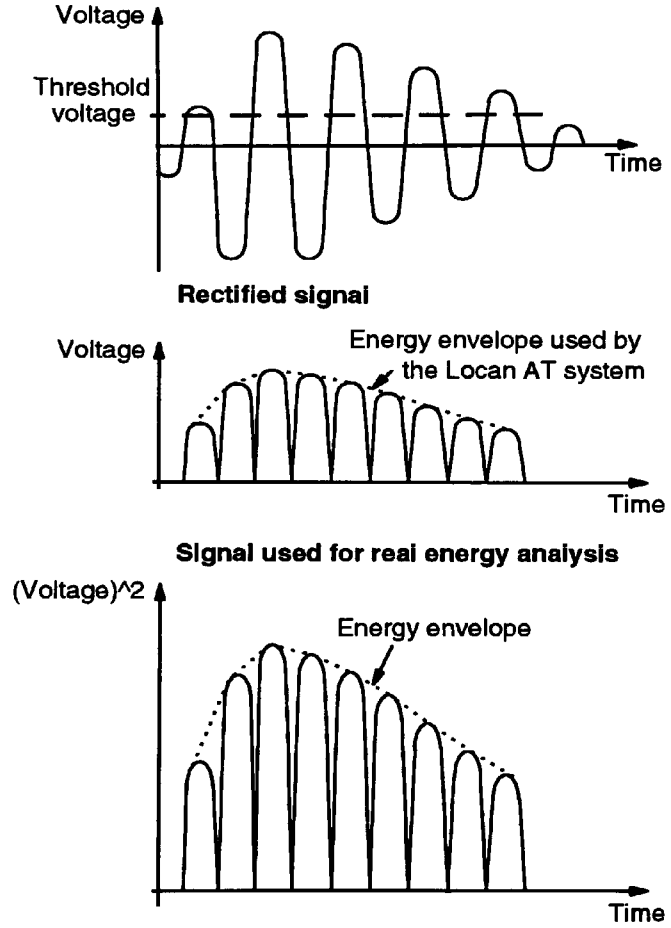

Figure 3.15: Comparison of the envelope which is used by the Locan AT system for energy count calculation with the envelope for real energy calculation.

3.6.3 AE Analysis

AE parameters describing the whole signal were used (see also section 2.2.4, page 65), since no direct wave arrival was possible taking into account directionality of sound waves [63,64], wave propagation under 45° [64] and the fact that no surface waves were present [66] (see also section 2.2.2, page 59). The energy count values

were mainly used in the analysis since they took signal length and amplitude into account (see also section 2.2.4, page 65). The Locan AT system offered a vast range of plots [73], of which mainly history or strain distribution plots were used. These show the strain, on the x-axis and an AE parameter, viz. energy counts, counts or number of signals on the y-axis. In this case every single column of a histogram represented the cumulative value or the average value of the AE-parameter for the respective strain increment (Figure 3.16).

In addition, the dependence of the AE on layer thickness was assessed by plotting the cumulative AE energy counts or AE counts for the tests as a function of thickness. The average AE energy count and count values per signal were calculated by dividing the cumulative value by the number of signals on the assumption that each signal corresponded to crack formation or crack growth. Thus changes in the cracking behaviour could be revealed by plotting these parameters as a function of thickness.

Other plots, such as distribution plots, showed the statistical distribution of an AE parameter. The parameter was plotted on the x-axis and the number of signals having a certain value was plotted on the y-axis. For the amplitude distribution, the y-axis was plotted in the log-scale to obtain the b-value (Figure 3.17). However, neither the b-value nor the other plots provided additional information.

The output of the TRA-board was fed into the Asyst wave analysis software to perform frequency and auto-correlation analysis on the AE signals (see also section 4.5).

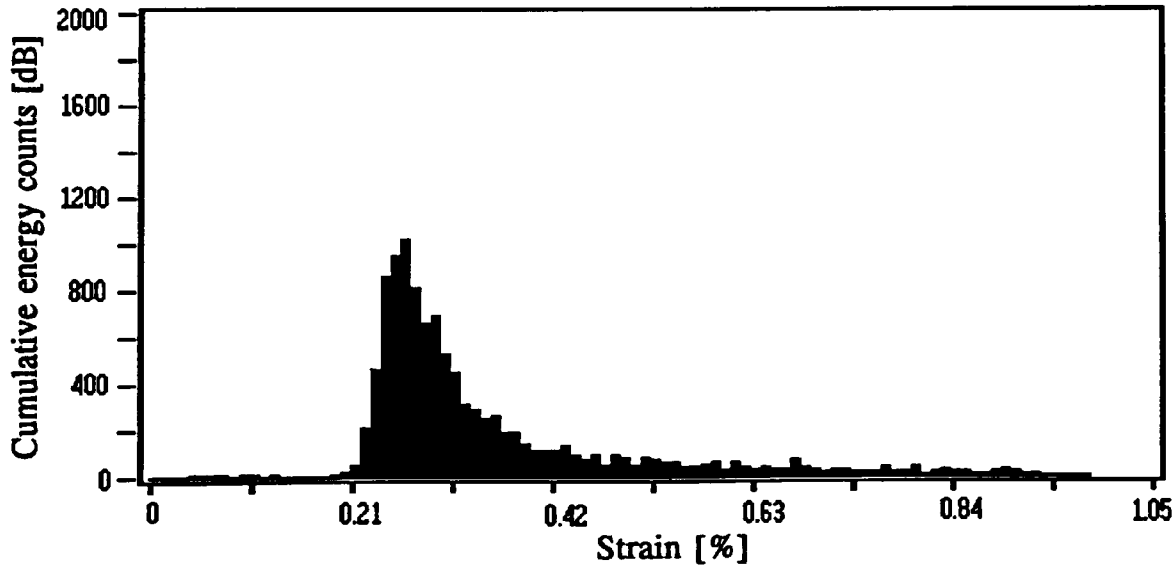

Figure 3.16: History plot showing the cumulative energy counts as a function of strain for a 8 μm thick nickel oxide scale tested in tension at room temperature.

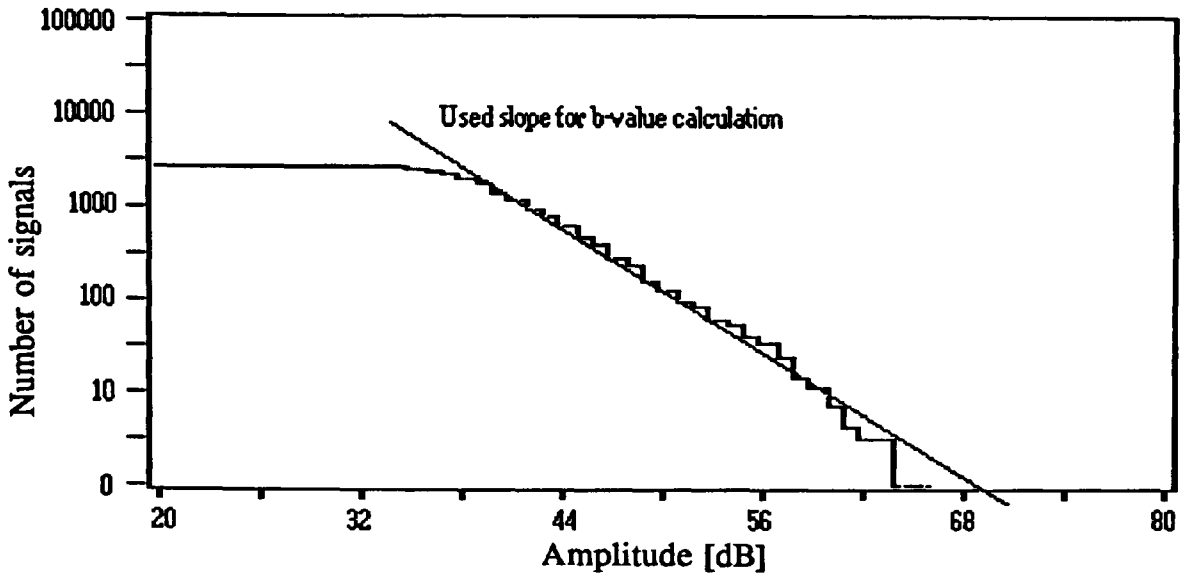

Figure 3.17: Distribution plot showing the logarithmic cumulative amplitude distribution for a 8 μm thick nickel oxide scale tested in tension at room temperature.

3.7 Post-Test Examination

Possible damage and cracking at the layer surface were examined using optical (Olympus BHM, Olympus Ltd, Japan) and scanning electron microscopes (Camscan Series 2, Camscan Ltd, UK). Cross-sections were either cold mounted in Epofix (Struers Ltd, Denmark) or hot mounted in conductive Bakelite (Bühler-Met, Bühler Ltd, UK), ground and polished to a final finish of 1 μm diamond using very light pressure to get good edge retention and avoid damaging the layer. The following parameters were determined microscopically:

(i) **The oxide thickness** was measured at 5 - 10 different positions in the cross-sections and averaged using an eyepiece containing an 0 - 100 scale.

(ii) **The crack spacing** was determined using SEM surface observations on minimum, maximum and average crack spacing[1] together with similar observations made on the cross-sections. In this context it is important to note that cracks originating at different positions sometimes approached each other when they propagated. The stress fields around the crack tips interfered and the driving forces for propagation were reduced when the cracks approached each other. However, the cracks did not arrest abruptly and overlapped probably as a result of the residual driving

---

[1]) Calibrations using a standard setting of 20 kV and 35 mm working distance, magnifications of 100, 200, 400, 500, 1000 and 1730 and a standard grid with known spacing showed that the actual magnification was in all cases only 80% of the indicated magnification on the electron microscope, which meant that the scale shown on the micrographs was in error. Therefore, the measurements taken with the photographs using the scale had to be divided by a factor of 0.8 to give the real spacing since all micrographs showing the crack spacing were taken with the standard setting.

force or the velocity of approach. Such overlapping resulted in very small crack spacings and was not accounted for by simple models of the dependence of crack spacing and thickness (see also section 2.1.2.3, page 37). It was not possible to distinguish in the cross-sections between real crack spacing and overlapping, therefore the minimum spacing was only measured at the surface and even then discrimination was sometimes difficult (Figure 3.18).

(iii) **Size, number, position and distribution of voids and delaminations** were measured in the cross-sections, being aware that mounting and polishing procedures introduced unknown amounts of mechanical damage which could have caused pull-out of oxide grains and delamination.

(iv) **The chemical composition** of the oxide layers was determined in the cross-sections using qualitative energy dispersive X-ray microprobe analysis, either at specific points (spot analysis) or by scanning of a predefined area (digital X-ray map) (Link AN 10000, Link Analytical Ltd, U.K).

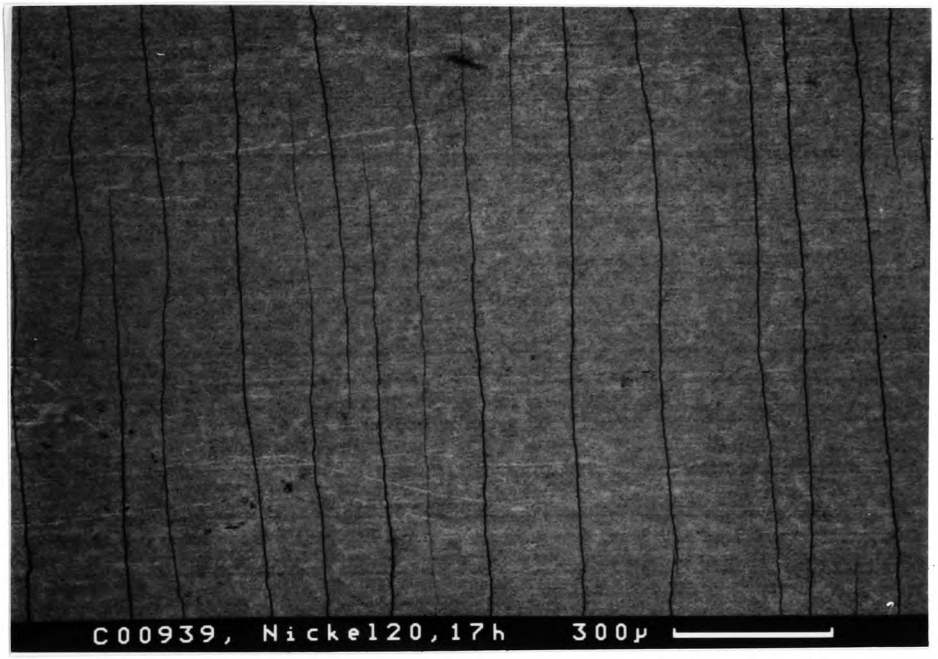

Figure 3.18: Backscattered SEM surface micrograph showing the overlapping of tensile cracks and the variation in the crack spacing.

3.7.1 Sulphur Decoration Technique

Sulphur decoration was used to decorate the crack surfaces with a thin layer of iron-sulphides at growth temperature, so that the original size and number of cracks could be observed even if healing or further cracking occurred at later stages [57]. However, this technique was restricted to cracks which had a connection to the oxide surface [27].

In this study, the bend test furnace was flushed for one hour with pure argon (flow rate 150 cm^3 min^{-1}) before a gas containing H_2S was introduced with the same

flow rate. The following gas (composition (1270 vpm H_2S, 41% CO_2, 25% CO, 21% H_2, Balance N_2) was used since it was readily available. After 5 minutes the specimens were loaded and 2 minutes later unloaded, but the H_2S was left for another 25 minutes before the furnace was flushed with pure argon and cooled to room temperature.

3.7.2 Platinum Marker Technique

Platinum marker experiments were performed to find the relative position of the original metal surface within the oxide layer and to see whether the metal surface acted as a potential site for voids. The metal samples were covered with a copper grid before an approximately 1 μm thick layer of platinum was applied by sputter coating[1]. Hence, the samples were coated with a discontinuous platinum layer which could not act as a diffusion barrier.

---

[1]) Edwards sputter coater: Type S150A
Atmosphere: Argon
HT voltage control: Level 11
Current: 10-14 mA
Copper grid size: 0.8 mm
Wire thickness: 0.3 mm

CHAPTER 4: Results and Discussion

4. RESULTS AND DISCUSSION

Tests were made on three layers in tension and compression to characterise the failure mechanisms (Table 3.5, page 92). The specimens were bent to different strains with a maximum of 1.12% at room and at oxide growth temperature, except for NiO in compression which was strained to 2.8% due to its high compressive strength (see also section 4.2.2). The layer surfaces were examined microscopically after testing and cross-sections were cold or hot mounted, ground, polished and examined microscopically (see also section 3.7, page 100). Undeformed samples were subjected to the same post-test examination to determine scale structure and possible pre-test damage.

Iron oxide on mild steel was selected since an oxide layer formed rapidly and enabled a series of quick tests to be performed, especially while the technique was being developed. The mild steel specimens were oxidised at 550 °C, i.e. below the eutectoidal decomposition temperature of wuestite (FeO) which is 570 °C, so that only haematite (Fe_2O_3) and magnetite (Fe_3O_4) were formed. Thus, stresses arising from the transformation of wuestite into magnetite and iron were avoided, which made failure and stress analysis easier.

The nickel/NiO system was selected because it formed a single phase oxide layer which was easy to model and had a high strength and good adhesion. The oxidation of nickel was carried out at 900 °C in order to ensure a high oxidation rate and thus produce films of sufficient thickness.

Finally, brittle lacquer was used as a model layer for the AE because it was brittle and had similar fracture characteristics to the oxide. Thus, AE emitted during its fracture was compared with the AE recorded during the failure of oxides. Above all, preparation time and effort was minimal compared to oxides.

4.1 Tests with Iron Oxide Grown on Mild Steel

Test Programme:

Tests were made in tension and compression on oxides up to 60 μm thick at room and at oxide growth temperature (550 °C) using a strain rate of $\sim 10^{-4}$ s^{-1}. The influence of the protective coating (Berkatekt 12) on oxide structure and oxide failure was assessed at room temperature under the same tests conditions (see also section 3.4 for specimen preparation, page 90).

At first tests were performed at room temperature to acquire experience in the interpretation of AE data. At room temperature it was possible to correlate AE with cracking by observing the state of the oxide before and after testing. In some cases a step-wise approach was used by testing a number of samples with the same oxide

thickness up to different strains and comparing the change in cracking with the change in AE. The subsequent tests at growth temperature, which were certainly more important for practical application, did not allow such an approach because there was always an unknown amount of damage occurring on cooling which made an accurate correlation impossible. In many cases the expertise gained from the tests at room temperature helped in explaining the fracture process.

Additional tensile tests were made at growth temperature to investigate whether the failure and critical failure strains were affected by a lower strain rate. A strain rate of $\sim 10^{-5}$ s^{-1} was chosen, because Schütze [9] predicted creep in magnetite at 550 °C if the void size was smaller than 5 μm.

Finally, tests with a different grinding mark direction were made to see whether surface roughness, i.e. surface defects, had a more profound effect on failure than the usually internally formed voids. It was implied that grinding marks are replicated at the oxide surface and are the cause of any major surface defects. Therefore, specimens were ground normal to the direction of the applied stress so that the marks were aligned in the same direction. In this way the marks would act as stress risers. Normally the specimens were ground parallel to the direction of applied stress and hence the marks were less critical.

Scale Morphology:

After oxidation in air at 550 °C oxide layers consisted of an outer dense layer of haematite (Fe_2O_3) and an inner layer of magnetite (Fe_3O_4). The haematite occupied generally between 20 - 30% of the whole layer thickness. The grain structure of the magnetite changed from a relatively dense equi-axed structure next to the substrate to more columnar crystals further away from the interface (Figure 4.1). The magnetite also contained a region of high void concentration approximately 30 - 40% away from the oxide surface. This line of voids was believed to be due to the diffusion characteristics of both metal-ions and oxygen-anions within the scale, which resulted in a high vacancy concentration and hence large voids in that part of the oxide. The largest void and highest void concentration occurred in samples oxidised for 17 h or more which had scales between 19 and 30 μm thick. Platinum marker experiments showed that the original metal surface was approximately one third away from the interface, i.e. it did not coincide with the line of voids.

Growth and cooling stresses resulted in small wrinkles in the haematite layer at the surface of oxides < 10 μm thick and in a few instances with oxides between 10 and 20 μm thickness. However, scales did not crack or spall on cooling from growth temperature and neither spalling nor cracking was observed in the oxides after preparation prior to testing at room temperature.

4.1.1 Tests with Iron Oxide in Tension

4.1.1.1 Crack Patterns

Oxides Tested at Room Temperature:

Tensile through thickness cracks normal to the direction of applied strain were found in all samples after testing. Cracks were long and straight usually extending to or from one edge of the specimen. The inter-crack spacing increased with increasing oxide thickness, for the same relative strain condition (Figure 4.2a-c); for similar oxide thicknesses the distance between cracks was the same. Cross-sections of the tested oxides confirmed the earlier observations on crack spacing and cracks always extended through the whole layer thickness (Figure 4.3).

Tests with oxides of the same thickness, bent to different maximum strains, showed that the crack spacing decreased with increasing strain (Figure 4.2c-d). Interface delamination started at higher strains and spallation was observed towards the end of the tests, mainly in oxides $\geq 19\mu m$ thick. Cracks which propagated along a chain of voids parallel to the interface within the oxide were observed in the cross-sections of oxides between 19 and $30\mu m$ thick. In many cases the outer part of the oxide had already spalled along the line of voids indicating that in this case the cohesive strength of the layer was smallest at this plane and it was, therefore, the origin for any delamination (Figure 4.4).

There was no difference in the cracking behaviour when the oxide was abraded or when it was selectively grown using the Berkatekt 12 coating.

Oxides Tested at Growth Temperature (550 °C):

Deformation at growth temperature enlarged the wrinkles in the haematite due to the effects of the Poisson's ratio which introduced a compressive stress normal to the applied stress. The number of wrinkles increased with deformation and the wrinkles acted in many cases as crack initiators (Figure 4.5a).

A number of samples tested at growth temperature showed buckled areas with the whole oxide detached from the substrate (Figure 4.5b) and in a few cases detached layers had actually spalled off. The occurrence of buckling and spalling was variable and difficult to relate to experimental parameters, such as maximum applied strain or cooling rate.

Two types of cracks were observed, (i) long cracks which were longer and straighter the thicker the oxide (Figure 4.6) and (ii) short cracks between the long cracks mainly in thin oxides ($\leq 20\ \mu m$). The number of short cracks decreased rapidly with increasing oxide thickness. The lower strain rate of $\sim 10^{-5}\ s^{-1}$ resulted in a higher crack spacing but cracks were very similar, except that very thin oxides $\leq 7\ \mu m$ showed predominantly short cracks (Figure 4.7). The crack spacing increased with thickness for

both strain rates (Figure 4.6 and Figure 4.7).

Although many cracks appeared to only partly penetrate the scale (Figure 4.8), sulphidation experiments performed to decorate cracks after deformation indicated that the whole thickness of the scale had been penetrated (Figure 4.9). Crack repair apparently occurred after deformation at growth temperature by crack closure during unloading and subsequent healing during cooling.

In addition, the effects of the grinding mark direction on the failure were assessed at 550 °C. However no change in crack patterns was found when the marks were normal or parallel to the direction of the applied stress.

Discussion:

For oxides of similar thickness, crack spacing was higher when strained at growth temperature. In all cases the crack spacing increased with oxide thickness in agreement with the models given in section 2.1.2.3 (page 37 and equation (2.17) and (2.18)) which neglected the effects of plastic stress relaxation processes such as substrate yielding at the base of the through-scale cracks, oxide creep and lateral oxide growth (see also section 4.4.1). They only considered the forces acting in an oxide area (Figure 4.10), hence the maximum strain sustained in the middle of an oxide layer is that supported by interfacial slip which gives a crack spacing L of [10]:

$$L = \frac{k\, h\, \sigma_{ox}}{\tau_y} \qquad (4.1)$$

where h is the oxide thickness, σ_{ox} is the tensile strength of the oxide and τ_y is the shear strength of the interface and k is a numerical factor ≥ 2 which depends on the shear stress distribution in the oxide segment. The ratio $r = \sigma_{ox}/\tau_y$ determines the slope of the lines in Figure 4.11 and is indicative of the relative shear strength of the interface. Evidence for Al_2O_3 shows that the tensile strength does not change significantly up to 600 °C [104]. Although iron oxide is less creep resistant, it has been assumed that the tensile strength of the oxide would be the same at room and at growth temperature. It follows from the data shown in Figure 4.11 that the shear strength of the interface must be approximately four times higher at room temperature than at growth temperature. This observation was supported by the appearance of all samples tested at temperature and hot mounted in Bakelite where shrinkage of the Bakelite had pulled the oxide from the metal substrate (cf. Figure 4.8a), whereas this was not so for samples tested at room temperature and mounted in the same way.

As shown in section 2.1.2.3 (cf. Figure 2.2, page 38), there is a critical strain above which the increase in strain is solely compensated by interface delamination and does not cause further tensile cracking. Evidence that oxides tested at growth temperature had already passed the transition was found in oxides >20 μm when crack

spacing was constant for oxides of similar thickness and strains >0.60 % (Figure 4.12a). Oxides >10 μm thick tested to 1.12% strain at room temperature showed the first signs of interface delamination and thicker oxides even spallation, therefore the transition point must have been between 0.6 and 1.12% (Figure 4.12b). Hence, the crack spacing could still decrease further for oxides <10 and <20 μm thick and tested at room and at growth temperature, respectively. So that the best-fit lines go through the origin as would be expected from equation (4.1) for an analysis strain level at which crack saturation is reached. This was not expected to influence the analysis shown above, because it was only based on the difference in slope between room and growth temperature tests.

It can also be seen from Figure 4.11 that the ratio σ_{ox}/τ_y is independent of strain rate, i.e. the tests with different strain rates at growth temperature had the same slope. However, the crack spacing was larger with a strain rate $\sim 10^{-5}$ s^{-1} presumably due to time dependent slip at the oxide metal interface, substrate yielding at the base of through-scale cracks and/or due to creep in the oxide which allowed additional deformation of the oxide (see also sections 4.1.1.4 and 4.4.1).

Although most micrographs showed fairly equi-spaced cracks, it is important to bear in mind that the absolute variation within one test was approximately 50% of the mean value (Figure 4.13). Such a large variation was not surprising, because in one case a crack might just have formed between two pre-existing cracks, whereas in the other extreme the tensile stress might be just below the critical stress which would cause an additional crack to grow. This consideration would already account for a variation by a factor of two. In addition the void size within the oxide was probably random, with the cracks originating at the points of high stress concentration within the scale, i.e. the most severe flaw and subsequent exploitation of different flaws.

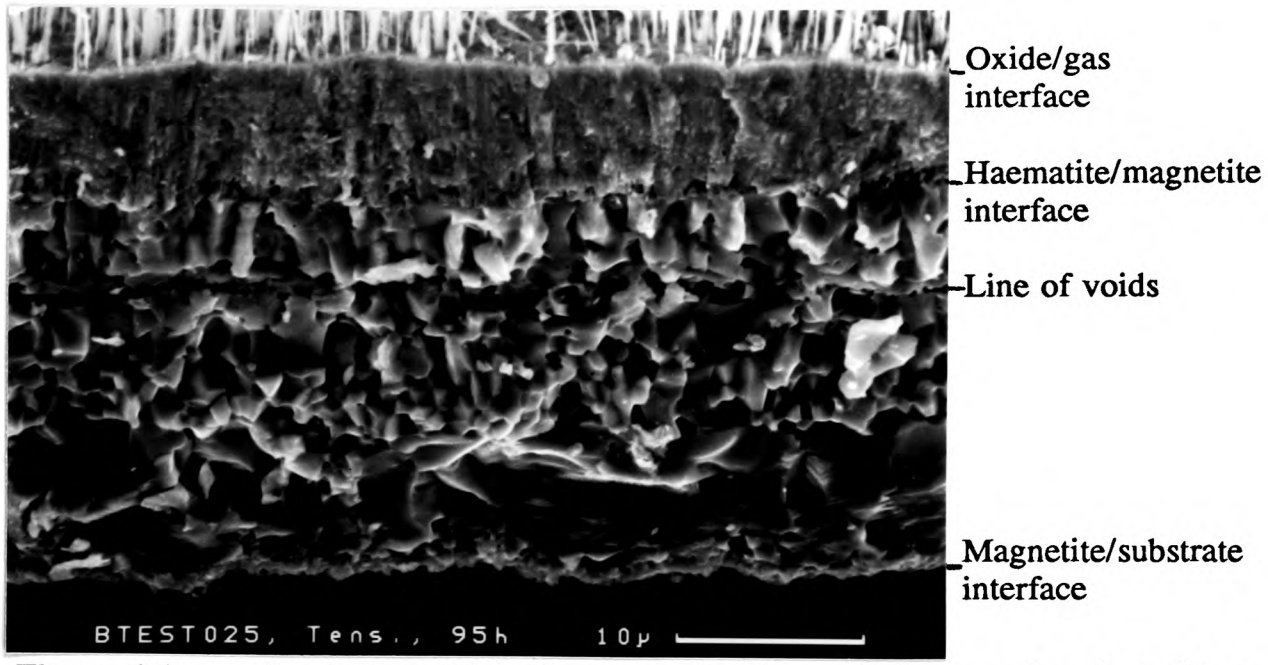

Figure 4.1: Secondary SEM micrograph showing a fracture surface in a 49 μm thick iron oxide after oxidation in a muffle furnace at 550 °C.

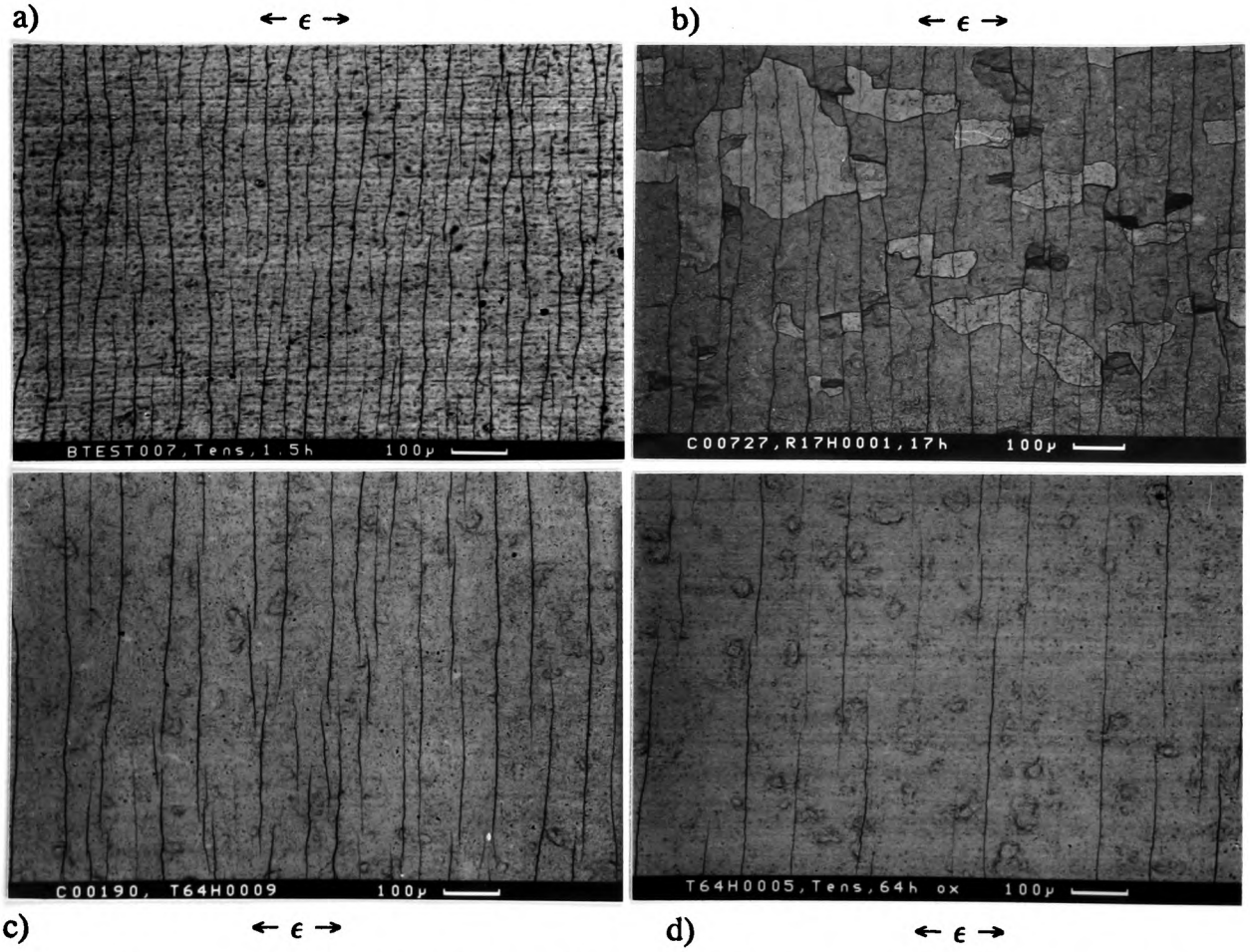

Figure 4.2: Backscattered SEM micrographs of tensile cracks in iron oxides after testing in tension at room temperature. (a) Thickness 11.5 μm, maximum strain 1.12%, (b) 19 μm, 1.12%, (c) 36 μm, 1.12% and (d) 40 μm, 0.56%.

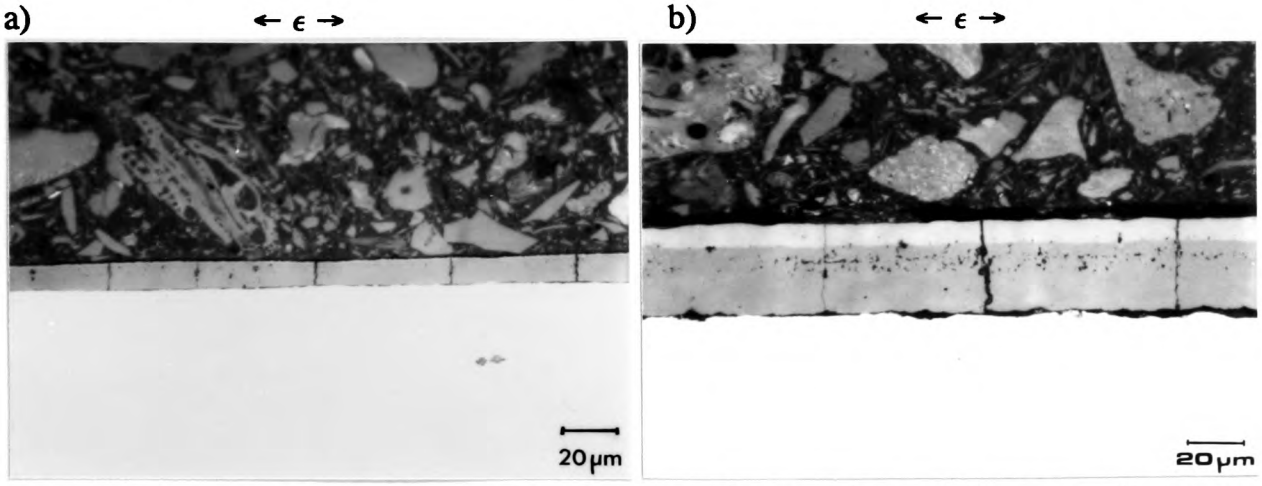

Figure 4.3: Optical micrographs of cross-sections of the equi-distant tensile cracks in iron oxides after testing in tension at room temperature. (a) Thickness 10-11 μm, maximum strain 1.12% and (b) 36 μm, 1.12%.

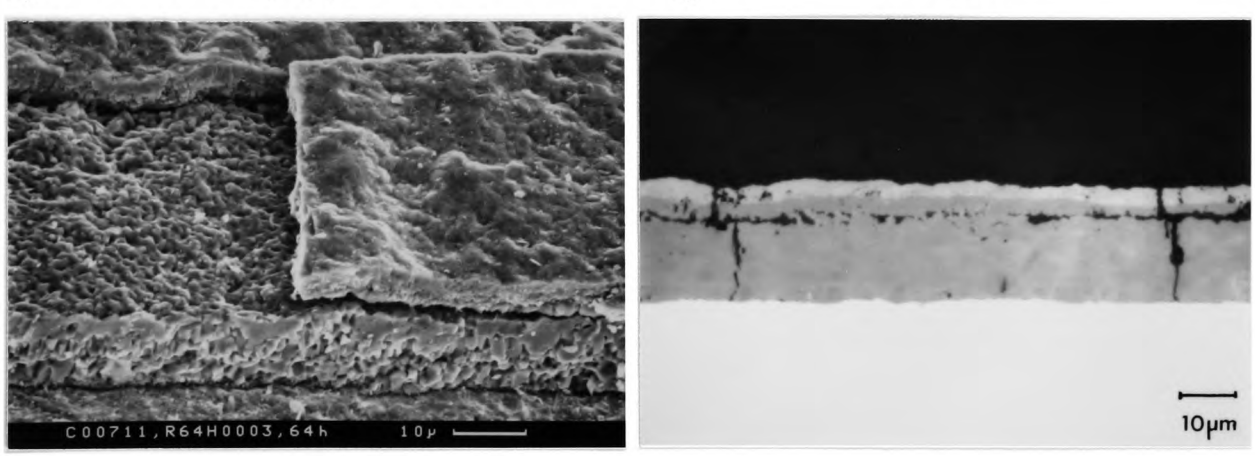

Figure 4.4: Micrographs (a) showing spallation of parts of the oxide (thickness 29 μm, max. strain 1.12%) and (b) a cross-section depicting delamination (23 μm, 0.85%) within iron oxides after testing in tension at room temperature.

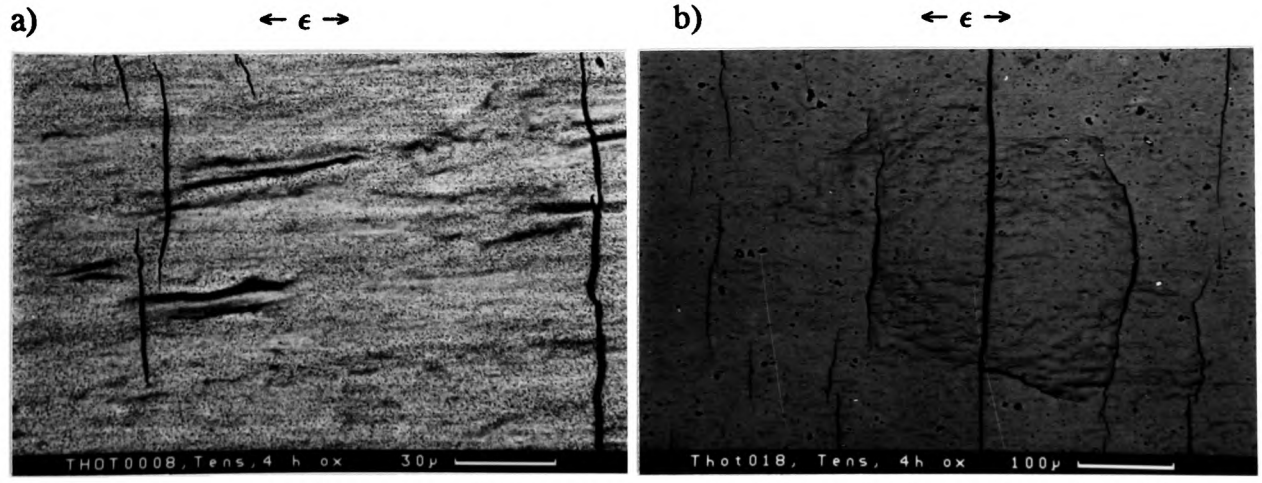

Figure 4.5: Backscattered SEM micrographs of (a) wrinkles and cracks (thickness 5 μm, max. strain 1.12%) and (b) a buckle (6.0 μm, 1.12%) in iron oxides after testing in tension at 550 °C. Strain rate $\sim 10^{-4}$ s^{-1}.

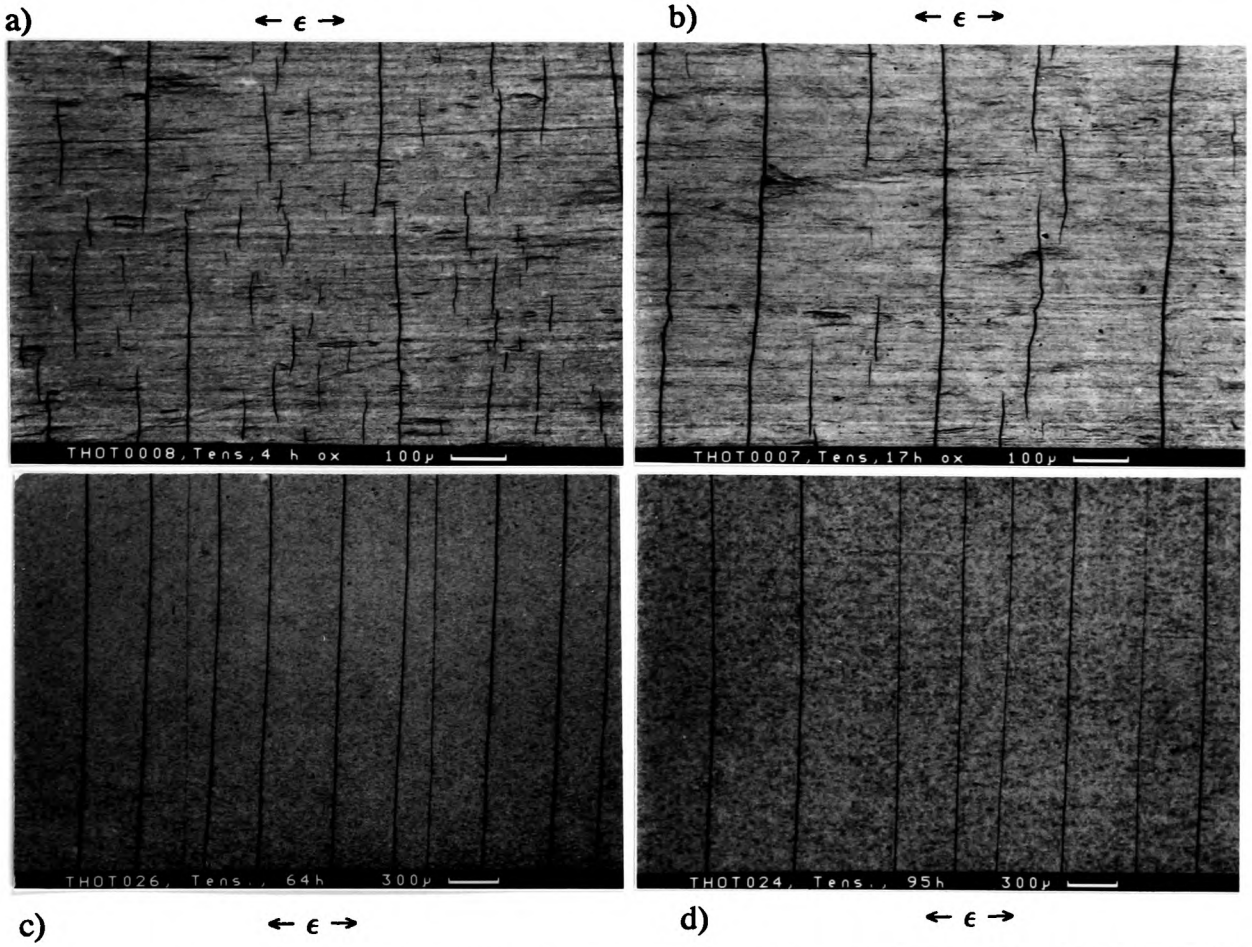

Figure 4.6: Backscattered SEM micrographs of iron oxides after testing in tension at 550 °C. Strain rate $\sim 10^{-4}$ s^{-1}. (a) Thickness 5 μm, max. strain 1.12%, (b) 9 μm, 1.12%, (c) 36 μm, 0.56%, (d) 46 μm, 0.56%.

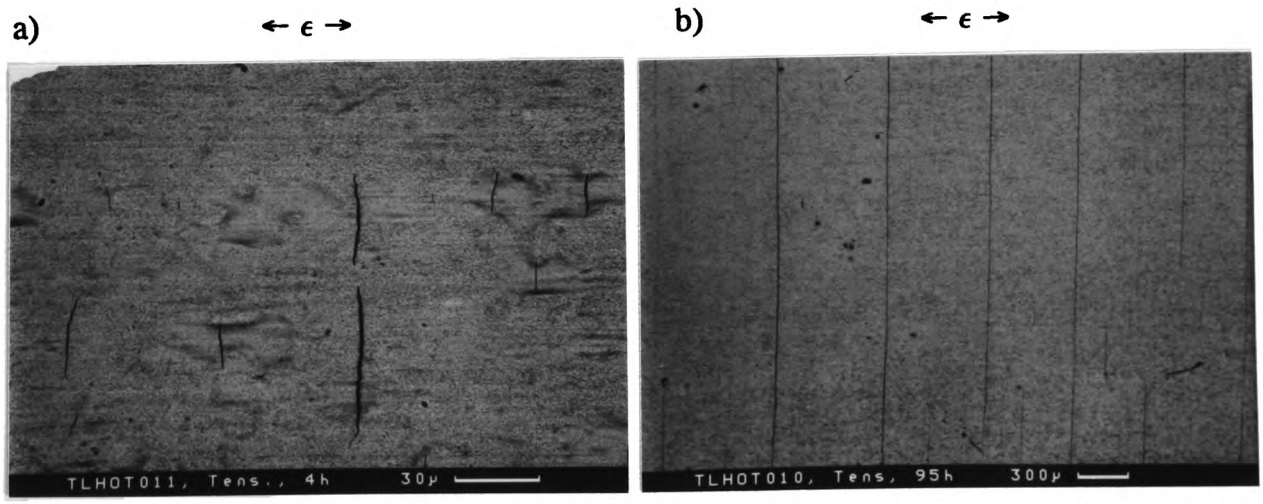

Figure 4.7: Backscattered SEM surface micrographs of iron oxides after testing in tension at 550 °C. Strain rate of $\sim 10^{-5}$ s^{-1}. (a) Thickness 6.5 μm, maximum strain 1.12% and (b) 44 μm, 0.56%.

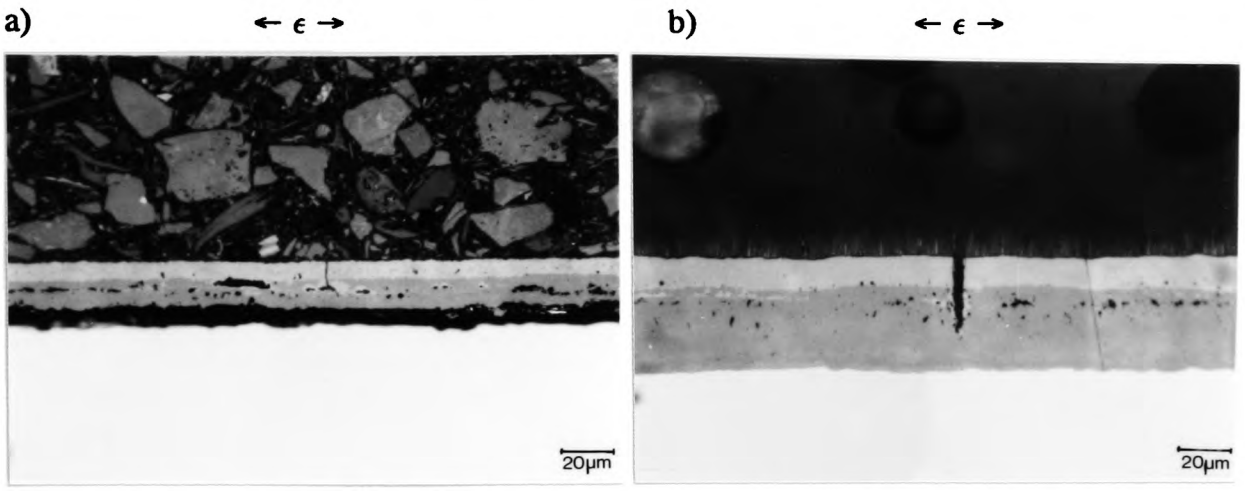

Figure 4.8: Cross-sections showing (a) a 19 μm thick oxide mounted in Bakelite (void size 0.4 h, max. strain 0.56%), (b) a 49 μm thick oxide mounted in Epofix (0.1 h, 0.56%) after testing in tension at 550 °C.

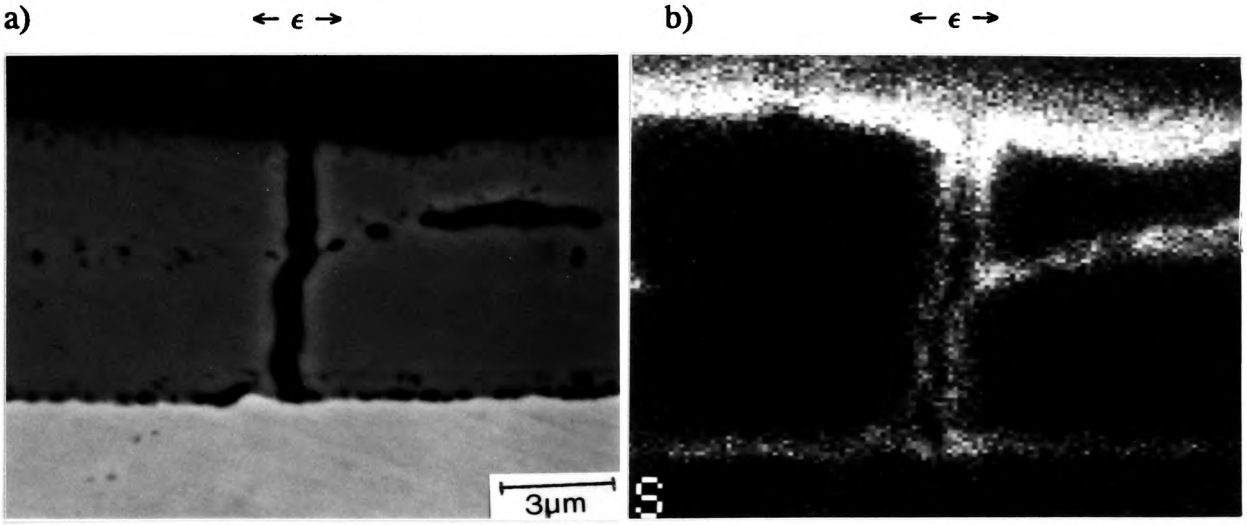

Figure 4.9: (a) Backscattered SEM micrograph of a 12 μm thick iron oxide after testing in tension at 550 °C and sulphur decoration (max. strain 1.12%). (b) X-ray image showing the presence of sulphur. Strain rate $\sim 10^{-4}$ s^{-1}.

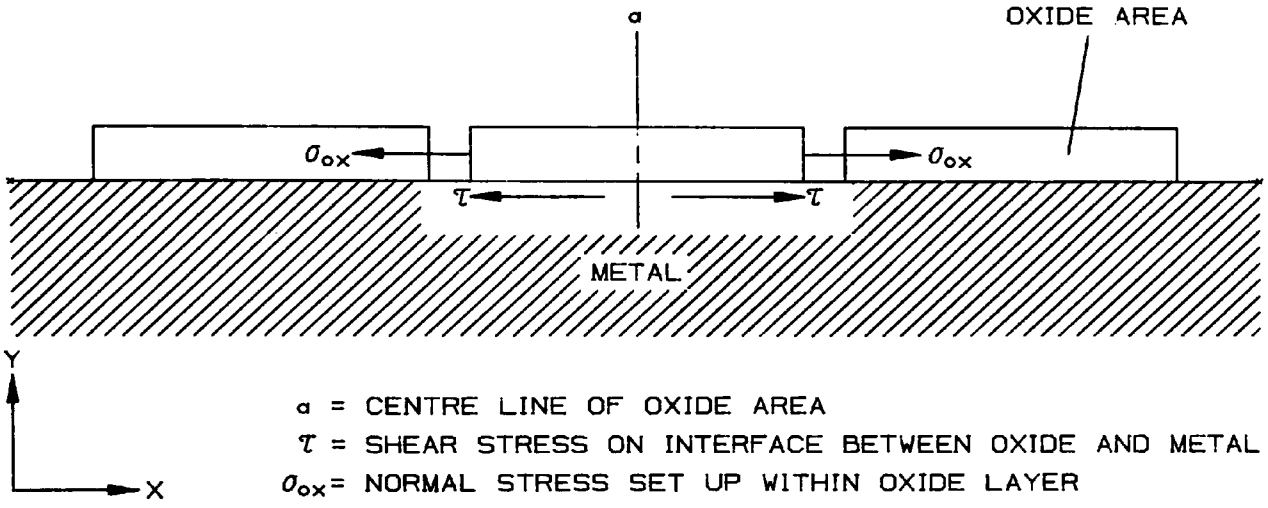

Figure 4.10: Schematic diagram of the shear and tensile stresses acting in an oxide area.

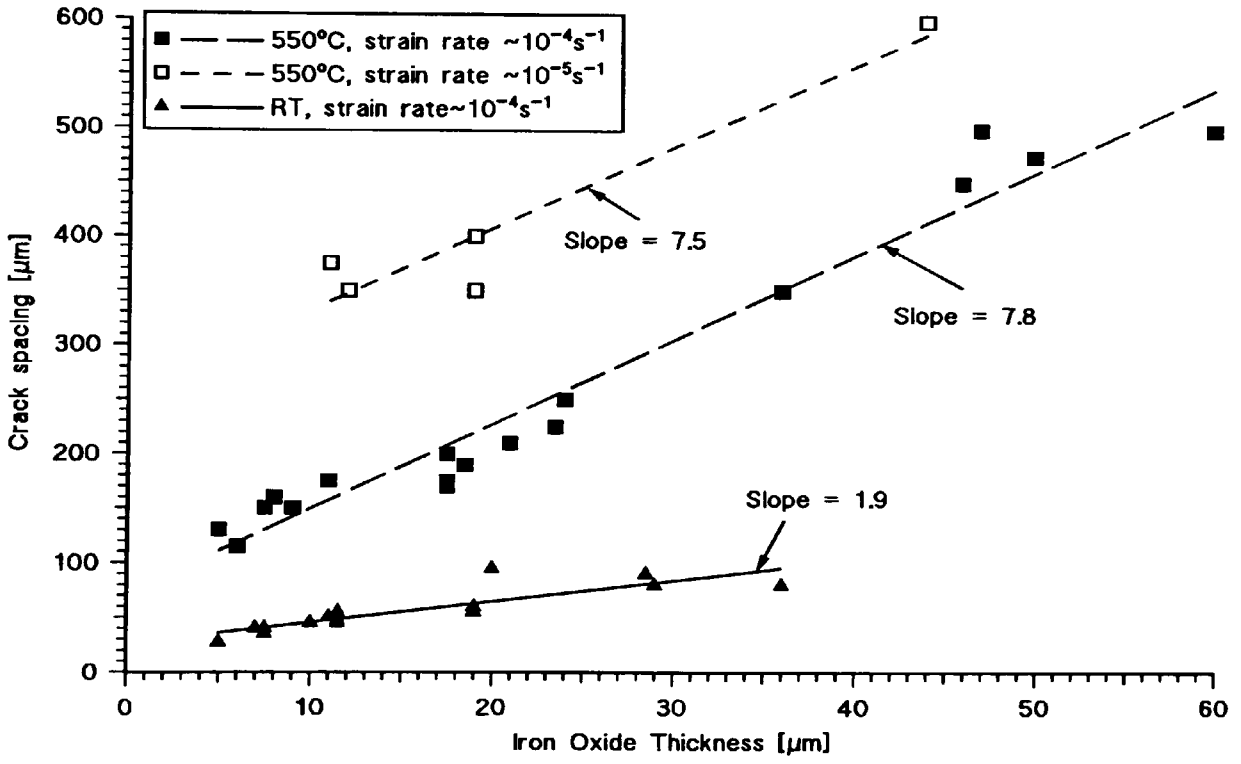

Figure 4.11: Crack spacing as a function of thickness for iron oxides tested in tension at room temperature (max. strain 1.12%) and at 550 °C (max. strain 0.56 - 1.12%) using different strain rates.

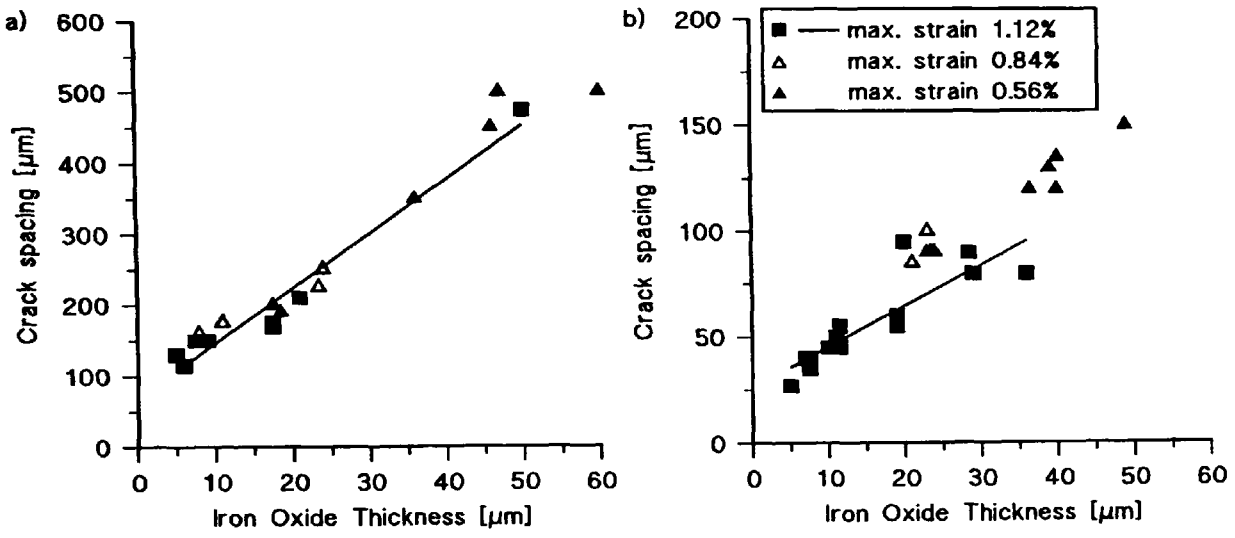

Figure 4.12: Plot showing the dependence of the crack spacing on the maximum strain for iron oxides tested in tension (a) at 550 °C and (b) at room temperature using a strain rate of $\sim 10^{-4}$ s^{-1}.

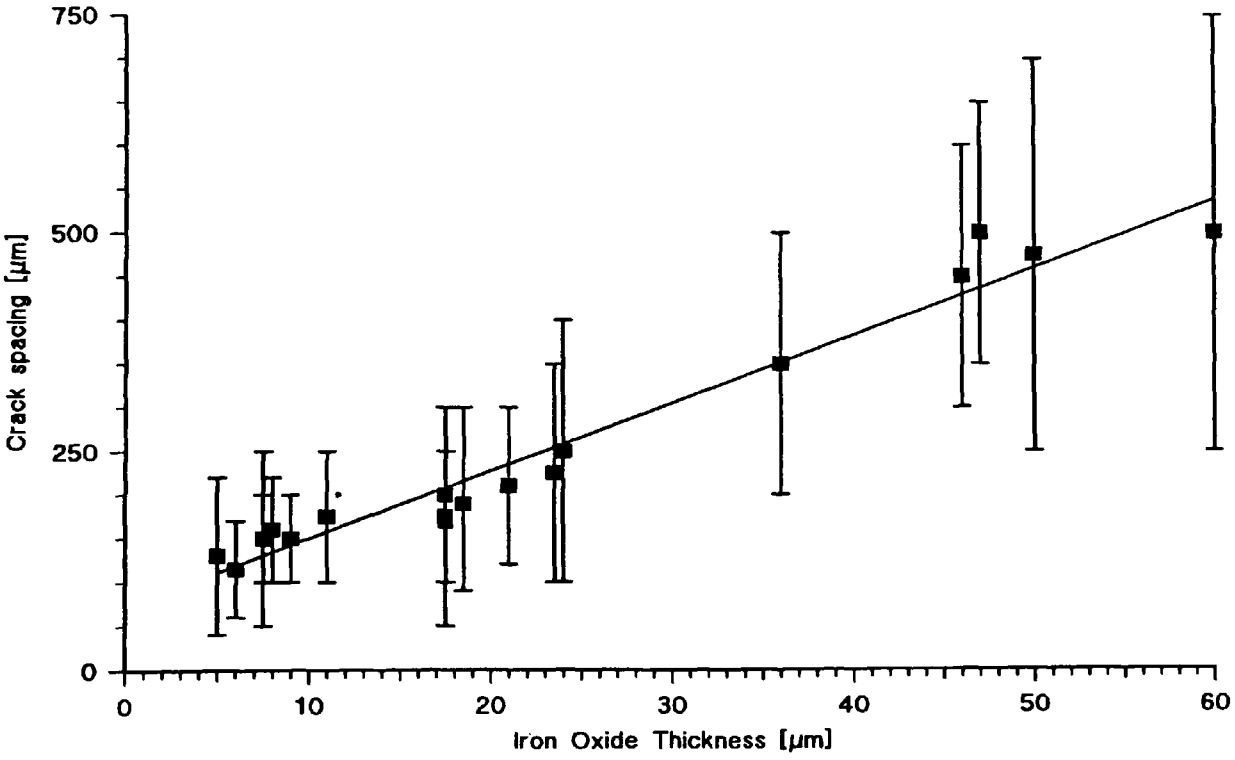

Figure 4.13: Plot showing the variation in the crack spacing as a function of thickness for iron oxides tested in tension at 550 °C using a strain rate of $\sim 10^{-4}$ s^{-1}.

4.1.1.2 Correlation of AE with Strain and Crack Patterns

Oxides Tested at Room Temperature:

Figure 4.14 shows a typical strain-distribution of the AE energy release for an 11 - 12 μm thick oxide. In this plot each single bar of the histogram represents the accumulated AE energy counts recorded in the respective period of time. Two regions can be clearly identified in this plot, a period of intense AE activity with high accumulated energy count levels after a few initial signals and a second period of high activity towards the end of the test. The two maxima are separated by a period of relative low AE activity. Figure 4.15 shows a typical AE history for oxides $\geq$ 19 μm thick which still shows the two regions but also considerable AE in between indicating that both regions overlap.

Oxides Tested at Growth Temperature:

A maximum in the rate of AE energy counts was recorded in all tests shortly after the onset of cracking (Figure 4.16). In no case was there an increase in AE towards the end of the tests. Oxides >25 μm thick had a number of AE signals with energy count numbers ≥ 100 dB shortly after the onset of cracking, which correlated well with the number of cracks stretching across the whole specimen width.

Discussion:

The first region of high AE activity at the beginning of the failure process was a result of the simultaneous creation of equi-distant cracks in the oxide. The second period of high activity was only recorded at room temperature and was caused by interface delamination and spallation as it was observed towards the end of the tests. These two regions were separated in oxides up to 12 μm thick and tested at room temperature by a period of low AE which can be accounted for by either the effects of elastic stress relaxation (see also section 4.3.1), plastic stress relaxation by interface slip or more likely by substrate yielding at the base of through-scale cracks (see also section 2.1.2.3, page 37).. In the latter case the oxide accommodated the increase in strain during plastic deformation of the substrate by localised yielding [3]. This resulted mainly in a widening of the existing cracks and produced therefore only a few AE signals. Interface delamination and hence AE could only start when the stress in the oxide started to increase again due to the work hardening of regions of the substrate. When through-scale cracking occurred at lower strains in thicker oxides the metal substrate was still deforming elastically and delamination at the interface was expected to occur at smaller strains. Indeed this appeared to have been the case for oxides $\geq$ 19 μm thick as shown in the plot for a 19 μm thick oxide (Figure 4.15).

Interface delamination was found in oxides >20 μm thick and strains >0.60 %

when tested at room or at growth temperature. However the increase in AE towards the end of the tests was only observed with oxides tested at room temperature. This supported the earlier evidence of lower interfacial strength and hence lower AE energy release during interface delamination at growth temperature.

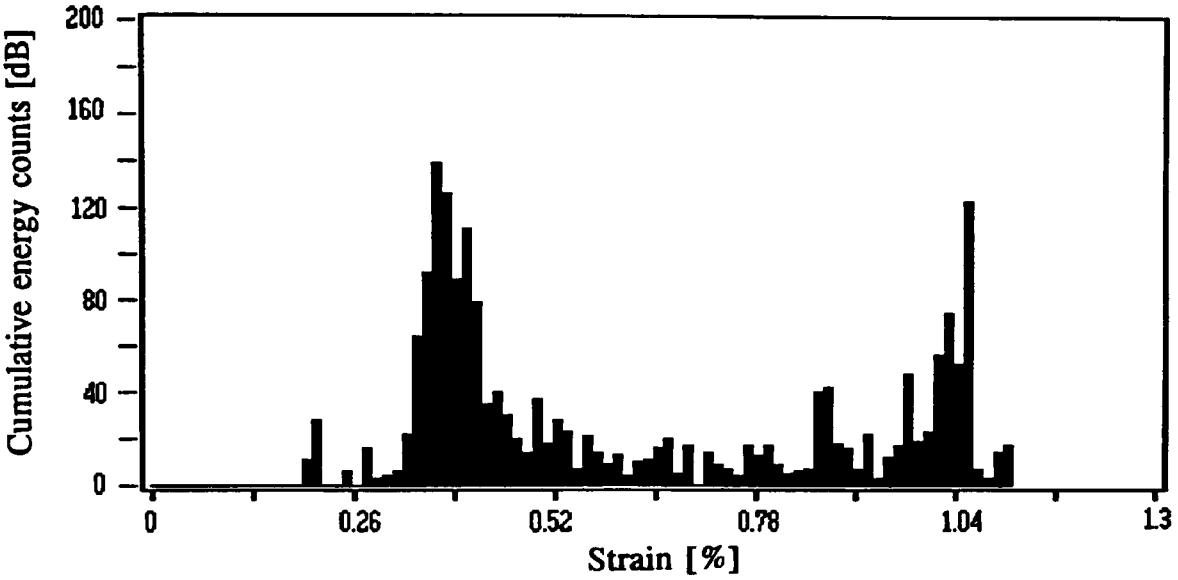

Figure 4.14: Histogram of the cumulative energy counts as a function of strain for an 11 - 12 μm thick iron oxide tested in tension at room temperature with a strain rate of $\sim 10^{-4}$ s^{-1}.

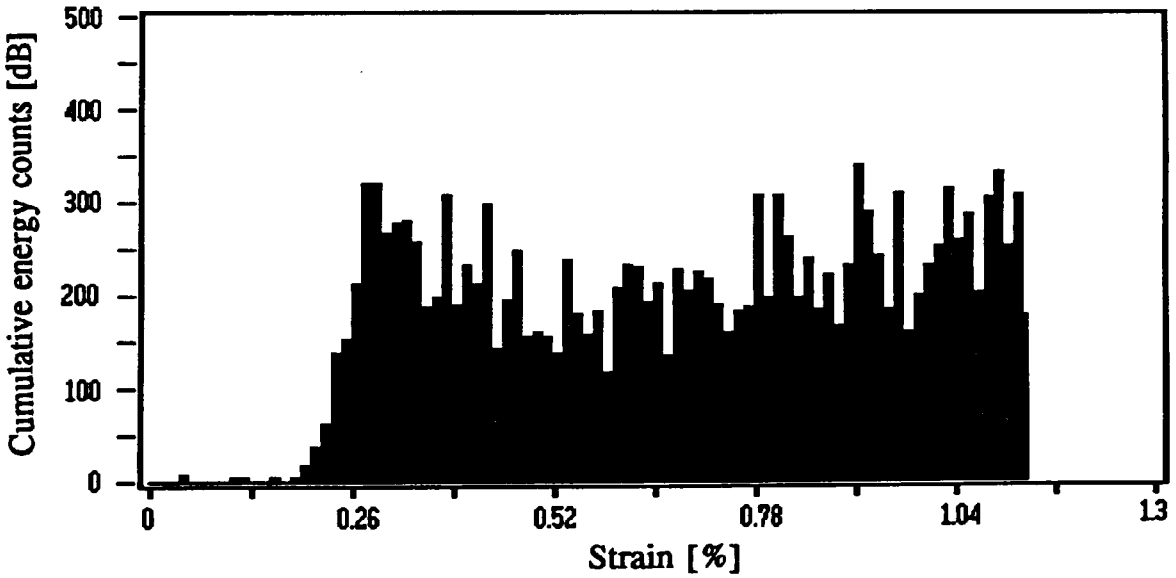

Figure 4.15: Histogram of the cumulative energy counts as a function of strain for a 19 μm thick iron oxide tested in tension at room temperature with a strain rate of $\sim 10^{-4}$ s^{-1}.

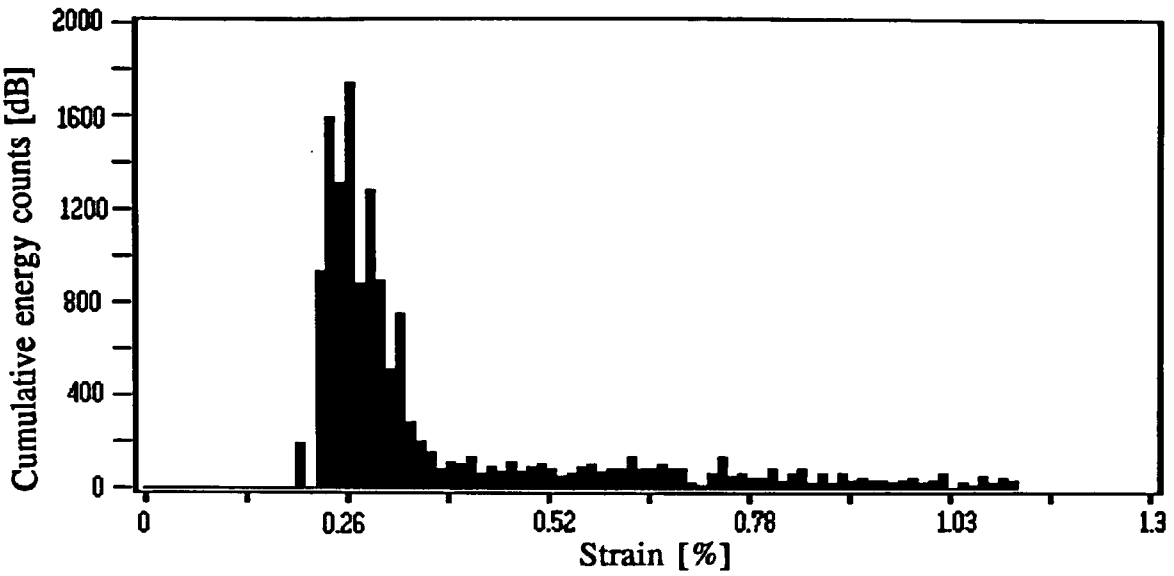

Figure 4.16: Histogram of the cumulative energy counts as a function of strain for a 9 μm thick iron oxide tested in tension at growth temperature (550 °C) with a strain rate of $\sim 10^{-4}$ s^{-1}.

4.1.1.3 Relationship between AE Parameters and Oxide Thickness

Comparison of data from tests on oxide scales of different thickness is complicated by the dependence of strain to failure on oxide thickness (see also section 4.1.1.4). To compare results from tests at the same absolute strain level is of little value since a thick oxide may already have started to spall at a strain value where a thin oxide is only in the first stages of through-scale cracking. This was confirmed by an analysis at a fixed strain level of 0.50% for the tests at room temperature, which gave similar trend lines with thickness as shown below, however the scatter of the results was much higher. Hence AE parameters from different tests on oxide scales were correlated for the same relative strain condition i.e. a strain increment of 0.30% above that for scale failure, when all tests had already passed the maximum rate of AE. Generally, some scatter in AE parameters was observed due to the varying nature of oxide and its failure. However there was an increase in AE with oxide thickness in all cases which was most pronounced for energy counts (Figure 4.17). This increase can be explained by the higher elastic strain energy released during fracture of a thicker scale to create new surfaces which have larger areas than those formed in thinner scales.

The average number of AE energy counts was higher for tests performed at growth temperature (using strains rates of $\sim 10^{-4}$ and $\sim 10^{-5}$ s^{-1}) when compared to the tests at room temperature (Figure 4.17a). This behaviour can be explained as follows:

The length of the cracks in oxides tested at room temperature increased only slightly with increasing thickness and cracking produced AE signals of similar energy,

hence the average energy count number increased only slightly with thickness in agreement with the linear increase of the new fracture surface area with thickness. In contrast, when tested at growth temperature, cracks became more rapidly longer as the oxide thickness increased so that the average energy counts increased more rapidly at growth temperature since the creation of new fracture surface area and hence the AE signal energy increased with both the thickness and the crack length. This was most noticeable in oxides > 25 μm and tested at growth temperature, which produced AE signals with energy count values of up to several hundred dB.

The way in which the oxide raft was produced for the tests at room temperature (abraded or selectively grown using Berkatekt 12) and the grinding mark direction did not influence the AE results.

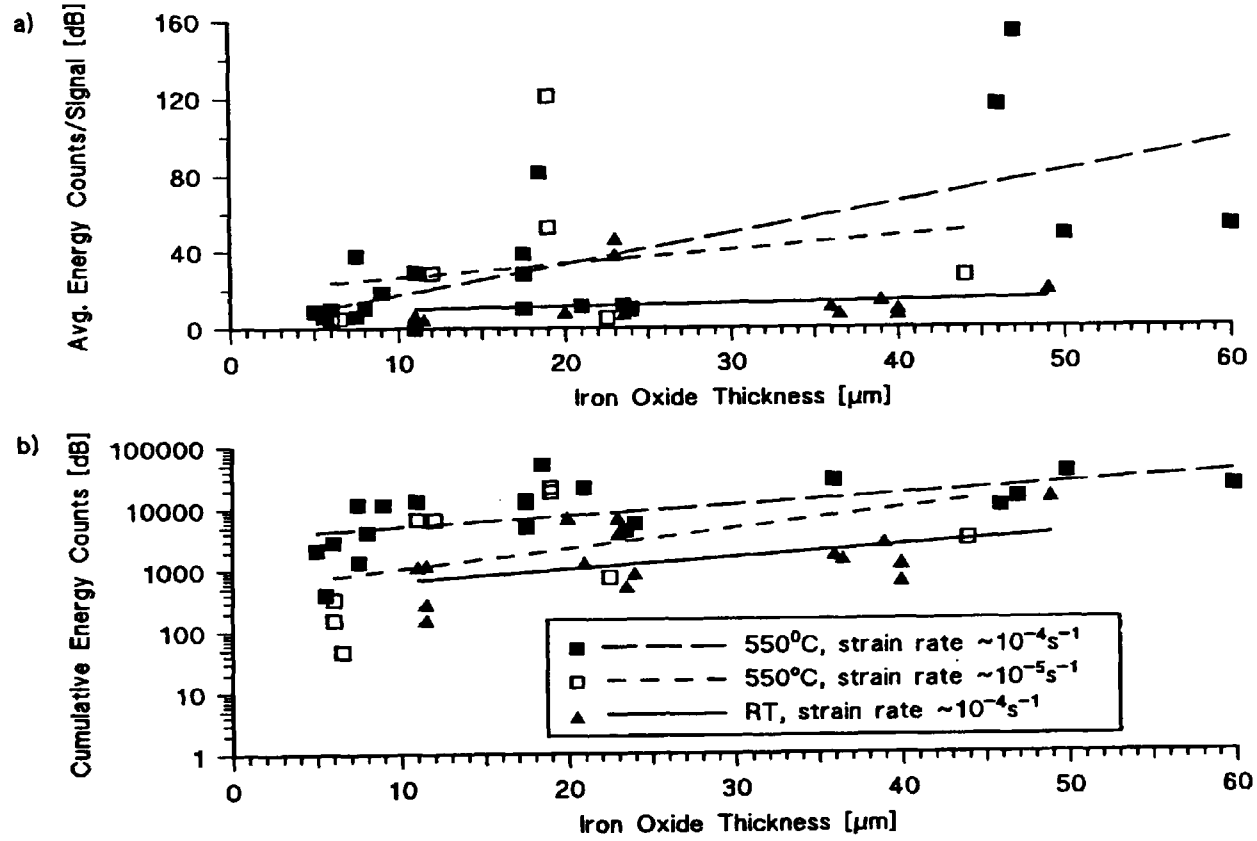

Figure 4.17: (a) Average energy counts/signal and (b) cumulative energy counts as a function of thickness for iron oxides tested in tension. Analysed at a tensile strain of 0.30% above first failure.

4.1.1.4 Oxide Failure Strains

The time from the start of the test to the first very high energy signal, or the first signal in a group of signals recorded in a short period of time, was used to calculate the strain at which macroscopic failure of the scale occurred (see also section 3.5.3 for the strain calculation, page 94). The validity of this assumption was confirmed in tests

which were terminated after a few AE signals had been generated. In each of these tests the number of high energy signals showed a one-to-one correlation with the number of cracks (Table 4.1).

The measured failure strains are shown in Figure 4.18a and Figure 4.19a as a function of oxide thickness for the tests at room and at growth temperature. The values decreased with increasing oxide thickness, however considerable scatter was found. Despite the high scatter a best-fit power law curve was drawn through the data points.

The variability in the data can be explained by a fracture mechanics analysis (see also section 2.1.2.3 (equation (2.12), page 39). For iron oxide the number of voids varied from one test to another even if carried out under the same conditions (cf. Figure 4.8, page 112) and could not be related to thickness. Thus the measured failure strains were plotted in Figure 4.18b and Figure 4.19b as a function of composite void size c, which was estimated from an examination of the polished cross-sections and use of the composite void size approach proposed by Hancock and Nicholls [2] (see also section 2.1.3, page 50). However such methods of estimating void size are prone to error due to uncertainties in metallographic preparation methods. In this context it was important to note that the grinding mark direction did not influence critical failure strains, i.e. surface defects did not affect cracking. Therefore only sharp scratches and indents in the oxide surface were included in the composite void size approach and not the usual waviness of the oxide surface. Importantly the shape of the curve for measured data closely followed a power law expected from the fracture mechanics model (Figure 4.18b and Figure 4.19b).

It is well known that additions of reactive elements such as Y, Ce, etc. improve scale adherence and it has been shown that scales are more compact with smaller voids [3] which agrees with the finding of the present study that scales with smaller voids had higher failure strains.

The difference in the critical failure strains at room and at growth temperature could be explained by consideration of the stress condition of the oxide prior to testing. Mismatch in thermal expansion coefficients of haematite, magnetite and mild steel left the oxide in a state of compression after cooling from growth temperature. Thus the early part of tensile strain applied on testing acted to overcome this compressive stress before the oxide was subjected to a net tensile stress. X-ray measurement showed that the compressive cooling strain in haematite is 0.18% and in magnetite 0.03%, which gave an average strain of 0.06 - 0.07% taking into account that the haematite occupied 20 - 30% of the scale. Similarly a calculation using thermal expansion coefficients for haematite, magnetite and the substrate given in ref. 10 showed that the cooling strain was approximately 0.04 - 0.05%, in agreement with that obtained from Figure 4.18b. The higher failure strains for oxides tested at growth temperature with a strain rate of $\sim 10^{-5}$ s^{-1} instead of $\sim 10^{-4}$ s^{-1} were due to time dependent creep (Figure 4.19b).

Schütze [9] has shown that creep is possible in magnetite under these conditions if the voids are smaller than 5 μm (cf. Figure 2.1, page 36), which was the case for the tested iron oxide scales.

Thus it was assumed that the oxide failed without any significant creep when loaded at a rate of $\sim 10^{-4}$ s^{-1}, and the difference in failure strain compared to the tests at room temperature was solely due to compressive cooling stresses. However creep increased the measured failure strain when the oxides were tested with a strain rate of $\sim 10^{-5}$ s^{-1} at 550 °C. A comparison of Figure 4.18 and Figure 4.19 indicates that with a strain rate of $\sim 10^{-5}$ s^{-1} the effect of the cooling strain at room temperature would offset the creep relaxation during deformation at growth temperature.

The measured failure strains were also used to determine the fracture toughness using a Young's modulus value of 210 GPa for room temperature [3] and assuming the same value for 550 °C and the relationship [2]:

$$\sigma_c = \frac{K_{IC}}{\sqrt{\pi c}} - \sigma_r \qquad (4.2)$$

where σ_c is the failure stress, σ_r is the residual stress and c is the composite void size. Values of 1.07 and 1.06 MN m$^{-3/2}$ for K_{IC} were obtained in the tests at growth and room temperature, respectively (Figure 4.20). These values were slightly lower than those quoted by Schütze [9], which was probably due to the fact that no extrapolation was made (see also section 2.1.3, page 50). The residual growth stresses at growth temperature were 23 MPa (tensile), which were in the same order as those obtained by Kataoka *et al.* [50]. The difference of 184 MPa between the intercept values for room and growth temperature tests was a measure of the compressive cooling stresses which compared well with the residual compressive stress of ~ 140 MPa found by X-ray strain measurement at room temperature. The lower strain rate of $\sim 10^{-5}$ s^{-1} gave an almost parallel line in the tests at growth temperature, as expected, since K_{IC} is a materials parameter and is believed to be constant up to ~ 600 °C [2]. In this case the difference in residual stress, compared to the tests at growth temperature with a strain rate of $\sim 10^{-4}$ s^{-1}, was an indication of the amount of creep in the oxide.

Iron oxide thickness [μm]	No. of AE signals with energy counts > 100 dB	No. of cracks found at the surface
11.0	6	6
11.0	11	11
37.5	7	7

Table 4.1: Comparison of the number of high energy signals with the number of cracks for tests which were stopped after a few AE signals had been recorded. Strain rate $\sim 10^{-4}$ s^{-1}.

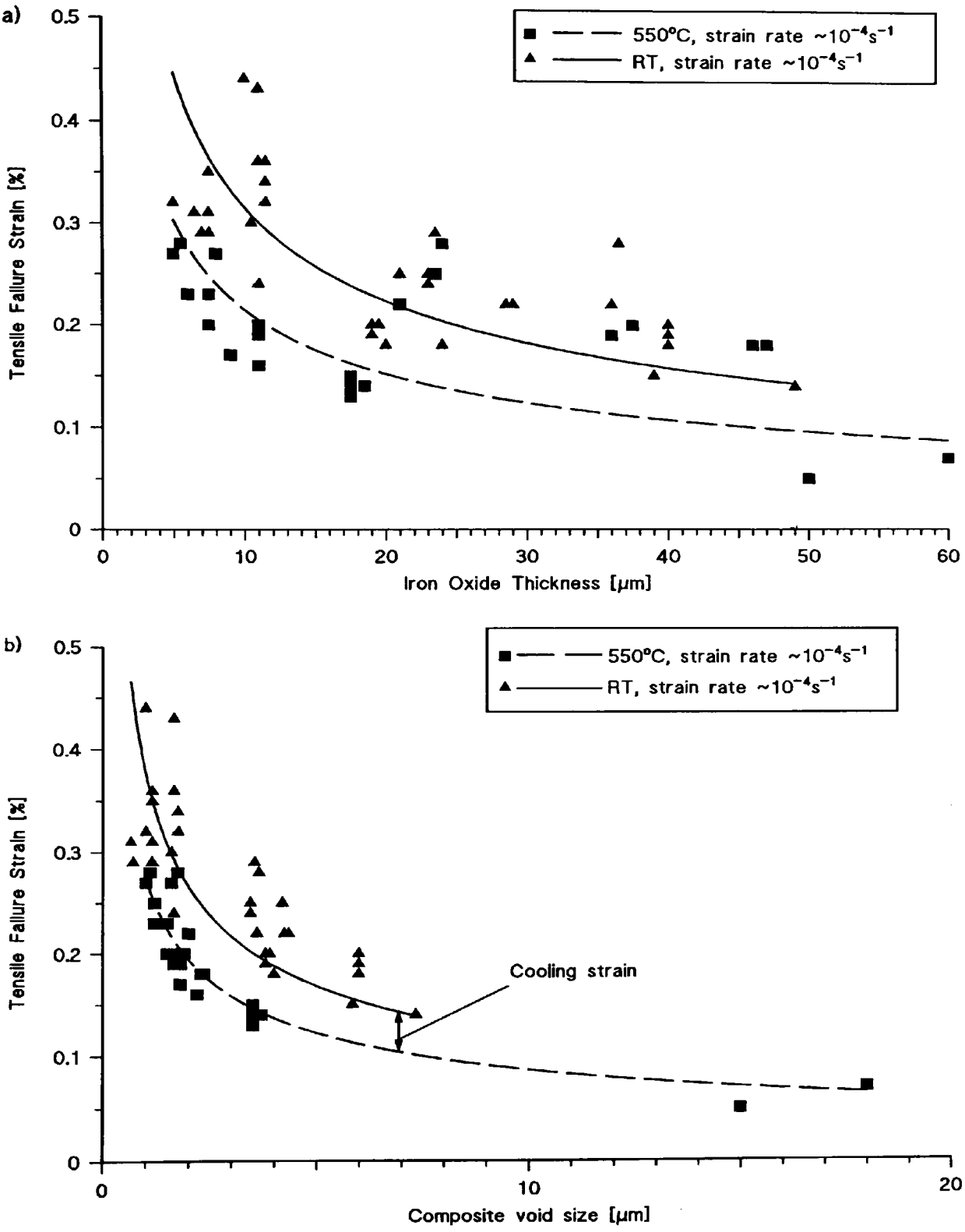

Figure 4.18: Measured failure strains as a function of (a) thickness and (b) composite void size for iron oxides tested in tension at room temperature and at 550 °C using a strain rate of $\sim 10^{-4}$ s^{-1}.

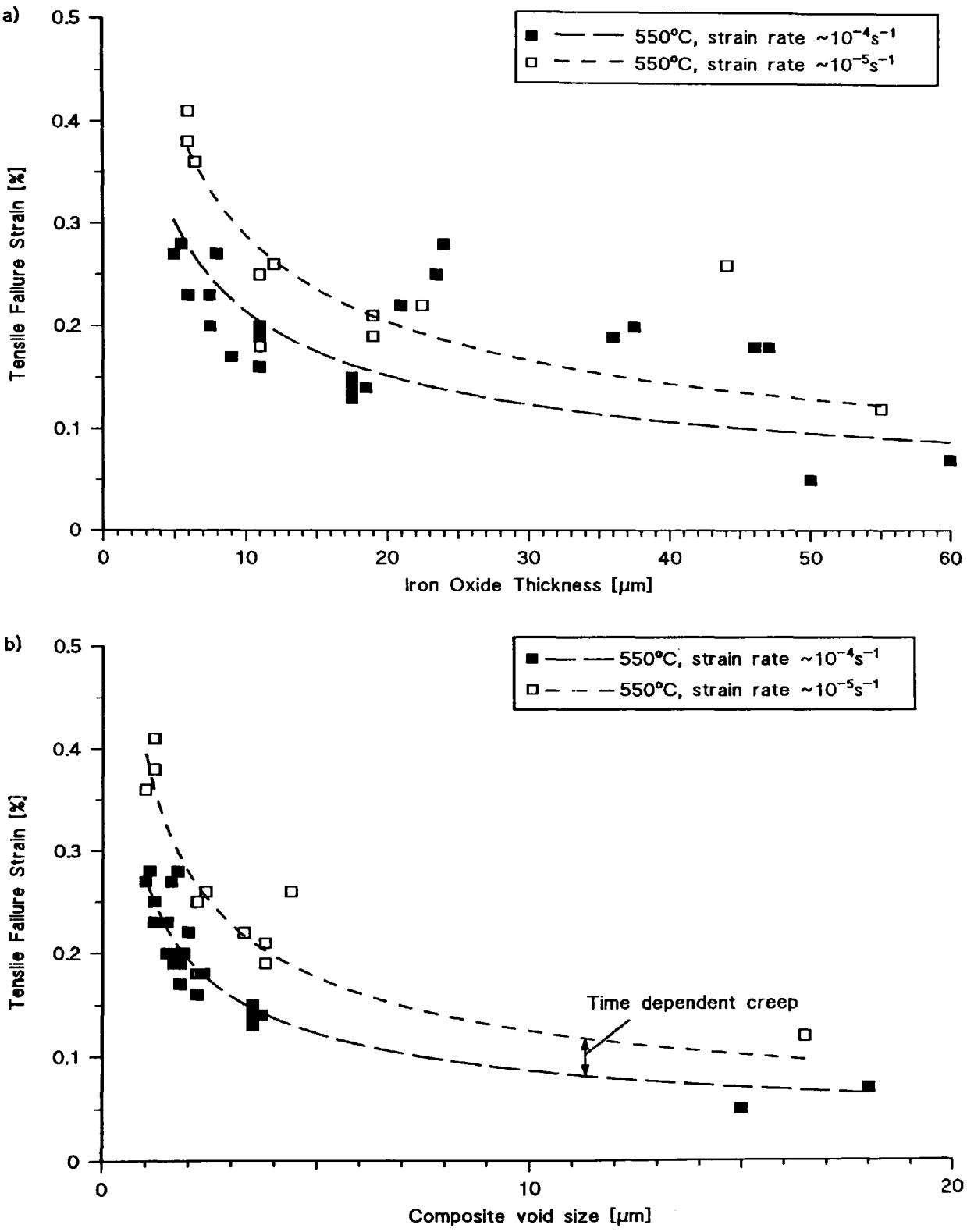

Figure 4.19: Measured failure strains as a function of (a) thickness and (b) composite void size for iron oxides tested in tension at 550 °C using strain rates of $\sim 10^{-4}$ and $\sim 10^{-5}$ s^{-1}.

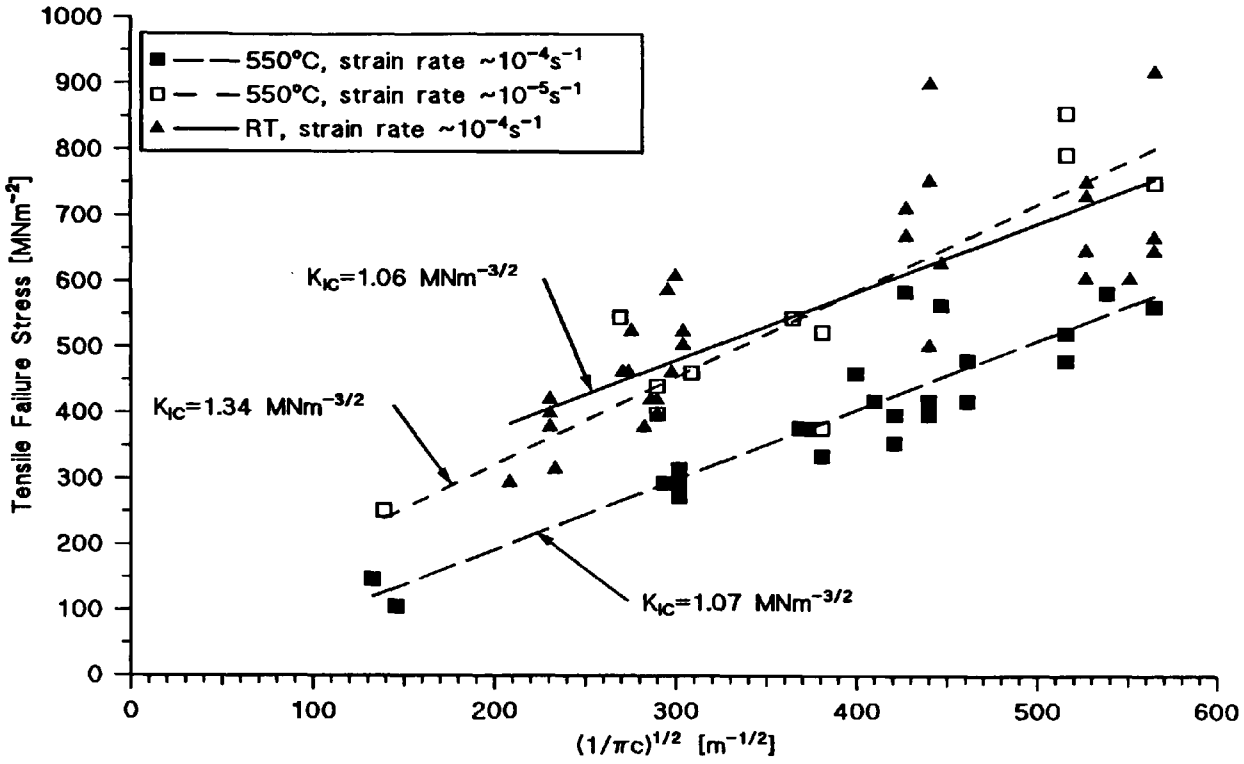

Figure 4.20: Fracture stress as a function of void size giving K_{IC} and residual stress σ_r for iron oxides tested in tension at room and at 550 °C using different strain rates.

4.1.2 Tests with Iron Oxide in Compression

Tests were carried out in the same way as for the previous tensile tests but with the oxide on the top side of the specimens. The strain to cause failure at growth temperature was much higher and could not be measured using AE because the tensile failure of the thin unwanted oxide underneath the Berkatekt coating on the tensile side of the beam produced considerable AE and interfered with the normal observations (see also section 3.2.4, page 84 and 3.6.1, page 95). This interference was only observed in compression at growth temperature and the thin unwanted oxide on the opposite side of the specimen was in all other tests mechanically stable and hence did not produce AE at the critical fracture strains being measured for the much thicker oxides being tested. Thus, above a critical strain AE could not be used to detect failure and the tests were stopped. Up to the critical strain no AE was recorded at growth temperature nor was there any traceable microscopic damage in the oxide after cooling. Hence, it was concluded that the oxide was still mechanically stable at these strain levels at growth temperature, and Curve B in Figure 4.21 shows the critical strain levels up to which no failure was observed compared to the measured failure strains for the same oxide at room temperature (Curve A). It must be borne in mind that the strain values

(Curve B) only represent the minimum values and actual failure strains at growth temperature could be much higher. Thus the following sub-sections only refer to the room temperature test results.

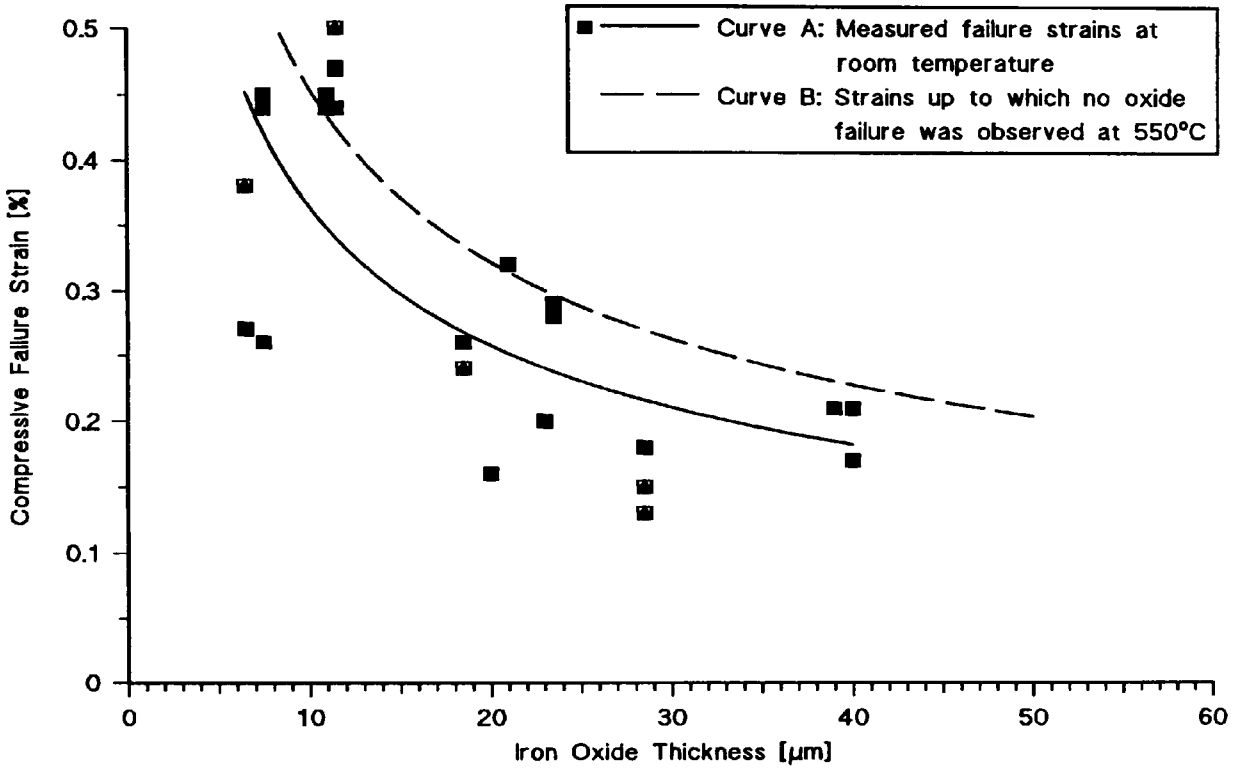

Figure 4.21: Strain levels up to which no failure was observed at oxide growth temperature in iron oxides under compression compared to the measured failure strains for similar oxides tested at room temperature.

4.1.2.1 Crack Patterns

Spallation initiated at the edge of the original oxide raft for oxides > 12 μm thick, due to interfacial failure caused by the accumulation of shear stress at this position (Figure 4.22b). In thinner oxides spallation occurred within the main area of oxide as well as at the edge (Figure 4.22a and Figure 4.23). In oxides between 19 and 30 μm thick, delamination also occurred along a line of voids in an outer part of the oxide (haematite and thin layer of magnetite) and in some cases spallation occurred (Figure 4.24). In this case, G_{ic} was probably least along these lines of high void density and delamination originated within the oxide before the interface failed. The strain to cause spallation of the whole layer decreased with increasing oxide thickness (Table 4.2). These strains were found for oxides ≤ 12 μm by stopping the tests at different strains and examining the surface. In thicker oxides most of the oxide spalled in one event which was manifested in a drop of the load by $\sim 5\%$.

In addition, micro- and macro-cracks were found in the direction of the applied strain in specimens with oxide thicknesses ≤ 20 μm and strains $> 0.25\%$ (Figure 4.25).

These tensile cracks were caused by the effect of the Poisson's ratio which induced a tensile strain in the oxide normal to the loading direction during elastic and plastic deformation of the substrate. A large number of these cracks was found in the magnetite layer of oxides where the outer part had spalled off (Figure 4.25b). The high void density and the even void distribution was also visible in that part of the oxide (Figure 4.24b and Figure 4.25b).

Cross-sections from all tests showed the beginning of interface delamination, typical of Route II failure (buckling). However, the mounting and the polishing procedure introduced unknown amounts of mechanical stress which could also cause interface delamination. The fracture surface left by spalled areas on oxides ≤ 12 μm thick was normal to the oxide-metal interface and interface cracks extended into the remaining oxide (Figure 4.26a). This confirmed that the Route II failure mechanism had operated for oxides ≤ 12 μm thick, whereas the metallographic results for thicker oxides suggested interfacial failure which started at the extreme edge of the original oxide raft. This did not conform strictly with either of the failure mechanisms given in Figure 2.5 (page 46), but is described mathematically by the equation (2.24) (page 46) which characterises interface delamination. The delamination within the oxide scale in 19 - 30 μm thick oxides followed Route II because the delaminated part of the oxide was thin enough (≤ 12 μm) to exhibit buckling and as above, evidence for this mechanism was found in the fracture surface left by the spalled area (Figure 4.26b). The change in failure mechanism can be explained by the quadratic increase of the buckling stability with thickness and therefore the shear stresses in oxides > 12 μm exceeded the critical interfacial shear strength before the buckling stability of the scale was reached.

There was no difference in the crack patterns when the oxide raft was prepared by abrasion or by selective oxidation.

Oxide thickness [μm]	Strain for failure initiation [%]	Strain for spallation [%]
≤ 12	0.26-0.50	>1.0
19-24	0.16-0.32	>0.9
28-29	0.13-0.18	>0.6

Table 4.2: Critical strain values for failure initiation and spallation.

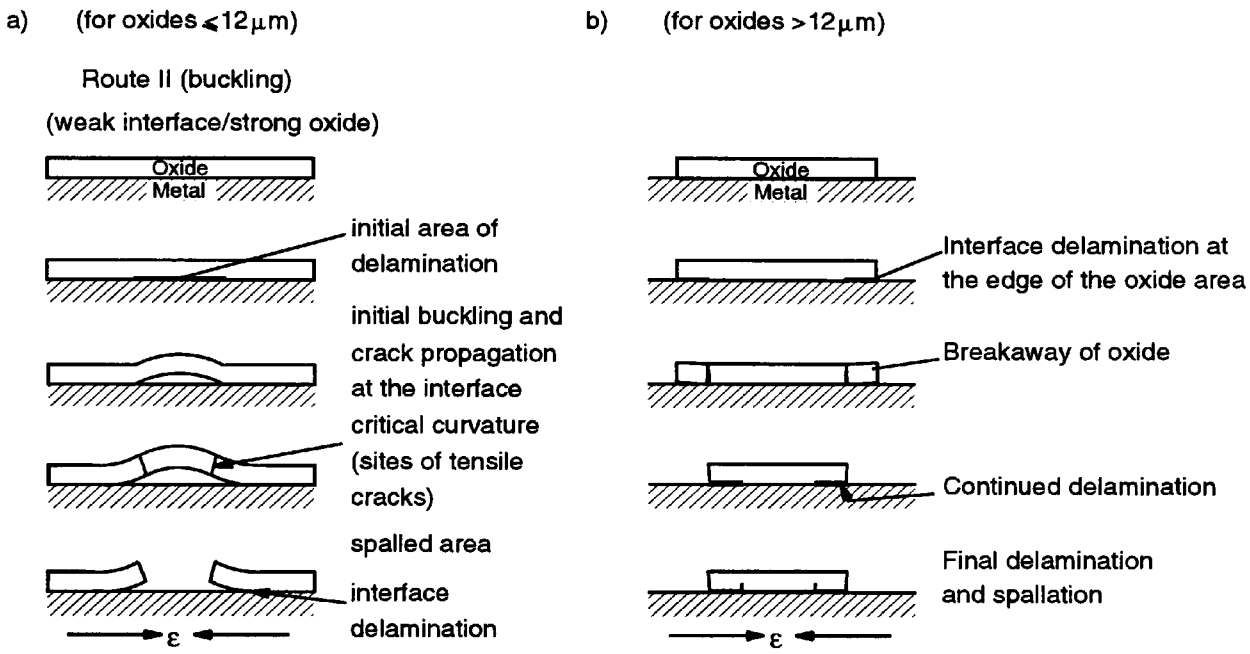

Figure 4.22: Schematic diagram of the observed failure mechanisms (a) for iron oxide ≤ 12 μm and (b) for iron oxide >12 μm.

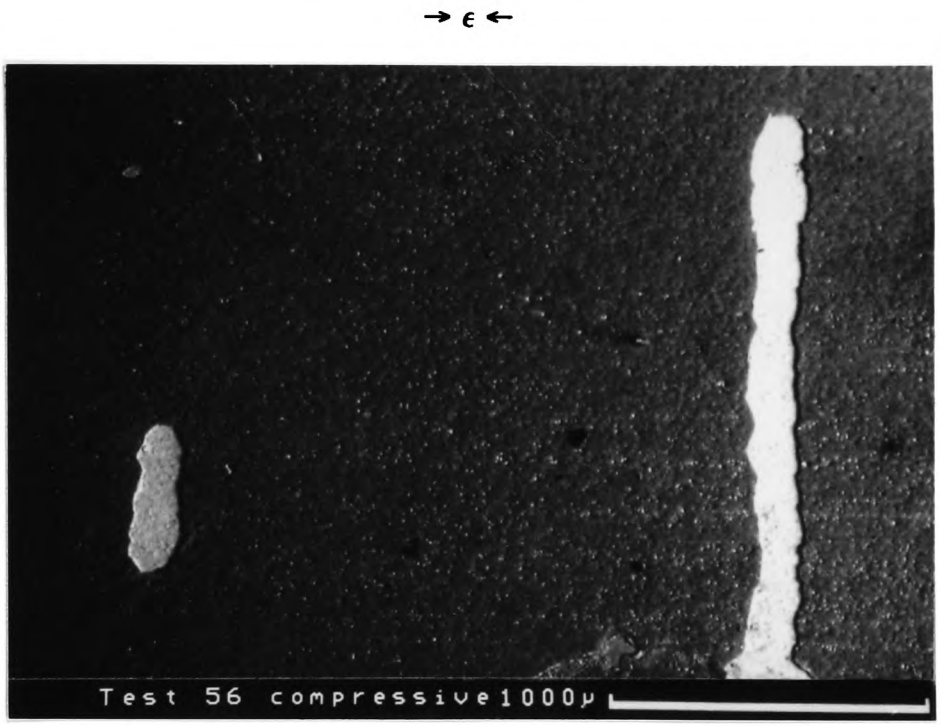

Figure 4.23: Backscattered SEM surface micrograph showing spalled areas within 10 - 12 μm thick iron oxide after testing in compression at room temperature to maximum strain of 1.12%.

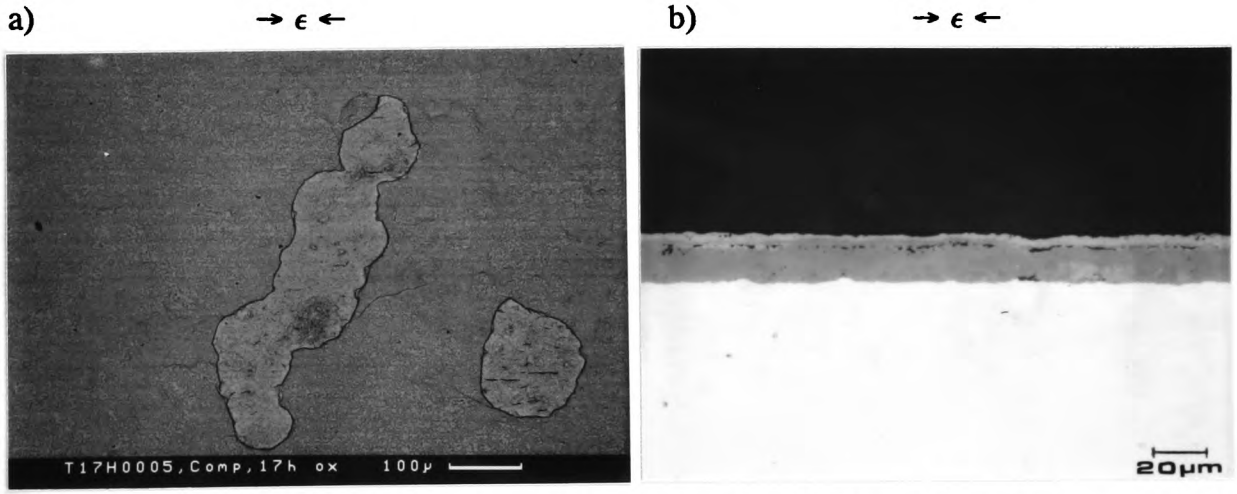

Figure 4.24: (a) Backscattered SEM micrograph of areas with only the outer part spalled (thickness 23 μm, max. strain 0.75%). (b) Cross-section showing delamination along voids within the iron oxide after testing in compression at room temperature.

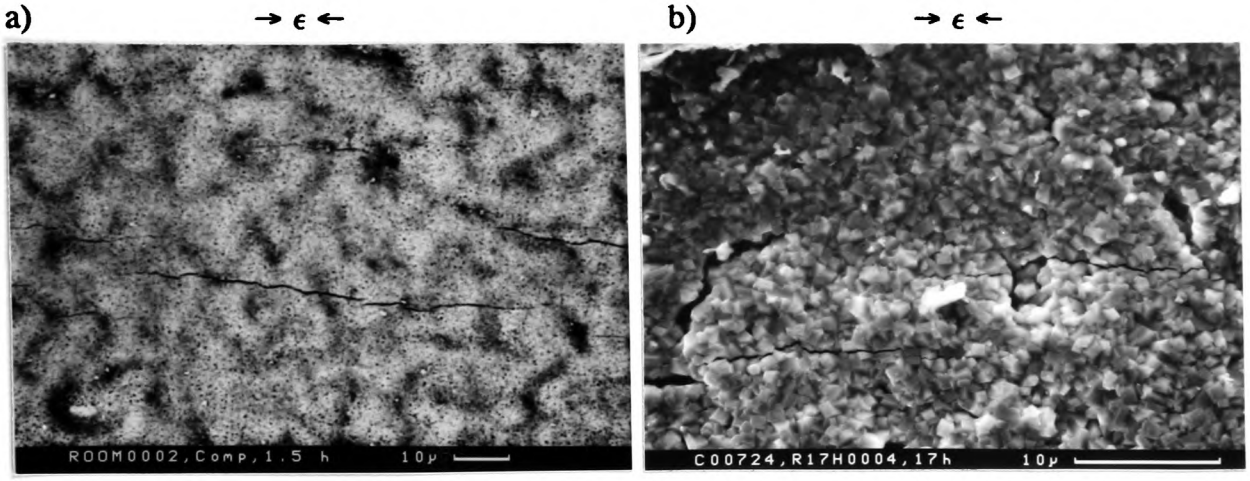

Figure 4.25: SEM micrographs of tensile cracks in the direction of the applied stress (a) at the outer surface (thickness 11 μm, max. strain 1.12%), (b) in the magnetite layer (19 μm, 1.12%) after testing in compression at room temperature.

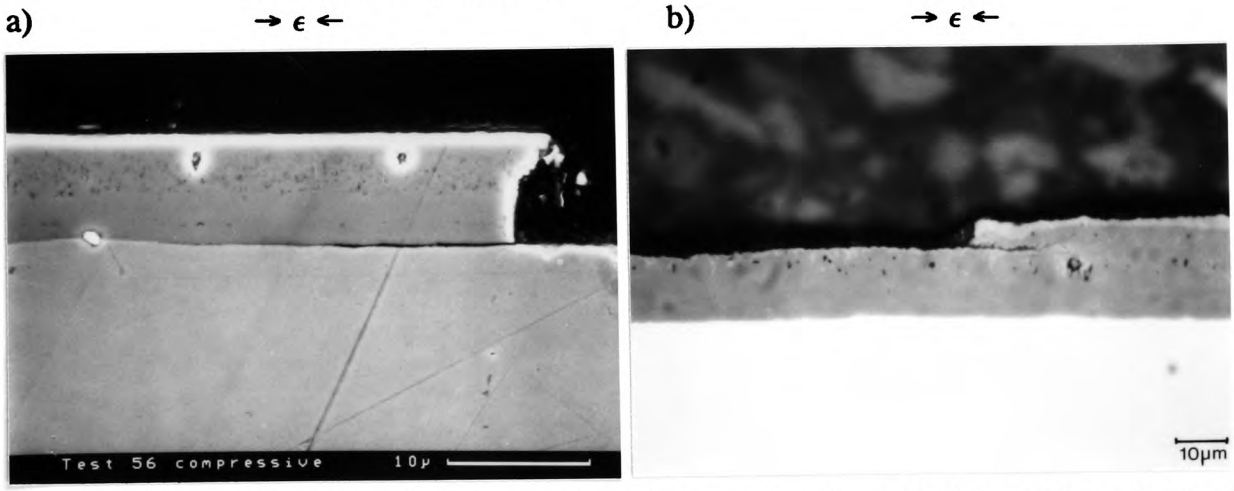

Figure 4.26: Cross-sections of the interface crack and vertical through-scale crack at the edge of spalled areas. In (a) the whole oxide had spalled (thickness 11 μm, max. strain 1.12%) and in (b) a part of the oxide (19 μm, 1.12%).

4.1.2.2 Correlation of AE with Strain and Crack Patterns

All AE parameters (average and cumulative number of AE counts, average and cumulative AE energy counts, amplitude and number of AE signals) increased as tests proceeded indicating that the build-up of strain in the specimen made failure more likely and when failure occurred, increasingly larger amounts of strain energy were released. The histograms in Figure 4.27, which show the average and cumulative AE energy counts as a function of strain, depict that increase.

The way in which the oxide raft was prepared did not influence the AE distribution with strain.

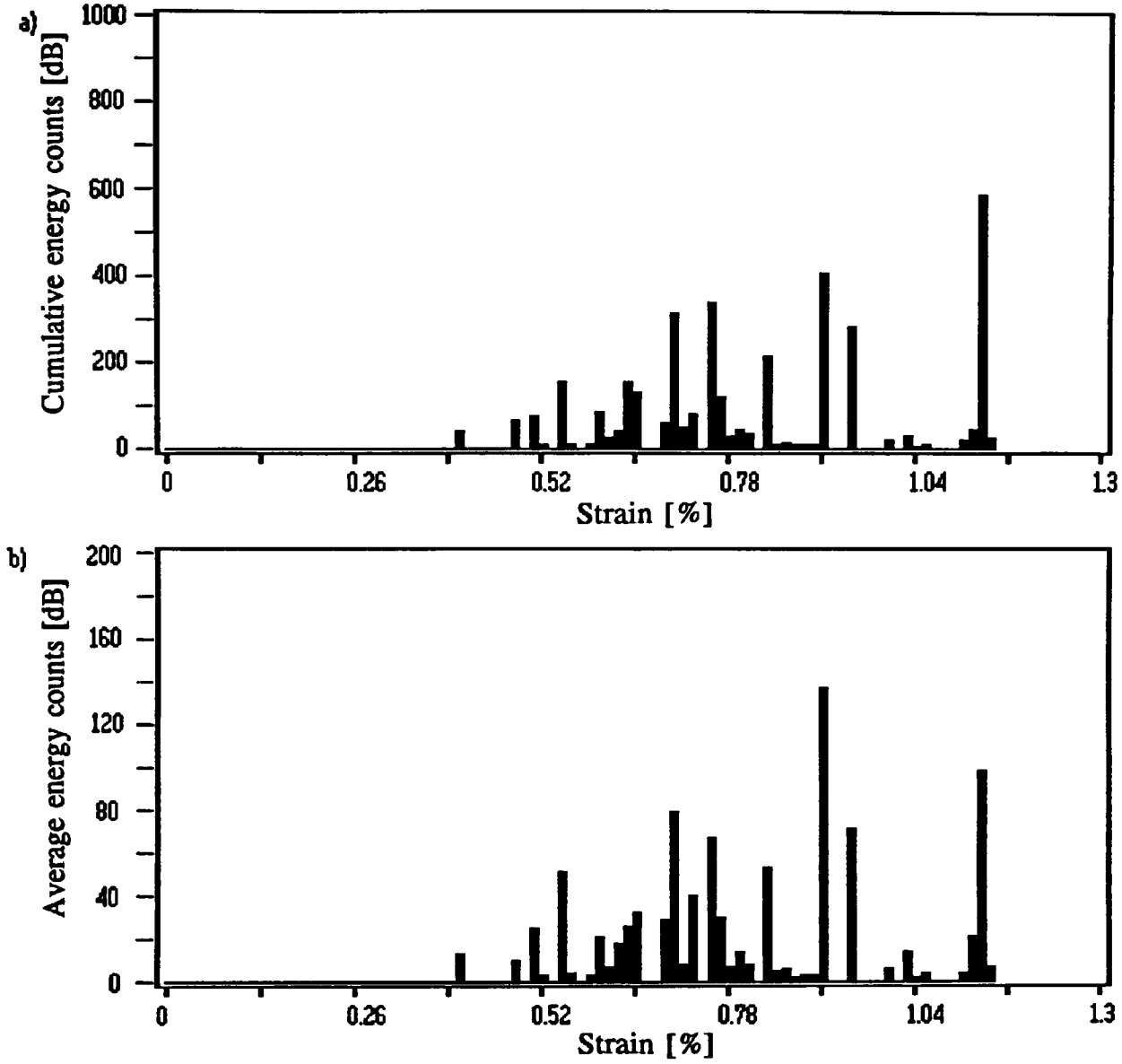

Figure 4.27: Histogram of (a) cumulative and (b) average AE energy counts as a function of strain for an 11 μm thick iron oxide tested in compression at room temperature. Strain rate $\sim 10^{-4}$ s^{-1}.

4.1.2.3 Relationship between AE Parameters and Oxide Thickness

As in section 4.1.1.3 (page 117), an additional strain increment of 0.30% above failure strain was selected for correlation purposes.

The cumulative AE count number and the cumulative AE energy count number increased with increasing oxide thickness (Figure 4.28) indicating higher energy release during failure of thicker scales. The smaller AE values in tests where Berkatekt 12 was used were due to the higher threshold used in these tests (Figure 4.28 and Figure 4.29). The average AE count number and the average AE energy count number per signal were independent of oxide thickness (Figure 4.29). This can be explained by step-wise propagation of the interface cracks and with each step an AE signal was emitted.

However the size of the steps was not expected to bear any relation to oxide thickness and hence the average values remained constant while the cumulative values were higher for thicker oxides. Spallation by through thickness cracking was expected to produce thickness dependent AE values, but it had yet to occur at the strains used in the analyses for Figure 4.28 and Figure 4.29 (see also section 4.4.2).

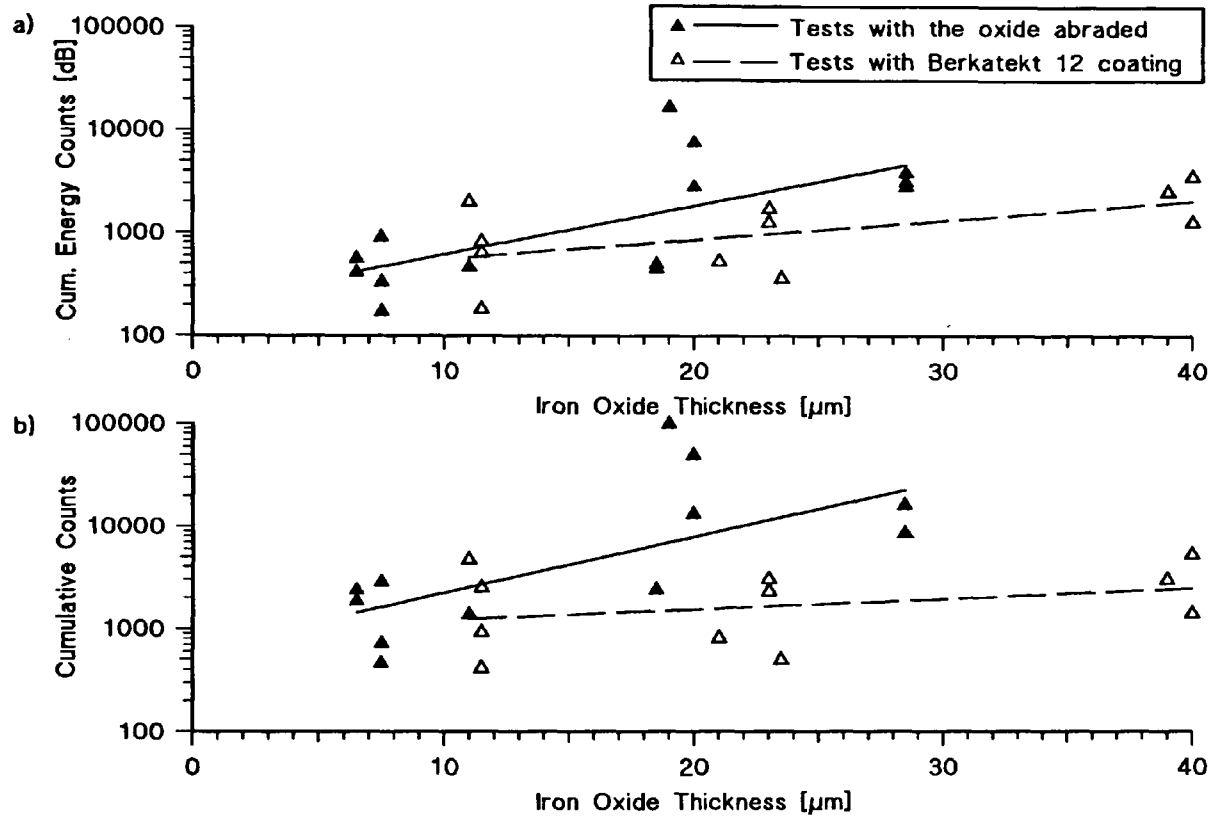

Figure 4.28: (a) Cumulative energy counts and (b) cumulative counts as a function of iron oxide thickness. Analysed at a compressive strain of 0.30% above that for scale failure at room temperature.

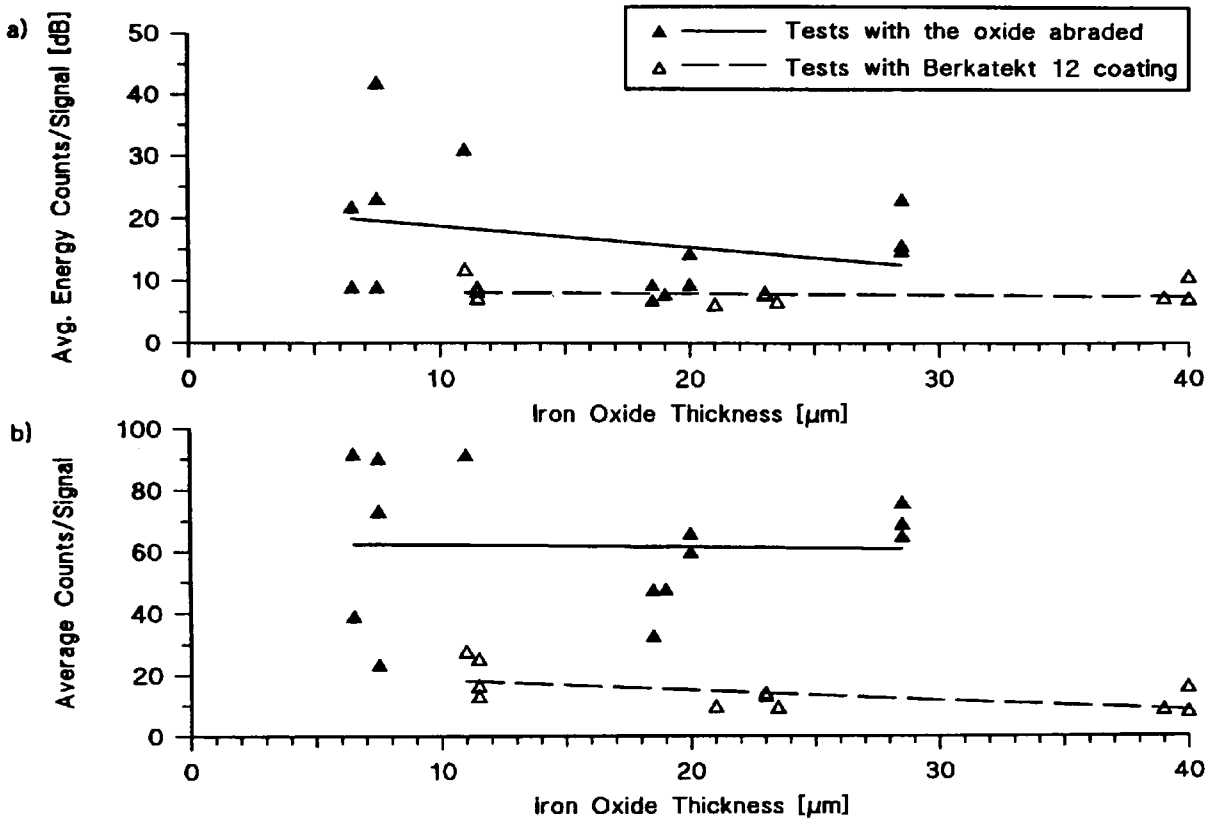

Figure 4.29: (a) Average energy counts/signal and (b) average counts/signal as a function of iron oxide thickness. Analysed at a compressive strain of 0.30% above that for scale failure at room temperature.

4.1.2.4 Oxide Failure Strains

As in the tests in tension the occurrence of AE was used to calculate critical compressive failure strains. It has been shown that the appearance of AE signals marked the start of microscopic or macroscopic failure, i.e. cracking preceded spallation [91,92].

Measured critical strains for crack initiation as a function of oxide thickness are shown in Figure 4.30. The critical strains have been compared with those calculated for Route I and Route II spallation, in particular with equation (2.24) (page 46) which describes interface delamination since oxide failure always started at the interface. It was assumed that the buckled region failed without crack propagation at the interface and hence a value of 100 μm was chosen for R, i.e. the radius of the initial delamination, based upon the observed size of spalled areas (cf. Figure 4.23, page 127). The measured size of R was not too far from the predicted dimensions of 160 and 190 μm from equation (2.39) and (2.40) (page 71), respectively, for an oxide thickness of 10 μm and a spallation strain of -1%. A Young's modulus of 210 GPa, a Poisson's ratio of 0.3 and a surface energy value of 4.5 J m^{-2} were taken from ref. 3, which gave a G_{IC}-value of 9.0 J m^{-2} assuming an idealised interface with an energy release rate

equal to that of bulk oxide [3]. The measured values (Curve A) lie above those predicted (Curve B) with the lower values being typical for tests where delamination and spallation of parts of the oxide proceeded along a line of voids. The observed buckling failure for oxides ≤ 12 μm is in reasonable agreement with the prediction based on Route II failure, i.e. buckling. In addition, the difference in the cooling stress due to the different thermal expansion coefficients for the haematite and magnetite layer might introduce additional forces promoting interface delamination, i.e. Route II failure. This would shift the initiation and spallation condition for Route II failure (cf. Figure 4.30) towards lower strain values and higher thicknesses i.e. make it consistent with the observed Route II failure for oxides ≤ 12 μm thick. In addition, the growth stresses could vary with position, relative to the interface, giving a complex unknown stress distribution within the oxide which could not be measured with currently available techniques. Consequently, more accurate predictions of failure based on the actual stress state in the oxide could not be made.

In fact the total strain in the oxide scale at the time of crack initiation was even higher because the oxide was in compression prior to testing due to the cooling stresses (see also section 4.1.1.4, page 118 and 4.4.2). Curve A gave an energy release rate of 20 J m^{-2} for the case of a stress free oxide prior to testing. The value does not account for the cooling stresses. However it is within the range of 4 - 40 J m^{-2} reported in ref. 18, but clearly above the value of 6 J m^{-2} given for the loss of 0.5% oxide on 20Cr-25Ni-Nb steel [5,12]. Evans and Lobb [11] also gave an average value of about 40 J m^{-2} for 50% spallation but a recent finite element analysis for the same oxide/substrate system suggested a value of 2 J m^{-2} [8,43].

The failure strains were very similar in tests with or without Berkatekt 12 coating, hence the coating did not influence the oxidation or the failure behaviour.

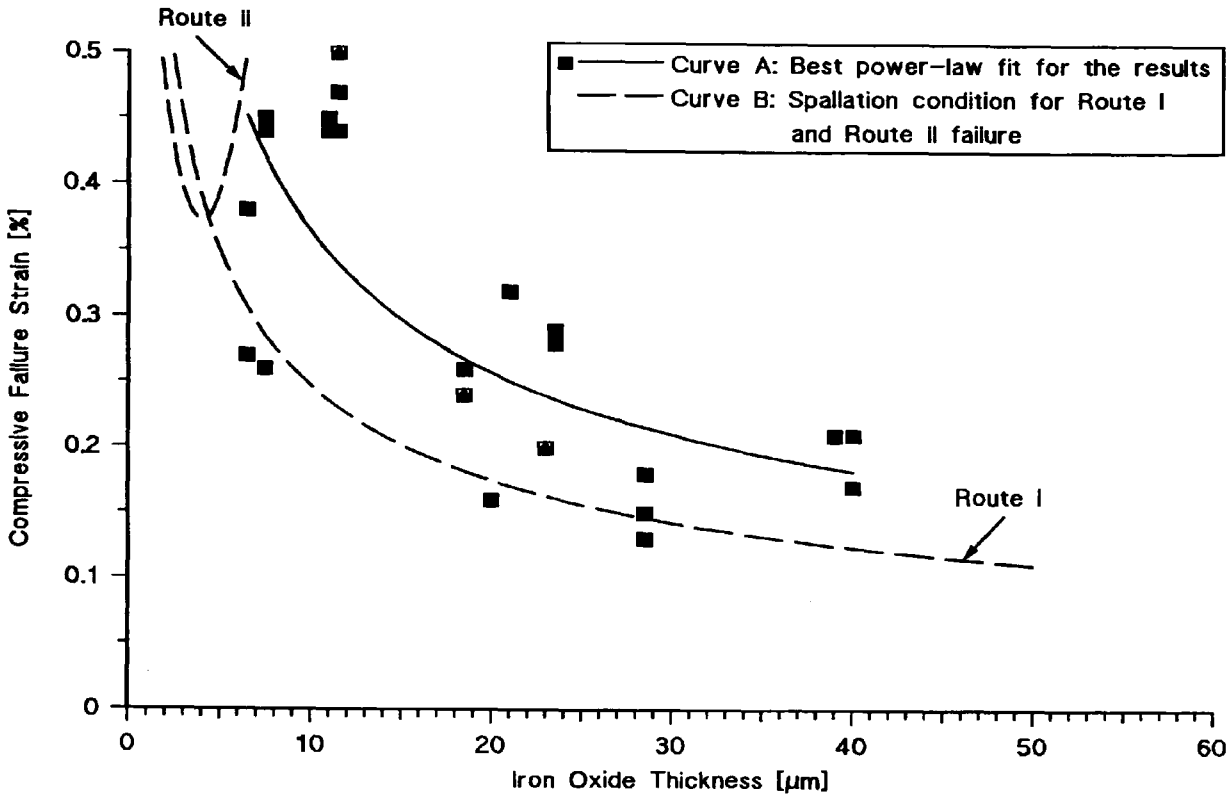

Figure 4.30: Comparison of the measured and calculated failure strains for iron oxide tested in compression at room temperature.

4.2 Tests with Nickel Oxide grown on 99% Pure Nickel

Test Programme:

Oxides layers up to 60 μm thick were tested in tension and compression at room and at growth temperature (900 °C) using a strain rate of $\sim 10^{-4} s^{-1}$. Additional tests were made in tension at room temperature to evaluate the influence of the protective coating on oxide structure and oxide failure.

Initially, samples were tested in tension at room and at oxide growth temperature to 1.12% strain. These tests were followed by similar tests in compression. However, due to the high compressive strength of the NiO, it was necessary to use thicker specimens (see also section 3.4, page 90) and samples were bent to 2.8% strain, because no failure was recorded in compression at the usual strain of 1.12%.

Scale Morphology:

NiO scales were duplex and consisted of an outer layer of columnar grains and an inner layer of equi-axed grains (Figure 4.31). The equi-axed layer was formed by inward transport of oxygen presumably along fissures that corresponded to grain boundaries [105] and columnar crystals were a result of outward diffusion of nickel cations through the oxide layer and their reaction with oxygen at the surface. The

relation between the equi-axed and the columnar layer was 0.8-1 : 1 for oxides ≥ 10 μm thick and the same relationship was assumed for thinner oxides. Platinum marker experiments proved that the boundary between the two layers corresponded to the original metal surface.

Fracture surfaces produced important information on the porosity of NiO. The outer columnar grains had only a few small pores at the grain boundaries, whereas the equi-axed layer showed a high number of evenly distributed pores (Figure 4.32). The interface was also uneven which could be a reason for its high resistance against delamination (see also section 4.2.1.1), and the size of these interface ripples remained constant for all oxide thicknesses. Generally the oxide structure and voidage were very similar to what is reported in the literature for NiO grown on 99% pure nickel [18,81].

The surface appearance of the oxide was changed when the samples were oxidised in the bend test furnace (Figure 4.33a and Figure 4.34a), or when they were oxidised with protective coating (Figure 4.33a-b and Figure 4.34a-b). In addition, the surface appearance varied depending on where the oxide grew within the bend test furnace, i.e. at the top or bottom side of the specimen (Figure 4.34c-d) or more importantly inside or outside of the ceramic bend jig (Figure 4.34a,d). No exact explanations could be found for some of the changes. However, neither crack patterns nor oxide failure strains were affected by the changes, as will be shown in the sub-sections 4.2.1.1 and 4.2.1.4.

Growth and cooling did not cause cracking and spalling of the oxide and neither cracking nor spalling was observed in the oxides after preparation prior to testing at room temperature.

4.2.1 Tests with Nickel Oxide in Tension

4.2.1.1 Crack Patterns

Oxides < 7 μm thick and tested at growth temperature showed only short randomly distributed cracks. However through-scale cracks with regular spacing were observed in all other tests. The spacing increased with increasing oxide thickness and the same relative strain level (Figure 4.35 and Figure 4.36). The spacing was larger for oxides tested at oxide growth temperature, but cracks were more wavy when formed at room temperature, i.e. they were more likely to follow the grain boundaries of the columnar grains particularly in thicker oxides.

It was more likely to find longer cracks in thicker oxides, although short cracks < 10 μm long could be found in all oxides no matter whether they were tested at room or at oxide growth temperature. The cracks were transgranular and intergranular (Figure 4.37), although it appeared that cracks started to increasingly follow the grain boundaries when they arrested within the oxide area (Figure 4.37b).

The observations on cracking and spacing were confirmed by the cross-sections and none of the oxides from any test showed delamination at the interface or between the columnar and equi-axed crystals. All cracks were through the whole thickness (Figure 4.38) although crack healing occurred at the crack tip on cooling to room temperature in oxides tested at growth temperature (Figure 4.38b). However this was on a much smaller scale than observed with iron oxide (see also section 4.1.1.1, page 106).

There was no difference in the crack patterns when the oxide was abraded after oxidation in the muffle furnace or when it was grown selectively in the bend test furnace using DPG 3582 protective coating and then tested at room temperature.

Discussion:

As shown in section 4.1.1.1 (Figure 4.11, page 113) the change in the tensile strength of the iron oxide would be small between room temperature and 550 °C and thus the major factor contributing to lower crack spacing in room temperature tests was believed to be the higher interfacial shear strength. For nickel oxide at 900 °C the tensile strength would be lower than that at room temperature which should result in a lower crack spacing, whereas the crack spacing actually increased at the higher temperatures (Figure 4.39). Thus an analysis based on the same model as in section 4.1.1.1 (equation (4.1), page 107) suggested that a much larger decrease in interfacial shear strength occurred which was probably related to the larger temperature differential compared with the results for iron oxide. At room temperature comparable values of slope were observed for both the iron and nickel system, and if the appropriate values of σ_{ox} are used, the interfacial shear strengths are approximately the same (see also section 4.4.1).

It should be noted that the samples had not reached the saturation crack density above which the increase in strain is solely compensated by interface delamination, because the crack spacing was dependent on the maximum strain (Figure 4.40) and there was no sign of delamination at the interface or spallation. Thus the experimentally derived data tend to underestimate the ratio $\sigma_{ox}:\tau_x$ expected from equation (4.1).

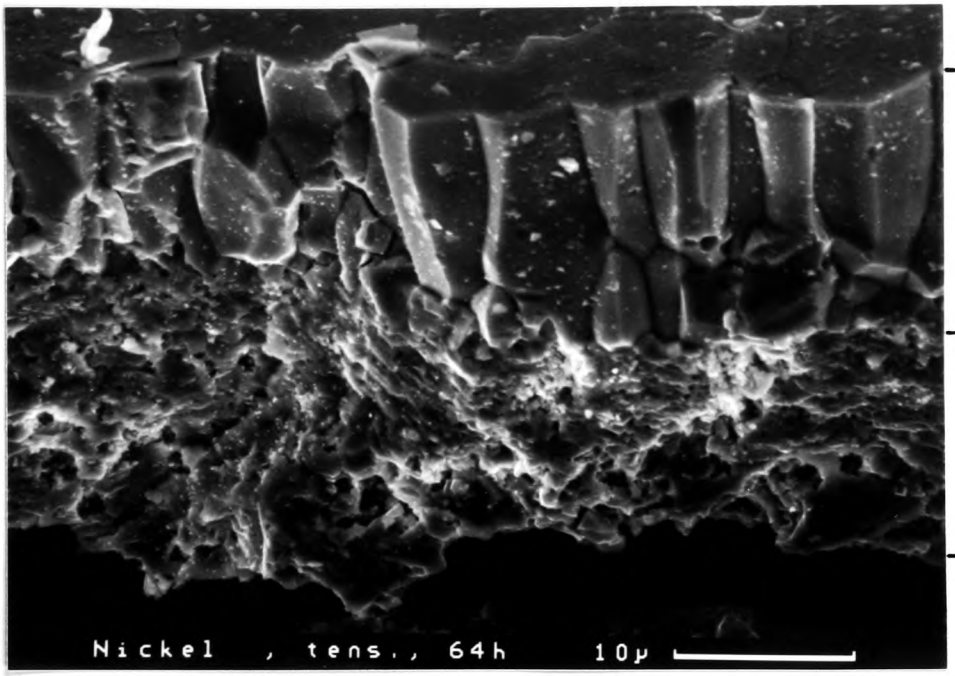

Figure 4.31: Secondary SEM micrograph showing a fracture surface in a 45 μm thick NiO after oxidation in a muffle furnace at 900 °C.

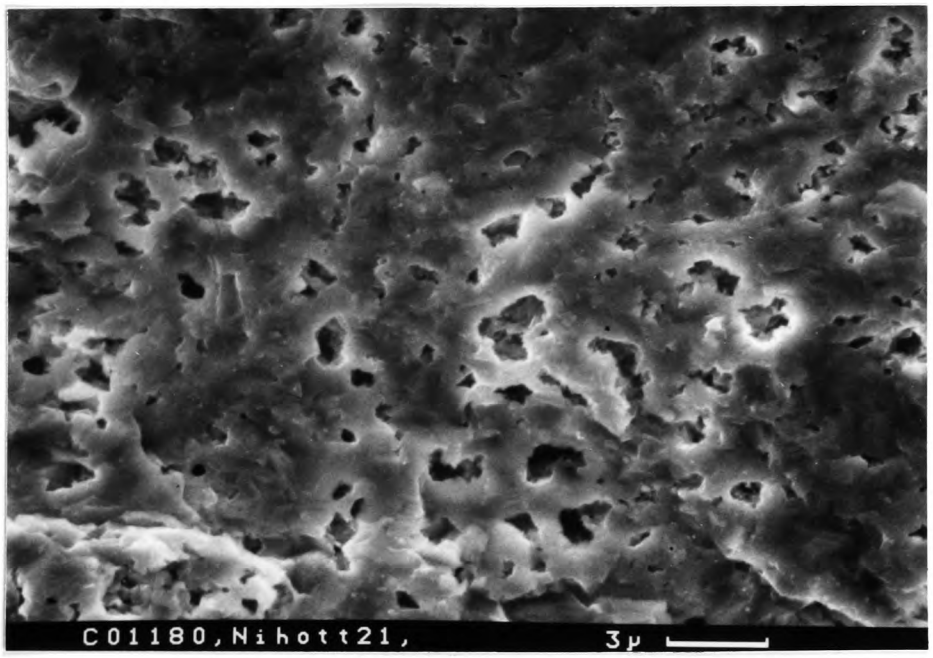

Figure 4.32: Secondary SEM micrograph of a fracture surface showing the pores in the equi-axed layer of a 19.5 μm thick NiO after oxidation in the bend test furnace at 900 °C.

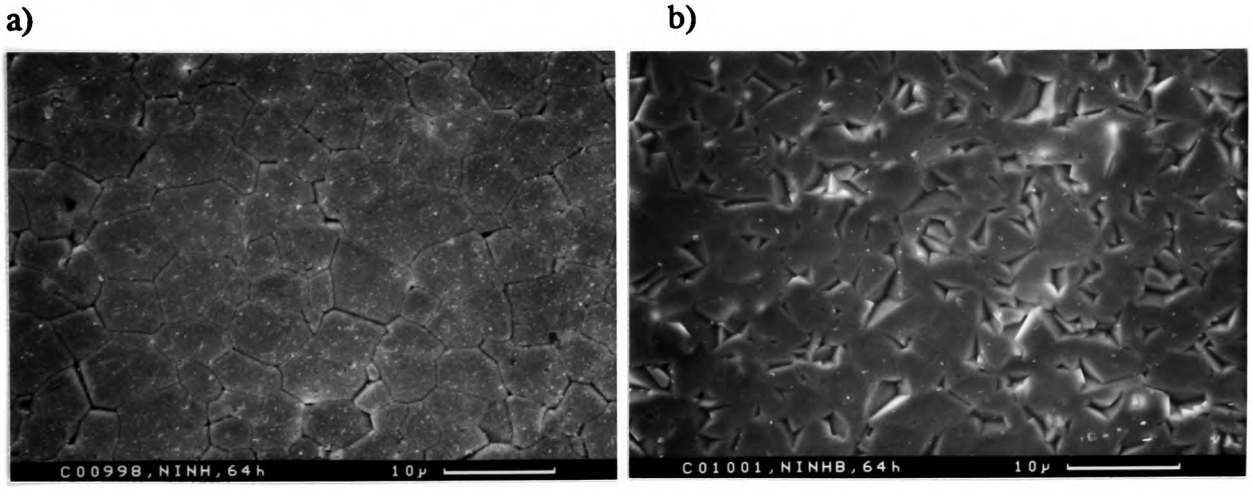

Figure 4.33: Secondary SEM micrographs showing the surface appearance of a 40 μm thick NiO after oxidation in a muffle furnace at 900 °C, (a) without and (b) with protective coating DPG 3582.

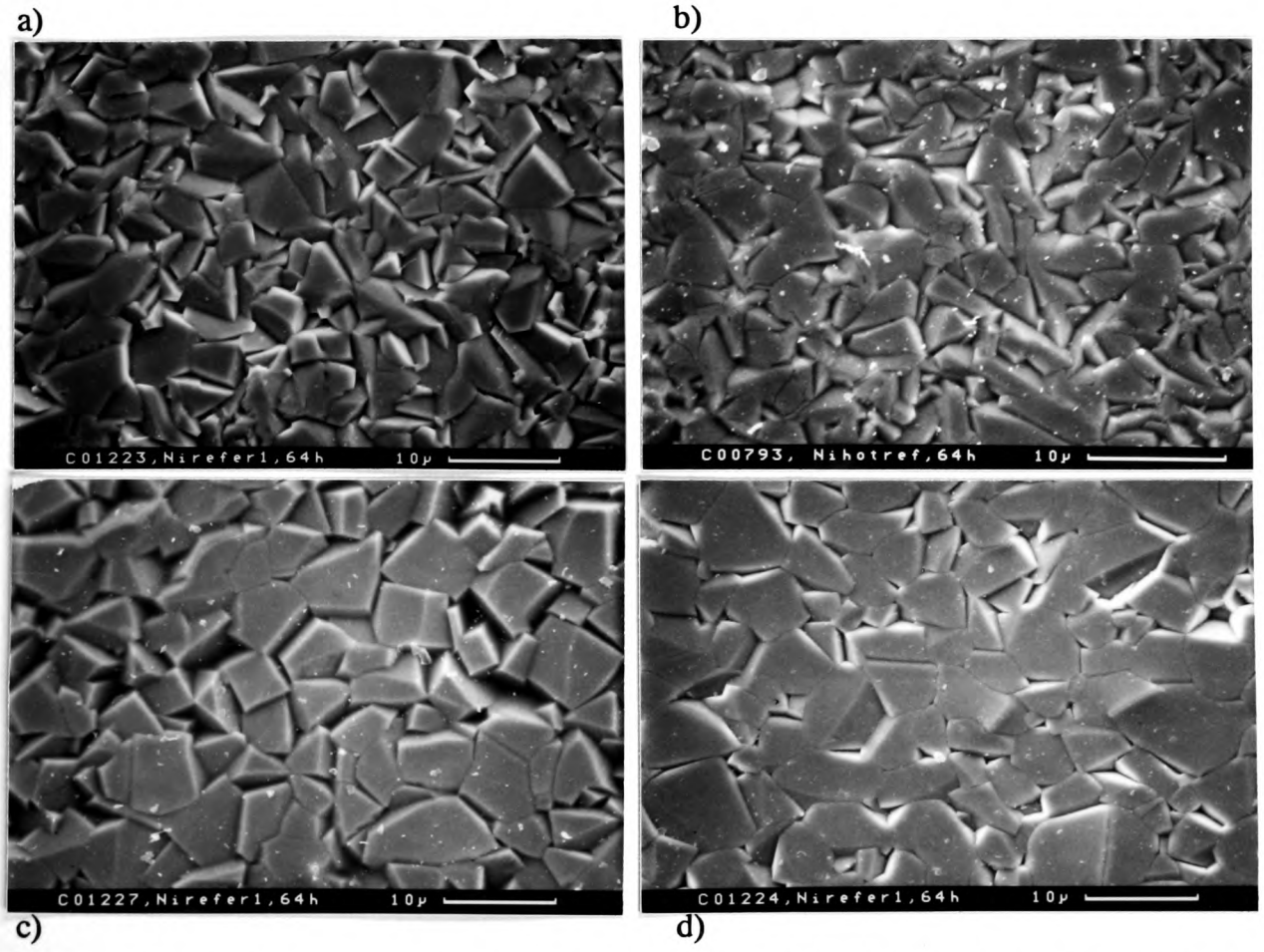

Figure 4.34: Surface appearance of a ~40 μm thick NiO after oxidation in the bend test furnace. (a) no coating - bottom side inside jig, (b) with coating, (c) no coating - top side inside jig, (d) no coating - bottom side outside jig.

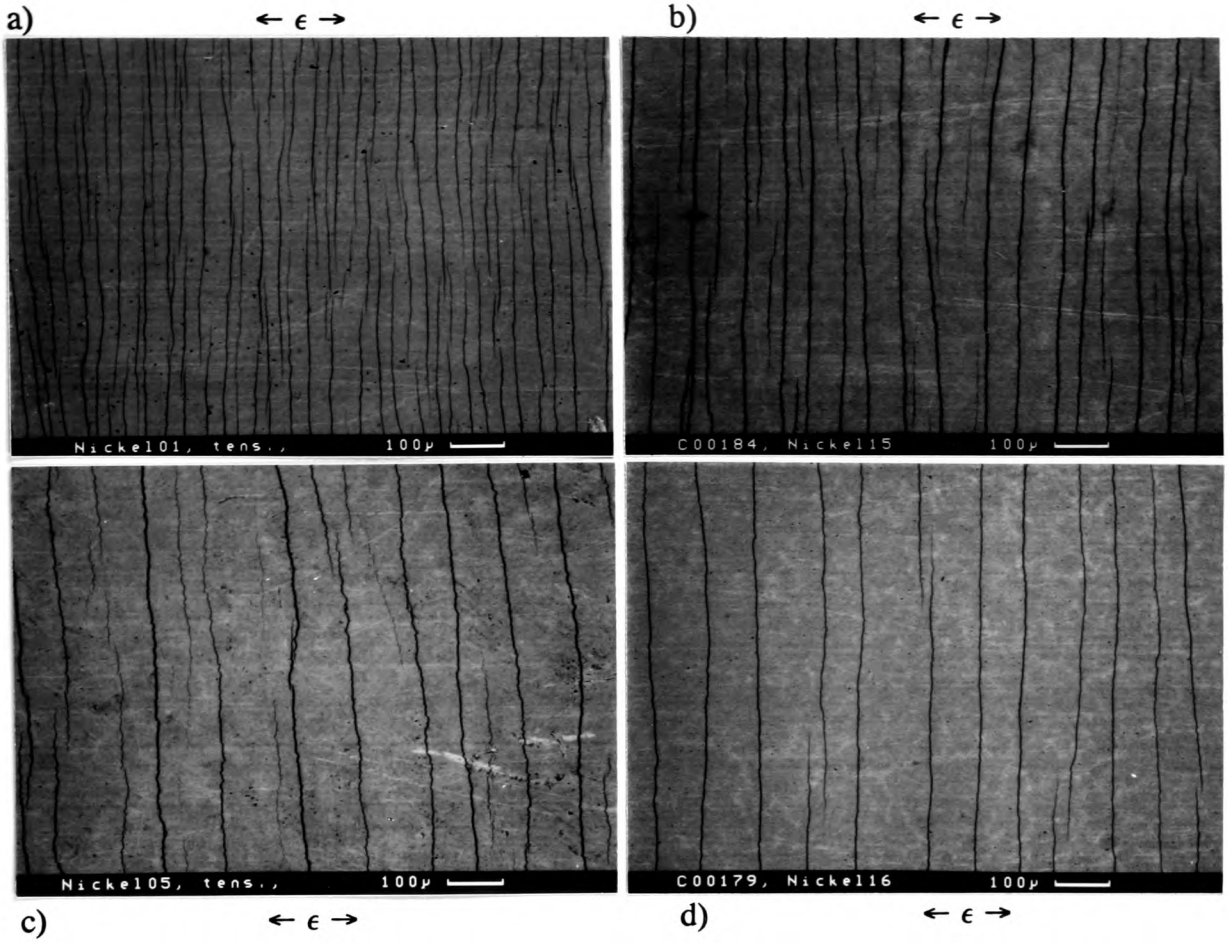

Figure 4.35: Backscattered SEM surface micrographs of tensile through-scale cracks in NiO after testing in tension at room temperature. (a) Thickness 7.5 μm, maximum strain 1.12%, (b) 19 μm, 1.12%, (c) 45 μm, 1.12% and (d) 19 μm, 0.56%.

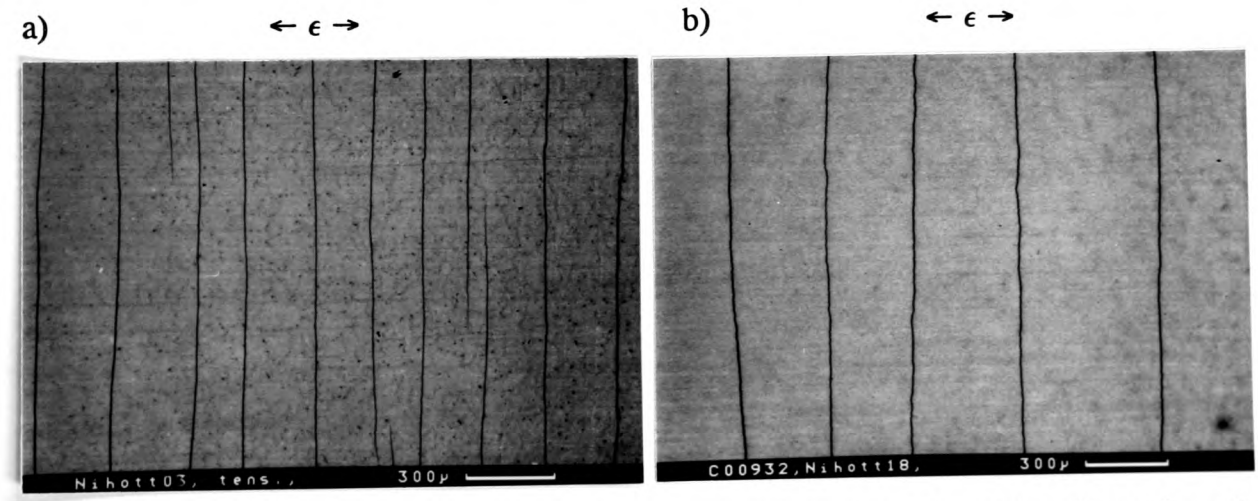

Figure 4.36: Backscattered SEM surface micrographs of tensile through-scale cracks in NiO after testing in tension at 900 °C. (a) Thickness 13.5 μm, maximum strain 1.12% and (b) 40 μm, 1.12%.

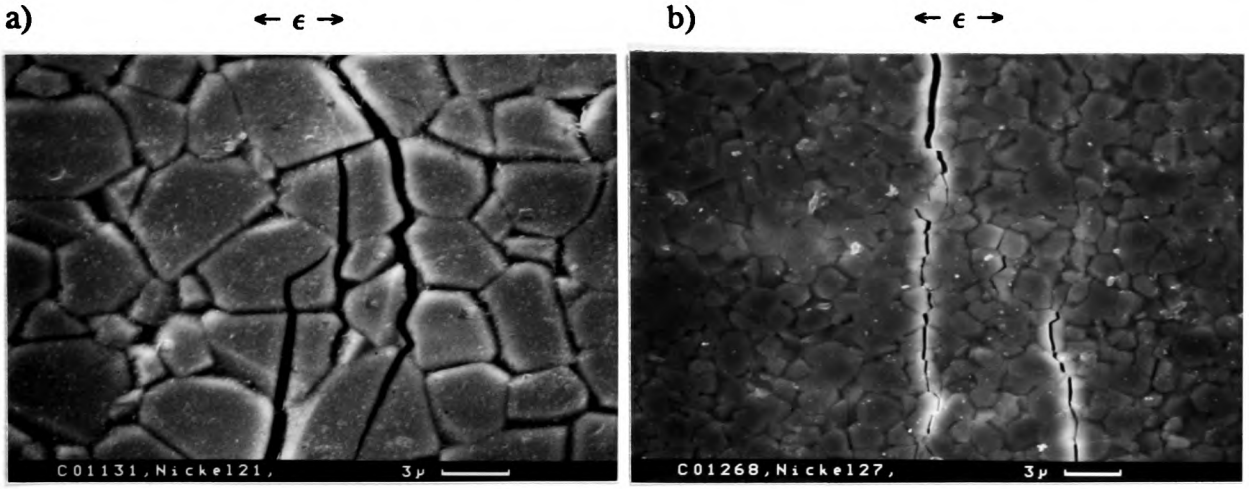

Figure 4.37: Secondary SEM surface micrographs showing crack tips in NiO after testing in tension at room temperature. (a) Oxide thickness 31 μm, maximum strain 1.12% and (b) 6.0 μm, 1.12%.

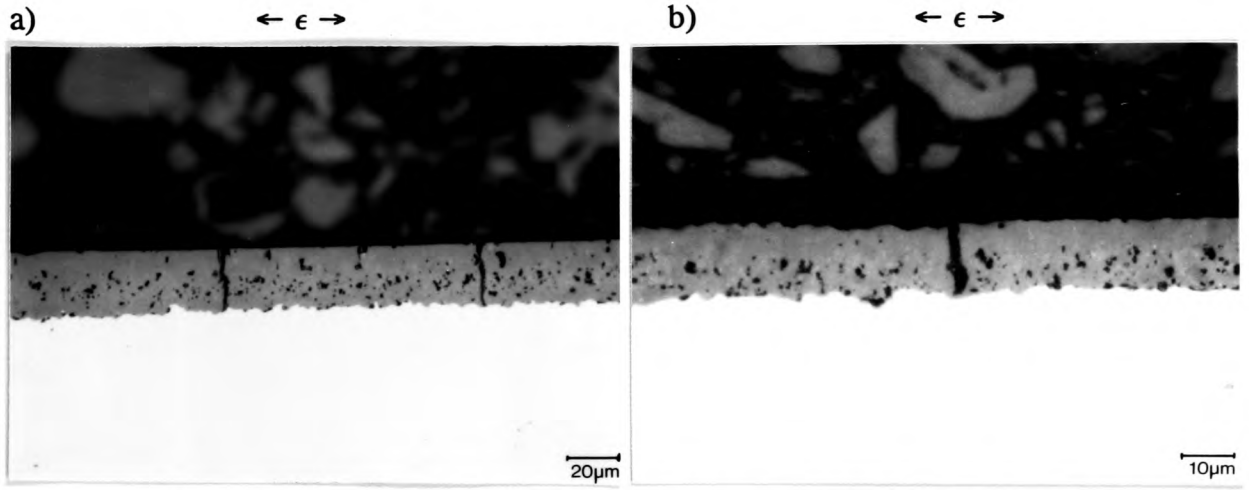

Figure 4.38: Optical micrographs of sections of equi-distant tensile cracks in NiO after testing in tension to a maximum strain of 1.12% (a) at room temperature, oxide thickness 27.5 μm and (b) at 900 °C, 13 μm.

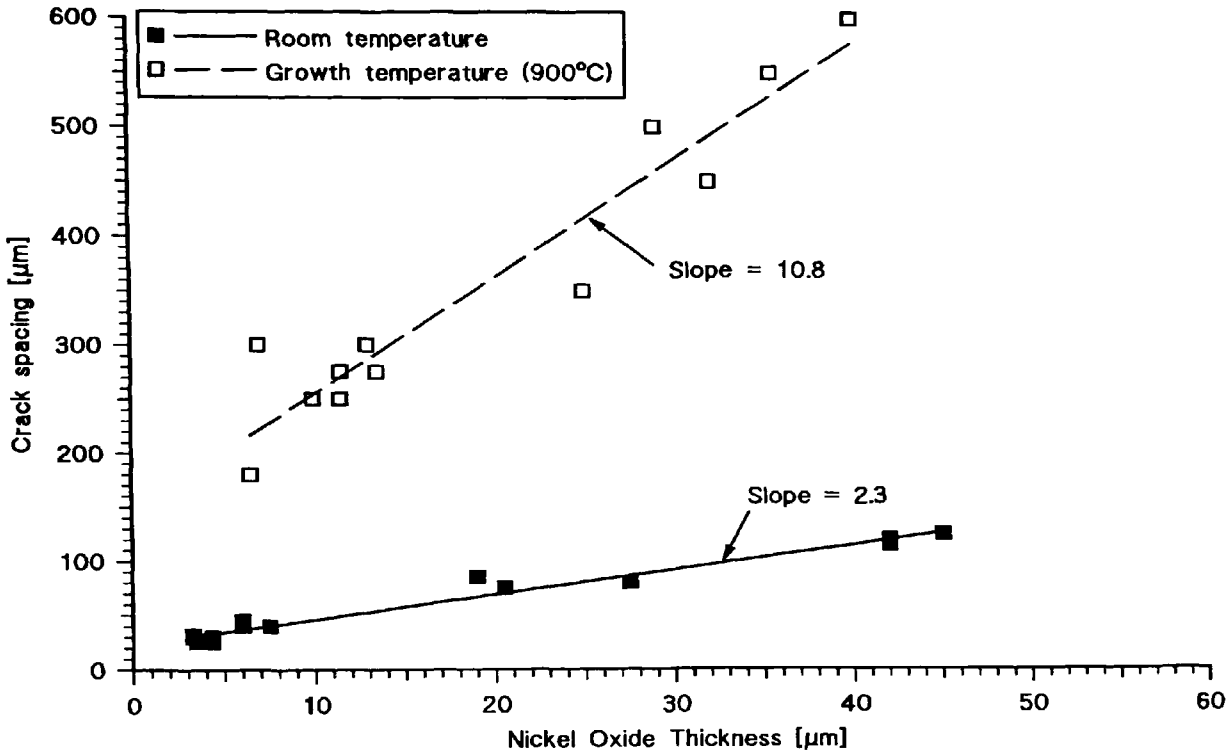

Figure 4.39: Crack spacing as a function of thickness for nickel oxides tested in tension at room temperature and at oxide growth temperature to a maximum strain of 1.12%.

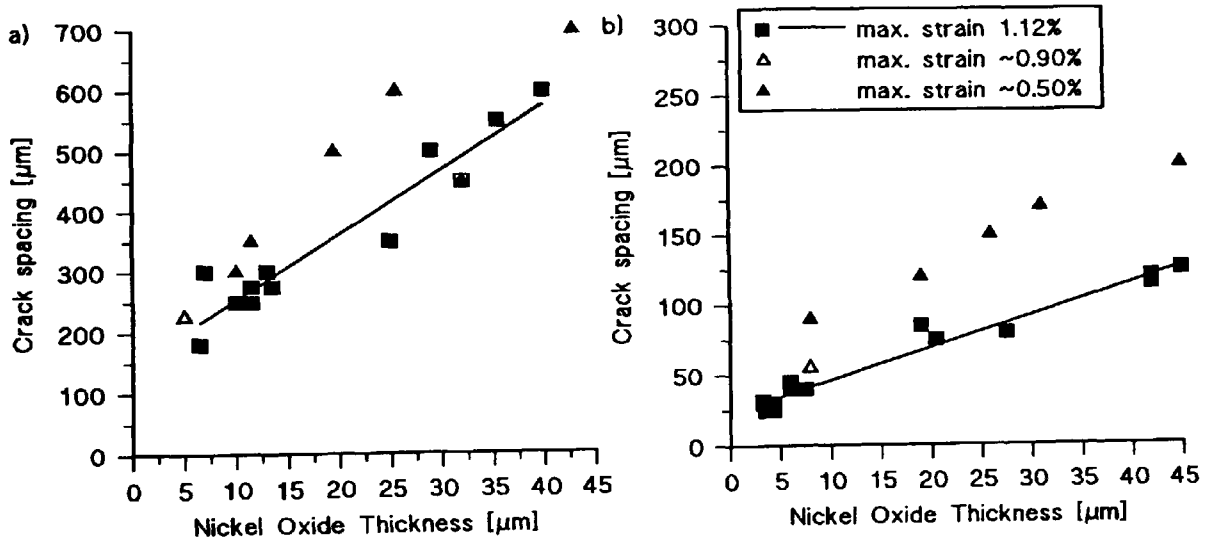

Figure 4.40: Plots showing the dependence of the crack spacing on the maximum strain for nickel oxides tested in tension (a) at growth and (b) at room temperature.

4.2.1.2 Correlation of AE with Strain and Crack Patterns

A typical plot showing the cumulative energy counts as a function of strain is given in Figure 4.41. The AE distribution with strain was the same for the tests at room and at growth temperature (Figure 4.42) and the results were very reproducible compared to iron oxide. The shape of the plots can be explained as follows:

Failure started with the creation of equi-distant cracks in the oxide which produced a maximum rate of AE. As the tests were continued, increasingly higher amounts of additional strain were required to produce further cracks due to elastic stress relaxation (see also section 4.3.1) and plastic stress relaxation (see also section 4.4.1). Thus the rate of AE decreased slowly, but did not stop. In none of the tests was there an increase of AE towards the end of the tests confirming the earlier observations regarding the lack of interface delamination.

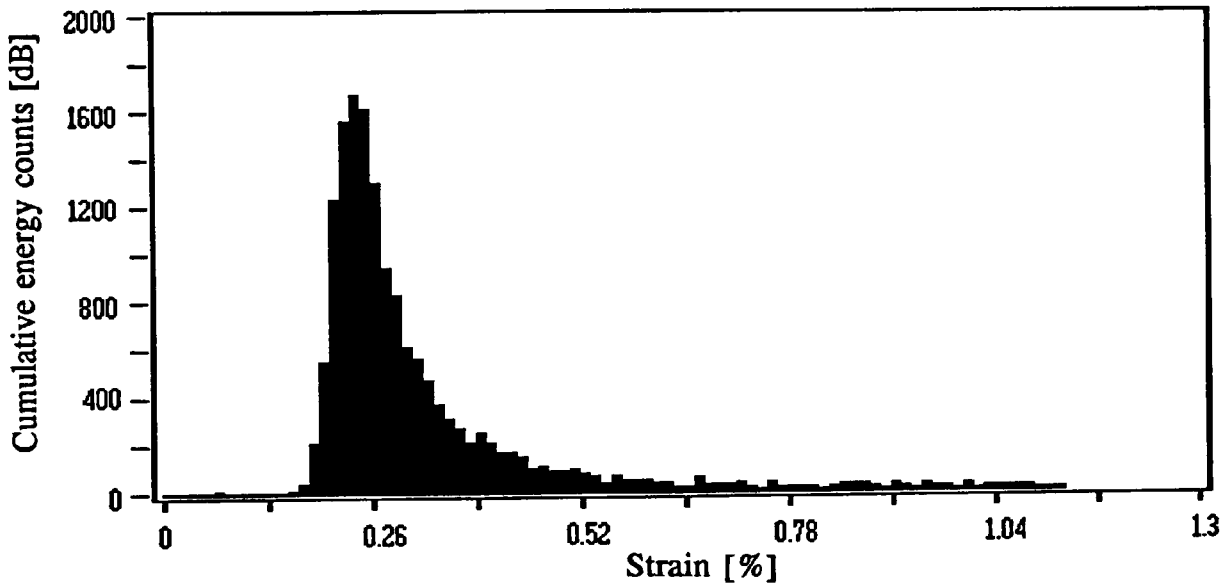

Figure 4.41: Histogram of the cumulative energy counts as a function of strain for a 7.5 μm thick NiO tested in tension at room temperature.

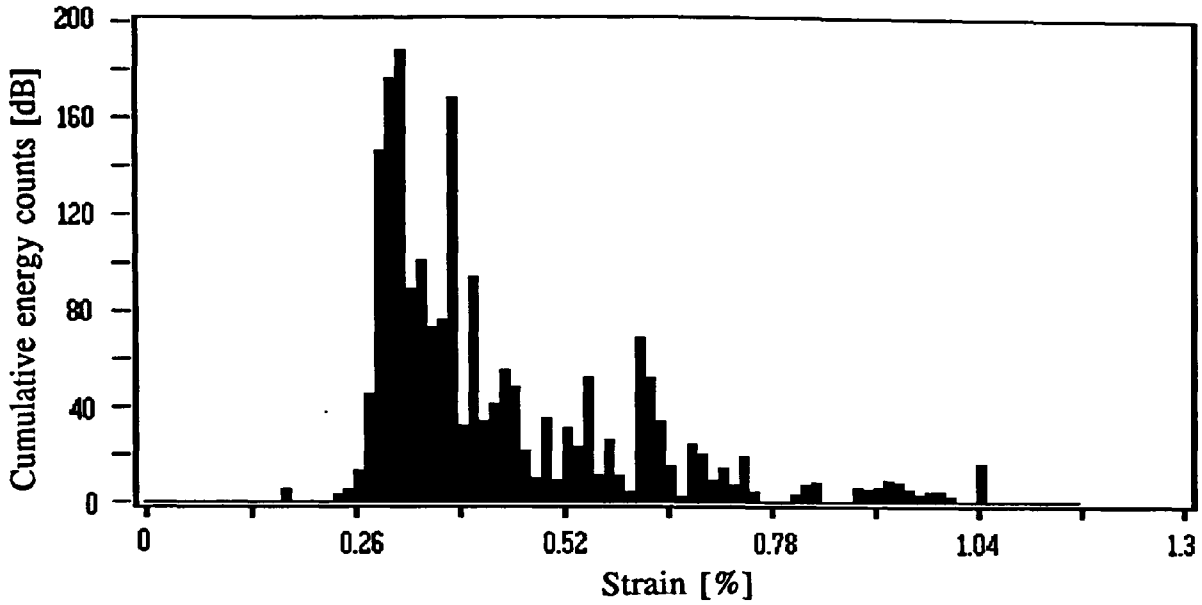

Figure 4.42: Histogram of the cumulative energy counts as a function of strain for an 11.5 μm thick NiO tested in tension at oxide growth temperature.

4.2.1.3 Relationship between AE Parameters and Oxide Thickness

The analysis was carried out at a strain level of 0.30% above the measured failure strain in order to allow a comparison with iron oxide.

The AE parameters increased with increasing thickness, which could be explained by the higher energy release during failure of thicker scales (Figure 4.43). The average AE energy counts per signal were similar for the tests at room and at growth temperature. However the cumulative energy count number was higher for the tests at room temperature because the number of recorded signals was much higher, which was due to the lower threshold used for the tests at room temperature and/or the higher number of cracks since the spacing was lower at room temperature (see also section 4.2.1.1, page 134).

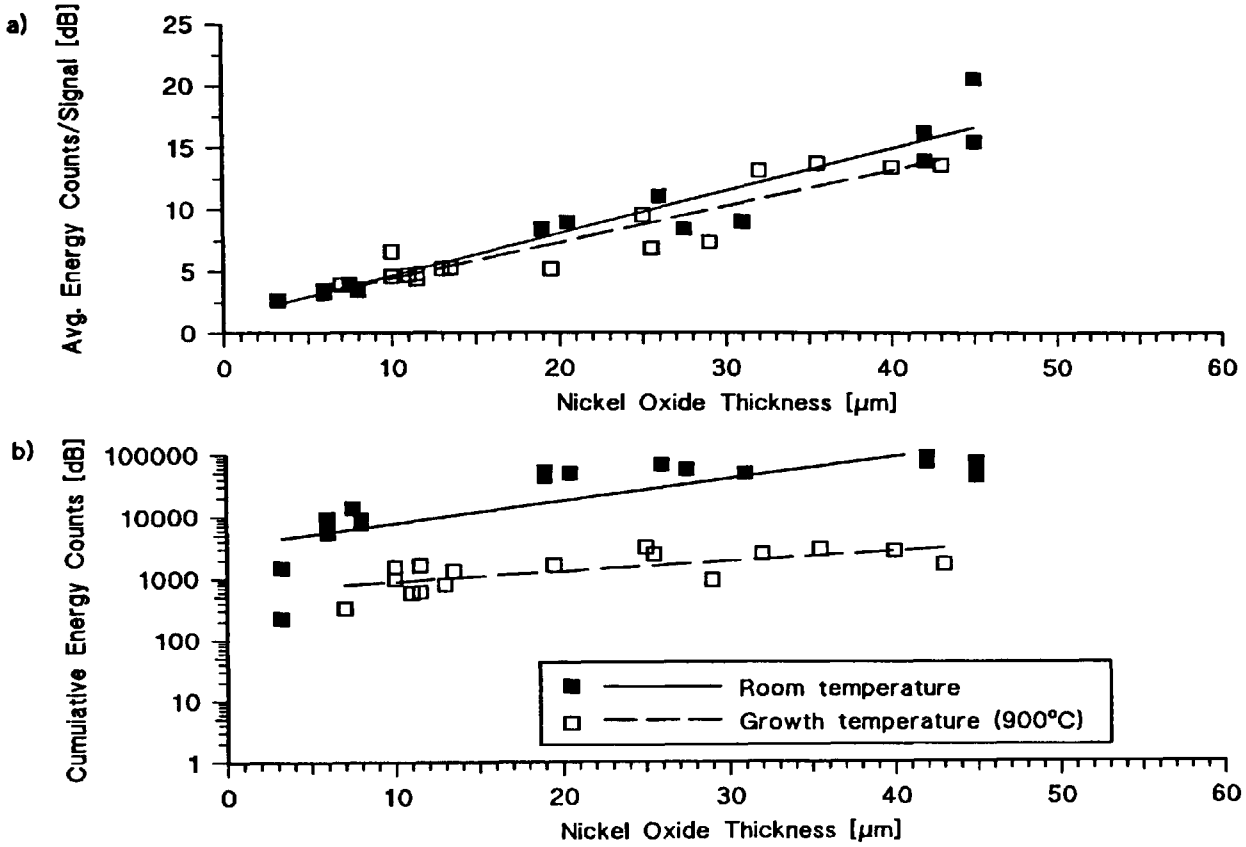

Figure 4.43: (a) Average energy counts/signal and (b) cumulative energy counts as a function of thickness for nickel oxides tested in tension. Analysed at a tensile strain of 0.30% above that for first failure.

4.2.1.4 Oxide Failure Strains

The work on iron oxide had shown that macroscopic failure is marked by the occurrence of a high rate of AE or high energy AE signals and the first incidence of such events was used to calculate critical failure strains.

The measured failure strains are shown in Figure 4.44 together with the best fit power-law curve assuming the behaviour is governed by linear elastic fracture mechanics (equation (2.12), page 39). As shown by the work on iron oxide in section 4.1.1.4 (page 118), comparison with fracture mechanics predictions depended strongly on the measured composite void size. For NiO the thickness of the equi-axed layer was used as a composite void size, because most of the voids were contained in this layer and these voids were found to interact mutually when applying the interaction rules given by Nicholls and Hancock [2]. A composite void size of 0.4 h was used for all nickel oxide scales and hence failure strains could simultaneously be plotted as a function of thickness or composite voids size.

Fracture strains at growth temperature were within the variation of 0.2 - 0.3% found by Barbehön [18] in NiO scales between 14 and 54 μm thick when tested at a

lower temperature of 800 °C but with a higher strain rate of $4x10^{-4}$ s^{-1}. However, they were higher than those at room temperature and this was assumed to be due to oxide creep (Figure 4.44). Indeed Schütze [9] predicted creep in NiO having defects < 5 - 10 μm when strained at a rate of ~ 10^{-4} s^{-1} at 900 °C, which gave a ratio of T/T_m of ~0.5 where T_m is the melting temperature of NiO of 2260 K (cf. Figure 2.1, page 36). Figure 4.31 and Figure 4.32 (page 136) show defects of the order of 1 - 3 μm; however defects are also expected to grow and coalesce during creep and thus failure occurred after a certain amount of creep when the defects exceeded a critical size. Careful examination of Figure 4.44 indicated that the difference between the measured failure strains at room and at growth temperature increased as the oxide thickness decreased as would be expected if controlled by creep processes, since thinner films had higher creep rates and it also took longer for the defect size to reach critical values. Further confirmation of the importance of creep in nickel oxide was obtained by conducting a test with a 13 μm thick oxide at a higher strain rate of $4x10^{-4}$ s^{-1} and the failure strain was found to be 0.27%, which is approximately half-way between the room and growth temperature failure strain, i.e. creep was reduced by one half when using the higher strain rate.

The different surface appearance after oxidation in a muffle furnace or after oxidation in the bend test furnace with DPG 3582 coating did not affect cracking and the measured failure strains at room temperature were within the normal variation (Figure 4.44).

The experimental data were also used to determine fracture toughness values, K_{IC}. Plots of the form σ_e as a function of $1/(\pi c)^{0.5}$, where σ_e is the failure stress are shown in Figure 4.45. The slope of the lines gave the K_{IC}-values whereas the intercept on the stress axis gave a measure of the residual stress present in the oxide (see also equation (4.2), page 120). A K_{IC}-value of 0.41 MN $m^{-3/2}$ was obtained in the tests at room temperature using a Young's modulus value of 190 GPa for room temperature [3]. The same value was used for 900 °C and this gave a K_{IC}-value of ~1.61 MN $m^{-3/2}$ for the growth temperature tests which was much higher, as would be expected from materials showing creep. Furthermore the K_{IC}-value for 900 °C is likely to be an overestimate due to the use of room temperature Young's modulus data. Both values were considerably smaller than the values of 2 - 6 MN $m^{-3/2}$ quoted for NiO on 99.2% pure nickel at 800 °C [9]. In this work void interaction for the determination of the composite void size was considered critical only in the direction normal to the applied stress in contrast to previously published data [2,9] (see also section 2.1.3, page 50) and thus the values derived from Figure 4.45 would be expected to be 2 - 4 times smaller. A compressive residual stress of 175 MPa was derived from the intercept in Figure 4.45 which is approximately the same as the growth stress quoted by Pivin *et al.* [51] but recent work by Liu *et al.* [52] showed that residual compressive cooling

stresses could be between 0 and 500 MPa for different nickel samples. Similarly, compressive residual stresses of 150 and 350 MPa were found for 25 and 45 μm thick nickel oxide scales, respectively, by X-ray strain measurement.

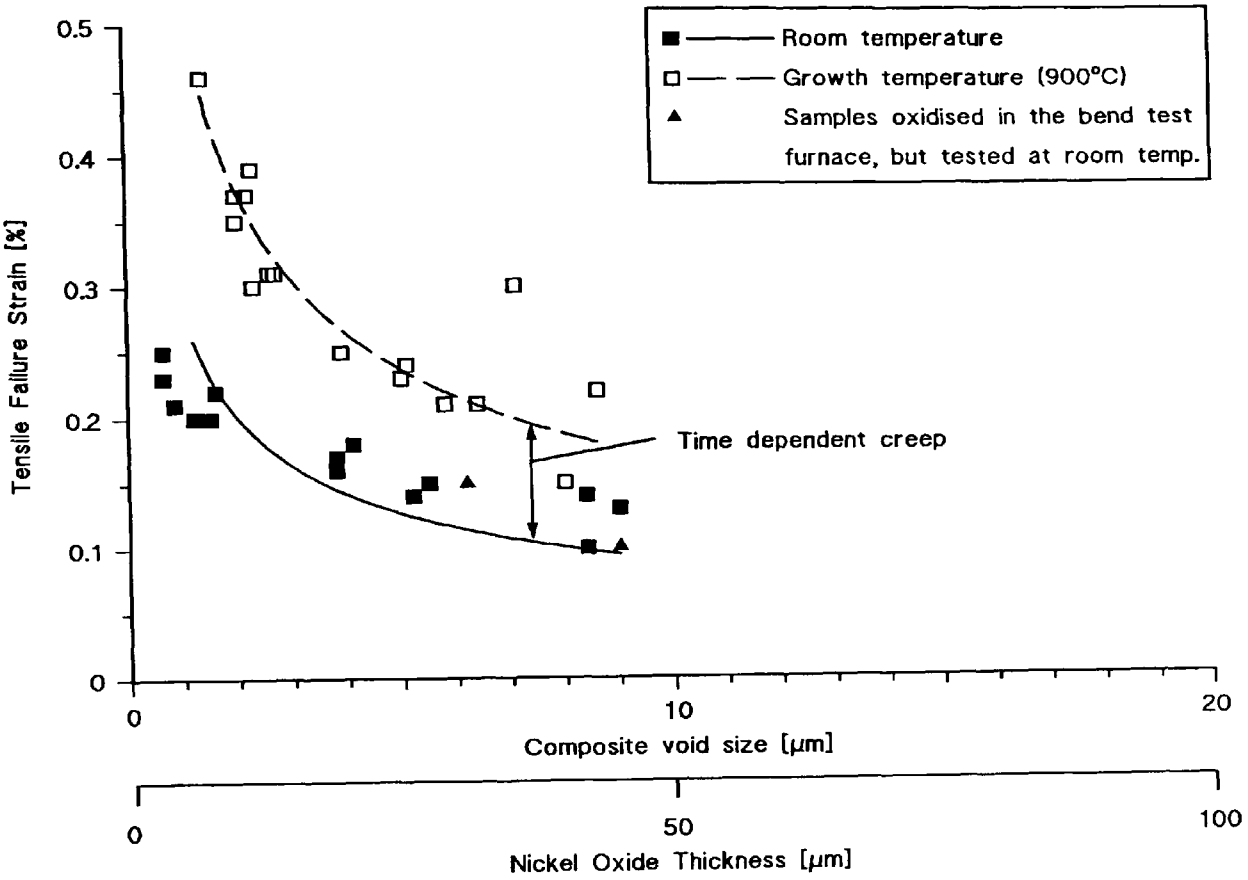

Figure 4.44: Measured failure strains as a function of thickness or composite void size for nickel oxides tested in tension at room and at oxide growth temperature.

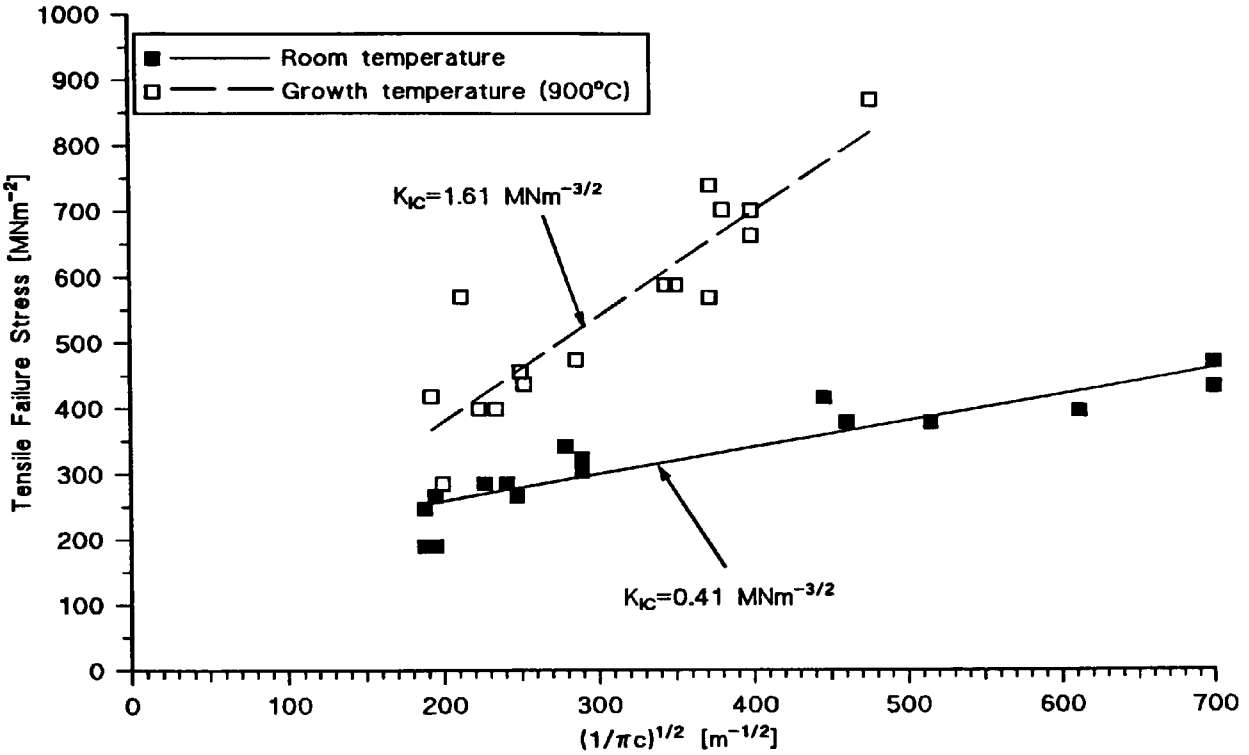

Figure 4.45: Fracture stress as a function of void size giving K_{IC} and residual stress σ_r for nickel oxides tested in tension at room and at oxide growth temperature.

4.2.2 Tests with Nickel Oxide in Compression

Tests were made at room temperature and at growth temperature. The strain to cause macroscopic failure at growth temperature was above 2.8% and could not be measured using the technique because it was not possible to apply strains >2.8% with the bend test furnace rig. Similarly, Barbehön [18] found such high strains (>2.8%) for macroscopic failure in nickel oxides <50 μm thick even with a much higher strain rate of 10^{-3} s^{-1} and a lower deformation temperature of 800 °C. In contrast, a recent study showed critical strains for microcracking of the order of 1 - 2% for NiO up to 800 °C using strain rates of $8x10^{-7}$ and $8x10^{-8}$ s^{-1}, although subsequent macrocracking and spallation required much higher strains of 6 - 12% at elevated temperatures [81]. In the present study AE from microcracking could not be detected because of the high set threshold at 900 °C. Hence no AE or macroscopic failure was expected nor observed at strains of <2.8%. In fact the actual strain for cracking could be much higher than 2.8% as shown above. The following sections 4.2.2.1 to 4.2.2.4 inclusive refer to the failure of NiO in the tests at room temperature.

4.2.2.1 Crack Patterns

Fracture zones on the surface were at an angle +/- 45° relative to the direction of applied stress, which is indicative of shear failure. These zones had a regular spacing and formed a diagonal network (Figure 4.46). The patterns can be attributed to shear deformation or failure of the oxide following the slip systems of the underlying substrate next to the interface because of the interface constraint. Failure started along these zones with microcracking (Figure 4.47). The affected oxide area either buckled at higher strains (Figure 4.46d and Figure 4.48a) or showed shear cracks within the oxide along which the oxide was wedged out (Figure 4.46c and Figure 4.48b). Subsequent spallation was mainly observed in thicker oxides because thinner oxides were only in the first stages of failure when the deformation was stopped at a strain of 2.8% due to the dependence of the strain to failure on oxide thickness. The width or size of the fracture zones increased with increasing oxide thickness (Figure 4.49). This change in size could be explained by considering the oxide as a plate. Buckling required a certain deformation curvature. However the buckling resistance of a plate increases with the square of the thickness for a given width. Thus as the thickness increased, growth of the delamination became energetically more likely than an increase in curvature. Hence the size of the buckles and the spacing increased with thickness but their numbers decreased.

Cross-sections were difficult to prepare because of pull-out of grains which were almost completely surrounded by microcracks. However, the observations on microcracking, shear cracking and delamination were confirmed in general (Figure 4.50).

Fracture surfaces and cross-sections through spalled or detached oxide areas confirmed that shear cracks under 45° were formed in the oxide (Figure 4.50 and Figure 4.51). The path of the shear cracks changed quite often near the columnar layer depending on whether further crack growth proceeded in a transgranular or intergranular manner. In this context the shear strength of the columnar oxide grains appeared to be higher than that of the grain boundaries, because cracks followed the grain boundaries rather than proceeding stepwise through the columnar grains as depicted in Figure 4.46e and Figure 4.51

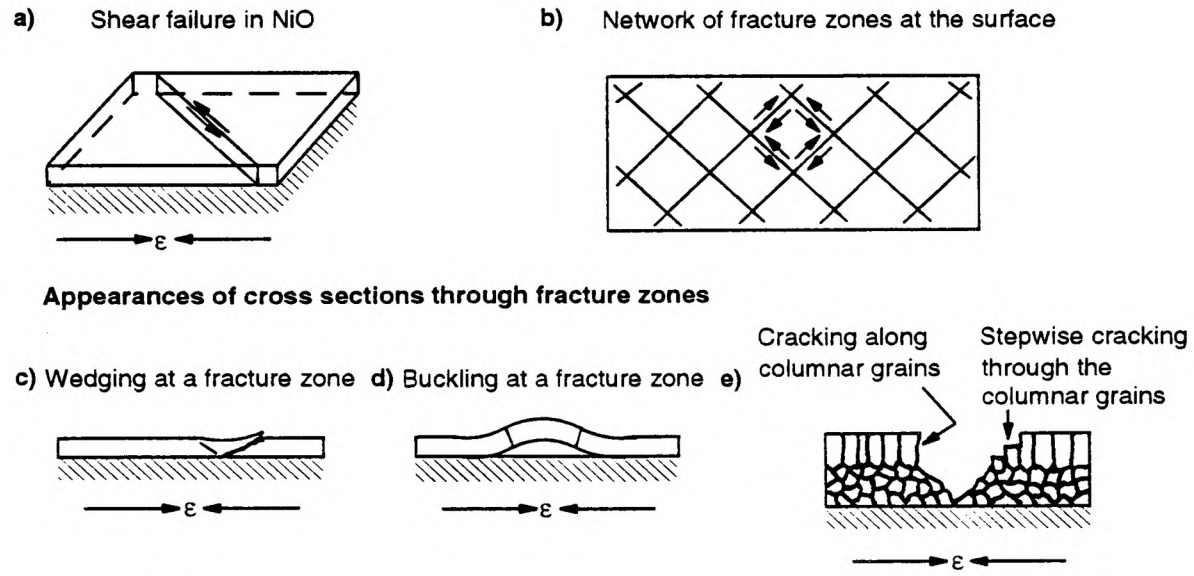

Figure 4.46: Schematic diagram of the observed failure mechanism in nickel oxide under compression.

→ ε ←

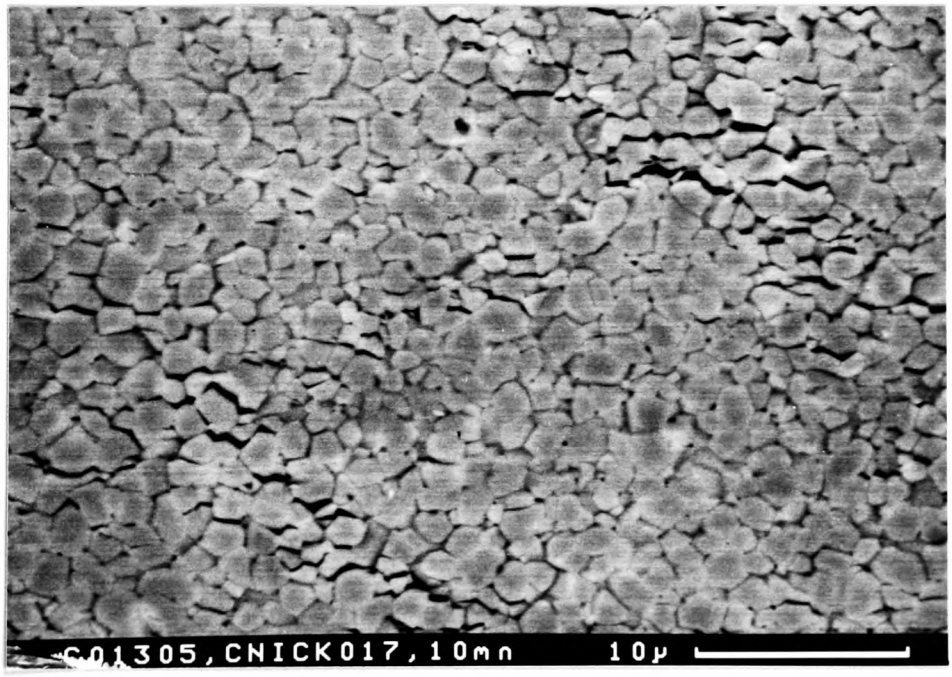

Figure 4.47: Backscattered SEM surface micrograph showing the microcracks along the fracture zones in a 6 μm thick NiO after testing in compression at room temperature to a maximum strain of 2.8%.

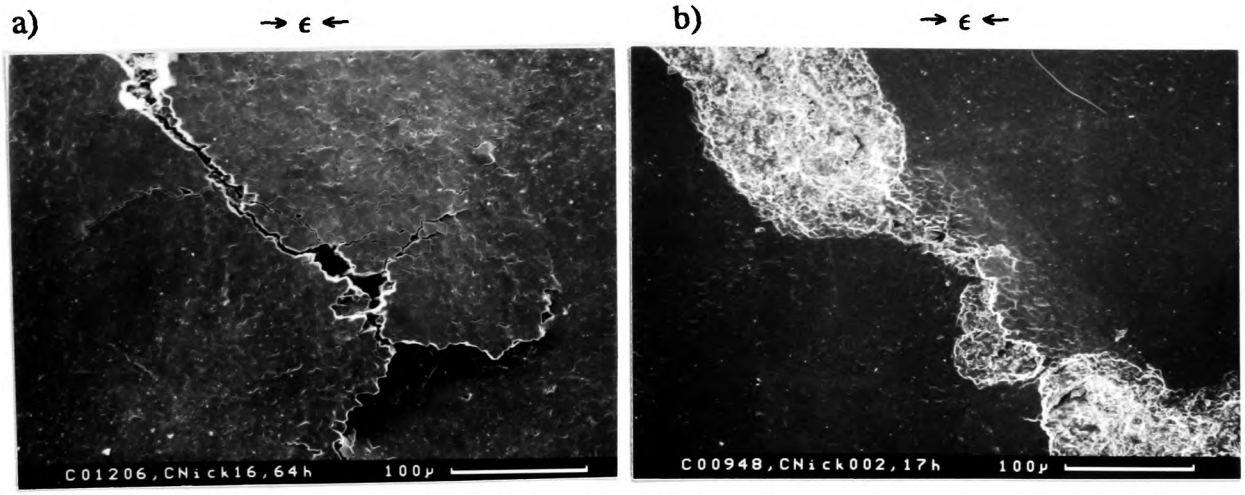

Figure 4.48: Backscattered SEM surface micrographs showing (a) a buckled NiO area (thickness 57.5 μm, maximum strain 2.8%) and (b) shear cracking and wedging (37.5 μm, 2.8%) along the fracture zones.

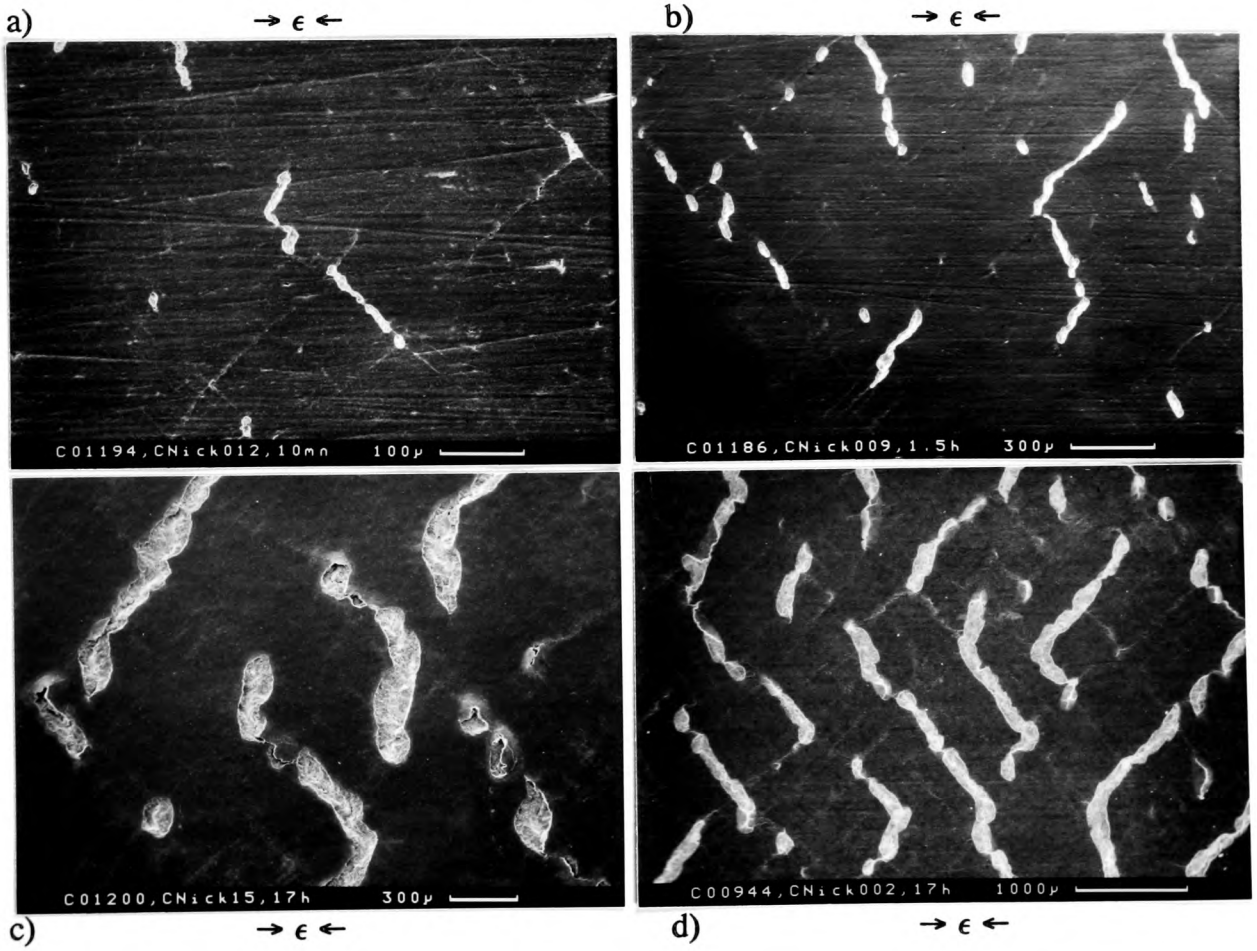

Figure 4.49: Backscattered SEM surface micrographs showing the fracture zones and spalled areas in NiO after testing in compression at room temperature. (a) Thickness 3.5 μm, max. strain 2.8%, (b) 9 μm, 2.8%, (c) 32 μm, 2.8% and (d) 37.5 μm, 2.8%.

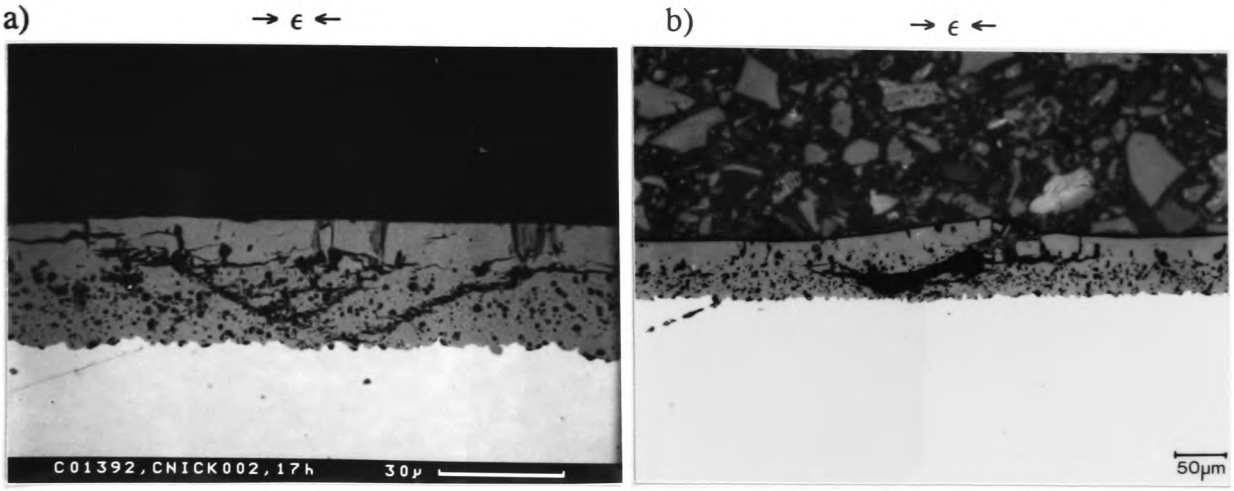

Figure 4.50: Optical micrographs of cross-sections showing shear cracks and delamination within the NiO after testing in compression at room temperature. (a) Oxide thickness 37.5 μm, maximum strain 2.8% and (b) 57.5 μm, 2.8%.

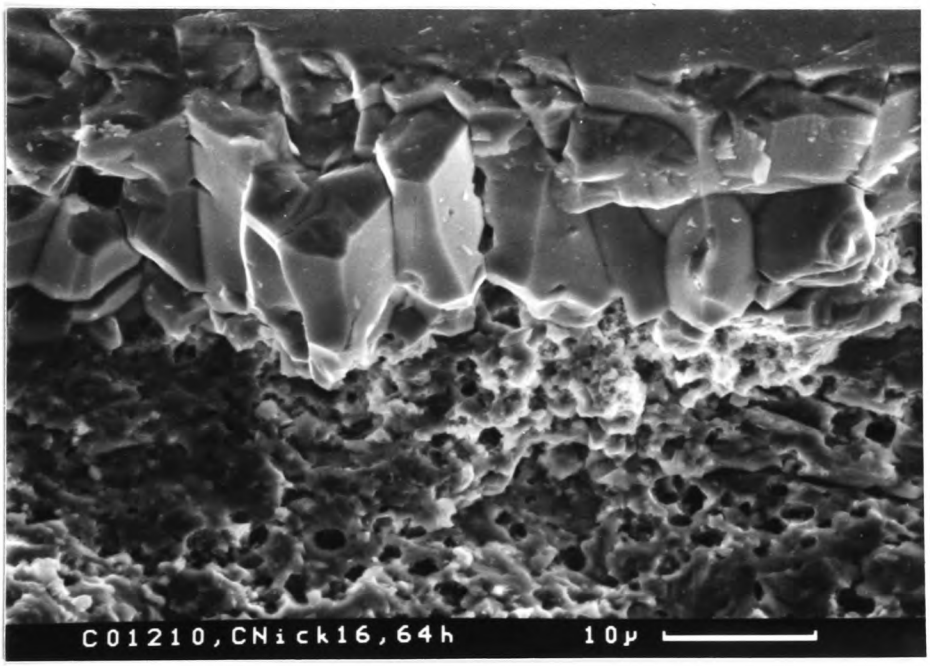

Figure 4.51: Secondary SEM micrograph showing the fracture surface of a spalled NiO area after testing in compression at room temperature. Oxide thickness 57.5 μm, maximum strain 2.8%.

4.2.2.2 Correlation of AE with Strain and Crack Patterns

Figure 4.52 shows a typical histogram of the cumulative AE energy counts as a function of applied strain. The number of energy counts increased with increasing strain as with iron oxide. The increase was also found with other AE parameters such as cumulative AE counts, number of signals or amplitude and was explained by the build-up of elastic strain energy during loading and its subsequent release during failure, since failure became more likely as the strain in the oxide increased as was the case with iron oxide. Generally, relatively few AE signals were recorded considering the high number of microcracks (cf. Figure 4.47, page 148) and the amount of spallation (cf. Figure 4.49, page 149). Thus it was believed that AE, from the smallest sources such as microcracking or small incremental crack growth, did not exceed the threshold and was thus not monitored as was the case in the tests at oxide growth temperature (see also section 4.2.2, page 146).

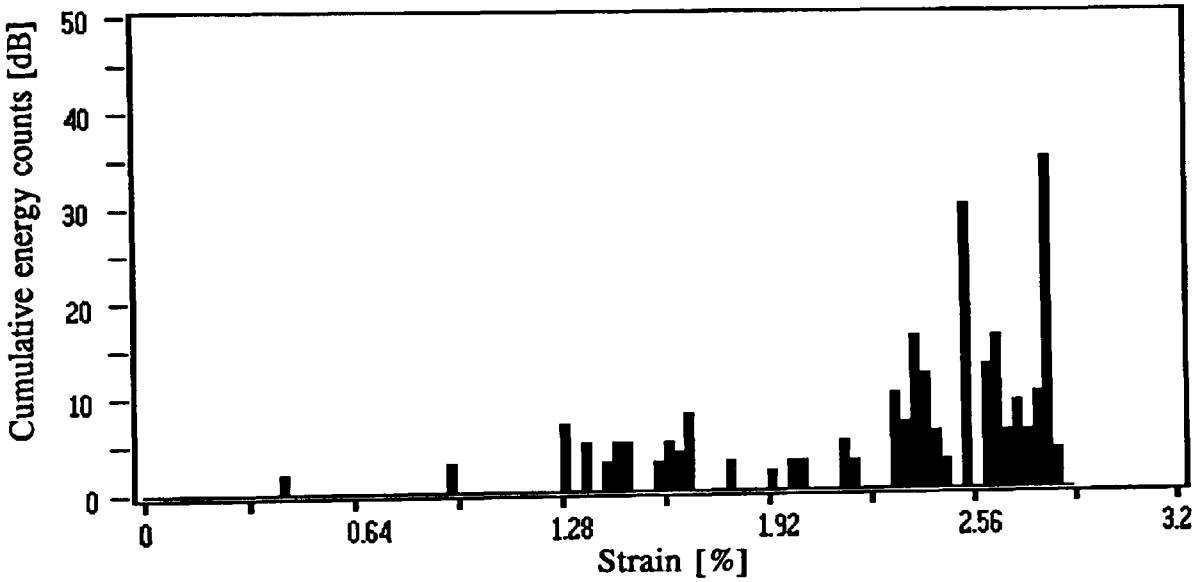

Figure 4.52: Histogram of the cumulative energy counts as a function of strain for a 6.0 μm thick nickel oxide tested in compression at room temperature.

4.2.2.3 Relationship between AE Parameters and Oxide Thickness

A larger strain increment of 0.75% above the failure strain (compared to the analysis with iron oxide) was chosen for this analysis, firstly because it equated to the same percentage of the higher total strain of 2.8% and secondly, because only the higher strain increment produced a significant number of signals for an analysis since the number of AE signals per unit strain increase was much lower than for iron oxide.

Figure 4.53 shows the results of the analysis in the form of cumulative and average energy counts as a function of oxide thickness. The increase of both parameters

could be explained by the dependence of AE on crack length and depth, i.e. fracture surface. The newly created fracture surface was larger in thicker oxides because microcracks and shear cracks which formed at the beginning of the failure process were longer and deeper in thicker oxides. A similar dependence was found with brittle lacquer in compression and in all tensile tests (see also section 4.4.1).

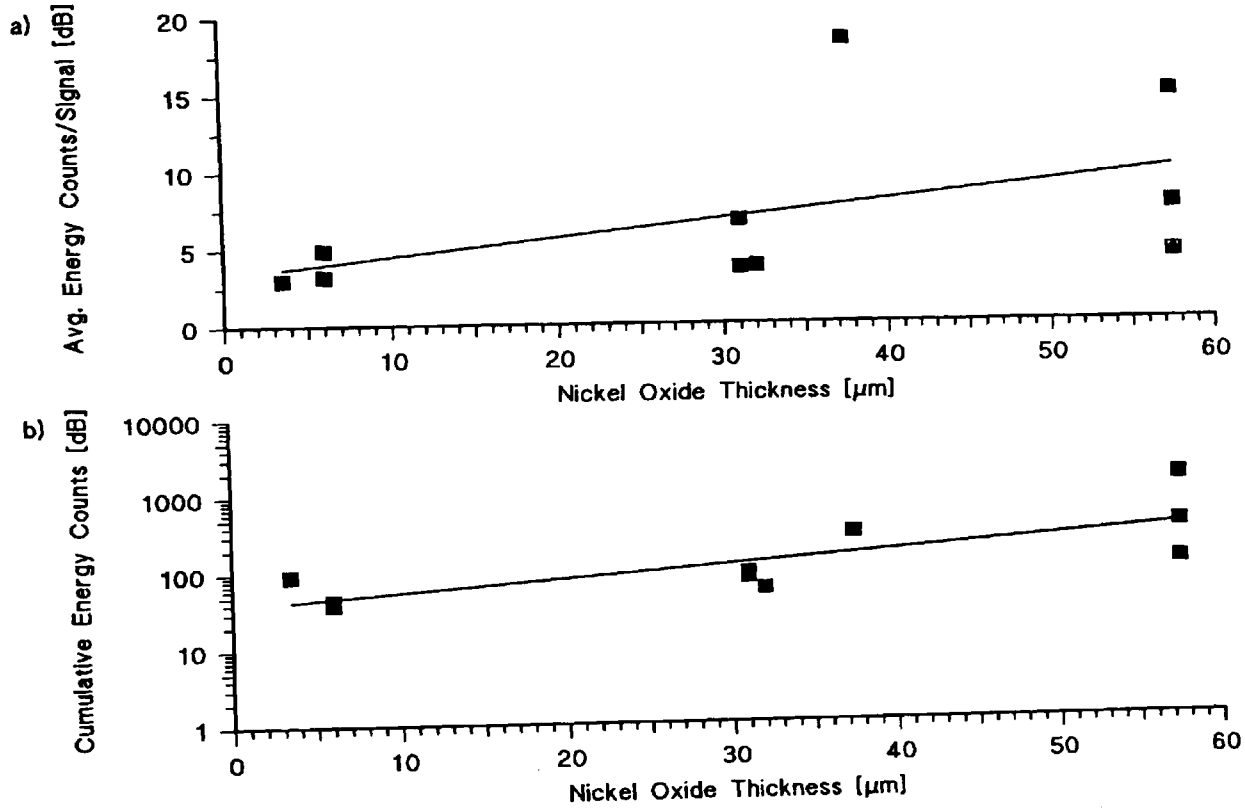

Figure 4.53: (a) Average energy counts/signal and (b) cumulative energy counts as a function of thickness for nickel oxides tested in compression. Analysed at a compressive strain of 0.75% above that for first failure.

4.2.2.4 Oxide Failure Strains

The measured failure strains (Figure 4.54) were compared with predictions based on Route I (wedging) failure because the failure proceeded in the same two stages, i.e. shear crack growth in the oxide at the initiation stage and propagation of an interface crack or a crack parallel to the interface at the spallation stage. The initiation condition (equation (2.23), page 46) is governed by the length of the initial shear crack, which could not be assessed and bore no relation to oxide thickness. Therefore the measured failure strains, i.e. the strain at which AE started, were compared with the model predictions for spallation or interface crack growth (equation (2.24), page 46) even though the first recorded AE might have corresponded to the initiation stage or any intermediate stage prior to spallation. Cracking preceded spallation which has been

confirmed by earlier observation on iron oxide (see section 4.1.2, page 123) and by other researchers [91,92]. Using values of 190 GPa for E for NiO and 0.3 for ν from ref. 3 in equation (2.24), the best-fit suggested an energy release rate of 385 J m^{-2} for a stress free oxide at the start of the test. This value was several times higher than the expected value of up to 40 J m^{-2} and it appeared that microcracking processes which occurred at the beginning of the failure process produced some stress relaxation without resulting in macroscopic failure. The deformation of the film appeared therefore pseudo-elastic, with a reduced Young's modulus where microcracking accounted for most of the deformation as postulated by Barbehön [18] (see also section 2.1.2.2, page 35). The actual elastic part of the deformation might have been as little as 0.2 - 0.5% as for iron oxide. Using a reduced Young's modulus or just the pure elastic part of the deformation in the best-fit would give a smaller energy release rate (see also section 4.4.2).

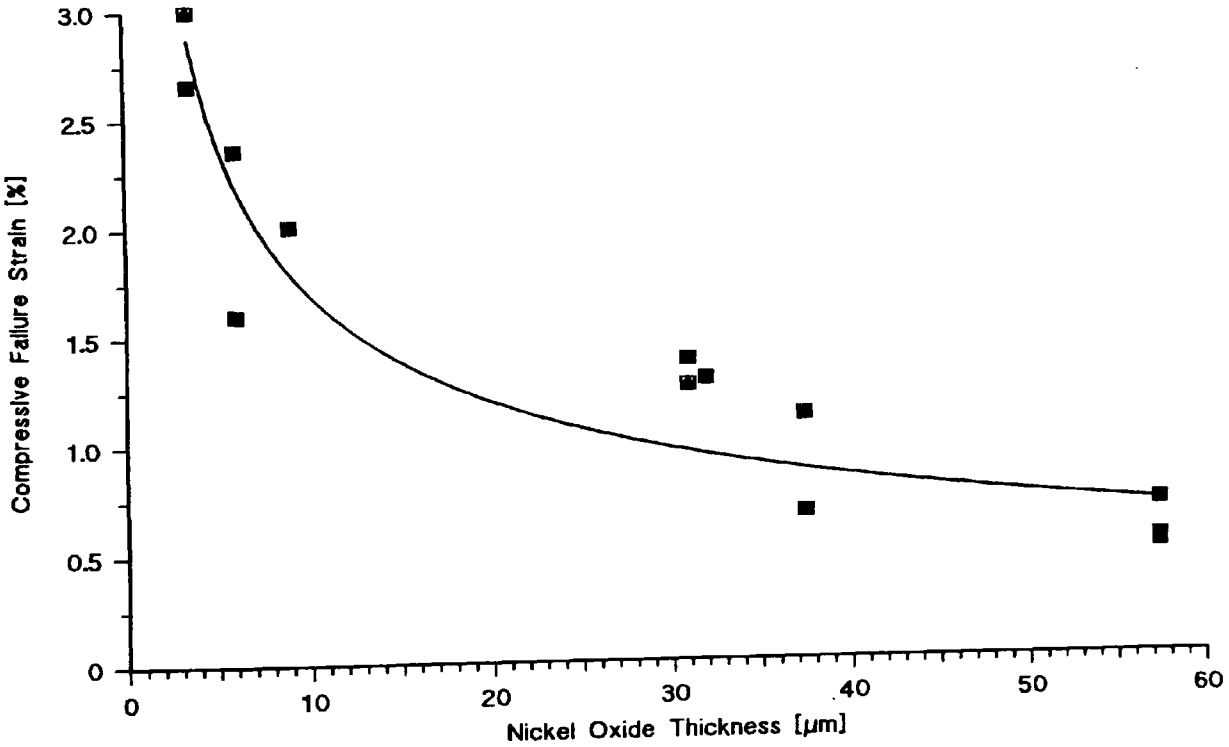

Figure 4.54: Measured failure strains for nickel oxides tested in compression at room temperature together with the best power-law fit.

4.3 Tests with Brittle Lacquer

To date, the different AE signal shapes found by Hall *et al.* [21] have only been observed in tests with oxide. It was therefore necessary to verify whether similar observations can be made with a different material when it is strained to failure under the same conditions. Only then could the observations be confirmed as a general phenomenon. The material should show the same brittle fracture patterns as oxide, and brittle lacquer was chosen as such a material because of its known brittle failure characteristics.

Test Programme:

Layers between 75 and 180 μm thick were tested in tension and compression at room temperature using a strain rate of $\sim 10^{-4}$ s^{-1}. Additional buckling tests, with the specimen in an upright position (Figure 4.55), were made to evaluate the influence of bend jig arrangement on the AE signal shape. The layers were applied on mild steel and an Al-alloy[1] with high tensile strength and linear elastic behaviour up to 1.12% strain in order to see whether substrate yielding has an effect on the fracture behaviour of brittle lacquer layers.

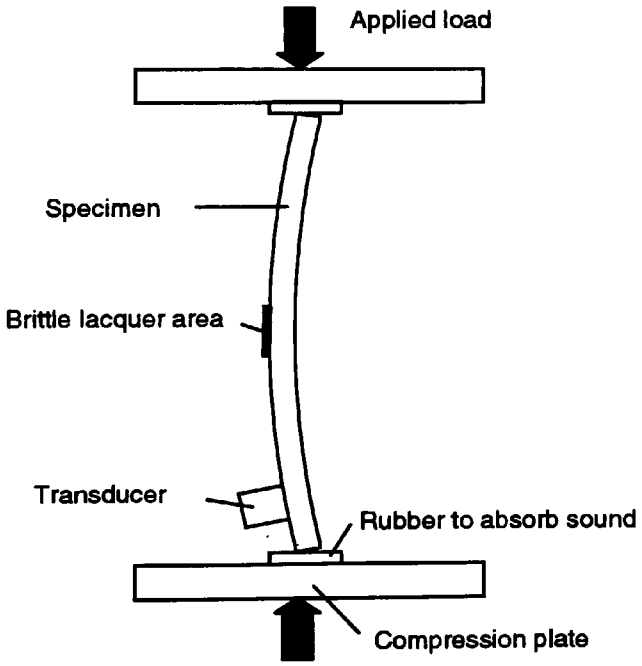

Figure 4.55: Schematic diagram showing the specimen alignment for buckling tests.

---

[1]) Aluminium-Copper-Magnesium-Silicon-Manganese Alloy according to BSI L 157: 1978

Cu:	3.9 - 5.0%	Mn:	0.4 - 1.2%
Si:	0.5 - 0.9%	Mg:	0.2 - 0.8%

Balance: Aluminium

Layer Morphology:

The lacquer surface had a glossy, orange peel-like appearance after spraying and drying. The coating also contained a few small bubbles. These bubbles are required for a good crack pattern and consistent threshold cracking according to the manufacturers instructions. However, excessive bubbling had to be avoided because it would obscure crack patterns. No cracks were found in the lacquer prior to testing.

4.3.1 Tests with Brittle Lacquer in Tension

Crack Patterns:

Through-scale cracks with equal spacing were observed in all tests (Figure 4.56). Some tests which were terminated at strains lower than the maximum strain of 1.12% showed that the distance between the cracks decreased slightly with increasing strain. These tests also indicated that only a small increase in strain above the critical strain for cracking caused most cracks to grow until they reached a certain density and further increase in crack density required increasingly larger amounts of additional strain. For example, cracking always started at a strain of approximately 0.05%. One test was stopped at 0.49% strain and had an average crack spacing of 0.38 mm giving approximately 26 cracks per cm. Another test was stopped at 0.97% strain and had an average crack spacing of 0.27 mm or approximately 37 cracks per cm. Thus an approximately 2-fold increase in the strain level above first failure resulted in only a 1.4-fold increase in the number of cracks. This is presumably due to elastic stress relaxation within the lacquer after cracking and can be explained as follows:

Assuming that stress relaxation effects were only significant over a small distance near the crack (see also section 2.1.2.3, page 37), then the creation of additional cracks was little affected during the initial cracking when the crack spacing was large. However as the strain increased, the crack spacing decreased and the effects of stress relaxation fields of neighbouring cracks started to interact with each other and hence delay further cracking. Thus increasingly larger additional strains were required to build up the critical fracture stress in the middle of a lacquer segment in order to form a new crack between two existing cracks. The second mechanism, which would account for such failure behaviour, was plastic stress relaxation as shown in section 2.1.2.3 (page 37). This mechanism could only take place in systems where the interface slips or the substrate yields at the base of through-scale cracks which could have been the case with mild steel but not with Al-alloy since it deformed purely elastically up to 1.12% strain. Thus, plastic stress relaxation was not considered to be operative in tests with brittle lacquer since layers applied to Al-alloy showed the same fracture patterns as those on mild steel. This was also supported by the fact that none of the layers showed any sign of interface weakening or delamination which would be characteristic

for plastic stress relaxation by interface slip. Further cracking was observed at strains above 1% and short cracks developed between the long cracks (Figure 4.57).

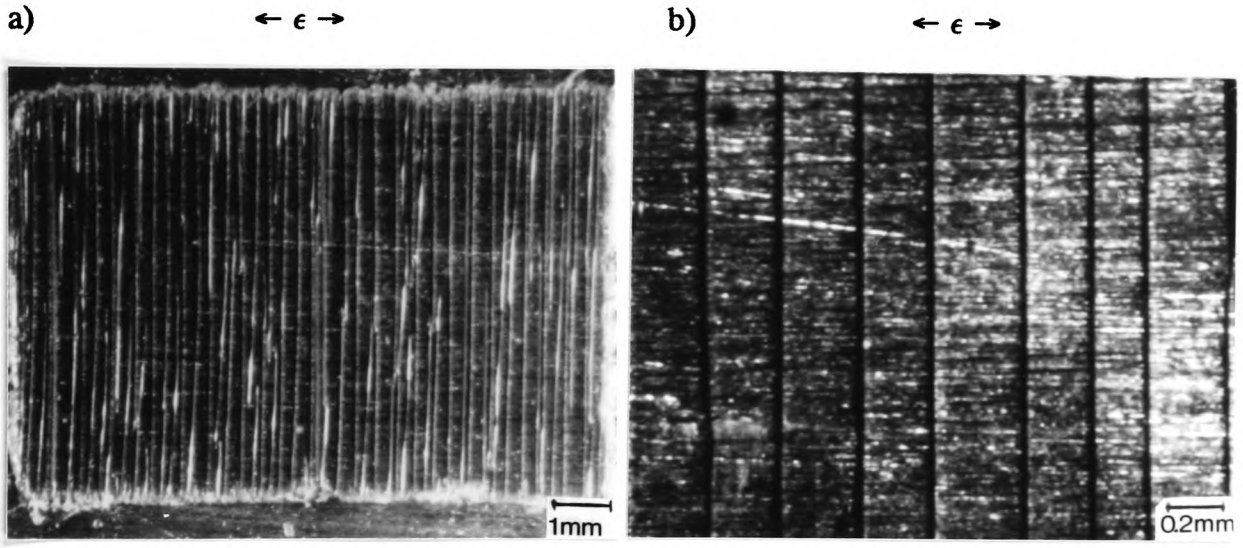

Figure 4.56: Surface micrographs of the cracks in (a) a 100 μm and (b) a 120 - 130 μm thick brittle lacquer layer after bending to a maximum tensile strain of 0.97%.

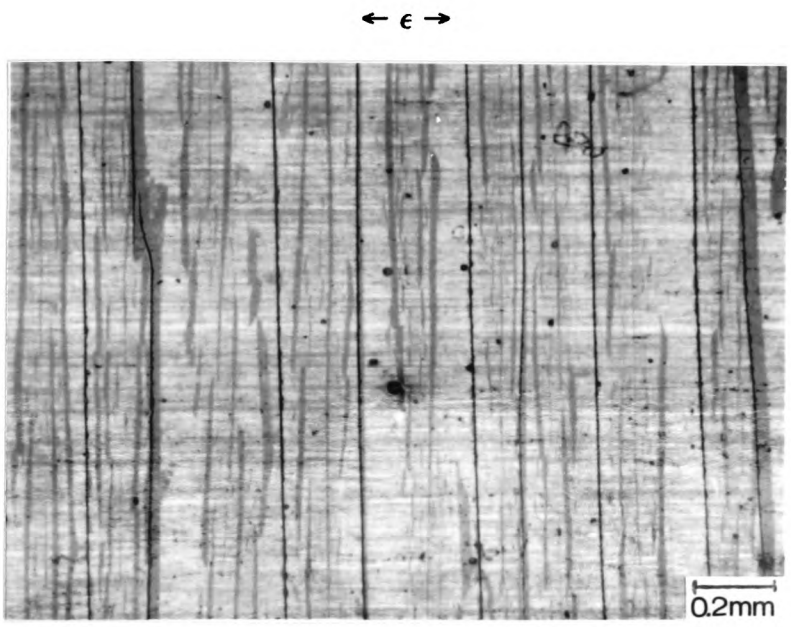

Figure 4.57: Surface micrograph of the cracks in a 120 - 130 μm thick brittle lacquer layer after bending to a maximum tensile strain of 1.12%. The grey shadows are light reflections and show the short cracks.

Correlation of AE with Strain and Crack Patterns:

A family of events after the first signal was found in all tests. This period of high activity was followed by a second period of decreasing activity with increasing strain (Figure 4.58). In addition, tests with a lacquer thickness of 180 μm and in a few instances also with 125 μm thick lacquer showed an increase in the AE activity towards the end of the tests which started at strains above 0.7 - 0.9% (Figure 4.59).

The plots could be explained by the earlier results on crack patterns. The first family of AE signals corresponded to the creation of equi-distant cracks where a small increase in strain produced many new cracks. The second period of decreasing activity was due to the formation of additional cracks which required increasingly larger amounts of additional strain to form them, and in most cases the AE activity fell relatively fast with strain after it had peaked at a maximum even though the strain rate remained constant. The increase of AE activity towards the end of the tests for 180 μm lacquer scales was due to the development of short cracks as observed earlier. The AE energy of short cracks in 125 μm thick scales was about the same level as the set threshold and an increase in AE intensity was not always recorded. In scales thinner than 125 μm no increase in intensity was recorded, although they showed short cracks at strains $>1\%$.

In addition, the number of signals recorded during failure of thin scales was generally smaller than the number of cracks, which also indicated that some of the AE signals from through-scale cracks did not exceed the threshold. For thicker scales the number of signals was at least equal to, or higher than, the number of cracks.

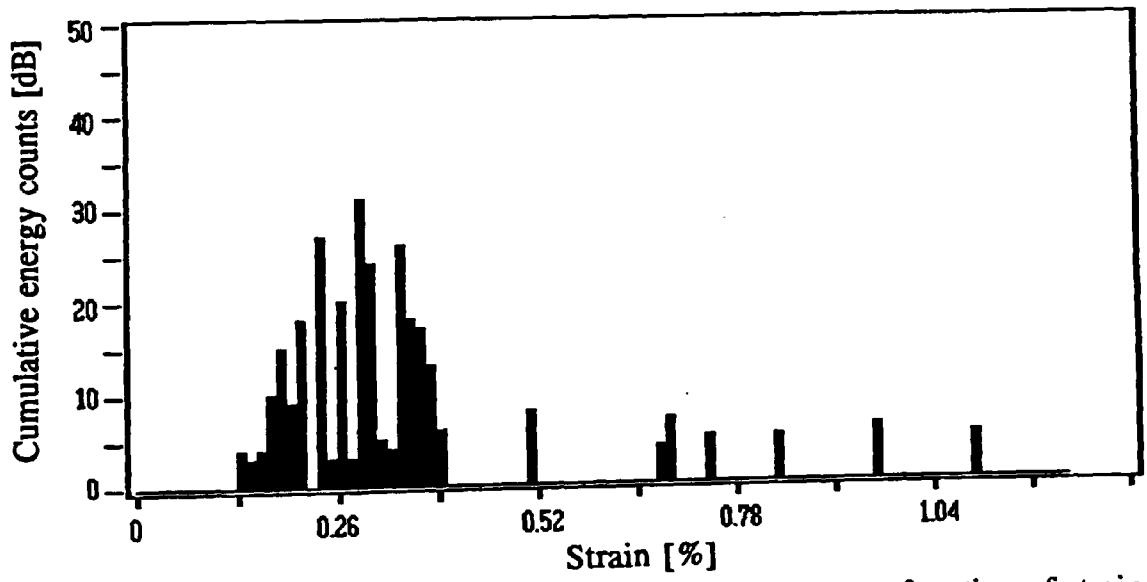

Figure 4.58: Histogram of the cumulative energy counts as a function of strain for a 90 μm thick brittle lacquer layer tested in tension.

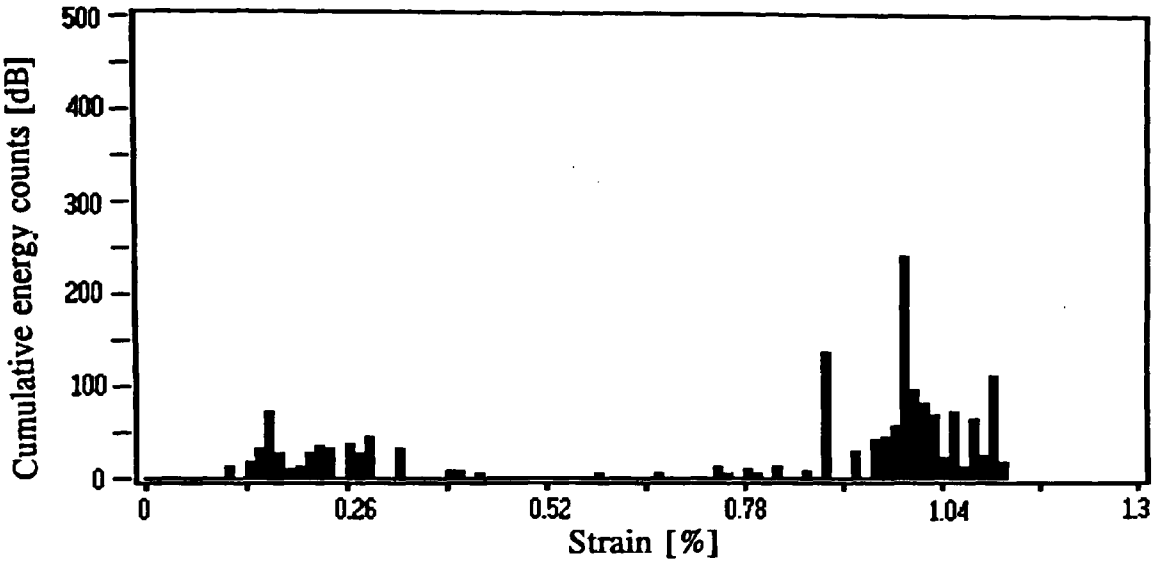

Figure 4.59: Histogram of the cumulative energy counts as a function of strain for a 170 - 180 μm thick brittle lacquer layer tested in tension.

Relationship between AE Parameters and Layer Thickness:

The failure strain of brittle lacquer was insensitive to thickness in the thickness range studied. Hence further analysis of the AE data was carried out, firstly at the maximum strain level of 0.97 - 1.12% and secondly, at a strain level of 0.65% where cracking had occurred; but the creation of short intermediate cracks had yet to start. AE parameters were analysed as average energy counts per signal and as cumulative energy counts up to the respective strain levels. The scatter in the data was highest when analysed at the maximum strains, especially for the 125 and 180 μm thick layers which showed an increase in AE activity towards the end of the tests (Figure 4.60). The second analysis at 0.65% strain produced more consistent results (Figure 4.61a), because it ignored the increase of the AE activity towards the end, which was variable and not found in all tests. Despite the scatter, trend lines were drawn in the plots to represent the best-fit linear approximation (Figure 4.61). These lines clearly show an increase of the AE parameters with increasing thickness due to the higher energy stored and subsequent release during cracking of thicker layers.

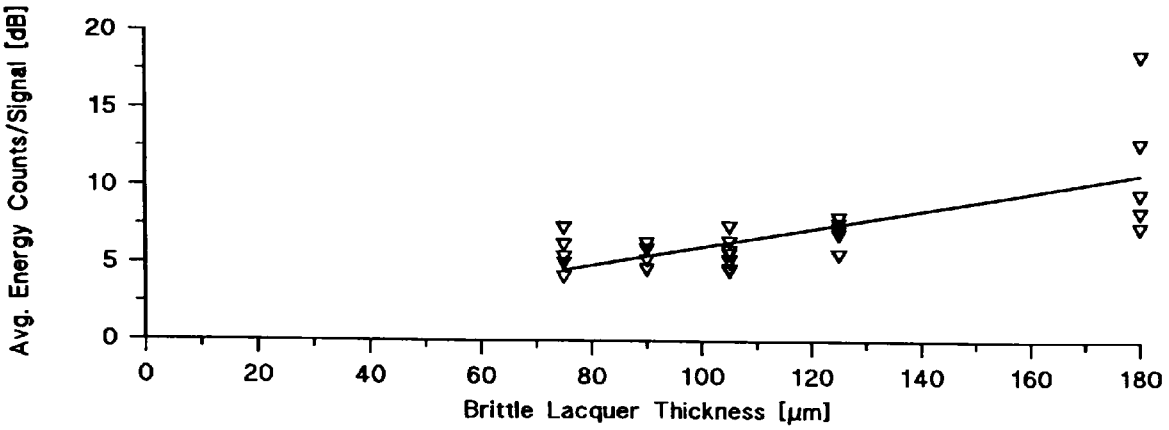

Figure 4.60: Average energy counts/signal as a function of lacquer thickness. Analysed at a varying tensile strain of 0.97 - 1.12%.

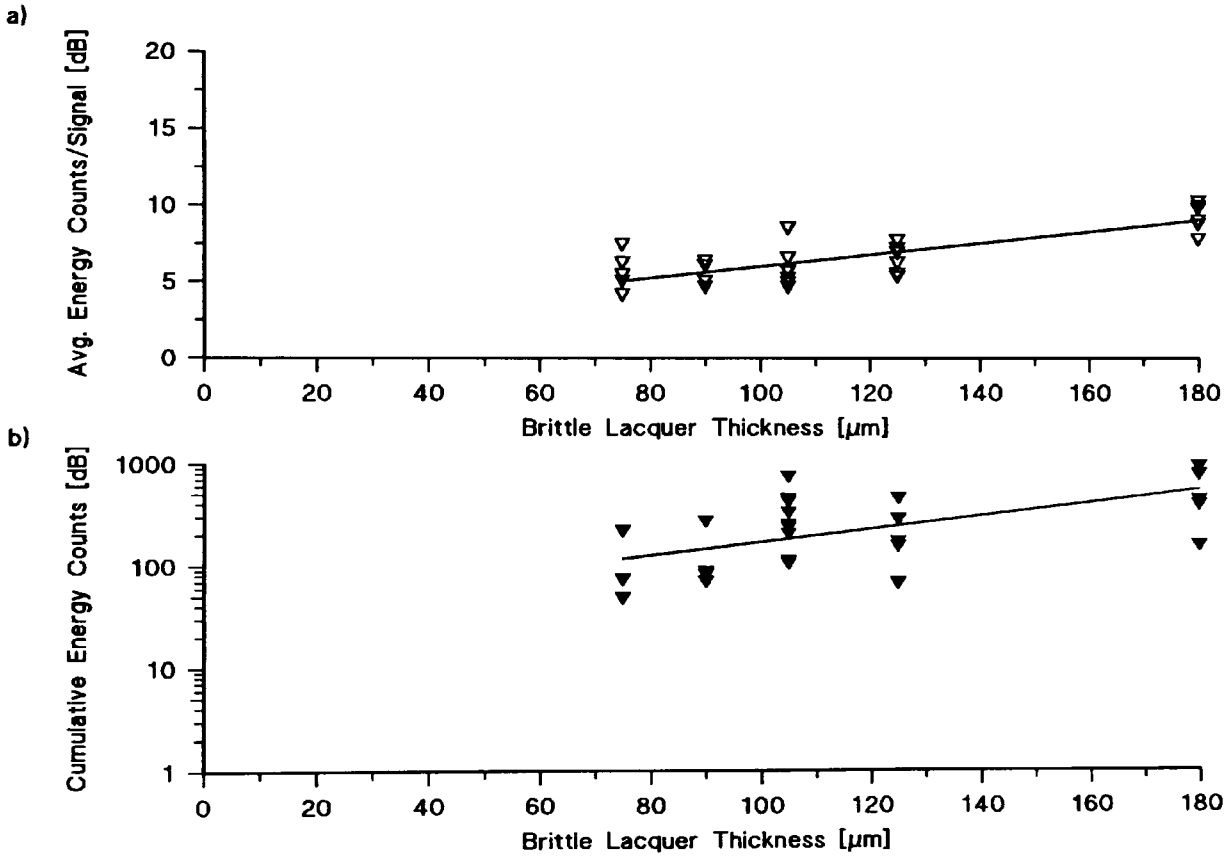

Figure 4.61: (a) Average energy counts/signal and (b) cumulative energy counts as a function of lacquer thickness. Analysed at a tensile strain of 0.65%.

4.3.2 Tests with Brittle Lacquer in Compression

Crack Patterns:

The brittle lacquer layers spalled mainly at the edge under compressive stress. In a few tests, spalled areas were also found within the main area of the lacquer raft (Figure 4.62). Microscopic observations showed that the spalled areas were surrounded by oblique shear fracture surfaces (Figure 4.63) indicative of Route I failure (strong

interface/weak scale) which started with the formation of shear cracks within the layer (Figure 4.64). These cracks acted as wedges for the cracks to extend to and along the interface until the particle was wedged out and spalled off. Furthermore, small adherent lacquer particles were found at the metal surface after the bulk of the lacquer had spalled which further supported Route I mechanism. In the case of Route II failure the crack would develop at the interface and propagate along the interface and never deviate into the layer until the buckle breaks off. This would leave the metal surface free of particles after the layer had spalled.

→ ε ←

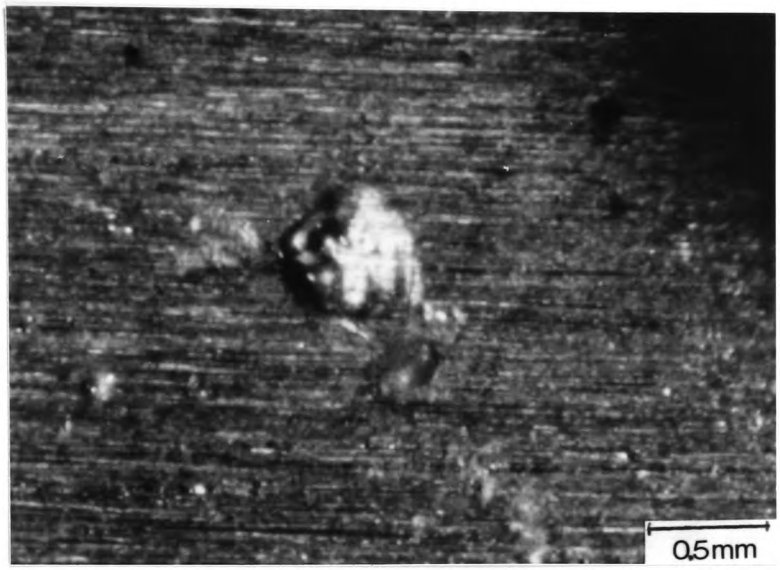

Figure 4.62: Optical micrograph showing a spalled area in the centre of a 120 - 130 μm thick brittle lacquer layer after bending to a maximum compressive strain of 0.97%.

→ ε ←

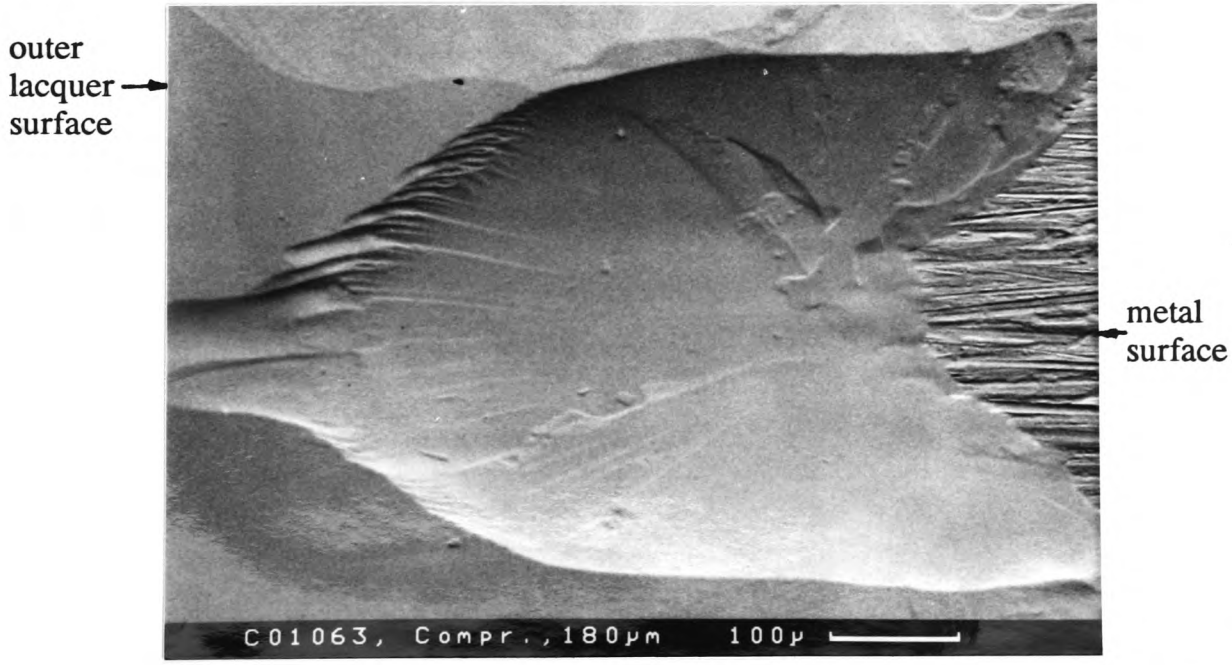

Figure 4.63: Backscattered SEM surface micrograph (topography) showing the oblique shear cracks surrounding a spalled area. Brittle lacquer thickness 120 - 130 μm. Maximum strain 1.12%.

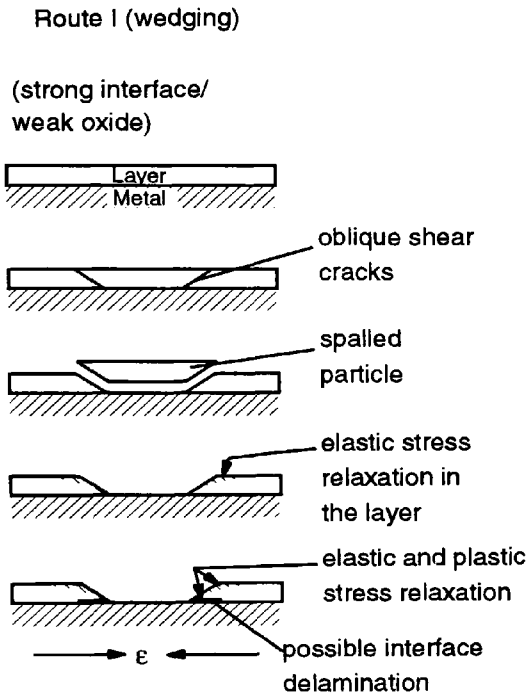

Figure 4.64: Schematic diagram of the observed failure mechanism in brittle lacquer under compressive stress.

Correlation of AE with Strain and Crack Patterns:

The AE distribution with strain was similar for the different AE parameters (cumulative and average energy counts, cumulative and average counts and the number of signals) and showed, in all tests, an increase as the strain increased (Figure 4.65). Hence both AE activity (which was shown by the number of signals) and AE intensity (which was shown by average energy counts and average counts) increased with increasing strain. This indicated that the subsequent stages of Route I failure had increasingly higher critical energy release rates (see also section 4.4.2).

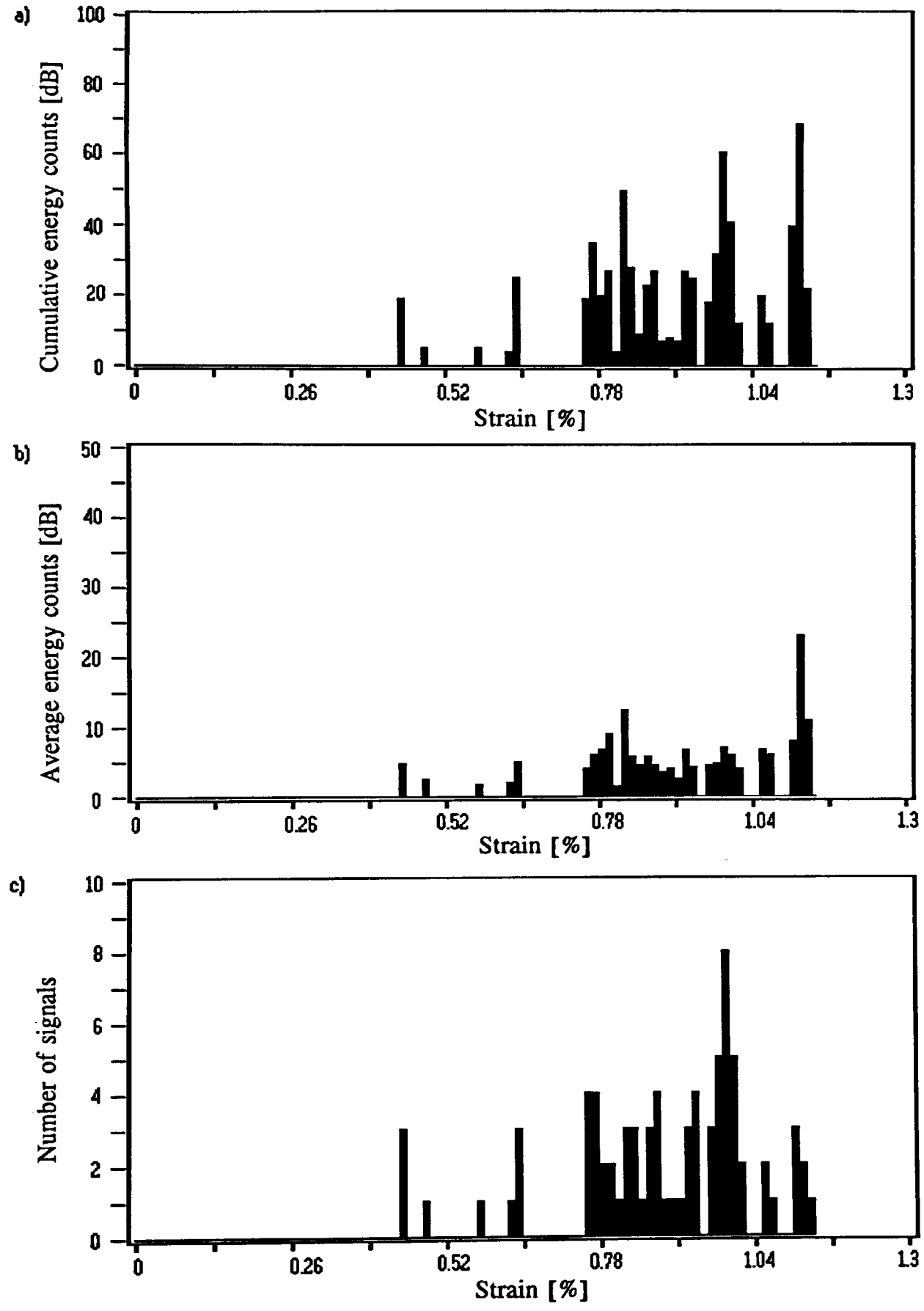

Figure 4.65: Histogram of (a) the cumulative energy counts, (b) the average energy counts and (c) the number of signals as a function of strain for a 100 - 110 μm thick brittle lacquer layer tested in compression.

Relationship between AE Parameters and Layer Thickness:

A single analysis at a constant strain level of 0.97% was possible, because failure started in all tests at very similar strains and no change in the crack pattern or increase in AE was found towards the end of the tests as happened in the tests with the layer in tension (see section 4.3.1, page 155).

Again, cumulative and average energy counts as well as cumulative and average AE counts increased with increasing lacquer thickness shown by a trend line in Figure 4.66 and Figure 4.67. The values increased with layer thickness because failure started with shear cracking within the brittle lacquer. The new fracture surface area swept out by the crack was larger the thicker the layer, thus the average counts and average energy counts increased with thickness. Another possible thickness dependent process could be crack surface friction arising from the oblique shear crack surfaces rubbing on each other when the lacquer is being wedged out (see also section 4.4.2).

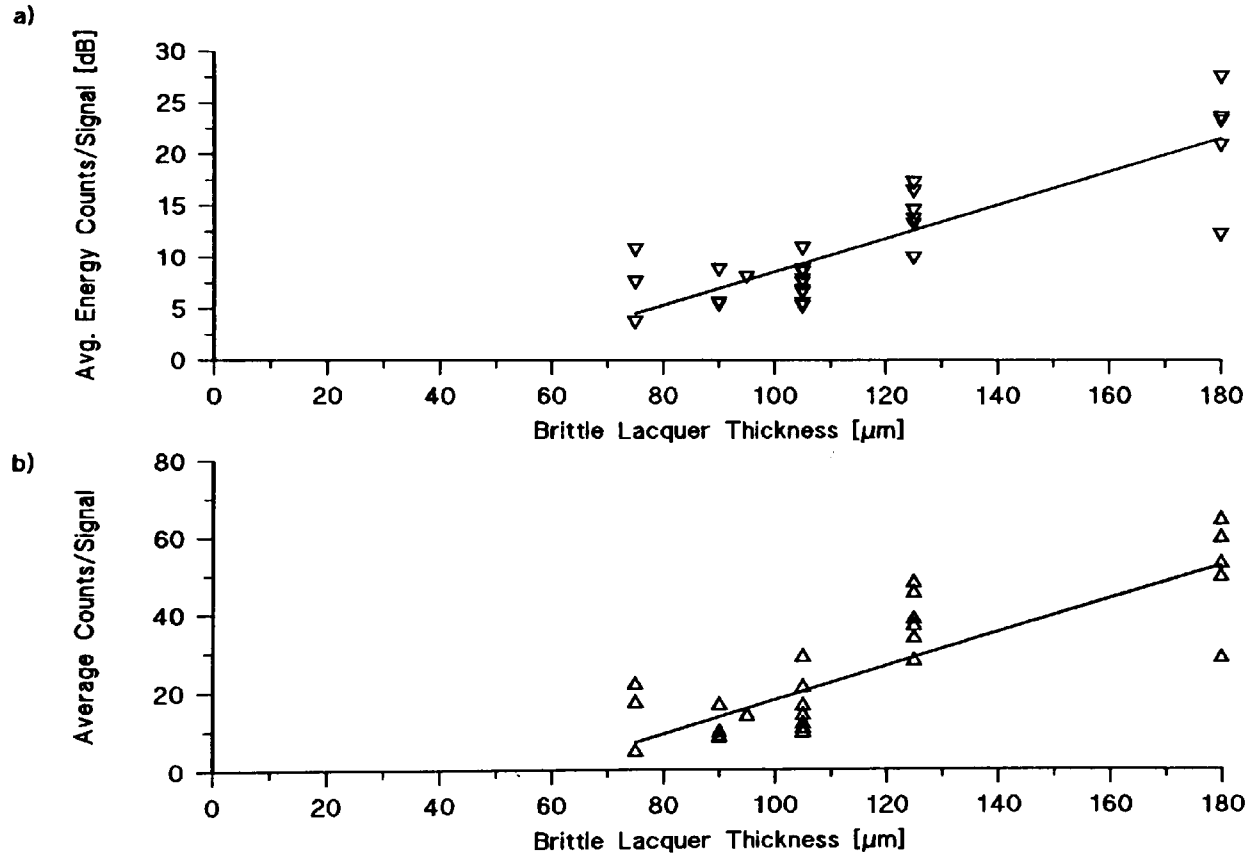

Figure 4.66: (a) Average energy counts/signal and (b) average counts/signal as a function of lacquer thickness. Analysed at a compressive strain of 0.97%.

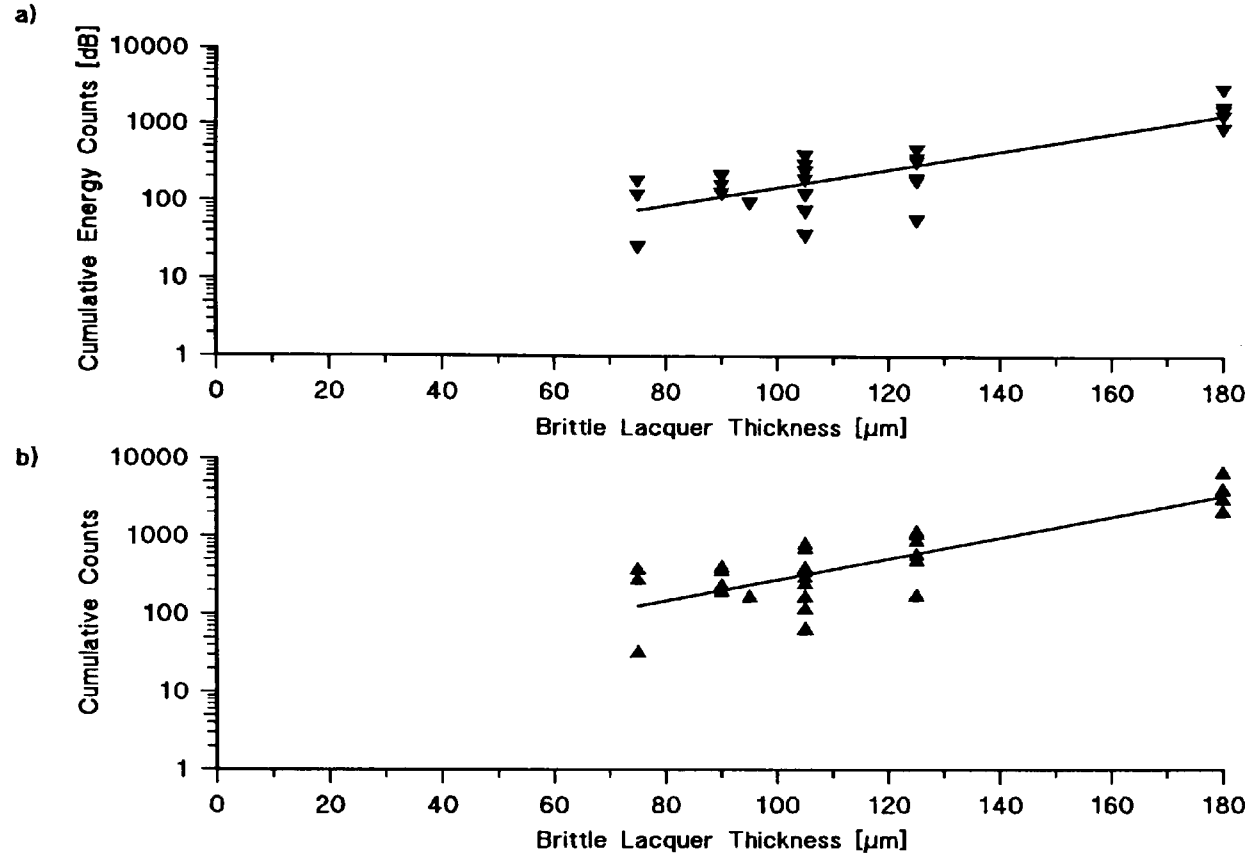

Figure 4.67: (a) Cumulative energy counts and (b) cumulative counts as a function of lacquer thickness. Analysed at a compressive strain of 0.97%.

4.3.3 Buckling Tests

These tests were performed to assess whether the bend jig and the alignment of the specimen had an influence on the AE and in particular on the signal shapes (cf. Figure 4.55, page 154 for specimen alignment).

Crack Patterns:

The crack patterns in tension and compression were essentially the same as in the earlier tests. However, buckling was localised and thus failure within the lacquer was restricted to the buckled region, resulting in either very small crack spacing or severe spallation at the buckled region in tension or compression, respectively.

Correlation of AE with Strain and Crack Patterns:

The AE signal distribution with strain could not be investigated because of the sudden nature of buckling and its unknown strain rate.

Relationship between AE Parameters and Layer Thickness:

The only analysis was done at the end of the tests at an unknown strain level. Therefore the cumulative energy count and cumulative count values could not be

compared with the results of the tensile or compressive tests because the analysis strain was different. The average energy counts and average AE counts per signal were compared with the results of the tensile and compressive tests because these parameters are more dependent on the layer thickness than on the strain. In fact both parameters showed good agreement in tension and compression with the earlier results. More importantly, the characteristic signal shapes for tensile or compressive failure were also found (see also section 4.5). It was therefore concluded that the bend jig and the specimen alignment had no significant influence on the AE and its signal shapes.

4.4 Comparison of the Results for the Three Layers

The AE energy count was the most consistent AE parameter and was therefore mainly used to analyse failure of the layers. Nevertheless other parameters such as counts and number of signals would have led to the same conclusions. The most reproducible AE results were obtained with NiO probably due to its simple and reproducible nature. A few AE signals were recorded even after the deformation was stopped with all three materials, indicating that some delayed cracking occurred, especially in compression. In general, AE was only a complimentary tool which supported failure mechanisms observed by microscopy (see below).

4.4.1 Comparison of the Results in the Tensile Tests

Failure Mechanisms:

Tests under conditions where oxide creep was observed, i.e. iron oxide at 550 °C with a strain rate of $\sim 10^{-5}$ s^{-1} and NiO at 900 °C, showed only short cracks in oxides <7 μm thick, which did not form a regular pattern indicating that only localised failure occurred. The main area of oxide deformed without failure which supported the view that thinner oxide creeps more readily and to a larger extent than thicker oxide layers (see also section 4.2.1.4, page 143).

Regularly spaced through-scale cracks normal to the direction of applied stress were found in all other tests with each of the three layers studied. The characteristics of the cracks in brittle lacquer did not change with increasing thickness, i.e. they were mostly across the whole width and short cracks appeared between existing cracks at strains $>1\%$. However, cracks in oxides were longer the thicker the scale and this effect was even more pronounced in the tests at growth temperature.

The mechanisms of stress relaxation accompanying the bending process are modelled in Figure 2.2 (page 38) as initial elastic stress relaxation which occurred as cracks were formed, followed by plastic stress relaxation at higher strains.

The tensile failure process can be explained by consideration of the crack patterns

and the plots showing the cumulative AE energy counts as a function of strain. Local elastic stress relaxation occurred by the first cracks nucleating in areas of highest stress concentration (which produced the first few AE signals). Equidistant cracks were rapidly established when the continuing straining caused the average stress level in the oxide to exceed the critical stress for failure and this was accompanied by a maximum in the rate of AE. Subsequently plastic stress relaxation processes such as plastic deformation, interface slip and dislocation movement accounted for an increasing proportion of the strain increase, although AE from such processes was not recorded due to the high threshold setting (see also section 3.6.1, page 95) and thus the rate of AE decreased. In the work on iron oxide, interface delamination occurred on further straining accompanied by an increase of AE towards the end of the tests (cf. Figure 4.14 and Figure 4.15, page 116), but with NiO no interface delamination or increase in AE was observed up to the maximum strain of 1.12%. A similar increase was also observed with brittle lacquer but this was due to the creation of short cracks which is a process not found in oxides.

At room temperature plastic stress relaxation could in principle be achieved by:

(i) interface slip and/or

(ii) substrate yielding at the base of through-scale cracks.

Two additional mechanism could be active in tests at oxide growth temperature. These were:

(i) oxide creep, if the stress in the oxide exceeded the critical stress for creep, and/or

(ii) lateral oxide growth, if the time scale of the deformation was sufficiently low.

Such a detailed distinction was beyond the scope of the present study. However, in the following a first estimation of the relative contributions is made for the three layers being tested.

Brittle lacquer did not show any interface slip and the crack patterns were the same regardless whether the substrate deformation was elastic or plastic. This led to the assumption that elastic stress relaxation was dominant because the presence of plastic stress relaxation would have resulted in different crack patterns or spacing in tests where mild steel was the substrate instead of Al-alloy (see also section 4.3.1, page 155).

The situation was much more complicated with oxides because the fracture patterns and AE also suggested the presence of plastic stress relaxation. The amount of elastic stress relaxation was expected to be very similar in the tests at room and at growth temperature but evidence for an increase in plastic stress relaxation at growth temperature was found in the plots of crack spacing as a function of oxide thickness Figure 4.11 (page 113) and Figure 4.39 (page 140). The analysis suggested that the lower interfacial shear strength of iron and nickel oxide at 500 and 900 °C, respectively, accounted mainly for the change in crack spacing. However it neglected

the effects of lateral oxide growth, substrate yielding at the base of the through-scale cracks and oxide creep. Lateral oxide growth was not considered active because of the high deformation rate. Substrate yielding at the base of through-scale cracks presumably resulted in some plastic stress relaxation in the tests at room (see also section 4.1.1.2, page 115) and probably even more in the tests at oxide growth temperature due to lower yield strength of the substrate. However the simple analysis equation (4.1) (page 107) did not allow such a distinction since it was only based on a consideration of the mechanical forces acting in an oxide area (Figure 4.10, page 113). Similarly oxide creep was observed in iron oxide at 550 °C with a strain rate of $\sim 10^{-5}$ s^{-1} and NiO at 900 °C. The overall contribution of creep to the failure strains was at most 0.2% for iron and nickel oxide based on the plots showing the failure strains as a function of oxide thickness. At room temperature the crack spacing varied between 30 and 130 μm for 5 - 45 μm thick iron and nickel oxides. Hence assuming the same contribution of creep to crack spacing as was the case for the failure strain, creep would only have resulted in an increase of the crack spacing by a few microns. However, the actual crack spacing at growth temperature increased to 115 - 700 μm. Thus creep was thought to be only a minor contribution.

Interface delamination and spallation was only found in iron oxide and as a result the crack spacing was found to be independent of strain in some of the iron oxides (cf. Figure 4.12, page 114). The observations confirmed that the iron oxide interface spalled more readily than the nickel oxide interface. As shown in section 2.1.3 (page 50) it is at present difficult to separate the factors of atomic strength, interface roughness and impurity element segregation which affect interfacial strength [3].

In summary, the tensile failure mechanisms for the three systems were very similar and slight differences were reflected in the cracking patterns and the AE results, e.g. tests with more severe cracking and delamination also had higher cumulative AE energy count values, or tests where delamination occurred within the iron oxide at room temperature also had higher energy count values.

A comparison of AE energy count data from different materials was complicated because of different AE propagation characteristics. Nevertheless a simple comparison was made for the average energy counts because the energy counts were least affected by the threshold setting and amplification (see also section 3.6.2, page 96).

The average energy counts increased with increasing thickness for the three systems (e.g. Figure 4.17, page 118). The increase can be explained by the models given in section 2.2.5 (page 68) which simply suggest that:

$$E_{AE} = K_1 \, \Delta A \qquad (4.3)$$

where K_1 is a constant incorporating the transfer function of the material, the sensor and the instrumentation, ΔA is the area of new fracture surface created by the crack growth

and E_{AE} is the number of energy counts associated with the crack growth. Assuming that the crack length ζ was similar for all materials and thicknesses, equation (4.3) can be rewritten as:

$$E_{AE} = K_2 \, h \tag{4.4}$$

where $K_2 = K_1 \, \zeta$. This explains the increase of the average energy counts per signal or per crack with thickness because cracks were always through the whole thickness.

The values in Figure 4.17 (page 118) and in Figure 4.43 (page 143) are quite similar for the two oxides, because both materials are brittle ceramics and thus expected to release similar energies during failure. In contrast brittle lacquer released less energy during failure (Figure 4.61, page 159) presumably because it had weaker bonds which failed with a lower energy release.

The cumulative energy counts also increased with layer thickness for the three tested materials because:

$$\sum E_{AE} = K_1 \sum_{i=1}^{n} \zeta_i \, h \tag{4.5}$$

where n is the number of cracks found in the layer at the analysis strain level. A quantitative comparison of the three systems could not be made because the analysis strains and hence the number of cracks was different for the three systems.

Critical Failure Strains and Model for Oxide Failure:

Equation (2.12) (page 39) gives the predicted failure strains based on a linear elastic fracture mechanics approach for a stress free material. However oxides are generally subjected to growth and cooling stresses and failure could also occur under conditions of plastic deformation or lateral oxide growth at elevated temperature. Thus the relationship between ϵ_c (equation (2.12) (page 39) and the measured failure strain ϵ_m is as follows:

$$\epsilon_c = \epsilon_m + \epsilon_{gr} + \epsilon_{cool} + \epsilon_{pl} + \epsilon_{lat} \tag{4.6}$$

where ϵ_{gr} is the growth strain, ϵ_{cool} is the cooling strain, ϵ_{pl} is the strain compensated by time dependent creep and ϵ_{lat} is the strain compensated by lateral oxide growth which is only expected during deformation in tension [13]. ϵ_{pl} and ϵ_{lat} always act to increase the measured failure strain, and since ϵ_{gr} and ϵ_{cool} are usually compressive, ϵ_m in tension is also increased by these strains. The failure strain ϵ_c can be replaced by equation (2.12) (page 39):

$$\sqrt{\frac{2\gamma}{F^2 \pi E c}} = \epsilon_{gr} + \epsilon_{cool} + \epsilon_m + \epsilon_{pl} + \epsilon_{lat} \tag{4.7}$$

Thus for the case of iron oxide at 550 °C strained at $\sim 10^{-4}$ s^{-1} where growth and cooling stresses are zero and lateral oxide growth and creep are negligible, $\epsilon_m = \epsilon_c$. The fracture surface energy γ for iron oxide at 550 °C was determined as 3.4 J m^{-2} using values of -210 GPa for E [3] of iron oxide at room temperature and the experimentally observed composite void sizes. F was 1.18 for an out-of-centre flaw of the length 0.4 h at a position of ~ 0.4 h from the oxide surface [45] which was found in most iron oxide scales.

The difference between these failure strains and the strains measured at room temperature was a measure of the cooling stresses and the observed difference for the tests at growth temperature with different strains rates was a measure of creep (Figure 4.68). Lateral oxide growth was regarded as negligible in the tests with iron and nickel oxide scales because of the high deformation rate used in this work.

Similarly the measured failure strains for NiO at room temperature would be smaller if the residual stresses are considered (Figure 4.69). This would suggest a γ-value of 0.8 J m^{-2} for NiO using 190 GPa for E for NiO [3], 1.18 for F as for the case of iron oxide and a composite void size of 0.4 h. Both fracture surface energy values from this work on iron and nickel oxide were of the order of those given in ref. 3.

In summary the fracture mechanics term accounts for the purely elastic part of the deformation up to failure. The scale parameters account for the additional deformation due to residual stresses and creep which are associated with a growing scale. A summary of the factors which contributed to oxide failure strains is given in Table 4.3. This raises the question of whether values from bulk oxides can be used in the fracture mechanics term since it only represents the elastic deformation.

Material	Test conditions		Factors which contributed to the measured failure strain		
	Temp.[°C]	Strain rate	ϵ_{gr}	ϵ_{cool}	ϵ_{pl}
Iron Oxide	20	$\sim 10^{-4}$ s^{-1}	~0	yes	no
"	550	"	~0	no	no
"	"	$\sim 10^{-5}$ s^{-1}	~0	no	yes
NiO	20	$\sim 10^{-4}$ s^{-1}	175 MPa*		no
"	900	"	175 MPa*	no	yes

Table 4.3: Summary of the factors which contributed to the measured oxide failure strains under the different test conditions. *) at present there is conflicting evidence in the literature whether residual stresses are due to cooling or growth [51,52]. The present work did not allow such a distinction.

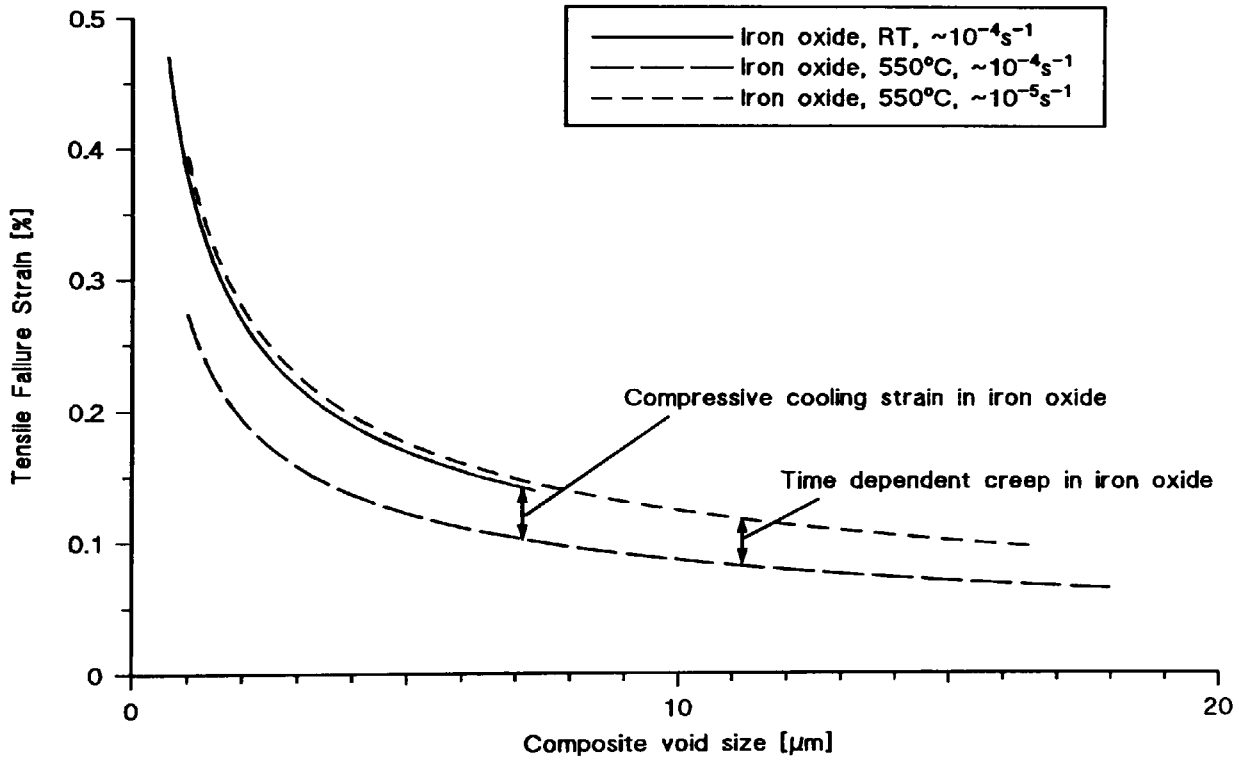

Figure 4.68: Comparison of the best-fit power law curves for the measured failure strains for iron oxide scales tested in tension. The factors which affected the failure strains are also given.

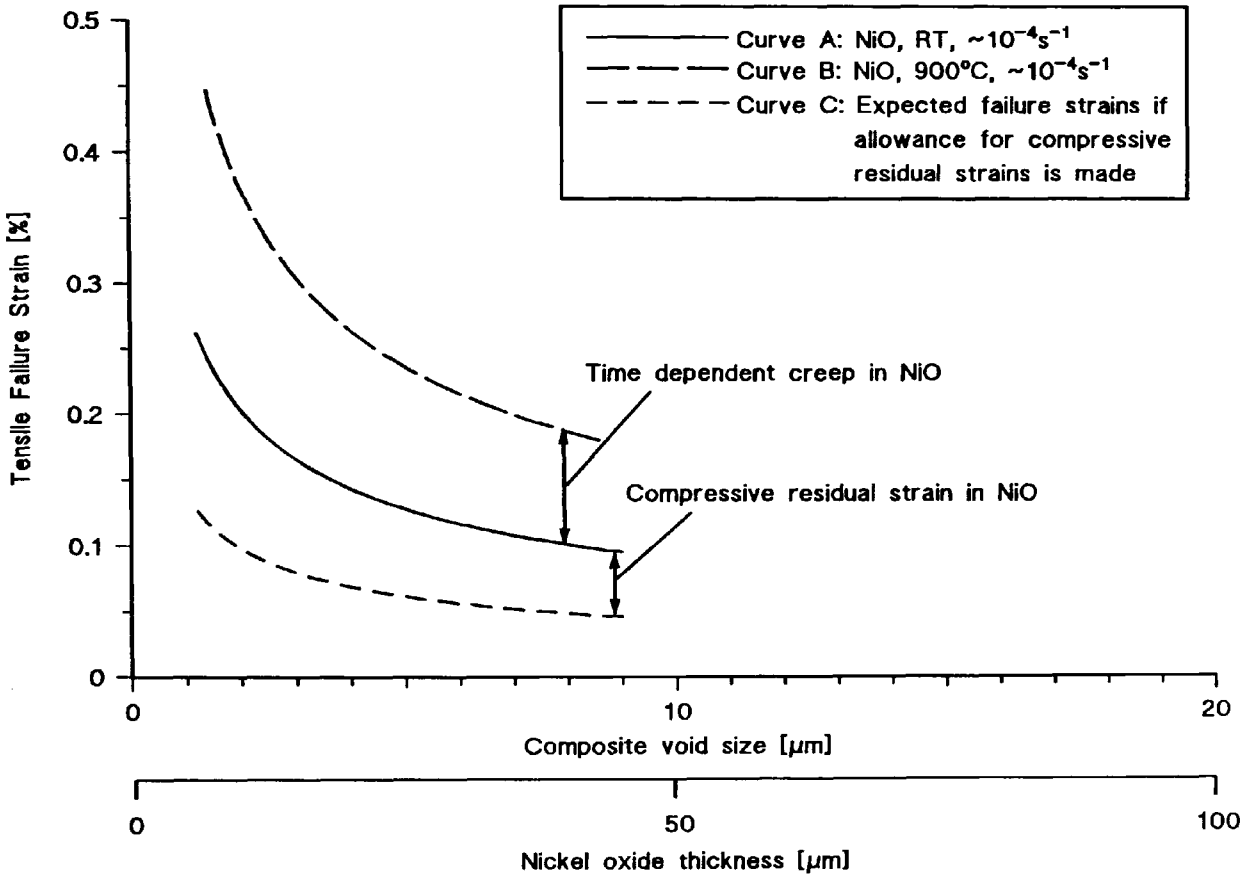

Figure 4.69: Comparison of the best-fit power law curves for the measured failure strains for nickel oxide scales tested in tension. The factors which affected the failure strains are also given.

4.4.2 Comparison of the Results in the Compressive Tests

Failure Mechanisms:

Microscopic observations were used to identify four different failure mechanisms summarised in Figure 4.70. Three of those mechanisms have previously been reported by other researchers (cf. Figure 2.5, page 46) and the fourth was due to the oxide geometry but it can be described mathematically by equation (2.24) (page 46) since it only required crack propagation at the interface (see also section 4.1.2.4, page 131).

A consideration of the different mechanisms suggested that all of them are feasible in a layer/substrate system. The relative values of resistance to buckling, shear strength of the interface and shear strength of the layer determined which mechanism occurred.

AE gave some information about the different fracture processes. The AE time distribution showed an increase in AE activity and intensity with increasing strain. This increase was similar for all three systems suggesting that failure became more likely as the strain increased. This also confirmed that the progressive stages during all four failure processes had successively higher critical energy release rates which, therefore,

occurred at different strain levels dependent on whether the energy stored had already exceeded the respective critical value for initiation.

The cumulative AE count number and the cumulative AE energy count number increased with increasing thickness for both oxides and brittle lacquer layers indicating higher energy storage and subsequent energy release during failure of thicker scales. The average AE count number and the average AE energy count number per signal also increased with thickness for nickel oxide and for brittle lacquer but remained constant for iron oxide. This can be explained as follows:

The failure of nickel oxide and brittle lacquer started with the initiation of a shear crack within the layer (Figure 4.70c and d). This process and its AE energy release was thickness dependent because the thicker the layer the longer the cracks and the larger the area of new fracture surface. However the amount of new surface produced by crack deviation and propagation at the interface is independent of thickness. Another possible thickness dependent process could be the crack surface friction caused by the rubbing of the shear cracks.

In contrast, the failure of iron oxide started with an interface crack which propagated along the interface in a finite number of steps until a critical delamination length was attained (Figure 4.70a and b). The AE data indicated that delamination of thicker oxides took place in several stages and that each stage had a similar energy release, which was not dependent on iron oxide thickness. Thus the cumulative values increased with thickness whereas the average values remained constant. Only the energy release during final spalling by through-scale cracking was expected to be thickness dependent. However this stage had yet to be reached at the strains used in the analyses for section 4.1 to 4.3 inclusive. In summary, the AE results give some support to failure mechanisms observed microscopically.

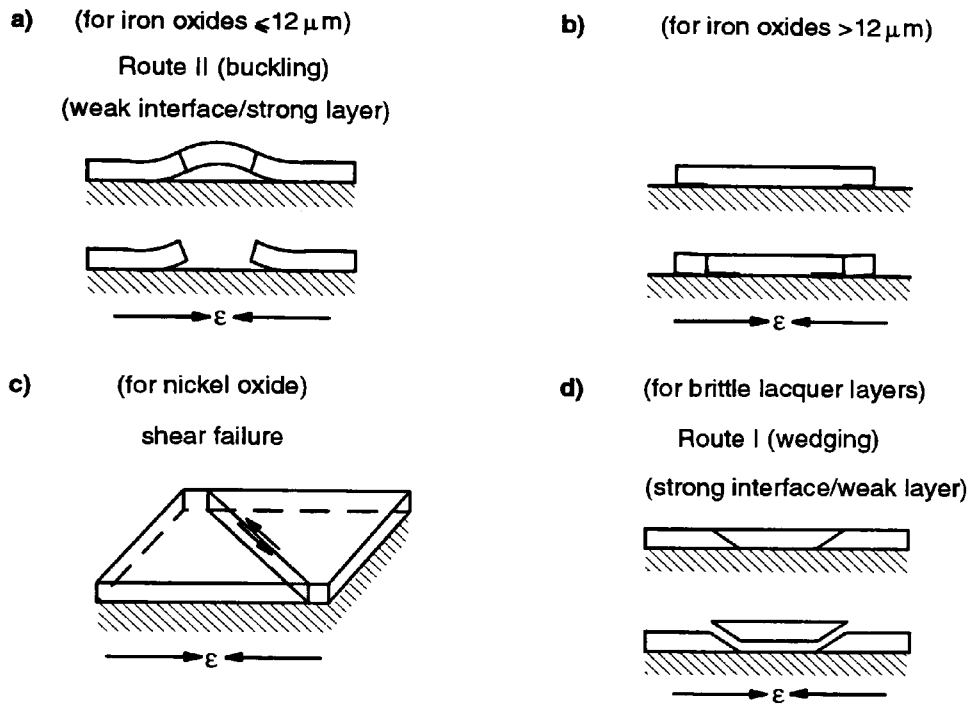

Figure 4.70: Summary showing schematically the different failure mechanisms observed with the three materials being tested.

Critical Failure Strains and Model for Oxide Failure:

The critical strain to cause macroscopic oxide failure decreased with increasing oxide thickness as was the case for failure in tension. The model given in the previous section (equation (4.6), page 169) should also be valid in general. However the respective initiation or spallation conditions for the different compressive failure mechanisms had to be inserted for ϵ_c in order to make any predictions. As shown in section 2.1.2.4 (page 45), the initiation conditions were dependent on the failure mechanisms observed. However the spallation conditions are the same, i.e. in all cases an interface crack must be able to grow or in cases where only parts of the oxide spalled a similar crack had to propagate parallel to the interface. Therefore the strains at which AE was recorded were compared for all systems with the spallation condition, i.e. crack propagation at the interface, even though the AE might have been recorded at an earlier stage during failure initiation by shear cracking.

The measured fracture strain values with iron oxide agreed reasonably well with the predictions and gave a value for $G_{IC}^{interface}$ of 20 J m^{-2} for a stress free oxide prior to testing (Curve A in Figure 4.71) (see also section 4.1.1.4, page 118 and 4.1.2.4, page 131). However, taking the compressive cooling strains of the order of 0.055% into account according to the model given in section 4.4.1 (equation (4.6), page 169) the best estimate for the actual value of $G_{IC}^{interface}$ was 27 J m^{-2} because the oxide was already in a state of compression prior to testing (Curve B in Figure 4.71).

The very high failure strains for NiO can also be explained using this model. In this case the pseudo-elastic behaviour resulting from the microcracking would be accounted for in the factor ϵ_{pl} because microcracking and the resultant stress relaxation could be considered as a form of pseudo-plasticity (see also section 2.1.2.2, page 35). The factor ϵ_e would then only account for the pure elastic deformation of the layer as expected because it is based on linear elastic fracture mechanics. Even though it was impossible in the present study to make any assumptions on the contribution of microcracking to the overall deformation, it is expected that the real energy release rate would be considerably smaller [18] (see also section 4.2.2.4, page 152).

In summary, the failure mechanism could be predicted if the relative buckling stability, the interfacial strength and the shear strength of the oxide were known. If the failure mode was known the initiation and spallation strains could then be calculated for any oxide by considering the overall stress in the oxide and possible plasticity effects.

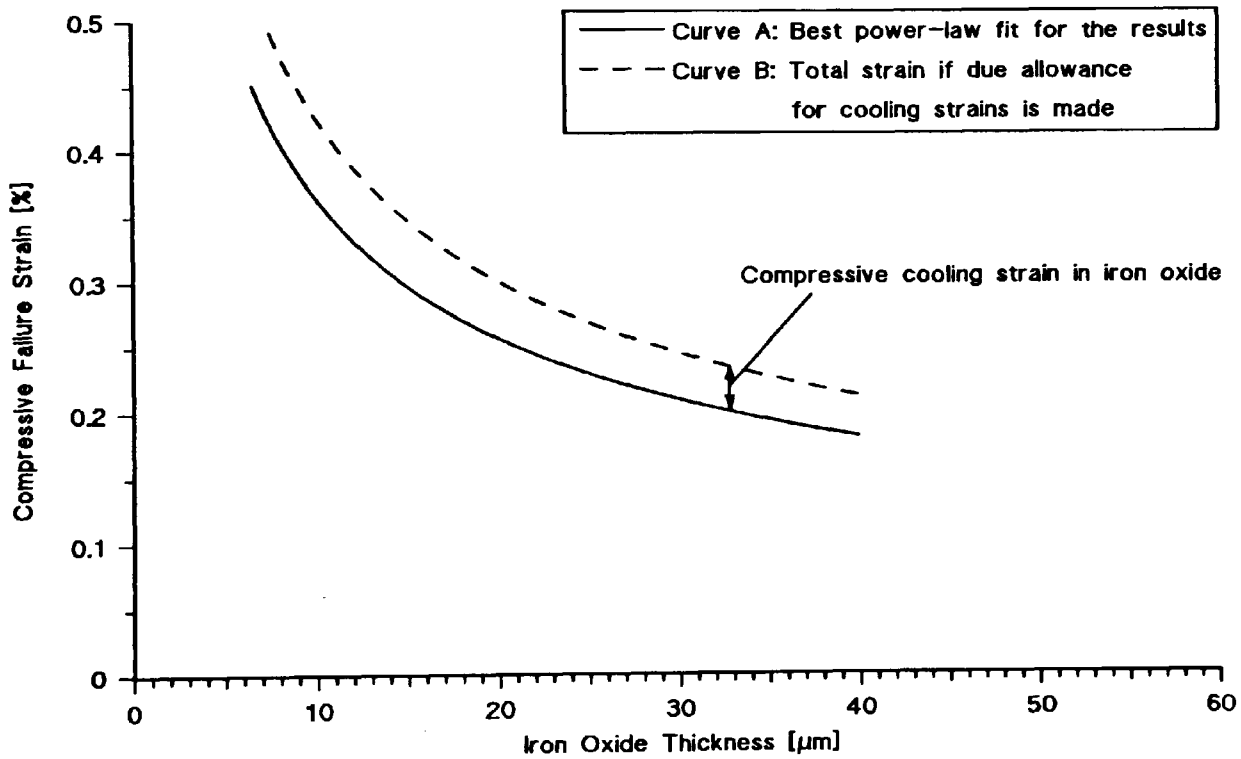

Figure 4.71: Best-fit power law curve for the measured failure strain for iron oxide tested in compression at room temperature. Allowance for compressive cooling strain prior to testing is made.

4.5 AE Signal Analysis

The AE signals obtained in the preliminary work by Hall *et al.* [21] were complex, but two characteristic signals shapes which are shown in Figure 1.1 (page 26) occurred frequently. Hence, classification was based on whether the displayed signal shapes corresponded to that of Figure 1.1a, Figure 1.1b or represented a mixture of

both. It was found that 50 - 70% of the signals had a tensile shape or a decaying shape similar to that in Figure 1.1a when the oxide failed under tensile stresses. When the oxide experienced compressive forces, 50 - 82% of the signals showed a compressive shape, i.e. a shape similar to that in Figure 1.1b. In both cases less than 30% of the total signals were of an uncharacteristic shape [21] and these results were very promising. However the particular analysis relied on the observer to classify the signals and was therefore subjective. Repeated analyses by different persons actually produced results which varied by up 25%. It was the intention of this study to reduce the subjectivity in the analysis by analysing the signals numerically.

The survey in section 2.2.5 (page 68) suggested that the frequency was a very suitable parameter for classifying AE caused by different failure mechanisms in oxides. Pattern recognition and classification techniques [107] have also been very successful in differentiating AE signals from different sources. However such pattern classification systems were not available for the present study because of the costs and the hardware requirement. In this study the auto-correlation function (ACF) was used together with frequency analysis by fast Fourier transformation (FFT) because auto-correlation could be used to detect periodicities in a given signal. Appendix C gives some aspects of the principles of FFT and auto-correlation. A periodicity was expected in the compressive signals because they showed some kind of echo. This was not the case in the tensile signals. It led to the unresolved question of how the signals were generated.

The tensile signals were believed to be a result of tensile through-scale cracks and therefore dominant during the initial stages of the tensile failure mechanism (Figure 2.2, page 38). The shape was explained as follows:

The signal rise time was very small and the signal almost immediately reached the maximum amplitude because the energy release from through-scale cracks was probably very brief and concentrated since the cracks are expected to run through the whole thickness without arrest. The energy then oscillated in the specimen and attenuated slowly, hence the signal amplitude decayed exponentially to zero as expected from a natural decay (see also section 2.2.2, page 59).

In contrast, the compressive signals were thought to be caused by shear cracking within the oxide or at the interface and therefore dominant during the initial stages of compressive failure. The repeating echoes in the signal were believed to be a result of the step wise slip. Each time the two surfaces of the shear cracks moved relative to each other a small fraction of the stored strain energy was released until the driving force, i.e. the residual stored strain energy in that particular part of oxide was too small to exceed the initiation potential of the next slip.

4.5.1 Development of the Signal Analysis Procedure

The ASYST software package version 3.10 (Asyst Software Technology Inc., USA) was used for the analysis. It only required an IBM PC XT/AT/PS 2 or compatible with 640 kByte RAM and a co-processor. Details of the software features are beyond the scope of this section and can be found in the user manuals. The software was not designed for AE signal analysis and therefore some adjustments had to be made in the configuration. The main problem was the random nature of the sampled AE data and signals covered many orders of magnitude in amplitude and length. The available signal analysis hardware and software did not offer such flexibility and signals had to be compressed into a window of fixed height and length.

Signal compression was partially achieved during data acquisition with the TRA-transient recorder board. The sampling rate of the board was set so that the whole frequency range of the transducer could be used for analysis. The signal length was adjusted to 1 ms to limit the amount of data to 2 kByte per signal. It also included 5% or 0.05 ms pretrigger, i.e. the beginning of the signal before it exceeded the threshold for the first time, in order to allow an analysis of the beginning of the signal. However this feature was not used in this analysis. The chosen input range of 0 - 10 V and the total amplifications of 60 dB or 65 dB represented the best available compromise for the layers being tested, which guaranteed that a large number of the AE signals were within the input range. The signal amplitudes were higher for thicker layers and some of the thickest oxides had a number of over-shoots, i.e. signals which exceeded the amplitude of 10 V. These signals could not be used for analysis. Ideally the input range should have been adjusted to every layer thickness examined, but this would have made a comparison more complex and was therefore omitted. On the other hand there was a large number of signals with all layer thicknesses which only used a small proportion of the whole window length. Therefore it was necessary to optimise the window length and position for the signal analysis. In this context a number of signals were analysed with window lengths of 0.5, 0.25 and 0.125 ms and windows which started at 0 ms (including the 5% pretrigger), at 0.05 ms (when the signal exceeded the threshold for the first time), at 0.25 ms and at 0.50 ms. The most important parameter in this selection procedure was the proportion of white noise in the analysed signal which was determined by the size of the frequency peak at 1 MHz (see also section 4.5.2). It was found that a window length of 0.25 ms at the position of 0.05 ms gave the best results [106]. It also appeared the most reasonable position because it included the part of the signal with the maximum amplitude, i.e. the main part of the signal. However there were still some signals which had a large proportion of white noise with the reduced window length and these signals were also omitted in the analysis.

Preliminary analysis had also shown that the signals had a small positive offset.

However a signal mean of zero was required for auto-correlation and therefore the offset value was subtracted from the signal prior to auto-correlation. In addition the output of the ACF was normalised to a scale of 0 - 1.

The actual analysis could start after these initial adjustments and Figure 4.72 shows a typical analysis print. Graph 1 shows the signal as captured with the TRA-board and the dashed lines show the reduced window. Graph 2 shows the reference signal, i.e. the part of the signal which was used in the analysis as depicted by the reduced window in Graph 1. Graph 3 shows the normalised ACF of the reference signal in Graph 2 and Graph 4 gives the FFT of the reference signal shown in Graph 2.

Graph 1: Graph 2:

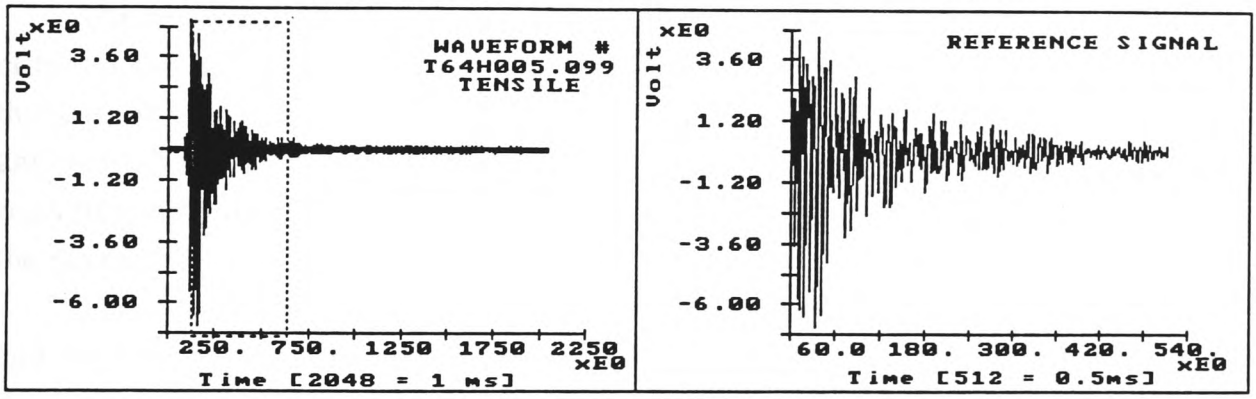

Graph 3: Graph 4:

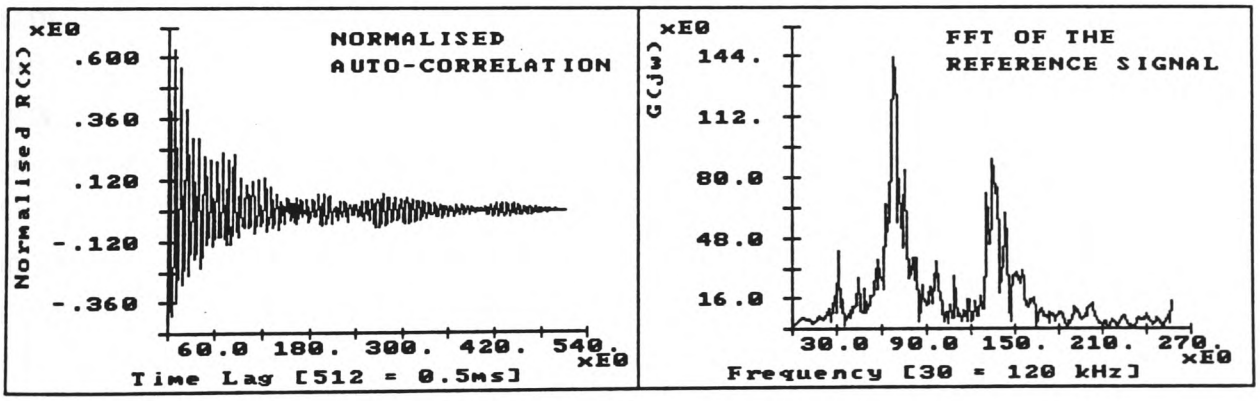

Figure 4.72: Typical analysis print for a AE signal from iron oxide subjected to tensile stress.

4.5.2 Results of the AE Signal Analysis

Three dominant frequencies were found in all signals. These were at ~120, ~300 and ~600 kHz. The first could not be related to either of the two signal types. Whereas the second was dominant in most of the signals having a tensile shape and the frequency peak at ~600 kHz was larger in signals which had a compressive shape. There were always signals which had both peaks [106]. In addition the size of the frequency peak at 1 MHz indicated the proportion of white noise in the analysed signal. Signals were omitted from the analysis if the 1 MHz peak was higher than any other frequency peak.

The relative magnitude of the two peaks at ~300 and ~600 kHz was used as one criterion for signal classification. The second criterion was the shape of the ACF. In this case it was found that tensile signals had an ACF which slowly decayed without any periodicity (Figure 4.73). However the ACF of compressive signals showed repeating maxima at different time shifts which are a clear indication of periodicity in the source signal (Figure 4.74) [106].

These two criteria were used for two types of analysis. The first was very simple and solely based on the FFT and therefore not subjective. The second was more detailed and involved both the FFT and the shape of the ACF, which made this analysis subjective, since it relied on the observer to decide whether the ACF contained repeating maxima, i.e. periodicity. It should be noted that in some cases the ACF showed both features, i.e. a gradual decay and small maxima which made classification difficult. In each case only the first 100 signals of a test were analysed because there was a greater chance of finding a purely tensile (through-scale cracking) signal or compressive (delamination or shear cracking) signal during the initial stages of the failure processes. At later stages interface delamination and through-scale cracking might have appeared simultaneously if the layer was subjected to tensile or compressive stresses. The sample number of 100 reduced the analysis time to acceptable levels and was also large enough to provide statistically reliable data. Signals from a few representative tests with the three materials were analysed.

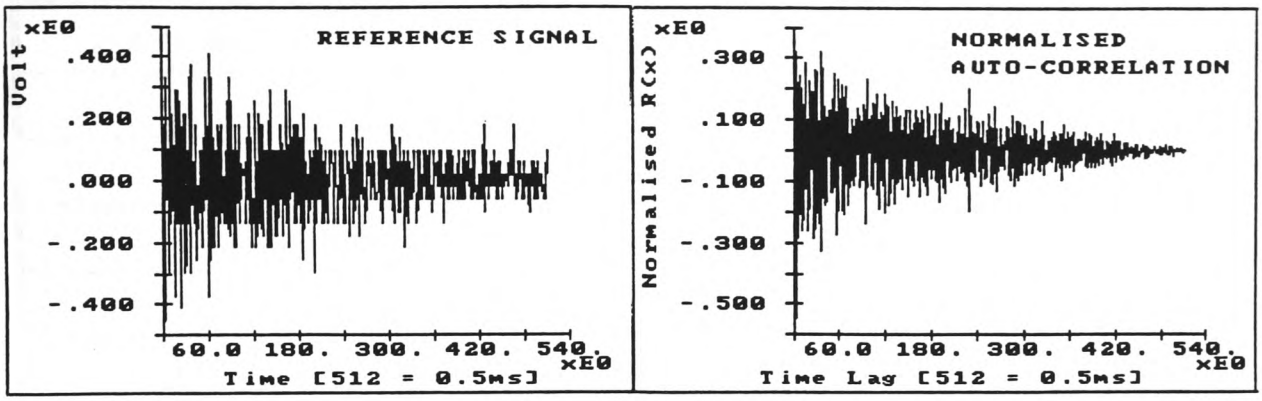

Figure 4.73: Plot showing the normalised ACF of a tensile signal.

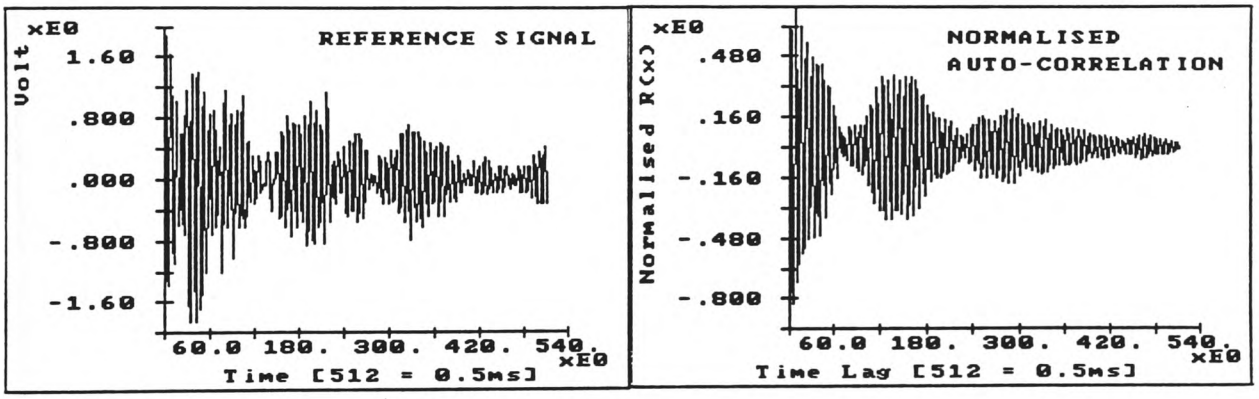

Figure 4.74: Plot showing the normalised ACF of a compressive signal.

First Analysis:

The relative height of the frequency peaks at ~300 and ~600 kHz was used as analysis criterion. A signal was classified as compressive if the peak at ~600 kHz was at least half as high than that at ~300 kHz. All the other signals were classified as tensile. A third category of unclassified signals was introduced for the over-shoots and those signals which had a large proportion of white noise. The results of the first analysis are given in Table 4.4 and 4.5. It was found that in tests with the layer in compression, on average 20.3% had the frequency peak thought to be typical for a compressive signal whereas in tensile tests on average only 9.1% had the same frequency peak.

Material	Thickness [μm]	T [%]	C [%]	U [%]
Iron oxide	8.0	87	6	7
"	10.0	88	11	1
"	11.0	91	9	0
"	11.5	86	6	8
"	19.0	67	8	25
"	23.0	85	9	6
"	23.0	75	12	13
"	36.0	99	0	1
"	39.0	74	19	7
"	40.0	98	2	0
Brittle lacquer	105.0	89	9	2
"	105.0	79	18	3
"	125.0	71	26	3
Nickel oxide	6.0	87	7	6
"	45.0	90	2	8
Brittle lacquer*	90.0	100	0	0
"	125.0	85	10	5
	Average	85.3	9.1	5.6

Table 4.4: Results of the first analysis for the tests with the layer subjected to tensile stress. T = tensile signals, C = compressive signals and U = unclassified signals. *) Buckling tests (see also section 4.3.3) [106].

Material	Thickness [μm]	T [%]	C [%]	U [%]
Iron oxide	6.5	85	10	5
"	11.0	53	4	43
"	11.5	95	3	2
"	11.5	90	4	6
"	20.0	79	15	6
"	23.0	76	21	3
"	23.0	81	19	0
"	39.0	68	31	1
"	40.0	94	3	3
"	40.0	85	14	1
Brittle lacquer	105.0	65	34	1
"	105.0	61	33	6
"	125.0	67	25	8
Nickel oxide	6.0	89	0	11
"	57.5	67	14	19
Brittle lacquer*	90.0	37	53	10
"	180.0	28	62	10
	Average	71.7	20.3	8.0

Table 4.5: Results of the first analysis for the tests with the layer subjected to compressive stress. T = tensile signals, C = compressive signals and U = unclassified signals. *) Buckling tests (see also section 4.3.3) [106].

Second Analysis:

Both FFT and ACF were used for signal classification and altogether six different combinations were found. These were classified as tensile or compressive (Figure 4.75). The FFT was the dominant criterion when it only showed a single frequency peak at ~300 kHz, which was thought to be characteristic of tensile signals (Case 1+2, Figure 4.75). In such cases the shape of the ACF was ignored. As before, a signal was classified as compressive when the frequency peak at ~600 kHz was at least half as high as any other peak (Case 3+4, Figure 4.75). Once more the shape of the ACF had

no effect. Classification was based on the shape of the ACF when the FFT showed both peaks with the peak at ~600 kHz less than half the size of that at ~300 kHz (Case 5+6, Figure 4.75). Hence Case 5 in Figure 4.75 was classified as compressive because the ACF showed several maxima which were typical for periodicity, i.e. a compressive signal. In contrast Case 6 in Figure 4.75 was tensile because the ACF did not show these maxima which was typical for tensile signals. As before a third class of unclassified signals was needed for those signals with too high an amplitude or too much white noise. Typical analysis prints for the different cases can be found in Appendix D and the results of the analysis are given in Tables 4.6 and 4.7. In the tensile tests on average 70.8% of the signals were tensile compared to only 23.6% compressive signals. In the compressive tests, the overall percentage of compressive signals (41.1%) for all tests was slightly less than that of the tensile events (50.9%). The results also indicate the possibility that a single tensile test produced a majority of compressive events or *vice versa*.

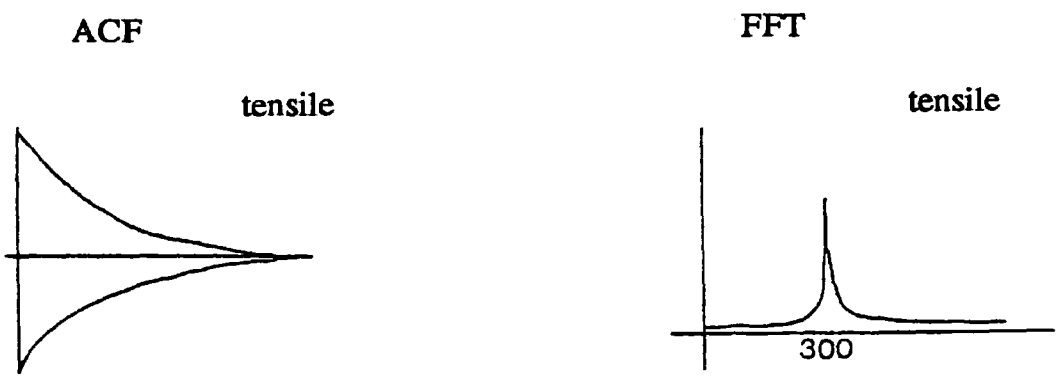

Case 1: Proposed signal type - tensile

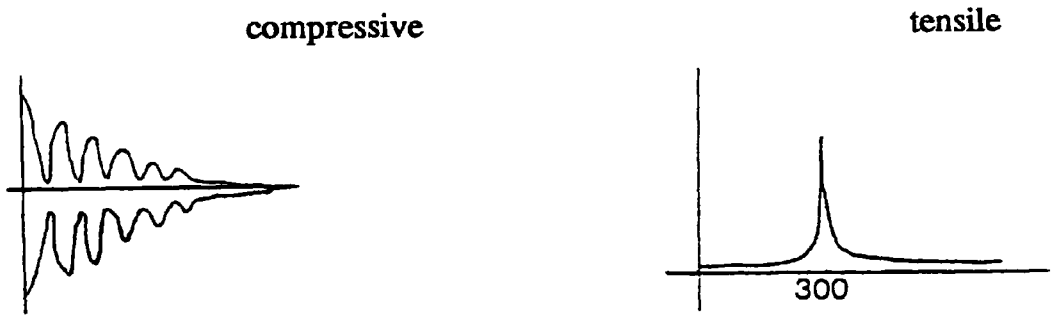

Case 2: Proposed signal type - tensile

Case 3: Proposed signal type - compressive

Case 4: Proposed signal type - compressive

Figure 4.75: Schematic diagrams showing the different cases for signal classification together with the proposed signal types tensile or compressive [106].

continued ...

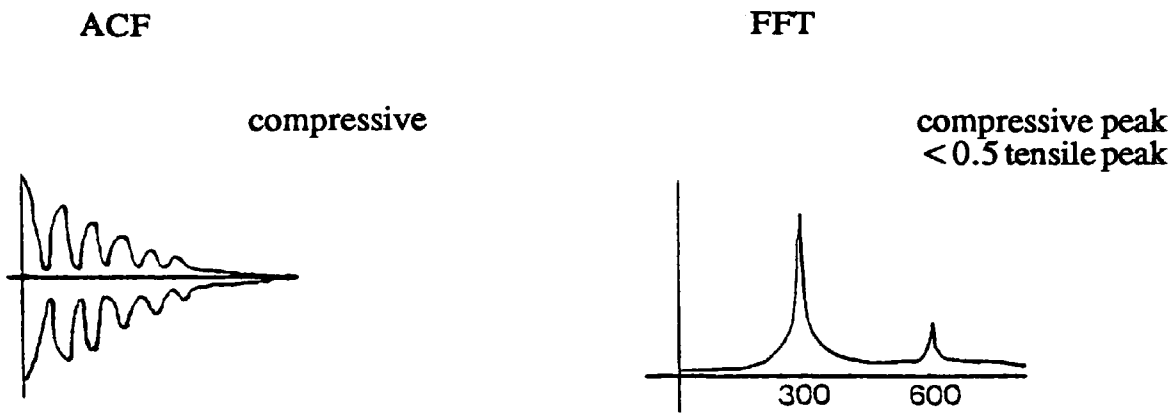

Case 5: Proposed signal type - compressive

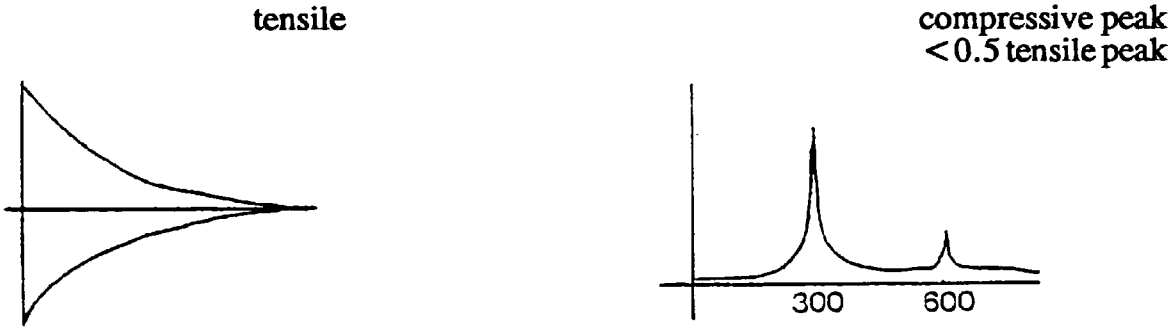

Case 6: Proposed signal type - tensile

Figure 75: Schematic diagrams showing the different cases for signal classification together with the proposed signal types tensile or compressive [106].

Material	Thickness [μm]	T [%]	C [%]	U [%]
Iron oxide	8.0	73	20	7
"	10.0	60	39	1
"	11.0	69	31	0
"	11.5	77	15	8
"	19.0	53	22	25
"	23.0	69	25	6
"	23.0	64	23	13
"	36.0	97	2	1
"	39.0	57	36	7
"	40.0	81	19	0
Brittle lacquer	105.0	62	36	2
"	105.0	61	36	3
"	125.0	64	33	3
Nickel oxide	6.0	83	11	6
"	45.0	80	12	8
Brittle lacquer*	90.0	82	18	0
"	125.0	71	24	5
	Average	70.8	23.6	5.6

Table 4.6: Results of the second analysis for the tests with the layer subjected to tensile stress. T = tensile signals, C = compressive signals and U = unclassified signals. *) Buckling tests (see also section 4.3.3) [106].

Material	Thickness [μm]	T [%]	C [%]	U [%]
Iron oxide	6.5	43	52	5
"	11.0	31	26	43
"	11.5	77	21	2
"	11.5	67	27	6
"	20.0	43	51	6
"	23.0	52	45	3
"	23.0	54	46	0
"	39.0	56	43	1
"	40.0	69	28	3
"	40.0	69	30	1
Brittle lacquer	105.0	47	52	1
"	105.0	39	55	6
"	125.0	43	49	8
Nickel oxide	6.0	70	19	11
"	57.5	48	33	19
Brittle lacquer*	90.0	34	56	10
"	180.0	24	66	10
	Average	50.9	41.1	8.0

Table 4.7: Results of the second analysis for the tests with the layer subjected to compressive stress. T = tensile signals, C = compressive signals and U = unclassified signals. *) Buckling tests (see also section 4.3.3) [106].

4.5.3 Discussion

Both analyses produced a different percentage distribution for the tensile and compressive tests. The first crude analysis was viewer independent and indicated that there must be a slight difference in the AE signals from tensile and compressive oxide failure. In this context the FFT appeared to be a promising parameter. The second more detailed analysis was made to harness the expected periodicities in the signals from tests with the layer subjected to compressive forces (see also section 4.5, page 175). The

ACF was therefore used in this analysis because auto-correlation can detect such periodicities. The analysis was based more on the shape of the ACF and hence more subjective. However it only produced significant data for the tensile tests but not for the compressive tests.

The results from both analyses were much less significant than those found by Hall *et al.* [21]. This discrepancy could be explained by the different experimental arrangement used, i.e. 4-point bend jig instead of a 3-point bend jig where the roller was in the zone of failure during compressive loading, or more likely by the fact that the analysis here was carried out numerically and hence was less subjective.

In summary, the preceding analyses still showed that there is a difference in the AE from tests with the layer subjected to compressive or tensile forces, i.e the failure mechanisms had an effect on the AE signals. On the other hand the results were not significant enough, in particular for the compressive tests, to allow the failure mode or failure mechanism to be determined solely on the basis of the AE signal parameters, viz. shape, FFT and ACF.

CHAPTER 5: Conclusions and Future Work

5. CONCLUSIONS AND FUTURE WORK

5.1 Conclusions

A new 4-point bend test technique has been used successfully to measure oxide failure strains in tension and compression with iron and nickel oxide at room temperature and 550 or 900 °C, respectively, using strain rates of $\sim 10^{-4}$ and $\sim 10^{-5}$ s^{-1}. Post metallographic examinations have been used together with the recorded AE to establish the failure mechanisms operating in these oxides and in brittle lacquer which was used as a model layer for the AE.

The main conclusions were:

1. Failure in tension started with the formation of equi-distant through-scale cracks which also produced a maximum AE activity. The rate of further cracking and AE was reduced by elastic and plastic stress relaxation processes. Interface delamination and hence AE only increased again when all stress relaxation processes had been exhausted which only happened in the case of iron oxide.
2. The spacing between the cracks in tension increased linearly with thickness. The larger spacing at growth temperature showed that plastic stress relaxation processes in form of interface slip, oxide creep or substrate yielding at the base of through-scale cracks dominated. The NiO interface had a higher resistance to delamination than the iron oxide interface.
3. The energy for crack formation increased with increasing layer thickness for all materials, due to the higher elastic strain energy released during fracture of thicker scales to create new surfaces which had larger areas than those formed in thinner scales.
4. Four failure mechanisms were found for the failure of the three layers under compressive forces. (i) Iron oxide scales $\leq 12\mu m$ thick showed interface delamination and buckling within the main area of oxide which was characteristic of Route II mechanism for weak interface/strong oxide cohesion. (ii) Thicker iron oxide scales failed by interfacial delamination initiated at the extreme edge of the oxide area, which was due to the oxide geometry. (iii) NiO showed shear failure with buckling and wedging along fracture zones which formed a regular pattern. The spacing and the size of the fracture zones increased with oxide thickness. (iv) Brittle lacquer failed by shear cracking within the layer which was characteristic of Route I mechanism for strong interface/weak cohesive bond.
5. Failure initiation and failure mechanism in compression depended on the relative shear strength of the oxide, the buckling stability of the layer and the relative shear strength of the interface. Spallation always required the propagation of a crack at the interface.
6. The energy of the AE signals increased with increasing strain in compression

indicating that failure became more likely and that increasingly larger amounts of elastic strain energy were released during compressive failure. The cumulative AE energy count and count number increased with increasing thickness for both oxides and brittle lacquer. However, the average AE energy count and count number per signal remained independent of thickness for iron oxide but increased with thickness for NiO and brittle lacquer, which could be used to explain the different failure mechanisms.

7. The proposed model for the prediction of failure in tension or compression included the fracture mechanics criteria for through-scale cracking or interface delamination respectively. The fracture mechanics parameters accounted for the elastic part of the deformation prior to failure and a second set of scale parameters was required to account for the behaviour of a thin growing scale on a thick substrate, viz. growth strains, cooling strains, plasticity and lateral oxide growth. The predictions agreed well with measured failure strains if allowance for both sets of parameters was made.

8. The composite void size was the critical fracture mechanics parameter for prediction of failure in tension. The higher failure strains for iron oxide at room temperature compared to those at 550 °C (when tested with a strain rate of $\sim 10^{-4}$ s^{-1}) were explained in terms of residual compressive cooling strains of ~ 0.05 - 0.06% which had to be overcome before the oxide experienced a net tensile stress. The lower strain rate of $\sim 10^{-5}$ s^{-1} with iron oxide at 550 °C gave approximately the same K_{IC}-value as when tested with a rate of $\sim 10^{-4}$ s^{-1}, although crack spacing and failure strains were larger due to time dependent creep under those conditions. Similarly the failure strains for NiO at 900 °C were higher than those at room temperature as a result of time dependent creep. A K_{IC}-value of ~ 1.1 MN $m^{-3/2}$ was obtained for iron oxide at room and at growth temperature. Values of 0.41 and ~ 1.61 MN $m^{-3/2}$ were found for NiO at room temperature and at 900 °C. The residual growth stresses were determined as approximately zero for iron oxide. The compressive residual stresses in NiO at room temperature were ~ 175 MPa and the fracture surface energy was 3.4 and 0.8 J m^{-2} for iron and nickel oxide, respectively.

9. The energy release rate for interfacial failure was the critical fracture mechanics parameter for prediction of failure in compression, and measured failure strains with iron oxide at room temperature were used to derive a strain energy release rate for interfacial failure of 27 J m^{-2}. Measured failure strains in NiO at room temperature were much higher than the predicted values. The difference was accounted for by microcracking, which is included in the scale parameters. In both cases failure strains at growth temperature were higher than at room temperature, but no direct measurements could be made due to experimental

difficulties.

10. Numerical analysis of the AE signals and their shapes showed that there are slight differences between the AE from failure under tension and compression. However, the results were not significant enough to determine the mode of failure by analysing a few AE signals.

5.2 Future Work

1. Thus far, measurements have only been performed on iron and nickel oxide scales and brittle lacquer layers. Therefore future work should concentrate on the more important chromium and aluminium oxides.
2. Failure strains should be compared with measurements obtained using a different technique which can also monitor failure under applied load such as the modified vibration technique shown in refs. 19,53.
3. Failure strains were calculated using specimen dimensions, jig dimensions and the time from the start of the test to the first AE assuming a constant crosshead speed. In addition allowance had to be made for the initial load (see also Appendix B). The failure strain could be determined more accurately by measuring the deformation of the specimen directly using non-contact techniques since any contact with the oxide or the specimen could be a source of erroneous AE. Such techniques would probably require some modification for application in a furnace environment.
4. The prediction of failure requires that values for Young's modulus, fracture surface energy, residual stress and oxide creep are known. However values for these parameters vary to some extent in the literature. Therefore it would be important to perform separate measurements of these parameters using at least two different techniques for each parameter. Such measurements would provide the necessary data which would be needed to make more accurate predictions with the given model.
5. The composite void size was critical for prediction of failure in tension. Estimation of the composite void size was done manually by applying the given interaction conditions [2]. In addition the composite void size was mainly established using polished cross-sections which may have been damaged by polishing. More reliable data were obtained from fracture surfaces. However in both cases the information was restricted to one plane, i.e. one section of oxide. Quantitative assessment could be obtained by using either standard SEM image analysis features or developing a new technique for automatic measurement of void size which can provide 3-dimensional information on void size, position and distribution. Acoustic microscopy could be used for this purpose.

6. Nicholls and Hancock [2] have proposed a conservative model for void interaction which simply says that interaction occurs if the spacing is less than one half of the total width of the two surrounding voids. In addition interaction was considered in x-,y- and z-direction independent of the applied stress. In the present study void interaction was only regarded to be critical in the direction normal to the applied strain. In order to arrive at a more realistic model the directionality of void interaction should be investigated. Important factors would be the void shape, the spacing and alignment of the voids relative to the direction of applied strain. Such a study could be done with the finite element method (FEM).
7. FEM could also be used to model failure mechanisms because conventional fracture mechanics cannot be used to predict interface cracking and delamination. Only FEM can model an oxide/substrate interface which is made up of a brittle material on one side and an elastic/plastic material on the other side. Evans [8,43] has already modelled Route I and Route II failure in compression. Similarly, the failure mechanism in tension could be modelled with particular focus on elastic and plastic stress relaxation processes. At the same time the relative importance of interface slip compared to substrate yielding at the base of through-scale cracks could be evaluated.
8. A small 4-point bend jig with loading facility could be made for use in an electron microscope, so that the growth of the cracks could be monitored with high resolution and correlated with the AE released during the growth. In this way it might be possible to relate AE signals to specific crack growth events.
9. The numerical analysis of the AE signals has revealed slight differences in the AE from tensile and compressive failure. Better classification of AE signals might be obtained using commercially available pattern recognition software.
10. Recent work by Scruby *et al.* [70,72] might enable absolute calibration of the AE system from the AE source to the analyser. If this can be achieved the measured AE energy counts could be related to the source energy. The source energy could be used to determine the fracture surface energy when the crack length and depth is known assuming that a constant proportion of the total strain energy is released as AE energy.

APPENDICES

APPENDIX A: Natural Frequencies of the Specimens

A.1 The Natural Frequency of the Longitudinal waves

The natural frequency of the longitudinal wave in a continuous solid is [108]:

$$\frac{\partial^2 u}{\partial t^2} = \frac{E}{\rho}\frac{\partial^2 u}{\partial x^2} \qquad \text{(A.1)}$$

The solution for a beam with two free ends is [108]:

$$f = \frac{k}{2l}\sqrt{\frac{E}{\rho}} \qquad \text{(A.2)}$$

where: k = 1,2,3...
l = specimen length in m
E = Young's modulus = 210 10^9 GPa for mild steel
ρ = density = 7860 kg m^{-3} for mild steel

Results:
for l = 0.1 m: f_1 = 25.8 kHz and f_2 = 51.7 kHz
for l = 0.2 m: f_1 = 12.9 kHz and f_2 = 25.8 kHz

A.2 The Natural Frequency of the Transverse Waves

The resonant frequencies of the transverse waves for the specimens were determined using the Rayleigh's method. However, the frequencies calculated with this procedure are always approximately 3 - 5% higher than the real natural frequency [108].

The Rayleigh quotient for transverse waves is [108]:

$$R(w) = \frac{\int strain\ energy}{\int kinetic\ energy} = 1 \qquad \text{(A.3)}$$

The total strain or potential energy of a beam is:

$$E_{strain} = \frac{1}{2}\int_0^l EI\left(\frac{d^2W(x)}{dx^2}\right)^2 dx \qquad \text{(A.4)}$$

where $W(x)$ is the deflection shape, E is the Young's modulus and I is the moment of inertia.

The total kinetic energy of a beam is:

$$E_{kinetic} = \frac{1}{2}\int_0^l \rho A\ W(x)^2\ dx \qquad \text{(A.5)}$$

where ρ is the density and A is the cross-section area of the beam. Assuming a sinusoidal deflection shape for the specimen having the form of:

$$W(x) = \sin\left(\frac{\pi x}{l} + \varphi\right) \qquad \text{(A.6)}$$

The Rayleigh quotient then becomes:

$$w^2 = \frac{EI\left(\frac{\pi}{l}\right)^4 \int_0^l \sin^2\left(\frac{\pi x}{l} + \varphi\right) dx}{\rho A \int_0^l \sin^2\left(\frac{\pi x}{l} + \varphi\right) dx} \qquad \text{(A.7)}$$

and with $w = 2\pi f$, the natural frequency became:

$$f = \frac{1}{2\pi}\sqrt{\frac{Eh^2\pi^4}{12\rho l^4}} \qquad \text{(A.8)}$$

Results:

for h = 1.8 mm and l = 0.1 m: f_1 = 421 Hz, f_2 = 842 Hz (for specimens tested at room temperature)

for h = 1.5 mm and l = 0.2 m: f_1 = 88 Hz, f_2 = 176 Hz (for specimens tested at growth temperature)

In this calculation the boundary and loading conditions were not taken into account and the deflection shape was only assumed and not calculated exactly. It was therefore necessary to verify the results by measuring the natural frequency using a low frequency transducer and a narrow band spectrum analyser (Bruel & Kjaer Type 2031). A comparison of the results was made below for a 1.8 mm thick and 0.1 m long specimen, which shows that the calculation produced reasonably accurate results.

Experiment:	Theory:
f_1 = 450 Hz	f_1 = 421 Hz
f_2 = 850 Hz	f_2 = 842 Hz

APPENDIX B: Error Assessment for the Fracture Strain Measurement

B.1 Errors in the Strain Calculation

The factor t equation (3.1) was the time at which failure occurred and had the following contributions:

$$t = t_1 + t_2 - t_3 \qquad \text{(B.1)}$$

where t_1 was the time reading from the Locan AT equipment at which failure occurred, t_2 was a time correction to account for the initial load and t_3 was a time correction which was only necessary for samples coated with Berkatekt 12 coating. It accounted for the indentation of the rollers into soft coating, during which the sample did not deform and stress and strain in the oxide remained constant. In this context the roller indentation depth has been measured on a series of samples coated with Berkatekt 12 which were tested at room temperature and at growth temperature. The measured indentation depth was used to calculate the time which was needed to create such an indent. The time was subtracted from the starting time of AE, because the crosshead movement in that time did not add to the overall deformation of the specimen. No such correction was required for the test with nickel oxide and DPG 3582 coating, since the coating was a sticky liquid and hence the rollers were in direct contact with the specimen.

The correction t_2 was necessary, because an initial load of 5 - 10 N was needed to ensure that specimen and rollers were in contact prior to testing so that the deformation started instantly and was directly proportional with time. Only then could the time measurement be used for the strain calculation (see also section B.2). However, the initial load caused a very small deformation, which added to the total deformation. It was accounted for by extending the load-time curve to zero load. The time was then determined on the time axes and added to the starting time of the AE, because this time was required to raise the load to the pre-load level (Figure B.1).

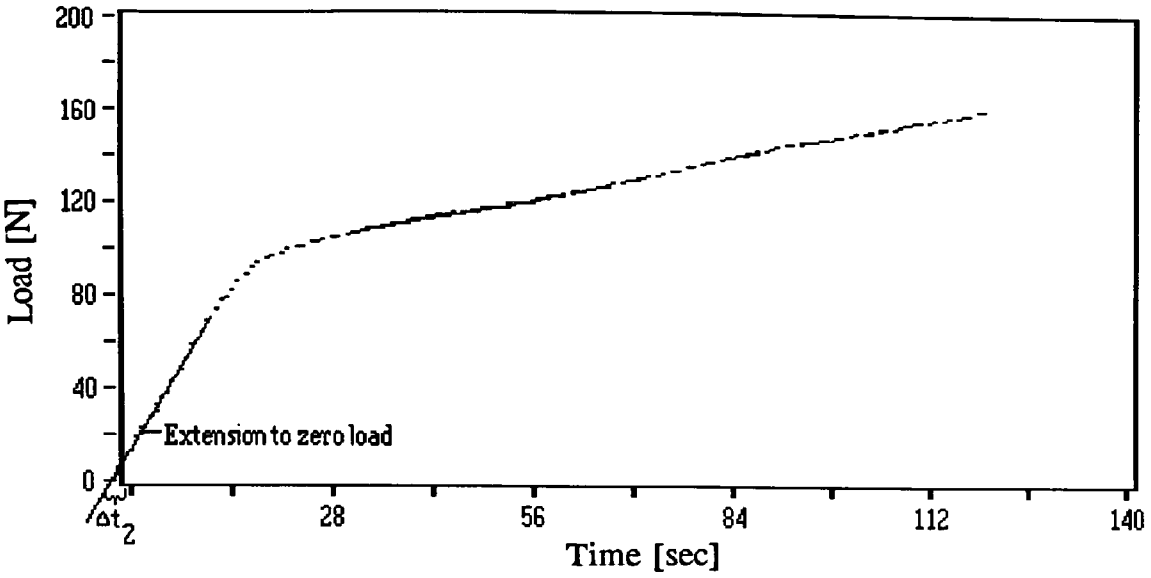

Figure B.1: Load as a function of time showing the compensation Δt_2 for the initial load.

Assessment of the single errors in the failure time measurement:

Δt_1 = +/- 1 sec The timer of the Locan AT was accurate within 0.001 second. However, a much larger value of +/- 1 sec was used to account for the uncertainties in determining the first AE signal from the oxide failure. The threshold was set so that a few randomly distributed signals were recorded in a calibration test. Therefore, it was not always possible to use the first signal in a test. Instead the first signal in a group of signals or the first high energy signal was used, which caused the error or uncertainty.

Δt_2 = +/- 0.5 sec

Δt_3 = +/- 1 sec

This gave a total error in the time measurement of Δt +/- 2.5 sec assuming that

$$\Delta t = \pm|\Delta t_1| + |\Delta t_2| + |\Delta t_3| \qquad \textbf{(B.2)}$$

Assessment of the single errors in the strain equation:

Δd=+/-0.05 mm

Δf =+/-0.04 mm (It was also found that the crosshead moved with a constant speed with less than 0.5% variation)

Δs =+/-0.1 mm

Δu =+/-0.1 mm

The maximum error in the strain calculation using the Gaussian error propagation law is:

$$\Delta F = \pm\left(\left| \frac{\partial F}{\partial x} \Delta \bar{x} \right| + \left| \frac{\partial F}{\partial y} \Delta \bar{y} \right| + \ldots \right) \qquad \textbf{(B.3)}$$

where $\Delta\bar{x}$ and $\Delta\bar{y}$ are the mean errors of the measured values or the estimated errors of the equipment.

The mean error is:

$$\Delta \bar{F} = \sqrt{\left(\frac{\partial F}{\partial x} \Delta \bar{x} \right)^2 + \left(\frac{\partial F}{\partial y} \Delta \bar{y} \right)^2 + \ldots} \qquad \textbf{(B.4)}$$

The estimated errors were approximately:

ε = 0.14% +/- 15% (maximum error)

ε = 0.14% +/- 11% (mean error)

for a 1.8 mm thick specimen not coated with Berkatekt 12, a crosshead speed of 2 mm min^{-1}, an outer roller spacing of 60 mm, an inner roller spacing of 20 mm and failure occurring at a strain of 0.14% or after 15 seconds.

When the failure occurred at a strain of 0.28% or after 30 seconds the estimated errors were approximately:

ε = 0.28% +/- 10% (maximum error)

ε = 0.28% +/- 6% (mean error)

The estimated errors were the same for tests at room and at oxide growth temperature. The factor t_3 caused an additional error of approximately 5% in tests with iron oxide grown on mild steel using Berkatekt 12 coating. Higher failure strains resulted in proportionately smaller errors, because the time measurement showed the same absolute errors for all tests. The contribution of the other errors was less than 10% and hence negligible compared to the errors caused by the time measurement.

B.2 Accuracy of the Strain Equation

Equation (3.1) was solely based on the deformation geometry of a beam in a 4-point bend jig which resulted from the relative displacement of the two roller pairs. It assumed linear elastic behaviour of the beam. However, the equation was also valid in the plastic region if the curvature between the rollers of the 4-point bend jig remained continuous, i.e. no localised yielding occurred. In order to see whether the equation could be used for strain calculation in the present study it was necessary (i) to measure the accuracy of the equation during linear elastic and plastic deformation and (ii) to investigate whether the strain in the beam was actually proportional to time during plastic deformation. In this context, a strain gauge was mounted on the surface and measured strains were compared with the calculated strains.

The calculated strains using equation (3.1) (page 94) were within +/-2% of the measured strains during elastic deformation. The strain was found to be proportional to time or crosshead movement during elastic and plastic deformation. The slope changed slightly at the elastic/plastic transition point and hence the calculated strains were smaller than the actual strain during plastic deformation (Figure B.2). However, this had only little effect on the oxide failure strain measurement since failure generally occurred during elastic sample deformation or at the beginning of the plastic deformation, i.e. at strains <0.5% when the change of slope had only a small influence, e.g. the error was ~7% at 0.5% strain. Hence, equation (3.1) could be used to calculate the failure strain during elastic and plastic deformation of the samples solely based on the time measurement.

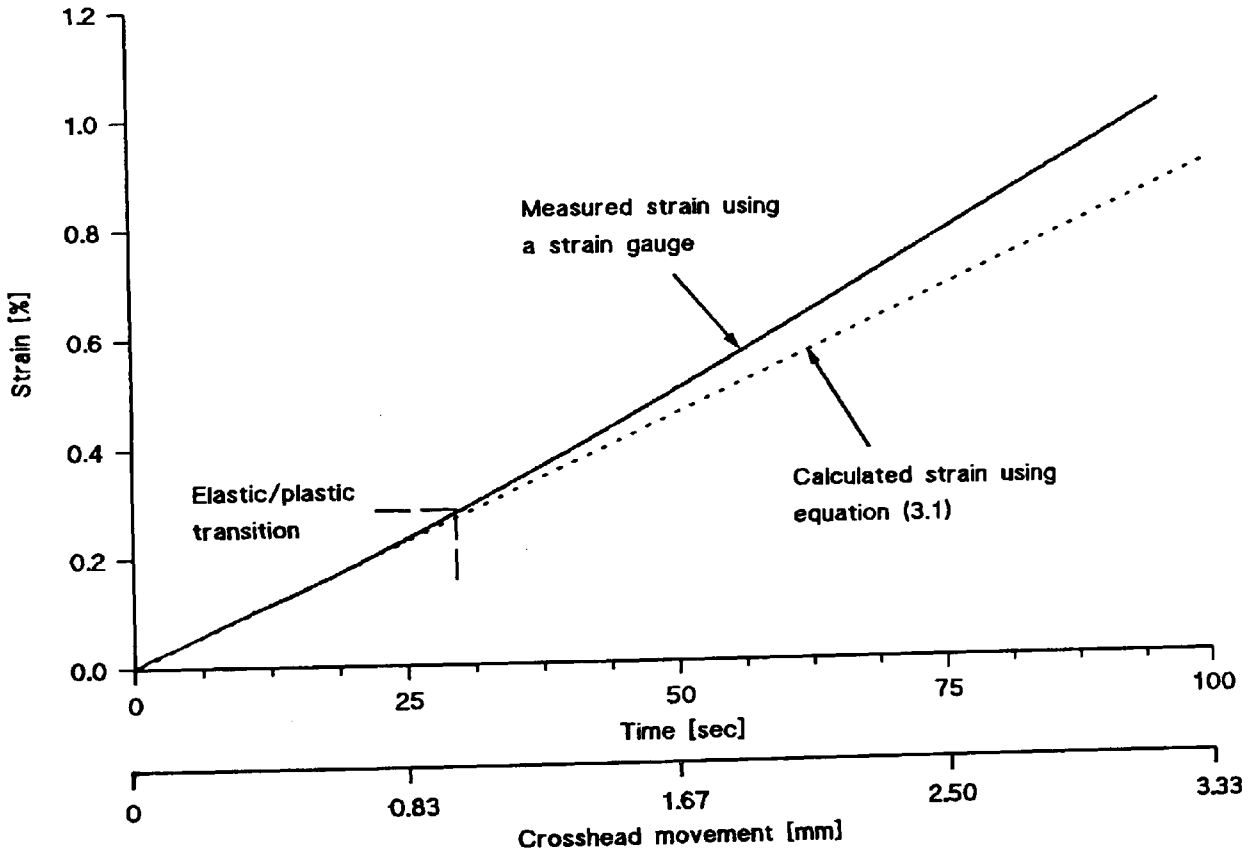

Figure B.2: Measured strain as a function of time or crosshead movement for a 10 μm thick iron oxide grown on mild steel and tested in tension at room temperature.

APPENDIX C: Some Aspects of the Auto-Correlation Function (ACF) and the Fast Fourier Transformation (FFT)

C.1 Auto-Correlation Function

The auto-correlation function (ACF) of a signal is an average measure of its time domain properties. The ACF r_{xx} is defined as [109]:

$$r_{xx}(\tau) = \lim_{T_o \to \infty} \frac{1}{T_o} \int_{-\frac{T_o}{2}}^{\frac{T_o}{2}} f(t)\, f(t+\tau)\, dt \qquad \text{(C.1)}$$

It is therefore equal to the average product of the signal $f(t)$ and a time-shifted version of itself, and is a function of the imposed time-shift τ. The above expression applies to the case of a continuous signal of infinite duration and a slightly modified version exists for signals of finite duration which is generally called finite ACF.

In the case of a sampled-data signal the product of the signal and its shifted version has only non-zero values when the shift is equal to a multiple of the sampling interval T and the ACF is therefore defined as [109]:

$$r_{xx}(k) = \lim_{N \to \infty} \frac{1}{2N+1} \sum_{m=-N}^{N} x_m\, x_{m+k} \qquad \text{(C.2)}$$

where x_m and x_{m+k} represent two values separated by kT seconds and the summation has $(2N+1)$ terms with the integer parameter m taken between $-N$ and $+N$. In the case of a signal of limited duration there is once again a finite version of the above expression. The precise definition of the ACF for finite and infinite signals tends to vary somewhat from text to text. Importantly they are all measures of the average product of a signal and its time shifted version [109]. The signal should be stationary and have a zero-mean i.e. any trend or offset should be removed before calculating the ACF [109].

Detection of periodicity is the main objective for ACF application. The correlated waveform of a periodic signal will tend to have several peaks repeated at certain time shifts. The peak at $\tau=0$ will have the largest possible value of the ACF. Whether the peak value is attained again at other values of τ depends on whether or not the various components in the signal are harmonically related but in any event it can never be exceeded.

The ACF was used because the repeating maxima in a compressive signal (cf. Figure 1.1b, page 26) were thought to be echoes, i.e. closely related to each other. ACF can be used to unearth such similarities within a signal and several maxima were expected in the auto-correlogram of a compressive signal.

Cross-correlation is a closely related function which describes the effects of time -

shifts imposed between two different signals [109]. Although it appeared suitable to reveal similarities between signals it was not used in the present study because of the difficulty of interpretation with random signals.

C.2 Fast Fourier Transformation (FFT)

The basis of the Fourier series is that a complex periodic waveform can be made up by the summation of sinusoidal and cosinusoidal waves of different frequencies. The Fourier transform does for the non-repetitive signal what the Fourier series does for the repetitive one [109]. The Fourier transform of a sampled-data signal is generally referred to as a discreet fourier transform (DFT). Fourier transform involves a large number of calculations and a careful investigation shows that many of the multiplication operations involved are repeated [109]. The fast fourier transformation (FFT) aims to eliminate such repetitions as much as possible and hence it increases the efficiency in calculation. FFT algorithms become more and more attractive as the number of signal samples increases and are generally most efficient when this number is an integer power of 2 (say 1024 and 2048) [109].

In the present study FFT was used to calculated the frequency spectrum of the AE signals.

APPENDIX D: Typical Prints of Different AE Signals and their Classification

Examples of tensile signals (CASE 1):

a)

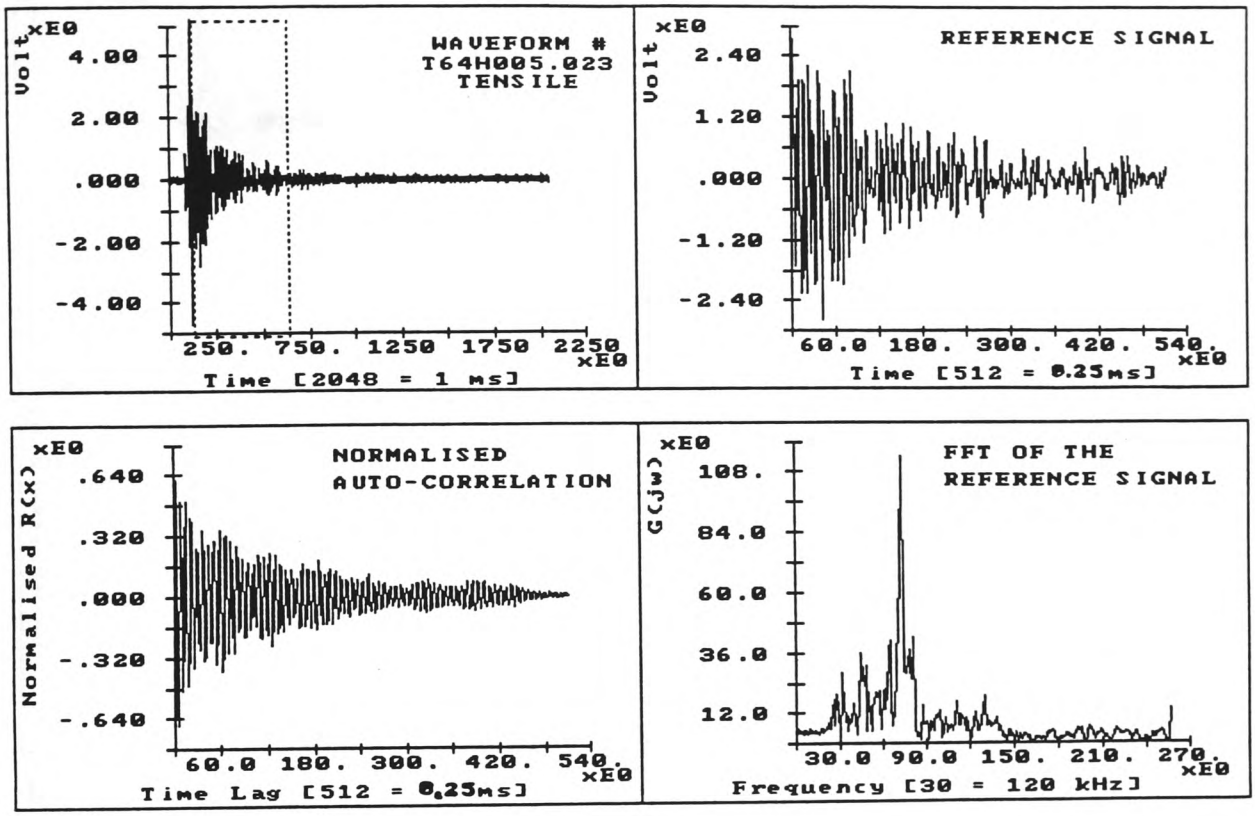

b)

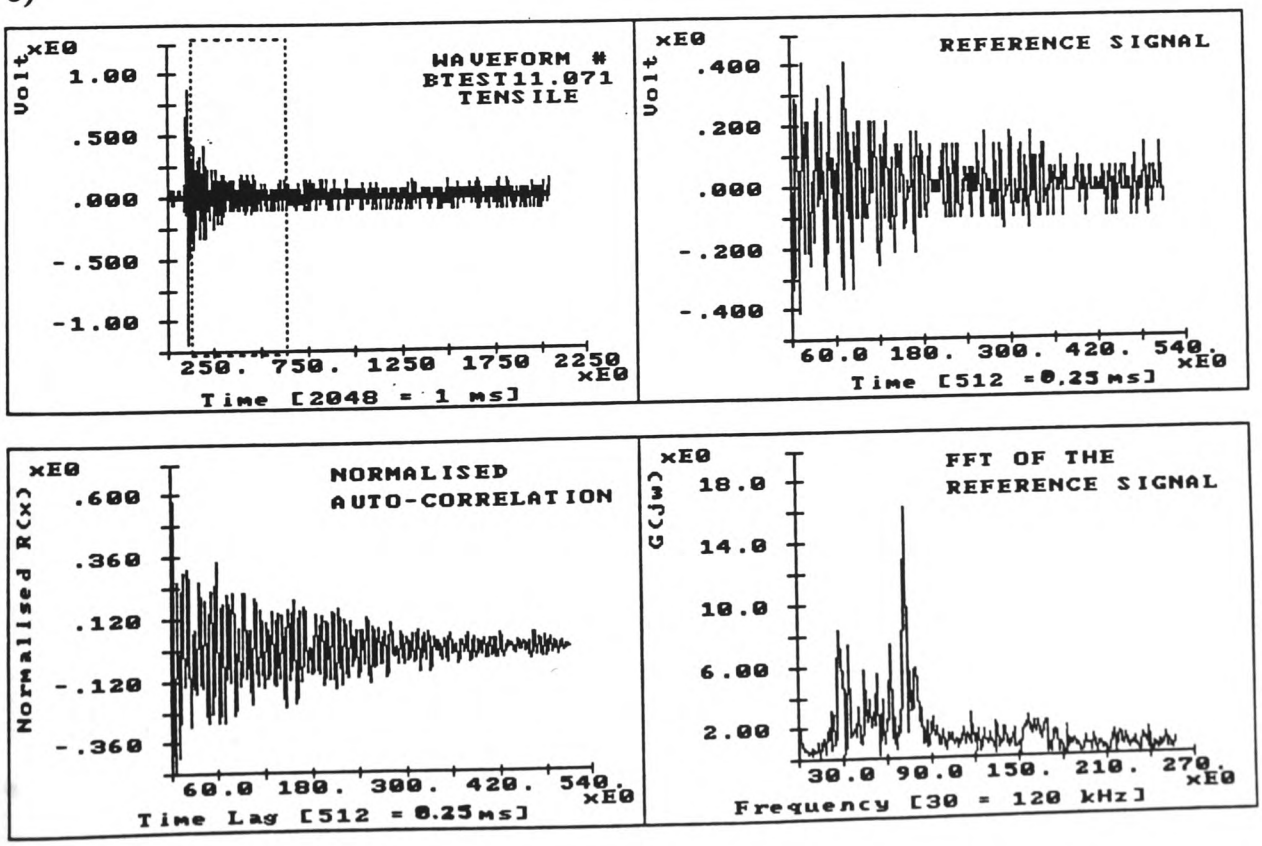

Examples of tensile signals (CASE 2):

a)

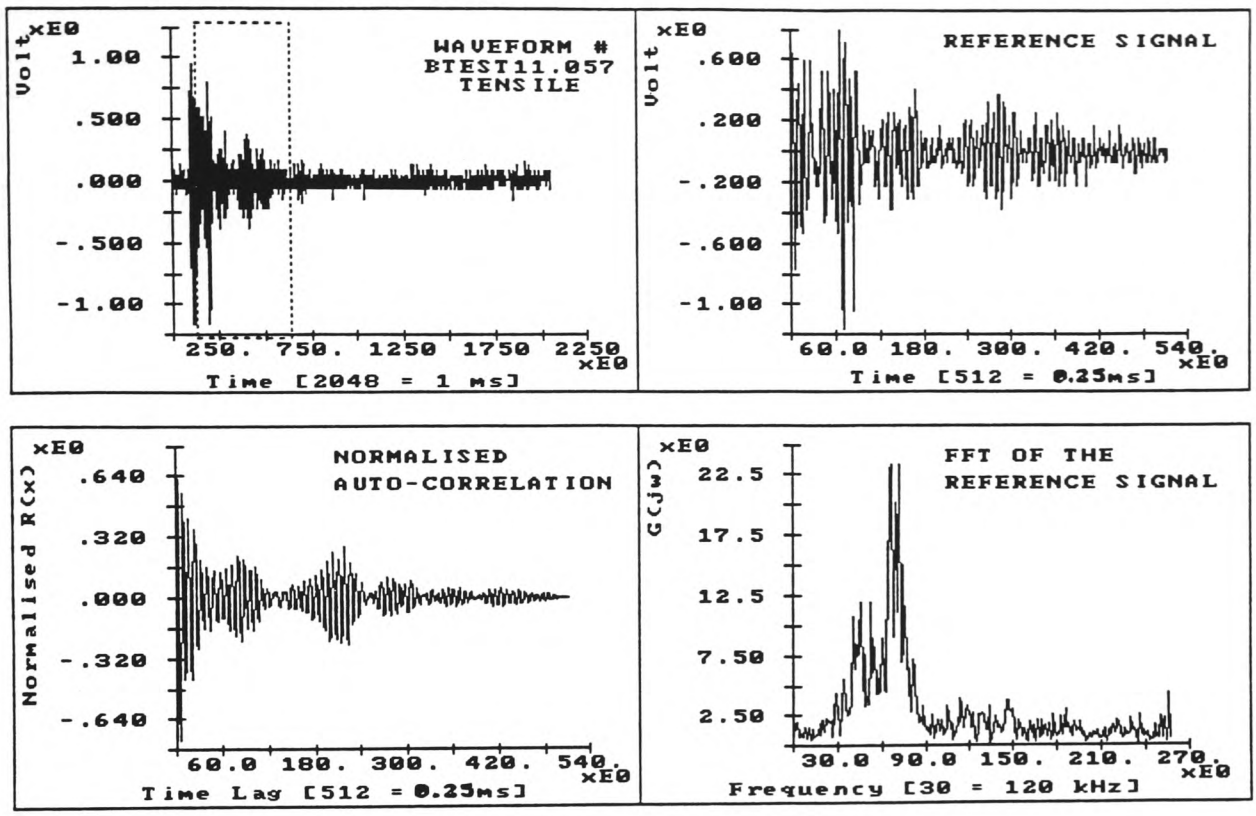

b)

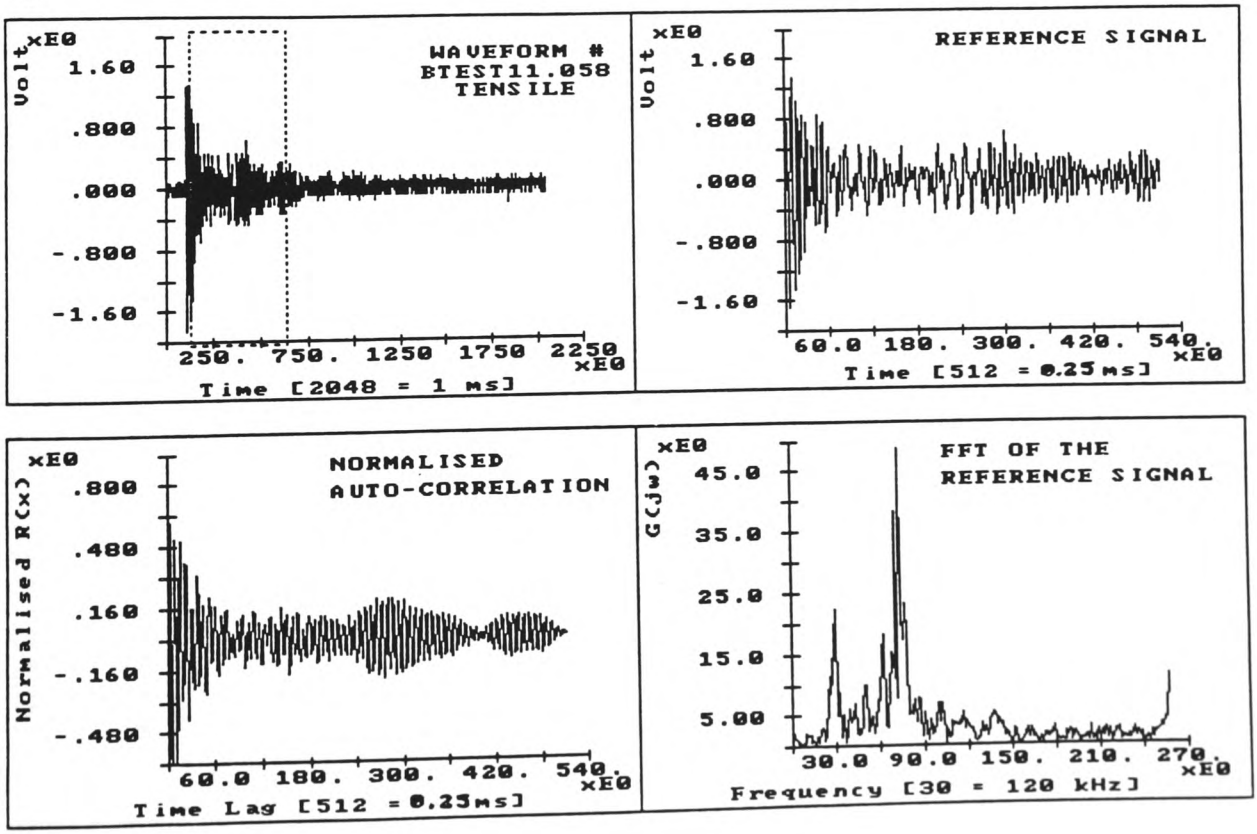

Examples of tensile signals (CASE 6):

a)

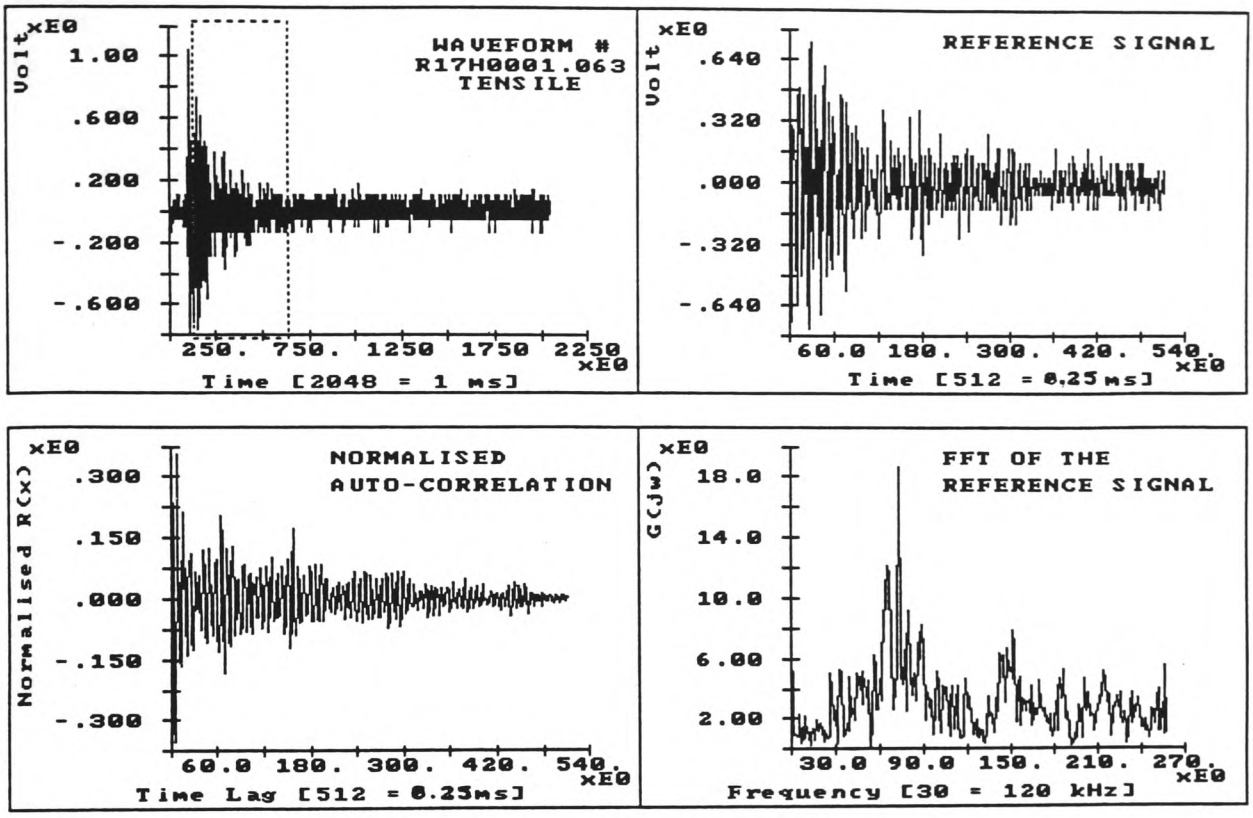

b)

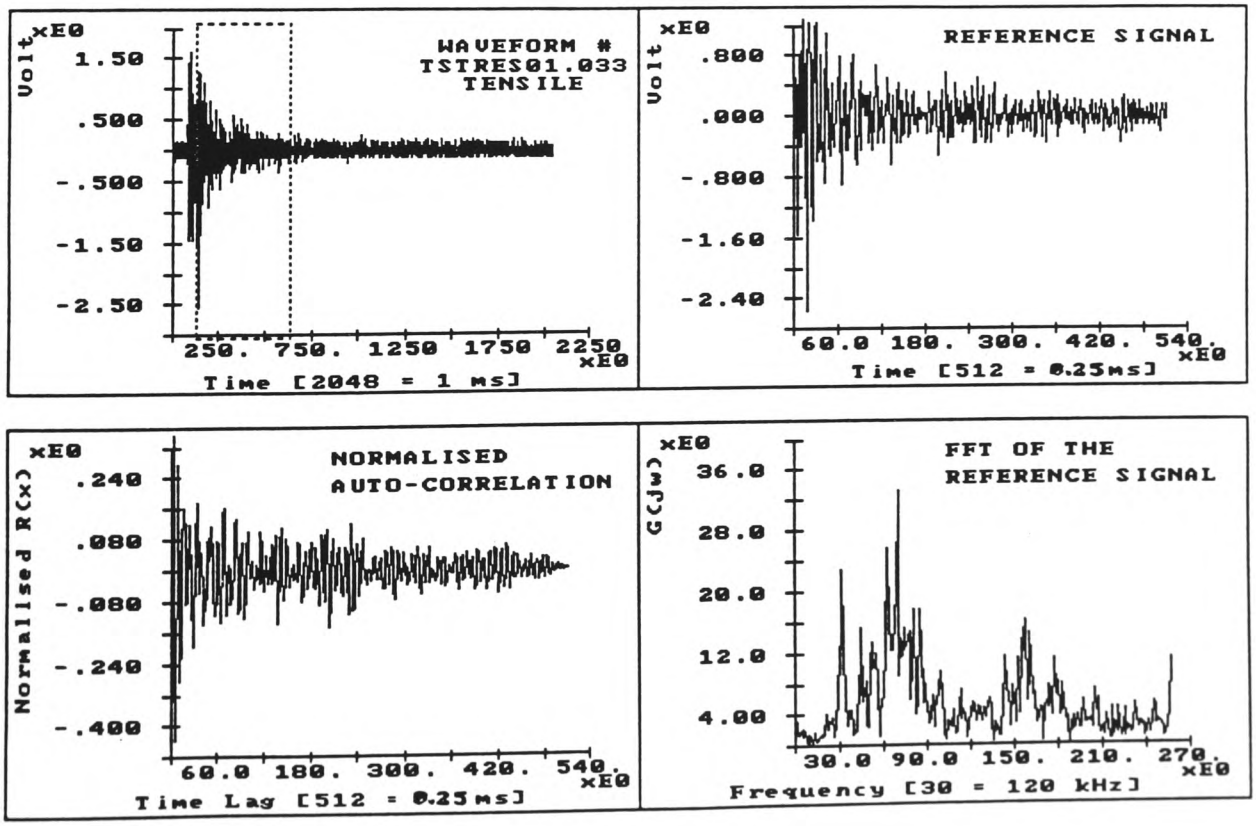

Examples of compressive signals (CASE 3):

a)

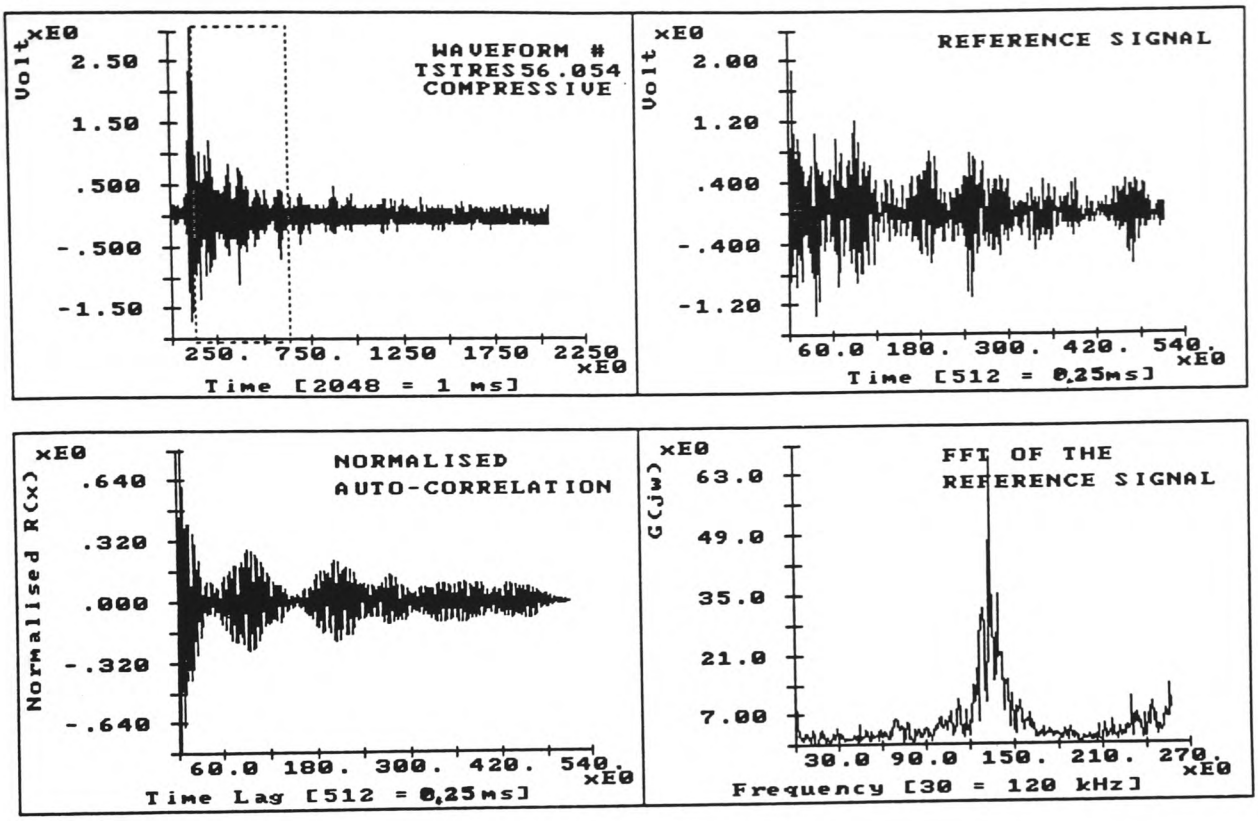

b)

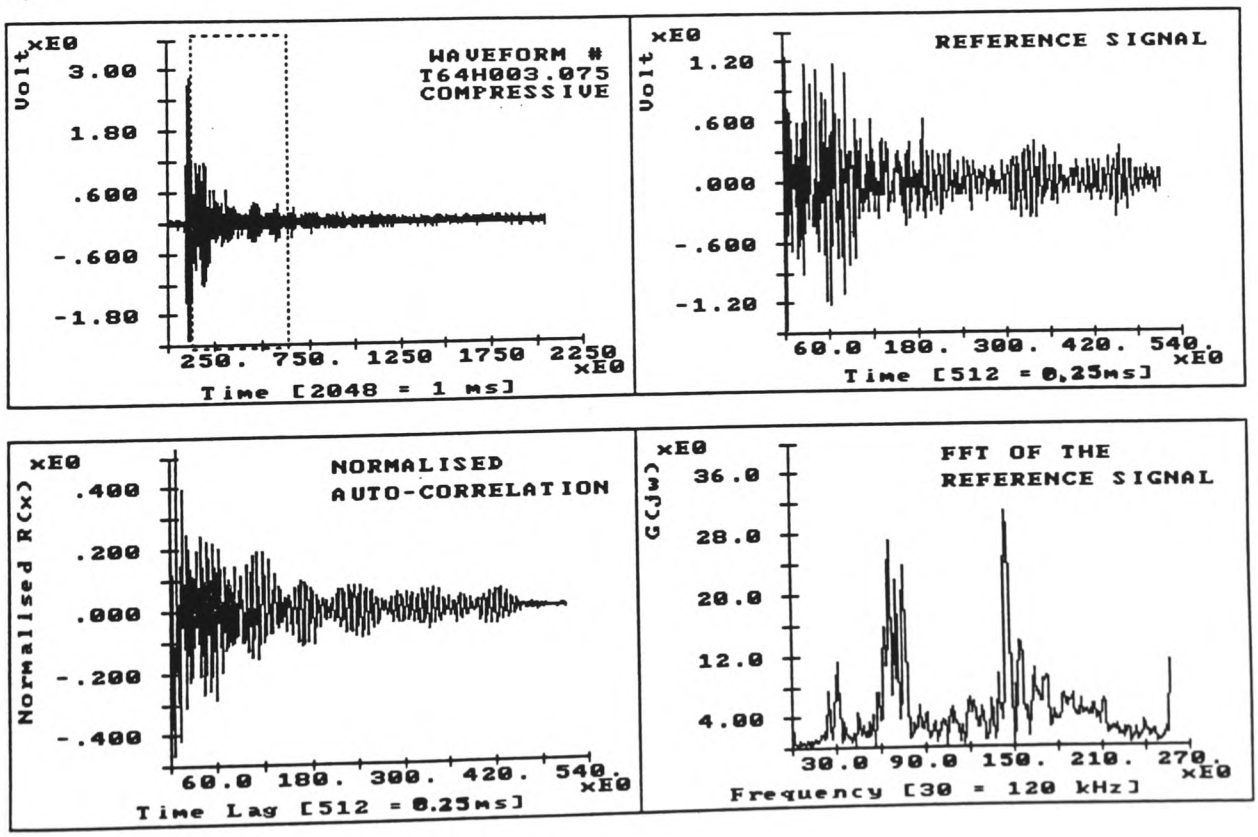

Examples of compressive signals (CASE 4):

a)

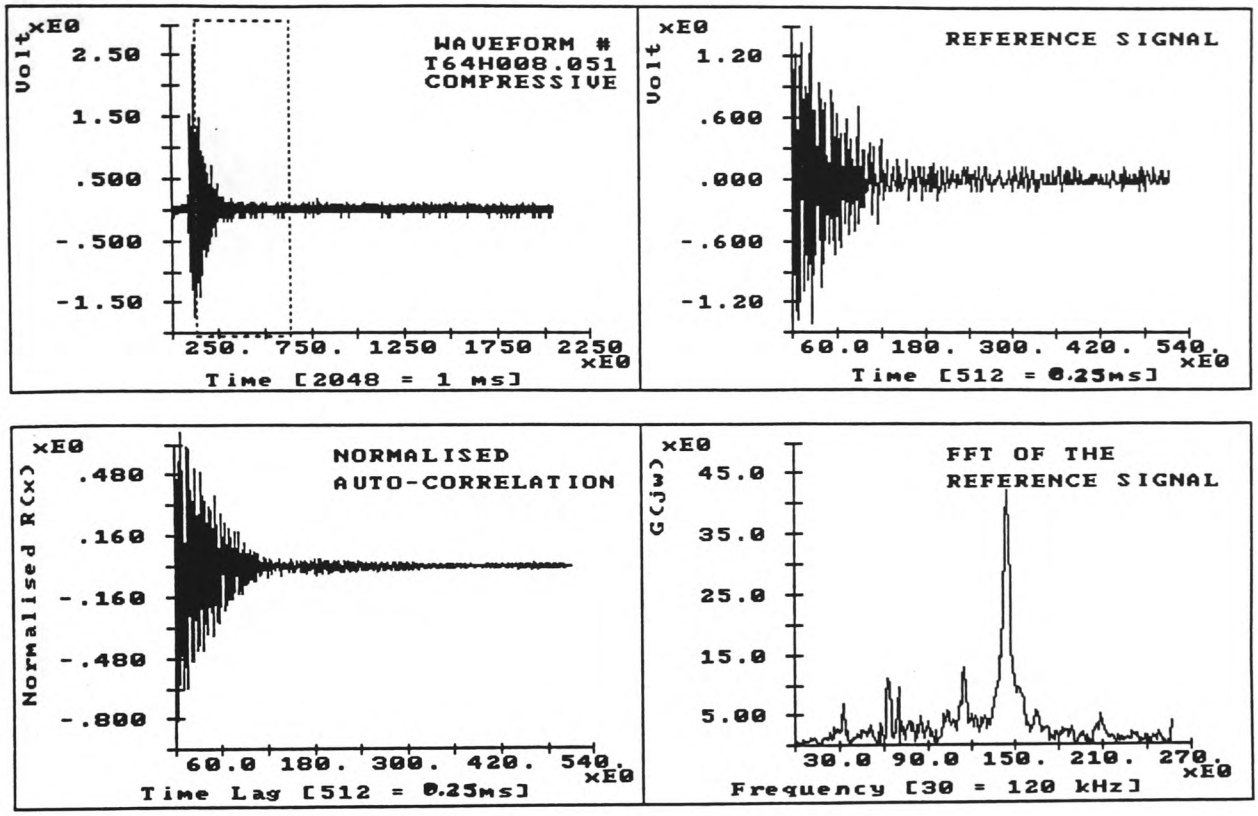

b)

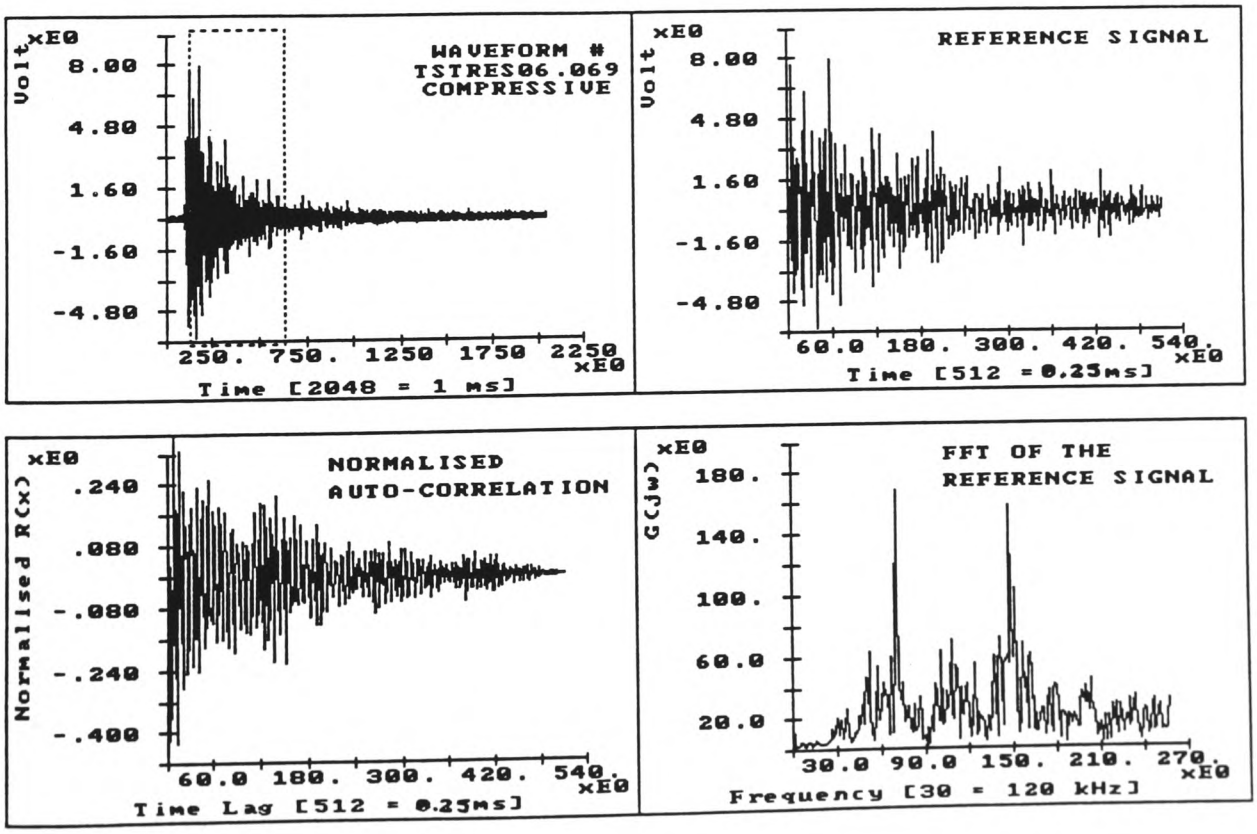

Examples of compressive signals (CASE 5):

a)

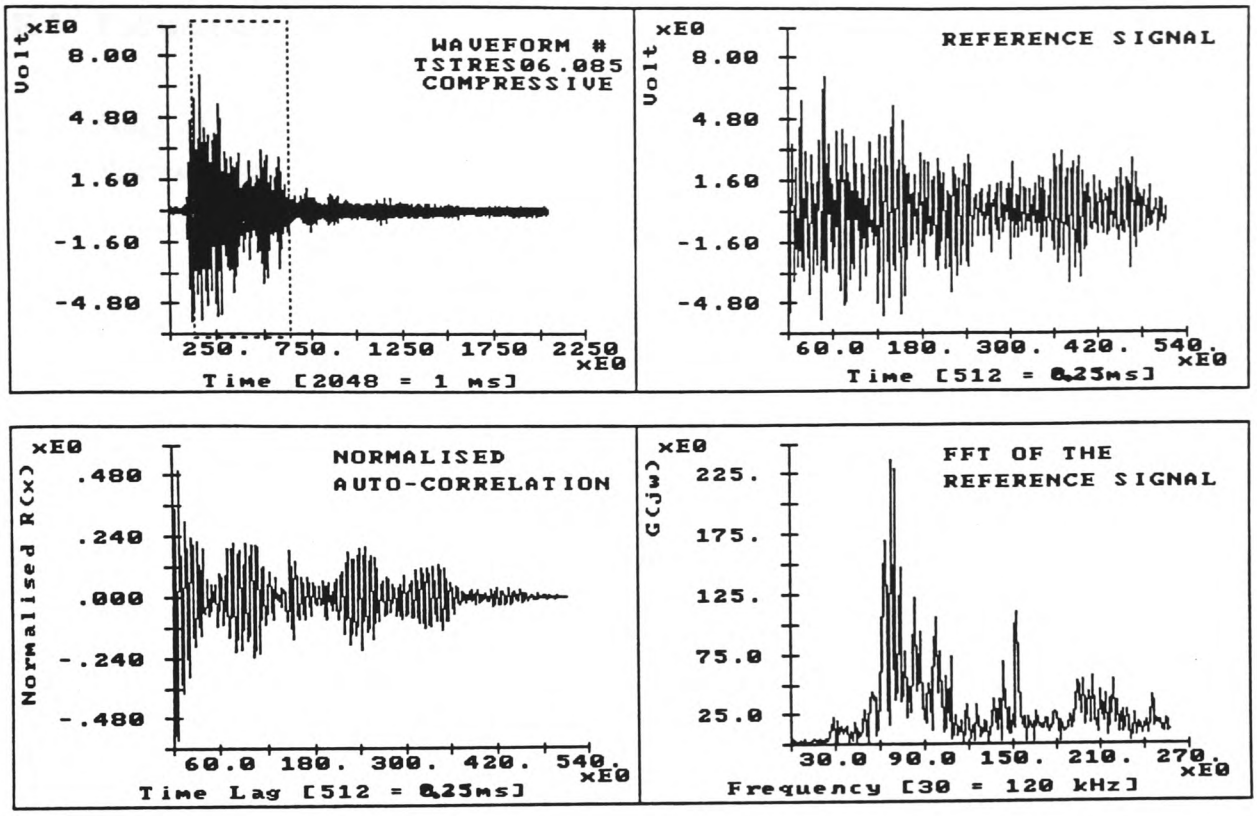

b)

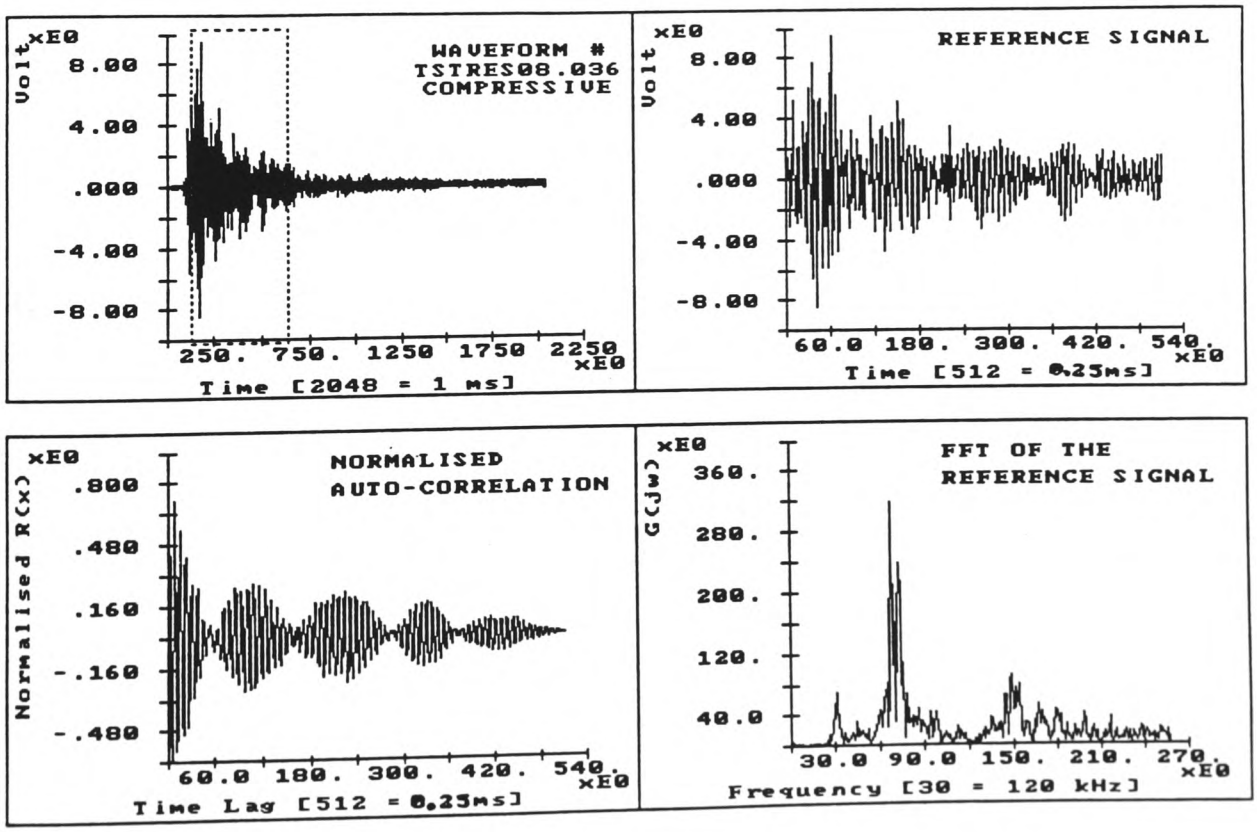

APPENDIX E: List of Publications and Presentations Associated with the Thesis

E.1 Publications

1. Nagl M. M., Hall D. J. and W. T. Evans. Tensile Cracking Behaviour of Oxide Scales. Refereed and accepted for publication in the Proc. of the NACE Conference on Life Prediction of Corrodible Structures (May 1992).

2. Nagl M. M., Evans W. T., Saunders S. R. J. and D. J. Hall. An Investigation of the Failure of Brittle Layers under Compressive Stresses using Acoustic Emission. Refereed and accepted for publication in Materials, Science and Technology (May 1992), to be published in Oct. 1992.

3. Nagl M. M., Evans W. T., Hall D. J. and S. R. J. Saunders. The Failure of Iron Oxide at Growth Temperature under Tensile Stress. Refereed and accepted for publication in the Journal de Physique (June 1992)

4. Nagl M. M., Saunders S. R. J., Evans W. T. and D. J. Hall. The Tensile Failure of Nickel Oxide Scales at Ambient and at Growth Temperature. Refereed and accepted for publication in Corrosion Science (September 1992)

5. Nagl M. M., Chin Y. S. and W. T. Evans. Analysis of the Acoustic Emission Generated by the Failure of Oxide Scales and Brittle Lacquer Layers. Submitted for publication in the Journal of Acoustic Emission.

E.2 Presentations

1. 'Tensile Cracking Behaviour of Oxide Scales' - NACE Conference on Life Prediction of Corrodible Structures, UK: Cambridge (September 1991).

2. 'The Failure of Iron Oxide at Growth Temperature under Tensile Stress' - 3rd International Symposium on High Temperature Corrosion and Protection of Materials, France: Les Embiez (May 1992).

3. 'The Tensile Failure of Nickel Oxide Scales at Ambient and at Growth Temperature' - Conference on Advances in Corrosion and Protection, UK: Manchester (June 1992).

REFERENCES

REFERENCES

[1] Osgerby S. and Dyson B. F. Effects of Oxygen on Creep Performance. *Mater. Sci. & Technol.* 1990, **6**, 2-8.

[2] Hancock P. and Nicholls J. R. Application of Fracture Mechanics to Failure of Surface Oxide Scales. *Mater. Sci. & Technol.* 1988, **4**, 398-406.

[3] Robertson J. and Manning M. I. Limits to Adherence of Oxide Scales. *Mater. Sci. & Technol.* 1990, **6**, 81-91.

[4] Tien J. K. and Davidson J. M. Oxide Spallation Mechanisms. *In:* Cathcart J. V., ed. *Proc. Symp. on Stress Effects and the Oxidation of Metals.* USA: AIME, 1974, pp. 200-219.

[5] Evans H. E. and Lobb R. C. Conditions for the Initiation of Oxide Scale Cracking and Spallation. *Corros. Sci.* 1984, **24**, 209-222.

[6] Evans H. E. and Lobb R. C. An Investigation of the Oxide-Spallation Process in a 20%Cr Austenitic Steel. *In: Proc. 9th Congress on Metallic Corrosion.* Ottawa: NRC. 1984, pp. 46-53.

[7] Schütze M. Failure of Oxide Scales on Advanced Materials due to the Presence of Stress. *In:* Saito Y., Önay B. and Maruyama T., eds. *Proc. Int. Symp. on Solid State Chemistry of Advanced Materials.* Amsterdam: Elsevier, 1992.

[8] Evans H. E. Cracking and Spalling of Protective Oxide Layers. *Mater. Sci. Eng.* 1989, **A120**, 139-146.

[9] Schütze M. Plasticity of Protective Oxide Scales. *Mater. Sci. & Technol.* 1990, **6**, 32-38.

[10] Armitt J., Holmes D. R., Manning M. I., Meadowcroft D. B. and Metcalfe E. The Spalling of Steam Grown Oxide From Superheater and Reheater Tube Steels. *Report FP-686.* Palo Alto: Electric Power Research Institute (EPRI), 1978.

[11] Evans H. E. and Lobb R. C. The Kinetics of Oxide Spallation from a 20Cr Austenitic Steel during Cooling. *In: Proc. EUROCORR'87.* Germany: Dechema, 1987, pp. 135-140.

[12] Evans H. E. Spallation of Oxide From Stainless Steel AGR Nuclear Fuel Cladding: Mechanisms and Consequences. *Mat. Sci. & Technol.* 1988, **4**, 415-420.

[13] Schütze M. Deformation and Cracking Behaviour of Protective Oxide Scales on Heat-Resistant Steels Under Tensile Strain. *Oxid. Met.* 1985, **24**, 199-232.

[14] Schütze M. The Healing Behaviour of Protective Oxide Scales on Heat-Resistant Steels After Cracking Under Tensile Strain. *Oxid. Met.* 1986, **25**, 409-421.

[15] Schütze M. and Rahmel A. Observations on the Cracking Behaviour of Oxide Scales During Creep of the Base Metal and on Creep Enhanced Internal Corrosion. *In:* Manning M. I. and Meadowcroft B., eds. *Proc. Conf. on Corrosion in Coal Conversion Systems.* London: Appl. Sci. Publ. Ltd. 1982, pp. 439-465.

[16] Barbehön J., Rahmel A. and Schütze M. Behaviour of the Scale on a 9.5Cr Steel under Cyclical Deformation of the Base Metal. *Oxid. Met.* 1988, **30**, 85-94.

[17] Barbehön J., Rahmel A. and Schütze M. Behaviour of Alloy 800 H under Cyclic Deformation and Superimposed Oxidation. *In: Proc. Conf. on High Temperature Alloys for Gas Turbines & Other Applications.* Holland: Reidel, 1986, pp. 1267-1277.

[18] Barbehön J. *Das Verhalten von Oxidschichten auf Metallen bei Zug-, Druck- und zyklischer Verformung.* Fortschritt-Berichte VDI Reihe 5 Nr. 138. Germany: VDI-Verlag, 1988.

[19] Hancock P. The Mechanical Properties of Growing Surface Oxide Scales. *In:* Cathcart J. V., ed. *Proc. Symp. on Stress Effects and the Oxidation of Metals.* USA: AIME. 1974, pp. 155-176.

[20] Nicholls J. R. and Saunders S. R. J. Testing Methods in High Temperature Corrosion. *In:* Rhys-Jones T. N., ed. *Surface Stability.* London: Institute of Metals, 1990, pp. 95-144.

[21] Hall D. J., Booth S. and Evans W. T. Use of Acoustic Emission to Identify Oxide Fracture Modes. *Mater. Sci. & Technol.* 1990, **6**, 53-55.

[22] Pardee W. J. and Graham L. J. Frequency Analysis of Two Types of Simulated Acoustic Emissions. *J. Acoust. Soc. Am.* 1978, **63**, 793-799.

[23] Clough R. B. and Simmons J. A. Reproducible Acoustic Emission Signatures by Indentation in Steels. *Mater. Eval.* 1981, **39**, 1026-1031.

[24] Huntz A. M. Scale Growth and Stress Development. *Mater. Sci. & Technol.* 1988, **4**, 1079-1087.

[25] Manning M. I. Geometrical Effects on Oxide Scale Integrity. *Corros. Sci.* 1981, **21**, 301-316.

[26] Manning M. I. Limits to the Integrity of Oxide Scales Growing on Curved Surfaces and Distending Metal Substrates. *In:* Guttmann V. and Merz M., eds. *Corrosion and Mechanical Stress at High Temperatures.* London: Appl. Sci. Publ. Ltd. 1981, pp. 323-338.

[27] Walter M. Verhalten ausgewählter Systeme Werkstoff/Oxidschicht bei Temperaturwechselbelastung. *Doctoral Thesis.* Germany: Technische Hochschule Aachen, 1991.

[28] Zhao J. G. and Huntz A. M. Theoretical Analysis of the Deflection Test Used in Single-Surface Oxidation of Metallic Samples. *J. Mater. Sci.* 1984, **19**, 3166-3172.

[29] Schütze M. Assessment of the Limits to the Protective Effect of Oxide Scales in High Temperature Technology Set by Deformation of the Substrate Material. *Int. J. Pres. Ves. & Piping.* 1991, **47**, 293-315.

[30] Frost H. J. and Ashby M. F. *Deformation-Mechanism Maps.* Oxford: Pergamon Press, 1982.

[31] Berchtold L., Sockel H. G. and Ilschner B. The Influence of Deformation on the Oxidation of Mild Steel. *In: Behaviour of High Temperature Alloys in Aggressive Environments.* London: Metal Soc., 1980, pp. 927-941.

[32] Cohrt H. and Thümmler R. Degradation Mechanisms of Thermal Barrier Coatings in Bending Tests. *Surf. & Coat. Technol.* 1987, **32**, 339-348.

[33] Saunders S. R. J. and Nicholls J. R. Coatings and Surface Treatments for High Temperature Oxidation Resistance. *Mater. Sci. & Technol.* 1989, **5**, 780-798.

[34] Barnes J. J., Goedjen J. G. and Shores D. A. A Model for Stress Generation and Relief in Oxide-Metal Systems during a Temperature Change. *Oxid. Met.* 1989, **32**, 449-469.

[35] Evans A. G. and Cannon R. M. Stresses in Oxide Films and Relationships with Cracking and Spalling. *Mater. Sci. Forum.* 1989, **43**, 243-268.

[36] Grosskreutz J. C. and McNeil M. B. The Fracture of Surface Coatings on a Strained Substrate. *J. Appl. Phys.* 1969, **40**, 355-359.

[37] Evans A. G., Crumley G. B. and Demaray R. E. On the Mechanical Behaviour of Brittle Coatings and Layers. *Oxid. Met.* 1983, **20**, 193-216.

[38] Riedel H. Deformation and Cracking of Thin Second-Phase Layers on Deforming Metals at Elevated Temperature. *Met. Sci.* 1982, **16**, 569-574.

[39] Heitzer J. The Interaction of a Crack with an Interface Crack as a Theoretical Model for Debonding. *Int. J. Fracture.* 1990, **46**, 271-295.

[40] Schütze M. The Role of the Interaction of Corrosion and Mechanical Factors for the Degradation of Materials. *Mater. Sci. Eng.* 1989, **A121**, 563-569.

[41] Wells C. H., Follansbee P. S. and Dils R. R. Mechanisms of Dynamic Degradation of Surface Oxide. *In:* Cathcart J. V., ed. *Proc. Symp. on Stress Effects and the Oxidation of Metals.* USA: AIME. 1974, pp. 220-244.

[42] Timoshenko J. and Goodier N. *Theory of Elasticity.* 3rd edition. New York: McGraw Hill, 1969.

[43] Evans H. E., Mitchell G. P., Lobb R. C. and Owen D. R. J. A Numerical Analysis of Oxide Spallation. *Report TD/FCB/REP/0070.* Berkeley (UK): Nuclear Electric Plc. 1990.

[44] Lobb R. C., Sasse J. A. and Evans H. E. Dependence of Oxidation Behaviour on Silicon Content of 20%Cr Austenitic Steels. *Mater. Sci. & Technol.* 1989, **5**, 828-834.

[45] Tada J., Paris P. C. and Irwin G. R. *Stress Analysis of Cracks - Handbook.* St. Louis: Paris Productions, 1974.

[46] Evans A. G. and Hutchinson J. W. Effects of Non-Planarity on the Mixed Mode Fracture Resistance of Bimaterial Interfaces. *Acta Metall.* 1989, **37**, 909-916.

[47] McLauchlin I. R. Berkelely (UK): Nuclear Electric Plc. *Private Communication.* 1992

[48] Birchall J. D., Howard A. J. and Kendall K. Flexural Strength and Porosity of Cements. *Nature.* 1981, **289**, 388-390.

[49] Rice R. W. Pores as Fracture Origins in Ceramics. *J. Mater. Sci.* 1984, **19**, 895-914.

[50] Kataoka K., Yamazawa T., Pyun Y.-J. and Homma T. An X-ray Study of Strain Generation Behaviour of a Steel-Scale System during High Temperature Oxidation in Air. *Transactions ISIJ.* 1984, **24**, 365-371.

[51] Pivin J. C., Morvan J., Mairey D. and Mignot J. Determination of the Stress Level in Growing NiO Films by X-ray Diffraction. *Scripta Metallurgica.* 1983, **17**, 179-182.

[52] Liu C., Huntz A.-M. and Lebrun J.-L. Investigation on Origins of Residual Stresses in Ni-NiO System by X-ray Diffraction at High Temperature. *to be published in Journal de Physique.* 1992.

[53] Hurst R. C., Davies M. and Hancock P. The Determination of Fracture Strains of Growing Surface Oxides on Mild Steel at High Temperatures. *Oxid. Met.* 1975, **9**, 161-169.

[54] Khanna A. S., Jha B. B. and Baldev R. Detection of Breakaway Oxidation and Spalling in the Oxide Scales of 2.25CR-1Mo Steel Using Acoustic Emission Technique. *Oxid. Met.* 1985, **23**, 159-176.

[55] Christl W., Rahmel A. and Schütze M. Application of the Acoustic Emission Technique for the Detection of Oxide Scale Cracking during Thermal Cycling. *Mat. Sci. Eng.* 1987, **87**, 289-293.

[56] Christl W., Rahmel A. and Schütze M. Behaviour of Oxide Scales on 2.25Cr-1Mo Steel During Thermal Cycling. II. Scales Grown in Water Vapour. *Oxid. Met.* 1989, **31**, 35-69.

[57] Christl W., Rahmel A. and Schütze M. Behaviour of Oxide Scales on 2.25Cr-1Mo Steel During Thermal Cycling. I. Scales Formed in Oxygen and Air. *Oxid. Met.* 1989, **31**, 1-34.

[58] Matthews J. R. *Acoustic Emission.* New York: Gordon and Breach Science Publ., 1983.

[59] Eisenblätter J. The Origin of Acoustic Emission - Mechanisms and Models. *In: Proc. of a Meeting on Acoustic Emission.* Germany: Deutsche Gesellschaft für Metallkunde, 1979, pp. 189-204.

[60] Spanner J. C. *Acoustic Emission - Techniques and Application.* USA: Intex Publishing Company, 1974.

[61] Williams R. V. *Acoustic Emission.* Bristol: Adam Hilger Ltd., 1980.

[62] Licht T. Acoustic Emission. *Technical Review No. 2.* Denmark: Bruel & Kjaer, 1979.

[63] Waschkies E., Gries H., Deuster G. and Höller P. Grundlagen, fortschrittliche Mess- und Gerätekonzepte sowie Ergebnisse der Schallemissionsprüfung. *Kernenergie.* 1989, **32**, 89-96.

[64] Waschkies E. Transfer-Functions Characterizing the Propagation of AE-Signals. *In:* Höller P., ed. *New Procedures in Nondestructive Testing.* Germany: Springer Verlag, 1983, pp. 447-457.

[65] Muravin G. B., Ship V. V., Lezvinskaya L. M. and Merman A. I. Energy Aspects of AE Inspection of Crack Development with the Use of Different Types of Waves. *Sov. J. Nondestr. Test.* 1989, **25**, 169-176.

[66] Krautkrämer J. and Krautkrämer H. *Werkstoffprüfung mit Ultraschall.* 3rd edition, Berlin: Springer Verlag, 1975.

[67] Rindorf H. J. Acoustic Emission Source Location in Theory and Practice. *Technical Review No. 2.* Denmark: Bruel & Kjaer, 1981.

[68] Fitch C. E. Acoustic Emission Signal Analysis in Flat Plates. *Report 1008.* Richland (USA):Battelle-Northwest Laboratory (BNWL), 1969.

[69] Fowler K. A. and Papadakis E. P. Observation and Analysis of Simulated Ultrasonic Acoustic Emission Waves in Plates and Complex Structures. *ASTM STP 505.* 1972, 222-237.

[70] Scruby C. B. and Drain L. E. *Laser Ultrasonics: Techniques and Applications.* Bristol: Adam Hilger, 1990.

[71] Graham L.J. and Alers G. A. Acoustic Emission in the Frequency Domain: Monitoring Structural Integrity by Acoustic Emission. *ASTM STP 571.* 1975, 11-39.

[72] Buttle D. J. and Scruby C. B. Characterisation of Particle Impact by Quantitative Acoustic Emission. *Report AERE R 13028.* UK:Harwell Laboratory, 1988.

[73] Pollock A. A. A Practical Guide to Acoustic Emission. *Locan AT Handbook.* USA: Physical Acoustics Corporation, 1988.

[74] Scruby C. B. Acoustic Measurement using Point-Contact Transducers. *J. Acoust. Emission.* 1985, **4**, 9-18.

[75] Nielson A. Acoustic Emission Source Based on Pencil Lead Breaking. *Report 80.15.* Denmark: Danish Welding Institute, 1980.

[76] Hill R. Reciprocity and other Acoustic Emission Transducer Calibration Techniques. *J. Acoust. Emission.* 1982, **1**, 73-80.

[77] Pollock A. A. Threshold, Gain, Sensitivity and Noise in ICC-based Systems. *Technical Note TN-103-16-1/88.* USA: Physical Acoustics Corporation, 1988.

[78] Pollock A. A. Acoustic Emission - 2: AE-Amplitudes. *NDT.* 1973, **6**, 264-269.

[79] Graham L. J. and Alers G. A. Spectrum Analysis of Acoustic Emission in A533-B Steel. *Mater. Eval.* 1974, **32**, 31-37.

[80] Raj B., Jha B. B. and Rodriguez P. Frequency Spectrum Analysis of Acoustic Emission Signals Obtained During Tensile Deformation and Fracture of an AISI 316 Type Stainless Steel. *Acta Metall.* 1989, **37**, 2211-2215.

[81] Küppenbender I. and Schütze M. Germany: Dechema Laboratory. *Private Communication.* 1991

[82] Lottermoser J., Waschkies E., Zenner P. and Götz J. Interpretationsmodelle bei der Schallemissionsprüfung auf der Grundlage der Unterscheidung unterschiedlicher Entstehungsmechanismen mittels Methoden der Signalanalyse. *In: Proc. 1st European Conf. on NDT.* Germany: Deutsche Gesellschaft für Zerstörungsfreie Prüfung. 1978, pp. 755-760.

[83] Esmail E. and Grabec I. Application of a Signal Recovery Technique to Acoustic Emission. *Ultrasonics.* 1978, **16**, 87-89.

[84] Sklarczyk C. Schallemissionsanalyse der Bruchvorgänge in Al_2O_3-Keramik. *Jülich-Spez.-Bericht.* Germany: Kernforschungsanstalt Jülich, 1990.

[85] Gerberich W. W. and Hartbower C. E. Some Observations on Stress Wave Emission as a Measure of Crack Growth. *Int. J. Fract. Mechanics.* 1967, **3**, 185-191.

[86] Khan M. A., Shoji T. and Takahashi H. Evaluation of Structural Integrity by AE and Fracture Mechanics Techniques. *Rep. Res. Inst. Strength & Fracture of Materials.* 1983, **16**, 25-36.

[87] Wen L. S., Zhang H. T., Zhou X. K., Guan K., Liao B. and Cao S. Acoustic Emission Research on the Fracture Behaviour of Plasma Sprayed Ni-Al Coating During Bend Testing. *Surf. J. Int.* 1986, **1**, 151-153.

[88] Almond D., Moghisi M. and Reiter H. The Acoustic Emission Testing of Plasma-Sprayed Coatings. *Thin Solid Films.* 1983, **108**, 439-447.

[89] Cox L. The Four-Point Bend Test as a Tool for Coating Characterization. *Surf. Coat. Technol.* 1988, **36**, 807-815.

[90] Khanna A. S., Jha B. B. and Baldev R. Application of Acoustic Emission Technique in High Temperature Oxidation Studies. *In: Proc. 10th Int. Conf. on Metal Corrosion.* India: Madras, 1987, Part 4, pp. 3443-3451.

[91] Bennett M. J. Real Time Studies of Scale Development and Failure. *Report AEA-InTec-0344.* UK: Harwell Laboratory, 1991.

[92] Bennett M. J., Buttle D. J., Colledge P. D., Price J. B., Scruby C. B. and Stacey K. A. Spallation of Oxide Scales from 20%Cr-25%Ni-Nb Stainless Steel. *Mater. Sci. Eng.* 1989, **A120**, 199-206.

[93] Jha B. B., R. Baldev and Khanna A. S. Frequency Analysis of AE Signal Obtained During Breakaway Oxidation and Internal Cracking of 2.25Cr-1Mo Steel at 900 C. *Oxid. Met.* 1986, **26**, 263-273.

[94] Jha B. B., Khanna A. S. and Baldev R. Study of the Oxidation Behaviour of 9Cr-1Mo Steel Using the Acoustic Emission Technique. *J. Mater. Sci.* 1987, **22**, 2823-2827.

[95] Evans A. G., Drory M. D. and Hu M. S. The Cracking and Decohesion of Thin Films. *J. Mater. Res.* 1988, **3**, 1043-1049.

[96] Hu M. S. and Evans A. G. The Cracking and Decohesion of Thin Films on Ductile Substrates. *Acta Metall.* 1989, **37**, 917-925.

[97] Evans A. G. and Hutchinson J. W. On the Mechanics of Delamination and Spalling in Compressed Films. *Int. J. Solid Structures.* 1984, **20**, 455-466.

[98] Ramsey P. M., Chandler H. W. and Page T. F. Bending Tests to Estimate the Through-Thickness Strength and Interfacial Shear Strength in Coated Systems. *Thin Solid Films.* 1991, **201**, 81-89.

[99] Clark J. N. Surface Coatings to Prevent Oxidation during High Temperature Acoustic Emission Studies of Steel. *British Journal of NDT.* 1979, **21**, 312-316.

[100] Ramachandra-Rao Y. V. P. and Madhu A. High Temperature Coatings on Mild Steel. *Transactions of the SAEST.* 1989, **24**, 105-112.

[101] Tsongas D. Investigation of the Oxidation Prevention Abilities of Commercially Available High Temperature Coatings and Paints and their Possible Use for AE Testing. *Final Year Project.* UK: Polytechnic of Wales, 1991.

[102] Goodfellow Catalogue. *Metals and Materials for Research and Industry.* UK: Goodfellow Ltd., 1992.

[103] Mitchell J. R. Unravelling the Mysteries of AE Energy Counts. *Technical Note TN-103-13-3/87.* USA: Physical Acoustics Corporation, 1987.

[104] Morrell R. *Handbook of Properties of Technical and Engineering Ceramics. Part II.* UK: HMSO, 1987.

[105] Harris A. W. and Atkinson A. Oxygen Transport in Growing Nickel Oxide Scales at 600 - 800 °C. *Report AERE R 13421.* UK: Harwell Laboratory, 1989.

[106] Chin Y. S. An Analysis of AE Signals Generated by the Fracturing of Oxide Scales. *Final Year Project.* UK: Polytechnic of Wales, 1991.

[107] Chan R. W. Y. and Hay D. R. A Case Study of Sensitivity of Some Pattern Classifiers used in Sorting Acoustic Emission Signals. *In: Proc. of the 8th Air Force/Defense Advanced Research Projects Agency Symp. on Qualitative NDT.* USA, 1981, pp. 413-420.

[108] Rao S. S. *Mechanical Vibration.* Berlin: Springer Verlag, 1986.

[109] Lynn P. A. *An Introduction to the Analysis and Processing of Signals.* 3rd edition, UK: Macmillan Education Ltd., 1989.